# Mid-Wavelength Infrared Type-II InAs/GaSb Superlattice for Photodetectors

Dhafer Omair Abdullah Alshahrani

A thesis submitted in partial fulfilment of the requirements for the degree of Doctor of Philosophy in the School of Physics and Astronomy

**June 2023**

# Summary

Type-II superlattices (T2SLs) have emerged as a promising technology for infrared detectors compared to the state-of-art mercury cadmium telluride (MCT). T2SLs have shown great potential for mid-wavelength infrared (MWIR) detectors but have yet to attain their theoretically predicted performance. Simulation, fabrication, and characterisation were utilised in this research project to improve the performance levels of MWIR T2SL detectors.

Using the molecular beam epitaxy (MBE) reactor, different interfacial growth schemes were used to accommodate internal strain caused by the lattice mismatches in T2SL. The project involves band heterostructure simulations, growth schemes, structural and optical characterisations, and electrical characterisation of fabricated T2SL p-i-n diode. Reference T2SL samples were evaluated by X-ray diffraction (X-RD), atomic force microscopy (AFM), and transmission electron microscopy (TEM). An 8-band k·p approach for band heterostructure simulation explains PL experimental findings. Photoluminescence (PL) measurements probe the band structure and bandgap energy information. T2SL p-i-n diodes fabrication process was optimised using standard photolithography. The diode electrical performance of the T2SLs was examined by current-voltage (I-V) measurements using a cryogenic probe station.

Investigation of structural and optical properties of the grown T2SL samples with interfacial growth schemes, namely incorporating an InSb compensation interface (IF) layer, was carried out to improve the material quality. AFM and TEM measurements revealed structural degradation due to the additional strain and lattice mismatch introduced by the InSb IF layers. However, including the InSb IF layer has improved the optical property of the T2SL. Band heterostructure simulation was performed to understand the possibility of atomic intermixing and segregation at the T2SL interfaces. Fabrication processes of T2SL single-pixel diodes were performed by wet etch, dry etch, and a combination of both approaches. The I-V characteristics revealed that the current density of the wet-etched devices is improved by approximately four orders of magnitude at low temperatures in comparison with the dry-etched devices, but they are comparable at high operating temperatures (HOT). Lastly, developments of wet etching processes were investigated using inorganic solutions, such as hydrochloric and phosphoric acids and organic solutions, including citric acid.

# Acknowledgements

## Funding and Scholarship

## Statement of Significant Contributions

I conducted photoluminescence (PL) measurements, current-voltage (I-V) and capacitance-voltage (C-V) measurements and performed data analysis. I also performed X-ray diffraction (XRD) data analysis. I undertook the device fabrication process of bulk reference and T2SL wafers and developed a wet chemical etching process.

The author would like to acknowledge the help and assistance of internal and external collaborators. First and foremost, the growth of T2SL samples was performed by Dr Baolai Liang, a crystal grower at the University of California, Los Angeles (UCLA), and the California NanoSystems Institute (CNSI) in the United States of America (USA). Dr Marie Delmas, an ex-postdoctoral researcher in the School of Physics and Astronomy at Cardiff University, initially performed the design, simulation, and fabrication of T2SL samples. After the design and growth of the samples, structural characterisations, including X-ray diffraction (X-RD), atomic force microscopy (AFM), and transmission electron microscopy (TEM), described in Chapter 5, were performed with the assistance from different collaborators. XRD and AFM were carried out by Dr Baolai Liang and his group at the CNSI; however, the author carried out XRD data analysis. Dr Juan Jiménez and Dr Francisco Morales, our collaborators at the University of Cadiz in Spain, performed TEM measurements and analysis of the samples.

Characterisation setups presented in Chapter 4, namely the photoluminescence (PL) and current-voltage (I-V) cryogenic probe station, were designed and assembled by Dr Marie Delmas and Dr Shiyu Xie. My colleague Dominic Kwan has provided initial training on PL and I-V systems. The author has performed PL and I-V measurements, data acquisition, and

analysis presented in this thesis. Furthermore, Dominic Kwan has helped me with the band heterostructure simulations (Nextnano software) presented in Chapter 5.

Dr Marie Delmas initially established a standard fabrication procedure for my research group, presented in Chapter 6. The CR manager in the School of Physics and Astronomy at Cardiff University, Dr Angela Sobiesierski, and her members provided ICS-CR induction and initial usage of device fabrication. But the overall guidance on the device fabrication process was provided by my supervisor Dr Manoj Kesaria. The sample fabrication processes using wet and dry etching methods, described in Chapter 6, were performed by Dominic Kwan and the author. Moreover, the author independently performed the fabrication work presented in the last chapter, Chapter 7.

# List of Publications

The research work presented in thesis Chapters 3, 5, and 6 has already been published in peer-reviewed scientific journals listed below.

1. **D.O. Alshahrani**, M. Kesaria, J.J. Jiménez, D. Kwan, V. Srivastava, M. Delmas, B. Liang, D. Huffaker, and F.M. Morales, Effect of Interfacial Schemes on the Optical and Structural Properties of InAs/GaSb Type-II Superlattices. *ACS Appl. Mater. Interfaces* 15, 8624-8635 (2023). https://doi.org/10.1021/acsami.2c19292

In this paper, I performed PL characterisation and analyses. Band heterostructure simulation was carried out with the help provided by my colleagues at Cardiff. External research collaborators conducted epitaxial growth and TEM characterisation. I wrote all the paper, excluding the sections on TEM characterisation and band heterostructure simulation. Hence, in this thesis, Sections 5.3.3.2, 5.3.4, and 5.4 include the research work published in this paper.

2. **D.O. Alshahrani**, M. Kesaria, E.A. Anyebe, V. Srivastava, and D.L. Huffaker, Emerging Type-II Superlattices of InAs/InAsSb and InAs/GaSb for Mid-Wavelength Infrared Photodetectors. *Adv. Photon. Res.* 3, 2100094 (2022). https://doi.org/10.1002/adpr.202100094

In this review article, I planned, structured, and wrote the whole paper with feedback from my group members. In this thesis, most of the literature review work (Chapter 3) has already been published in this review paper—particularly all sections in Chapter 3, excluding Sections 3.6 and 3.7.

3. M. Kesaria, **D.O. Alshahrani**, D. Kwan, E. Anyebe, and V. Srivastava, Optical and Electrical Performance of 5 μm InAs/GaSb Type-II Superlattice for NOx Sensing Application. *Mater. Res. Bull.* 142, 111424 (2021). https://doi.org/10.1016/j.materresbull.2021.111424

In this article, the epitaxial growth of the device was performed by external research collaborators. I undertook PL measurements and analyses. I performed device fabrication and modelling with the assistance provided by my group members. I wrote most of the paper with feedback and suggestions from my group members. This thesis contains some of the published work in this paper, particularly Sections 5.3.3.1 and 6.4.1.

4. D.C.M. Kwan, M. Kesaria, E.A. Anyebe, **D.O. Alshahrani**, M. Delmas, B.L. Liang, and D.L. Huffaker, Optical and Structural Investigation of a 10 µm InAs/GaSb Type-II Superlattice on GaAs. *Appl. Phys. Lett.* 118, 203102 (2021). https://doi.org/10.1063/5.0045703

This is an additional work which is not directly relevant to my thesis. In this paper, I assisted in carrying out PL measurements and offered feedback and suggestions on the manuscript.

## List of Conference Participations

The author has presented the research work at the following internal and external conferences described below. I have presented my work at seven conferences, as shown below. I also have four participations as a co-author.

1. **D.O. Alshahrani**, J.J. Jiménez, D. Kwan, V. Srivastava, F.M. Morales, M. Kesaria, Effect of Interfacial Engineering on the Structural and Optical Quality of a 5 µm Type-II InAs/GaSb Superlattice. *UK Semiconductors (UKS)* Conference (2022), the $6^{th}$ – $7^{th}$ of July 2022, Hallam Sheffield University, Sheffield, UK, Talk.

2. **D.O. Alshahrani**, The Effect of Interfacial Engineering on the Structural and Optical Properties of a 5 µm Type-II InAs/GaSb Superlattice. Early Career Researcher (ECR) Poster Competition (2022), the 28th of June 2022, The School of Physics and Astronomy, Cardiff University, Cardiff, UK, Poster (I awarded the second-joint prize/place in the poster competition).

3. **D.O. Alshahrani**, J.J. Jiménez, D. Kwan, V. Srivastava, F.M. Morales, M. Kesaria, Effect of Interfacial Schemes on the Structural and Optical Quality of a 5 µm Type-II InAs/GaSb Superlattice. *Semiconductor and Integrated Optoelectronics (SIOE)* Conference (2022), the $12^{th}$ – $14^{th}$ of April 2022, The School of Physics and Astronomy, Cardiff University, Cardiff, UK, Talk.

4. **D.O. Alshahrani**, D. Kwan, E. Anyebe, D.L. Huffaker, V. Srivastava, and M. Kesaria, Optical and Electrical Performance of a 5 µm InAs/GaSb Type-II Superlattice Photodiode for $NO_X$ Gas Detection. *Mid-Infrared Optoelectronic Materials and Devices (MIOMD)* Conference (2021), the $1^{st}$ – $3^{rd}$ of September 2021, University of Surrey, Surrey, UK, (Online) Talk.

5. **D.O. Alshahrani**, Optical and Electrical Characteristics for MWIR InAs/GaSb Type-II Superlattice. *Condensed Matter Physics Postgraduate (CMP-PG)* Conference (2021), the $7^{th}$ of April 2021, The School of Physics and Astronomy, Cardiff University, Cardiff, UK, (Online) Talk.

6. **D.O. Alshahrani**, D.C.M. Kwan, D.L. Huffaker, E. Anyebe, and M. Kesaria, Mid-Wavelength Infrared (MWIR) Type-II InAs/GaSb Superlattice for $NO_x$ Sensing. *Semiconductor and Integrated Optoelectronics (SIOE)* Conference (2021), the 30th of March – 1st April 2021, The School of Physics and Astronomy, Cardiff University, Cardiff, UK, (Online) Talk.

7. **D.O. Alshahrani**, Type-II Superlattices for MWIR Sensing. *Physics Chat* (2021), the 26th of February 2021, The School of Physics and Astronomy, Cardiff University, Cardiff, UK, (Online) Talk.

8. P.D.O' Dowd Phanis, D.C.M. Kwan, **D.O. Alshahrani**, and M. Kesaria, Theoretical Modelling of a Type-II InAs/GaSb Superlattices for Long-Wavelength Infrared Detectors. *Semiconductor and Integrated Optoelectronics (SIOE)* Conference (2022), the 12th – 14th of April 2022, The School of Physics and Astronomy, Cardiff University, Cardiff, UK, Poster.

9. D.C.M. Kwan, **D.O. Alshahrani**, E. Anyebe, D.L. Huffaker, and M. Kesaria, Type-II InAs/GaSb Superlattices on GaAs for 10 μm Infrared Detection. *Mid-Infrared Optoelectronic Materials and Devices (MIOMD)* Conference (2021), the 1st – 3rd of September 2021, University of Surrey, Surrey, UK, (Online) Talk.

10. D.C.M. Kwan, **D.O. Alshahrani**, D.L. Huffaker, E. Anyebe, and M. Kesaria, Long-Wavelength Infrared (LWIR) Type-II InAs/GaSb Superlattice on GaAs. *Semiconductor and Integrated Optoelectronics (SIOE)* Conference (2021), the 1st of April 2021, The School of Physics and Astronomy, Cardiff University, Cardiff, UK, (Online) Talk.

11. P.D.O' Dowd Phanis, D.C.M. Kwan, **D.O. Alshahrani**, D.L. Huffaker, and M. Kesaria, Modelling Type-II Superlattices for Long-Wavelength Infrared Detectors. *Semiconductor and Integrated Optoelectronics (SIOE)* Conference (2021), the 1st of April 2021, The School of Physics and Astronomy, Cardiff University, Cardiff, UK, (Online) Poster.

**Table of Contents**

X

# List of Abbreviations

| Symbol | Definition |
|--------|------------|
| AFM | Atomic Force Microscopy |
| ALD | Atomic Layer Deposition |
| AR | Anti-Reflection |
| BEP | Beam Equivalent Pressure |
| BF-STEM | Bright Field-Scanning Transmission Electron Microscopy |
| BTB | Band-to-Band Tunnelling |
| $C_B$ | Conduction Band |
| CQD | Centre for Quantum Devices |
| Diff | Diffusion |
| EBIC | Electron-Beam Induced Current |
| EBR | Edge Bead Removal |
| ECP | Electrochemical Passivation |
| EDX | Energy-Dispersive X-ray Spectroscopy |
| EQE | External Quantum Efficiency |
| FIB | Focused Ion Beam |
| FIR | Far Infrared |
| FPA | Focal Plane Array |
| FTIR | Fourier Transform InfraRed |
| FWHM | Full Width at Half Maximum |
| G-R | Generation-Recombination |

| | |
|---|---|
| HCl | Hydrochloric |
| HF | Hydrofluoric |
| HH | Heavy Hole |
| HOT | High Operating Temperature |
| HR(S)TEM | High-Resolution (Scanning) Transmission Electron Microscopy |
| HR-TEM | High-Resolution Transmission Electron Microscopy |
| ICP | Inductively Coupled Plasma |
| IF | Interface |
| IPA | Isopropanol Alcohol |
| IQE | Internal Quantum Efficiency |
| IR | Infrared |
| LH | Light Hole |
| $LN_2$ | Liquid Nitrogen |
| LDVT | Linear Differential Variable Transformer |
| LWIR | Long-Wavelength Infrared |
| MBE | Molecular Beam Epitaxy |
| MC | Minority Carrier |
| MCT | Mercury Cadmium Telluride |
| MEE | Migration Enhanced Epitaxy |
| ML | Monolayer |
| MOCVD | Metalorganic Chemical Vapour Deposition |
| MQW | Multi Quantum Well |
| MWIR | Mid-Wavelength Infrared |

| | |
|---|---|
| NFE | Nearly Free Electron |
| NID | Non-Intentionally Doped |
| NEP | Noise Equivalent Power |
| NIR | Near Infrared |
| PC | Photoconductor |
| PD | Photodetector |
| PECVD | Plasma Enhanced Chemical Vapour Deposition |
| PIPS | Precision Ion Polishing System |
| PL | Photoluminescence |
| PR | Photoresist |
| PV | Photovoltaic |
| PVD | Physical Vapour Deposition |
| QCIRPD | Quantum Cascade Infrared Photodetector |
| QDs | Quantum Dots |
| QE | Quantum Efficiency |
| QW | Quantum Well |
| QWIPs | Quantum Well Infrared Photodetectors |
| RHEED | Reflection High-Energy Electron Diffraction |
| RIE | Reactive Ion Etching |
| RSEMI | Reticulated Shallow Etch Mesa Isolation |
| SAED | Selected Area Electron Diffraction |
| SEM | Scanning Electron Microscopy |
| SLS | Strained-Layer Superlattice |

| | |
|---|---|
| SNR | Signal-to-Noise Ratio |
| SRH | Shockley-Read-Hall |
| SWaP | Size, Weight, and Power |
| SWIR | Short-Wavelength Infrared |
| T2SL | Type-II Superlattice |
| TAT | Trap-Assisted Tunnelling |
| TEM | Transmission Electron Microscopy |
| TIS | Teledyne Imaging Sensors |
| UHV | Ultra-High Vacuum |
| UV | Ultraviolet |
| $V_B$ | Valence Band |
| VLWIR | Very Long-Wavelength Infrared |
| XRD | X-Ray Diffraction |

# List of Physics Constants

| Constant | Symbol | Value | Unit |
|---|---|---|---|
| Boltzmann | $K_B$ | $1.38 \times 10^{-21}$ | $m^2\ kg\ s^{-2}\ K^{-1}$ |
| Electron charge | q | $1.60 \times 10^{-19}$ | Coulomb |
| Free electron rest mass | $m_0$ | $9.11 \times 10^{-31}$ | kg |
| Free space permittivity | $\varepsilon_0$ | $8.854 \times 10^{-12}$ | $F.m^{-1}$ |
| Planck | h | $6.63 \times 10^{-34}$ | $m^2\ kg\ s^{-1}$ |
| Reduced Planck | $\hbar$ | $1.055 \times 10^{-34}$ | $m^2\ kg\ s^{-1}$ |
| Stefan-Boltzmann | σ | $5.6703 \times 10^{-8}$ | $W/m^2 K^4$ |
| Wien | b | 2898 | μm.K |
| X-ray wavelength | λ | 0.15406 | nm |

# List of Samples

The table underneath provides an outline of the samples used in this research work. For simplicity, the sample names are kept consistent throughout the thesis.

| Sample ID | Material | Substrate | Design | First Mentioned |
|-----------|----------|-----------|--------|-----------------|
| Sample A | (7/4) monolayers (MLs) of InAs/GaSb T2SL | GaSb | Reference | Chapter 5 |
| Sample B | | GaSb | Reference | |
| Sample C | | GaSb | *pin* photodiode | Chapter 6 |
| Sample D | GaSb substrate | GaSb | Reference | Chapter 7 |
| Sample E | InAs thin film | GaAs | Reference | |
| Sample F | InAs thin film | InAs | *pin* photodiode | |
| Sample G | (12/4) monolayers (MLs) of InAs/GaSb T2SL | GaAs | Reference | |
| Sample H | InGaAs | InP | *pin* photodiode | |
| Sample I | AlGaAsSb thin film | InP | *pin* photodiode | |
| Sample J | InAs/AlSb T2SL | GaSb | *pin* photodiode | |

# List of Figures

## List of Tables

# Chapter 1: Introduction

## 1.1    Infrared detection and applications

The infrared (IR) spectral band refers to the electromagnetic radiation between 0.7 and 1000 μm that is emitted by objects with temperatures greater than 0 K. Detection of electromagnetic radiation in the transparent atmospheric window between 3 and 6 μm, also known as the mid-wavelength infrared (MWIR) spectral band, enables prevalent detector applications. The detectors have several uses, such as chemical detection [1], medical diagnostics [2], space and astronomy [3], security and defence [4], and navigation and objects identification [5]. A significant challenge that humanity faces globally is environmental pollution. Toxic gases such as carbon dioxide ($CO_2$), carbon monoxide (CO), nitric oxide (NO), nitrogen dioxide ($NO_2$), and methane ($CH_4$) have significant absorption signatures in the MWIR spectral range, which has increased the demand for powerful and sensitive MWIR detectors (see Figure 1.1).
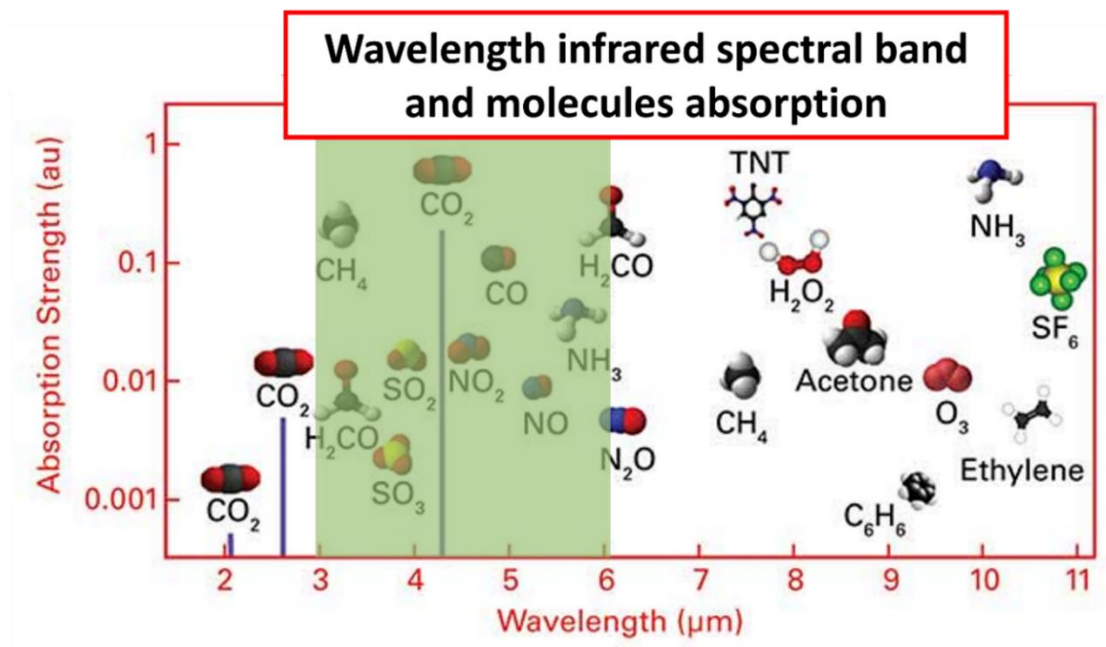
Figure 1.1: Absorption of toxic gases and molecules in the IR spectral band between the wavelengths 2 and 11 μm. The highlighted green region shows the various toxic gases which can be detected in the MWIR region (3-6 μm). The figure is adapted from reference [6].

For instance, NO and NO$_2$ gases, known as NO$_x$, are highly toxic and detrimental to air quality and are regarded as the principal cause of air pollution, resulting in smog and acid rain [7]. NO$_x$ is a harmful gas created during the combustion of fossil fuels in power plants [8] and automobile engines [9], as well as during lightning strikes [10]. It plays a crucial role in a variety of functions in the human body, which is generated in inflammatory processes [11]. Therefore, monitoring NO$_x$ concentration is a vital aspect of automotive manufacturing. For this reason, sensitive and powerful detectors operating at a high temperature within the MWIR range are required for the low-cost detection of these toxic gases.

## 1.2   Dominant and emerging technologies for infrared detection

Mercury cadmium telluride (MCT/HgCdTe), indium antimonide (InSb), and quantum well-infrared photodetector (QWIP) are currently the most dominant detectors in the market. MCT, an II-VI semiconductor material, offers low dark current, has flexible bandgap energy, benefits from high quantum efficiency (QE~80 %), and has strong optical absorption [12]. Nevertheless, MCT is afflicted with high material toxicity boosting restrictive regulations [13], poor uniformity, manufacturing complexity, and high cost and low producibility yield [14], [15]. InSb and QWIPs, III-V semiconductors, combine the advantages of excellent material uniformity and mature material growth. However, InSb can only operate at a low-temperature range between 80 and 100 K, limiting its application for uncooled IR imaging systems [16]. QWIPs suffer from low quantum efficiency (QE~15 %) and high dark current in the MWIR regime [17]. Overall, to attain a high signal-to-noise ratio (SNR) at high operating temperatures (HOT), these dominant IR technologies continue to rely on cryogenic cooling systems, which hampers their capabilities for small size, weight, and power consumption (SWaP) applications [18]. Therefore, due to the limitations involved with those material systems, research activities have been undertaken to search for alternative material systems for MWIR detectors that combine the robustness of III-V materials with the high performance of MCT.

Type-II superlattice (T2SL) material systems, namely the ''Ga-based or containing'' InAs/GaSb, have emerged as a promising candidate and competitive technology with the current state-of-art detectors. Sai-Halasz and Esaki initially proposed the idea of InAs/GaSb SL in 1977 [19]. Ten years later, it was then proposed for use in IR detection applications by Smith and Mailhiot

[20]. In 1996, the first high-performance detector based on InAs/GaInSb T2SL was reported [21]. Since then, T2SL has received more attention for IR detection and has become a promising technology with immense potential to surpass the current state-of-the-art MCT detectors. This is primarily due to the favourable quality of T2SL material and detector, including the reduction of band-to-band (BTB) tunnelling current resulting from the larger electron effective mass and lower mobility [22] and suppression of non-radiative Auger recombination [23], [24], [25] due to the tunability of bandgap energy and spatial separation of electrons and holes. Not only that, but T2SL has additional advantages, such as excellent material uniformity over large areas, structural stability due to strong chemical bonds [26], [27], low growth and manufacturing costs [28], and availability of lattice-matched substrates [28]. Due to these substantial advantages, T2SL has been theoretically predicted to exceed the current state-of-art MCT detectors. Despite the rapid progress, the performance level of InAs/GaSb T2SL has not yet reached the performance level of MCT detectors. Consequently, this argument has opened a possible research route to determine what limiting mechanisms impact the performance level of T2SL.

Figure 1.2 depicts a summary of increased research publications on the developments of InAs/GaSb T2SL material quality and device performance over the past five decades. The percentage of research publications was around 11 % since the initial investigation of this material system in the 1970s. The proportion then increased to approximately 19 % between 1990 and 2000. Between 2001 and 2010, research activities on Ga-based T2SL IR detectors increased to approximately 31.5 %, indicating an increase in the number of published research articles on the topic. Lastly, the number of research publications has been growing again to reach 38.7 % over the last ten years, which indicates that there is room for research developments to optimise T2SL materials and devices.

This research work, therefore, investigates different research aspects to enhance the performance level of MWIR InAs/GaSb T2SL detectors with the ultimate goal towards allowing them to fulfil their predicted performance level, overcome the performance level of MCT, and be the leading technology for use in the next generation of HOT applications. Section 3.7 provides more details on the overall aim and objectives of the current research work, but the research objectives are herein briefly presented. In this research project, the objectives below have been set to fulfil the overall aim.
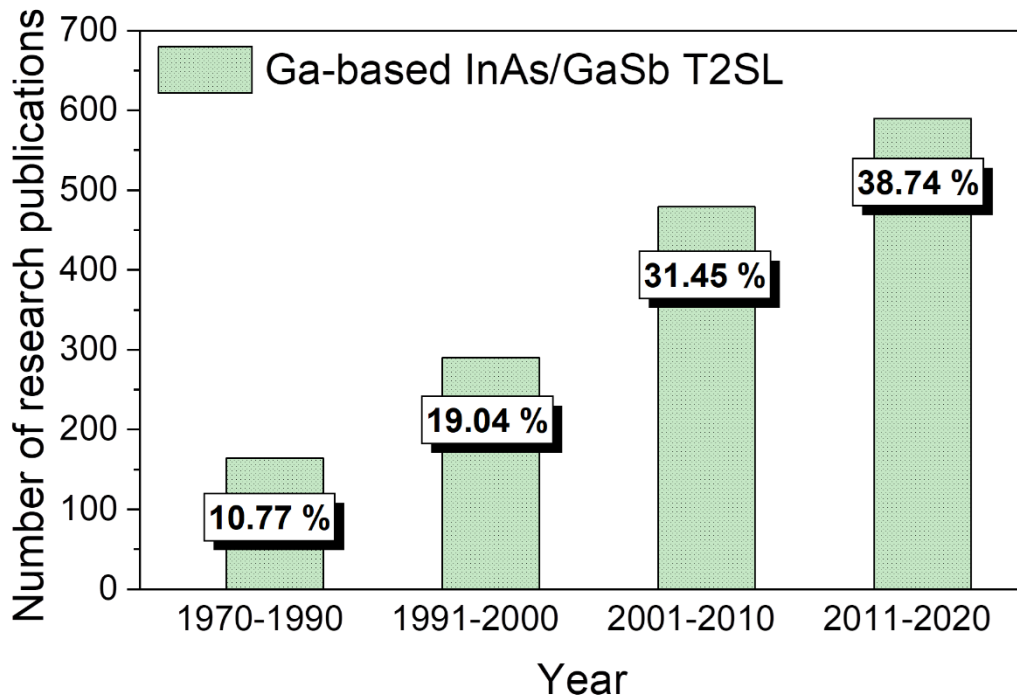
Figure 1.2: A summary of the number of research articles published on Ga-based InAs/GaSb T2SL between 1970 and 2020, expressed as a percentage. Web of Science search results utilising ''InAs/GaSb type-II superlattices'' in the titles, abstracts, and keywords.

- Material growth and characterisation of T2SLs using different interfacial schemes

For this objective, samples were epitaxially grown using various growth schemes. The impact of interfacial growth schemes on the materials' characteristics was then studied using various methods, such as X-ray diffraction (XRD), atomic force microscopy (AFM), photoluminescence (PL), transmission electron microscopy (TEM), and band heterostructure simulation.

- Development of T2SLs device fabrication schemes

For this objective, T2SL devices were fabricated using different etching methods, including wet etching, dry etching, a combination of both, and surface protection/passivation. The I-V measurements used a cryogenic probe station to evaluate the devices' electrical performance.

- Development of Sb-based structures using alternative etching recipes

For this objective, the wet etching approach was developed using alternative recipes. These include phosphoric, sulphuric, hydrochloric, and citric acids. The performance of the fabricated devices was evaluated by I-V characterisation.

Typical IR 384 x 288 focal plane arrays (FPAs) consist of small-sized ~25μm pixels with interspacing of around 10 μm [29]. The realisation of FPA of InAs/GaSb T2SL photodiodes necessitates an etching technique that can yield devices with clean etched pixel sidewall surfaces and favourable anisotropic characteristics.

Semiconductors can be fabricated into devices using either wet or dry etching methods. Despite the relative ease of use and cost-effectiveness of wet chemical etching compared to dry etching, fulfilling the necessary criteria with conventional wet chemical etchants for III-V semiconductor materials remains challenging. Their tendency to undercut the mesa sidewalls is the primary reason [30]. Another issue is the frequent formation of an oxidation layer during GaSb etching in an acidic environment or an acid/hydrogen peroxide ($H_2O_2$) solution [31]. This oxide layer impedes the etching process, develops a rough surface, and increases leakage current. Furthermore, it is apparent that in order to qualify conventional wet etchants for etching T2SL single or pixel devices, it is necessary to address the issues of surface roughness and poor anisotropy that these etchants produce [30], [31]. On the other hand, the dry etching approach is more favourable and offers some advantages, including high control precision, good uniformity, and isotropy [32].

Therefore, we have devised various etching techniques in this thesis, including wet chemical etching, dry etching, combining the two, and surface passivation. I-V measurements were carried out to examine the impact of dissimilar etching approaches on the device's electrical properties.

## 1.3   Thesis structure

The organisation of the thesis is presented as follows. Chapter 1 has already introduced the research field and its need. This chapter has provided insights into IR detection and its applications and the dominant and emerging technologies.

Chapter 2 provides the fundamental concepts and background of the physics behind MWIR T2SL-based detectors. This chapter contains the physics of IR radiation, a discussion of different detector types, semiconductor band structure, and strained layers epitaxy. The chapter ends with the figures of merit of IR detectors.

Chapter 3 discusses the current research and reviews the existing state-of-art T2SL materials and devices' performance compared with the MCT detectors. It explores other research developments and advances made in T2SL IR detectors, including barrier IR detectors and quantum cascade infrared photodetectors (QCIRPDs). This chapter also highlights the motivation behind the current research work.

Chapter 4 provides a detailed description of the experimental and theoretical methods used for this research work. This chapter includes precise research tools for growing materials, characterisation, simulation, and device fabrication.

Chapter 5 reports on the structural and optical properties of the grown T2SL samples. Herein, after the growth of reference samples on GaSb substrates using different interfacial growth schemes of the SLs, a comparative structural and optical characterisation are undertaken to provide a detailed study of the influence of the interfacial schemes on the properties of the samples.

Chapter 6 reports on the fabrication process and electrical characterisations of T2SL single-pixel detectors. It also reports on the developments in the fabrication process using different etching techniques, including wet and dry etching and surface protection. The efficacy of the fabricated devices is then compared to that of the most advanced T2SL and MCT detectors presently available.

Chapter 7 outlines the wet etching developments of Sb-based material systems using alternative wet etching recipes to fabricate InAs/GaSb T2SL utilising other wet etching recipes. This chapter uses several material systems to optimise the etching process. Various chemicals are investigated, including phosphoric, sulphuric, citric, and hydrochloric acids, and preliminary outcomes are reported.

Chapter 8 summarises the overall research work and outcomes, discusses the limitations, and offers suggestions for future research work.

# Chapter 2: Scientific Background

This chapter provides a detailed description of the fundamental concepts and physics of IR radiation and the band structure of semiconductor materials. Strained layer epitaxy and its effect on the band structure are discussed. The operating principles of various types of IR detectors are described in terms of their suitability for different applications. Finally, the figures of merit of photodetectors are explained.

## 2.1    Concepts of infrared radiation

Electromagnetic radiation is present in a continuous range of wavelengths, as seen in Figure 2.1. Only a fraction of the electromagnetic radiation spectrum is perceptible to the human eye. Particular wavelength ranges are divided and named from shortest to longest wavelength. The electromagnetic radiation spectrum can be categorised as follows: gamma rays (nm), X-rays (nm), ultraviolet (UV) light (nm), visible light (nm), IR (nm), microwaves (mm-cm), and radio waves (cm-km); which are depicted in Figure 2.1. The IR radiation can be characterised as photons that move at the speed of light in a wave-like manner. The energy of each photon is inversely proportional to its wavelength: $E_{photon}$ = $h\nu$ = $hc/\lambda$ (eV), where $h$ is Planck's constant, $\nu$ is the frequency, $c$ is the speed of light, and $\lambda$ is the wavelength. The IR radiation spectrum has a broad range of wavelengths ranging between 0.7 μm and 1 mm with a low atmospheric transmission window between 5 and 8 μm and is divided into the following sub-groups [33]:

- Near-infrared (NIR) region is from 0.7 to 1.4 μm,

- Short wavelength infrared (SWIR) region is between 1.4 and 3 μm,

- Mid-wavelength infrared (MWIR) region is between 3 and 5 μm,

- Long-wavelength infrared (LWIR) region is between 8 and 14 μm,

- Very long wavelength infrared (VLWIR) region is between 14 and 32 μm,

- Far-infrared (FIR) region is between 32 μm and 1 mm.
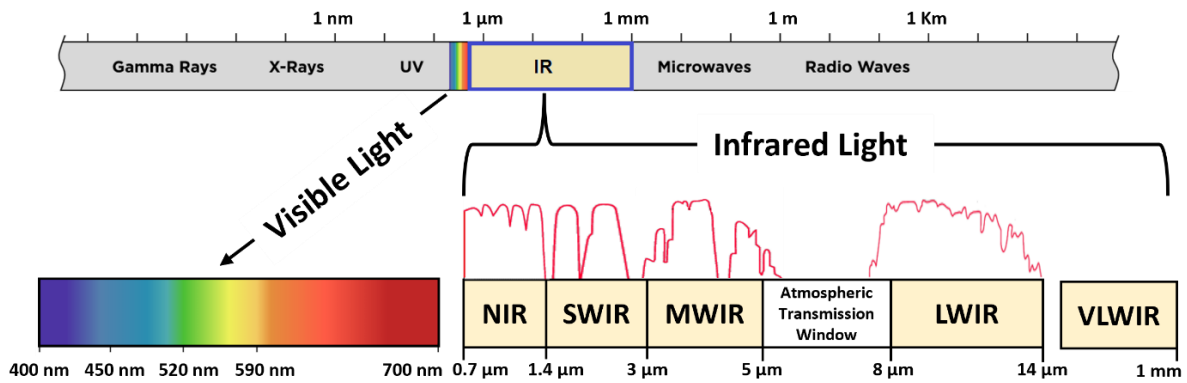
Figure 2.1: Electromagnetic radiation spectrum of light and the corresponding wavelengths. As can be seen, the atmospheric absorption window is from 0.7 up to 14 µm with a low atmospheric transmission window between 5 and 8 µm.

## 2.2    Blackbody radiation

There are three significant laws associated with blackbody radiation. These laws are discussed in this section.

### 2.2.1   Planck's law

The probability distribution of the wavelength emitted by a blackbody at a particular temperature is explained by Planck's law, expressed as follows [34]:

$$B(\lambda, T) = \frac{2hc^2}{\lambda^5} \frac{1}{exp^{\left(\frac{hc}{\lambda K_B T}\right)} - 1} \tag{2.1}$$

where $B(\lambda,T)$ is the blackbody radiation as a function of wavelength and temperature, $h$ denotes a Planck's constant in which $h = 6.626 \times 10^{-34}$ J.sec, $c$ is the speed of light, $K_B$ is a Boltzmann constant where $K_B = 1.38 \times 10^{-21}$ J/K.

### 2.2.2   Stefan – Boltzmann law

Stefan – Boltzmann law is defined as how much energy is radiated per unit area per unit time or how much power is emitted by an object with a temperature ($T$). This law can be expressed using the following equation [34]:

8

$$J = \sigma T^4 \qquad\qquad\qquad (2.2)$$

where $\sigma$ is the Stefan – Boltzmann constant in which $\sigma$ = 5.6703x10⁻⁸ W/m²K⁴, and T is the temperature in Kelvin. The total power radiated from an object is:

$$P = J A \varepsilon \qquad\qquad\qquad (2.3)$$

where $A$ is the surface area of the object, $\varepsilon$ denotes the emissivity, usually between 0 and 1. Hence, an ideal radiator, such as a perfect blackbody that absorbs all incident radiation, would have an emissivity value of $\varepsilon$ = 1. In contrast, any object that does not absorb all incident radiation emits less total energy and is characterised by its emissivity value as $\varepsilon$ < 1.

### 2.2.3  Wien's displacement law

Wien's law states the relationship between the wavelength associated with the maximum intensity at a specific temperature as expressed in the following formula [34]:

$$\lambda_{max} = \frac{b}{T} \qquad\qquad\qquad (2.4)$$

where $\lambda_{max}$ is the maximum wavelength of the radiated emission from an object, $b$ refers to Wien's constant, equal to 2898 µm.K, and $T$ is the temperature in Kelvin. For example, a human has an internal body temperature of 310 K, so the maximum wavelength calculated using Wien's law is approximately 9.3 µm. This is invisible light which is located in the LWIR spectrum region.

Figure 2.2 depicts the three curves of different temperatures and the calculated Wien's wavelength. It can be noted that when the temperature increases, measurements at lower wavelengths are required. In addition, the wavelengths at each peak intensity of blackbody radiation shift from higher (invisible light) to lower (visible light) wavelengths as the temperature rises.
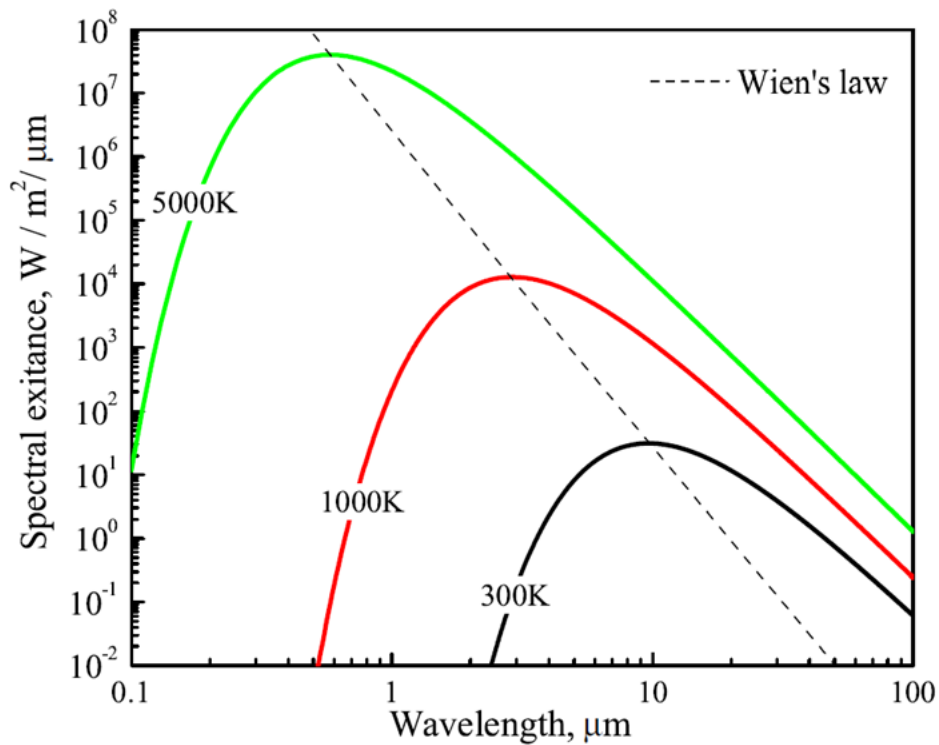
Figure 2.2: Radiant spectral emission of a blackbody versus wavelength at different temperatures (300 K, 1000 K, and 5000 K). The figure is adapted from reference [33].

## 2.3 Semiconductors band structure

The electronic band structure of a solid in solid-state physics characterises the spectrum of energy levels available to electrons. It also identifies the energy ranges that electrons are prohibited from occupying, referred to as bandgaps or forbidden bands. Band theory determines the energy bands and bandgaps by analysing the permissible quantum mechanical wave functions for an electron in a periodic lattice of atoms. Band theory has effectively elucidated various physical characteristics of solids, including electrical resistivity and optical absorption. Moreover, it serves as the fundamental basis for comprehending the functionality of all solid-state devices, such as transistors and solar cells. Two complementary models for electrons in solids are nearly free electron model and tight-binding model [35]. In a nearly free electron model, electrons move almost freely within the material. Their electronic states resemble free electron plane waves, only slightly perturbed by the crystal lattice. In a tight binding model, electrons are tightly bound to individual atoms. It considers the hybridisation of atomic orbitals into molecular orbitals with different energies [36].

10

### 2.3.1 Nearly free electron (NFE) model

The free electron model features a continuous distribution of permissible energy values ranging from zero to infinity. This is illustrated in the following equation:

$$\epsilon_k = \frac{\hbar^2}{2m}\left(k_x^2 + k_y^2 + k_z^2\right) \tag{2.5}$$

where periodic boundary conditions are applied to a cube with side length L,

$$k_x^2 + k_y^2 + k_z^2 = 0\ ;\ \pm\frac{2\pi}{L}\ ;\ \pm\frac{4\pi}{L}\ ;\ .... \tag{2.6}$$

The free electron wavefunctions have the following structure:

$$\psi_k(\boldsymbol{r}) = \exp(i\boldsymbol{k}\cdot\boldsymbol{r}) \tag{2.7}$$

They represent running waves and carry momentum p = ℏk. The band structure of a crystal is commonly described using the nearly free electron (NFE) model, where the band electrons are considered to be minimally affected by the periodic potential of the ion cores. This model addresses nearly all qualitative inquiries on the behaviour of electrons in metals.

It is known that Bragg reflection is a distinctive characteristic of wave propagation in crystals. Bragg reflection of electron waves in crystals involves energy gaps. These energy gaps play a critical role in distinguishing between insulating and conducting solids.

We will discuss the physical explanation for the energy gaps in a linear solid with a lattice constant of a. Figure 2.3 quantitatively displays the low energy sections of the band structure. Part (a) represents totally free electrons, while part (b) depicts electrons that are nearly free, but with an energy gap occurring at $k = \pm\frac{\pi}{a}$.
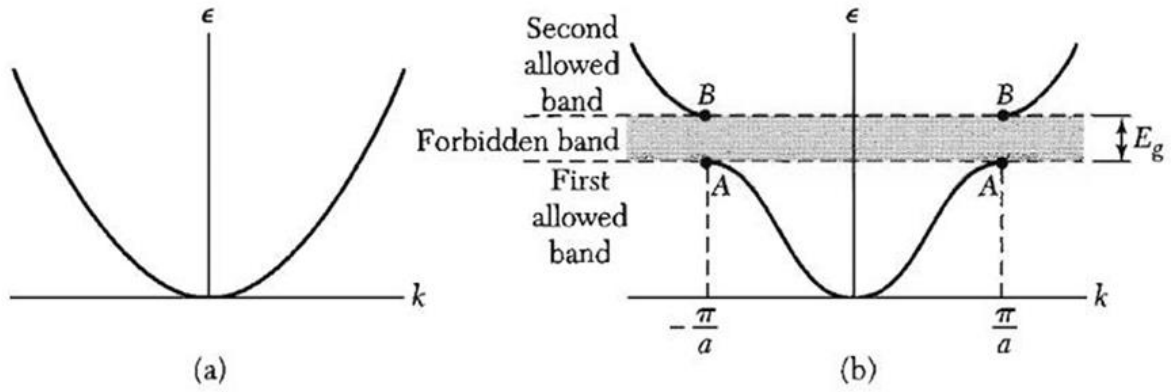
Figure 2.3: (a) Plot of energy E versus wavevector k for a free electron and (b) plot of energy versus wavevector for an electron in a monatomic linear lattice of lattice constant a. The energy gap $E_g$ shown is related to the first Bragg reflection at $k = \pm\frac{\pi}{a}$; other gaps are found at higher energies at $k = \pm\frac{n\pi}{a}$ for integral values of $n$. This figure is adapted from reference [37].

The Bragg condition $(k + G)^2 = k^2$ for diffraction of a wave of wavevector k becomes in one dimension,

$$k = \pm\frac{1}{2}G = \pm\frac{n\pi}{a} \tag{2.8}$$

where $G = 2\pi n/a$ is a reciprocal lattice vector and $n$ is an integer. The first reflections and the first energy gap occur at $k = \pm\pi/a$. The region in k space from $-\pi/a$ to $\pi/a$ represents the first Brillouin zone of this lattice. Other energy gaps occur for other values of the integer $n$.

The wavefunctions at $k = \pm\pi/a$ are neither the free electron traveling waves $\exp(i\pi x/a)$ or $\exp(-i\pi x/a)$. At these specific values of k, the wavefunctions consist of equal components of waves moving in opposite directions. When the Bragg reflection condition $k = \pm\pi/a$ is met by the wavevector, a wave traveling to the right is Bragg-reflected to travel to the left, and vice versa. Each subsequent Bragg reflection will reverse the direction of travel of the wave. A standing wave is a wave that remains stationary and does not propagate in any direction.

Standing waves symbolise the time-independent state. Two distinct standing waves can be created from the two travelling waves,

12

$$\exp\left(\pm\frac{i\pi x}{a}\right) = \cos\left(\frac{\pi x}{a}\right) \pm i\sin\left(\frac{\pi x}{a}\right) \qquad (2.9)$$

so that the standing waves are

$$\psi(+) = \exp\left(\frac{i\pi x}{a}\right) + \exp\left(\frac{-i\pi x}{a}\right) = 2\cos\left(\frac{\pi x}{a}\right) \qquad (2.10)$$

$$\psi(-) = \exp\left(\frac{i\pi x}{a}\right) - \exp\left(\frac{-i\pi x}{a}\right) = 2i\sin\left(\frac{\pi x}{a}\right) \qquad (2.11)$$

The standing waves are designated as $(+)$ or $(-)$ based on whether they reverse sign when $x$ is replaced with $-x$. Both standing waves consist of an equal combination of right- and left-directed travelling waves.

## 2.3.2 Origin of the bandgap energy

The two standing waves $\psi(+)$ and $\psi(-)$ accumulate electrons in distinct locations, resulting in varying potential energy values inside the lattice's ion field. This is the region where the energy gap is located. The probability density of a particle is given by the expression $\rho = \psi^*\psi = |\psi|^2$. For a pure traveling wave $\exp(ikx)$, the charge density is constant since $\rho = \exp(-ikx)\exp(ikx) = 1$. The charge density varies for linear combinations of plane waves. Let us consider the standing wave $\psi(+)$ in Equation (2.10); in this case, we have,

$$\rho(+) = |\psi(+)|^2 \; \alpha \; \cos^2 \pi x/a \qquad (2.12)$$

This function accumulates electrons (negative charge) on the positive ions located at $x = 0, a, 2a, \ldots\ldots$ in Figure 2.4, where the potential energy is at its minimum.
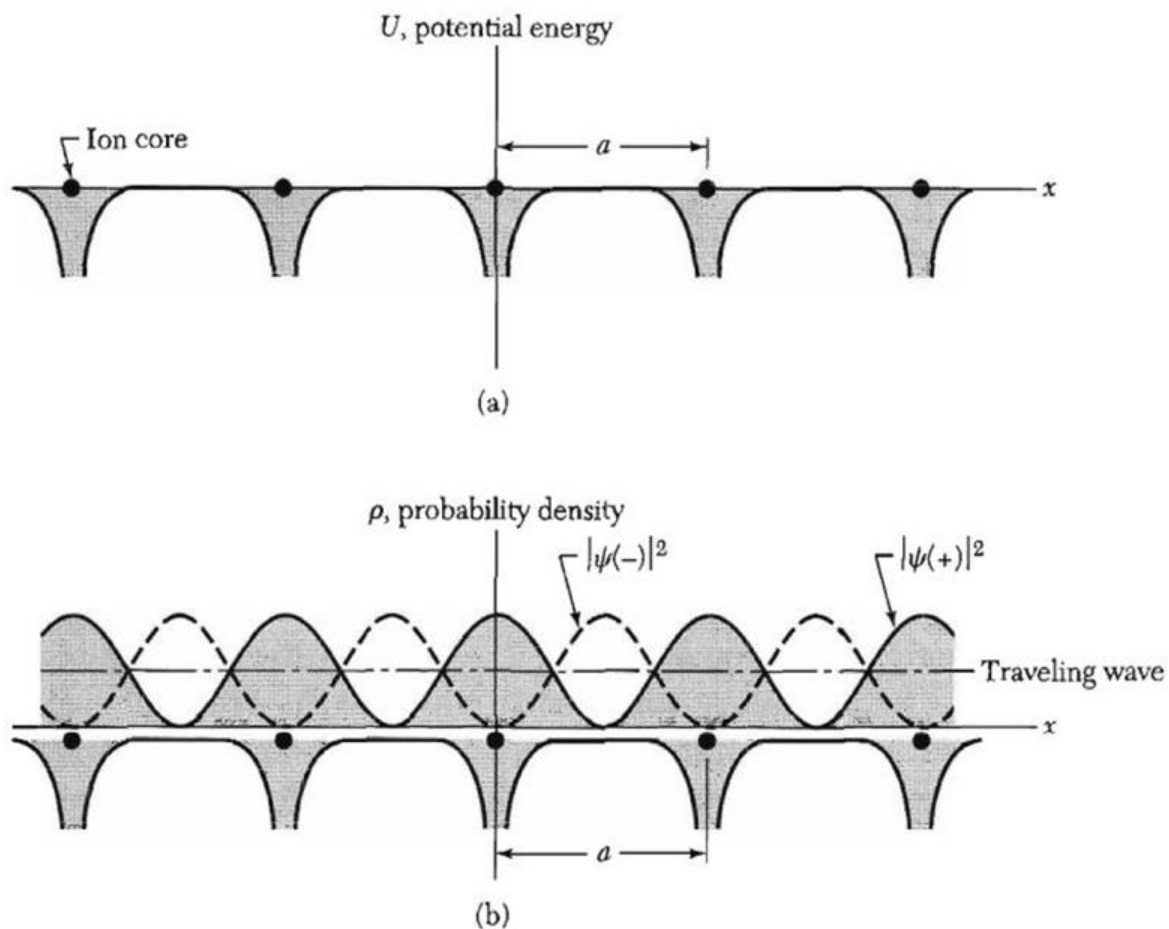
Figure 2.4: (a) The potential energy of a conduction electron varies in the field of a linear lattice's ion cores. (b) The probability density distribution $\rho$ in the lattice is given by $|\psi(-)|^2 \alpha \sin^2 \pi x/a$; $|\psi(+)|^2 \alpha \cos^2 \pi x/a$; as well as for a traveling wave. The wavefunction $\psi(+)$ accumulates electronic charge on the positive ions' cores, reducing the potential energy compared to the average potential energy experienced by a traveling wave. The wavefunction $\psi(-)$ accumulates charge in the region between the ions, increasing the potential energy compared to a traveling wave. This figure is crucial in comprehending the origin of the energy gap. This figure is adapted from reference [37].

Figure 2.4(a) illustrates the change in electrostatic potential energy of a conduction electron caused by the positive ion cores. The ion cores carry a positive charge due to the ionisation of atoms in the metal, when valence electrons are removed to create the conduction band. An electron in the vicinity of a positively charged ion possesses a negative potential energy, resulting in an attractive force between the two particles.

For the other standing wave $\psi(-)$ the probability density is,

$$\rho(-) = |\psi(-)|^2 \alpha \sin^2 \pi x/a \qquad\qquad (2.13)$$

which concentrates electrons away from the ion cores. Figure 2.4(b) displays the electron concentration for the standing waves $\psi(+), \psi(-)$, as well as for a traveling wave.

When calculating the average or expected values of the potential energy over these three charge distributions, it is observed that the potential energy of $\rho(+)$ is lower than that of the traveling wave, while the potential energy of $\rho(-)$ is higher than the traveling wave. An energy gap of width $E_g$ exists when the energies of $\rho(-)$ and $\rho(+)$ differ by $E_g$. Just below the energy gap at points A in Figure 2.3(b) the wavefunction is $\psi(+)$, and just above the gap at points B the wavefunction is $\psi(-)$.

- Metals and insulators

When the valence electrons completely occupy one or more bands while leaving others vacant, the crystal will exhibit insulating properties. An insulator will not conduct current when subjected to an external electric field. It is assumed that the electric field is not strong enough to disrupt the electronic structure. If a band is completely filled and there is an energy gap separating it from the next higher band, it is impossible to alter the overall momentum of the electrons continuously when all available states are occupied. No alterations occur when the field is implemented. Unlike free electrons, the value of k does not increase uniformly in a field in this case. A crystal can act as an insulator if the primitive cell of the crystal contains an even number of valence electrons. Electrons in tightly bonded inner shells are an exception to band theory. When a crystal contains an even number of valence electrons per primitive cell, it is important to determine if the energy bands overlap. When energy bands overlap, rather than a single filled band resulting in an insulator, two partially filled bands can lead to a metallic state, as illustrated in Figure 2.5. This figure depicts the occupied states and band structures of an insulator, a metal, or a semimetal.
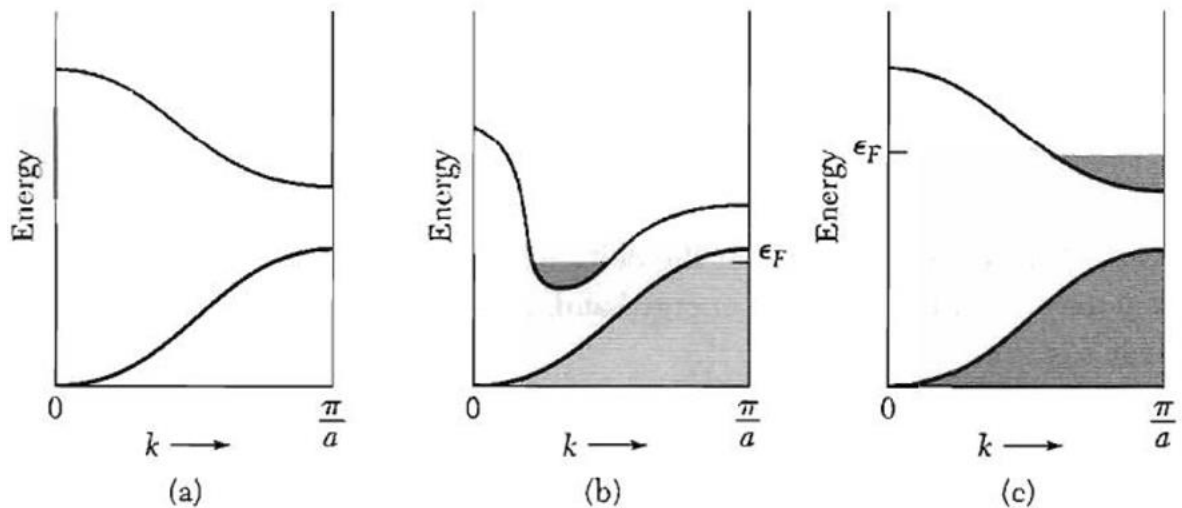
Figure 2.5: A schematic diagram illustrates the occupied states and band structures of (a) an insulator, (b) a metal or semimetal due to band overlap, and (c) a metal due to electron concentration. In (b) the overlap is not required to happen in the same directions within the Brillouin zone. When there is a small overlap involving only a few states, it is referred to as a semimetal. This figure is adapted from reference [38].

Alkali metals and noble metals each have one valence electron in their primitive cell, classifying them as metals. Alkaline earth metals possess two valence electrons per primitive cell, potentially behaving as insulators. However, their energy bands overlap, resulting in metallic properties, though not of high quality. Diamond, silicon, and germanium have two valence four atoms each, resulting in eight valence electrons per primitive cell. The bands do not overlap, making the pure crystals insulators at absolute zero.

### 2.3.3  Direct and indirect bandgap semiconductors

Semiconductor materials can be classified into direct and indirect bandgaps based on the bandgap's nature and the carriers' optical transition. As an illustration, in direct bandgap materials, such as GaAs, InAs and InSb, the transition of electrons and holes occurs between the conduction band minimum and valence band maximum at the same momentum (k-space), as shown in Figure 2.6(a). Therefore, the resultant transition of this process leads to providing energy difference ($E_g$) with the emission of light (photon). On the other hand, if the transition of electrons and holes occurs at different momentum (k-points), this process is called indirect transition, as shown in Figure 2.6(b); such a process occurs in silicon (Si) and germanium (Ge) materials (group IV semiconductors). Hence, the energy released in this

16

process is not converted into light emission. Still, it might undergo some defect state within the bandgap and part of the energy contributes as heat (or thermal loss) to the lattice of the materials.
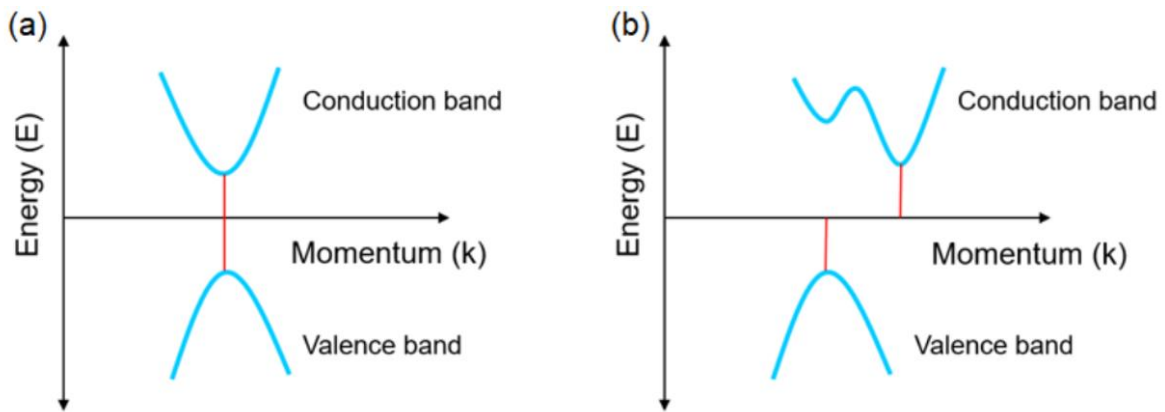


Figure 2.6: Bandgap structures for semiconductors. (a) Direct bandgap in which the valence band maximum and conduction band minimum are located at the same k-point, and (b) indirect band structure in which the valence band maximum and conduction band minimum are situated at different k-points.

### 2.3.4  Band structure alignments

The energy band structure for two different non-intentionally doped semiconductor materials is represented in Figure 2.7. As can be seen, the conduction and valence band energies for the two materials are represented as $E_{c(A)}$, $E_{c(B)}$ and $E_{v(A)}$, $E_{v(B)}$, respectively. The Fermi energy level is defined as the energy halfway between the conduction and valence bands and refers to as $E_{f(A)}$ and $E_{f(B)}$. The conduction and valence bands' energy difference for materials A and B has been indicated as the conduction and valence band offsets ($\Delta E_c$ and $\Delta E_v$). $\chi^A$ and $\chi^B$ are referred to as the electron affinities for materials A and B, which are defined as the energy needed for an electron to liberate from the conduction band to the vacuum level. Determination of the conduction band offsets for both materials can be done by calculating the difference between the electron affinities as follows [39]:

$$\chi^B - \chi^A = \Delta E_c \qquad (2.14)$$

where $X^A$ and $X^B$ are the electron affinities for materials A and B, in which each semiconductor material exhibits its own $X$ parameter. This $X$ value determines the band structure alignment of the two materials. Moreover, the valence band offsets for both materials are determined using the following expression [39]:

$$\left(X^B + E_{g(B)}\right) - \left(X^A + E_{g(A)}\right) = \Delta E_v \qquad (2.15)$$

The bandgap energy can also be defined as the energy difference from the conduction to valence bands as follows [39]:

$$E_{g(A)} - E_{g(B)} = \Delta E_c + \Delta E_v \qquad (2.16)$$
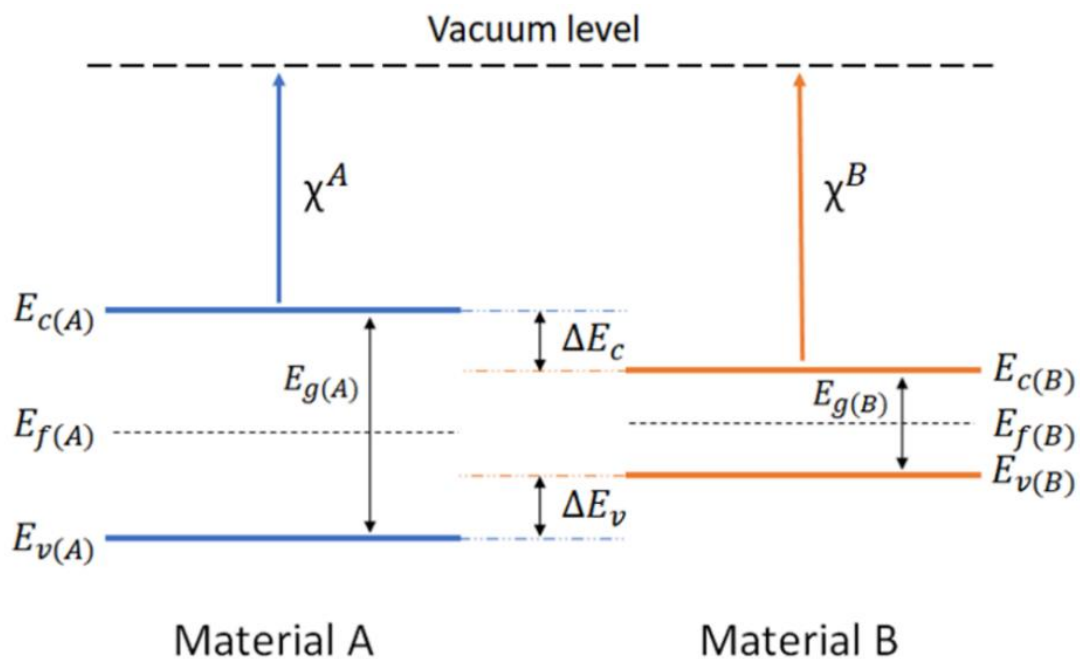


Figure 2.7: Band structure for two different undoped materials A and B where the bandgap energy for material A is higher than material B. $X^A$ and $X^B$ refer to the electron affinity in which the energy required to liberate electrons to move from the conduction band to the vacuum level. $E_{c(A)}$, $E_{v(A)}$, $E_{c(B)}$, and $E_{v(B)}$ are referred to as the conduction and valence band energies of materials A and B, respectively. $E_{f(A)}$ and $E_{f(B)}$ are the fermi energy levels for these two materials. $\Delta E_c$ and $\Delta E_v$ refer to the differences between the conduction and valence bands and the energy bandgaps are labelled as $E_{g(A)}$ and $E_{g(B)}$.

Therefore, when the two semiconductor materials are joined together, this generates energy discontinuities at the IF due to the fermi energy levels and electron affinities differences,

which forms a heterojunction structure. Figure 2.8 shows various possibilities and classifications of band structure alignments depending on the conduction and valence band offsets ($\Delta E_c$ and $\Delta E_v$) and electron affinities ($X$). These different types of band structures are classified as type-I and type-II, which are discussed in the following sections.

### 2.3.4.1   Type-I heterojunction

As schematically shown in Figure 2.8(a), in type-I band alignment, the conduction band of the material with the larger bandgap is of higher energy than the material with the smaller bandgap, and vice versa, the valence band of the material with the larger bandgap has lower energy than the material with the smaller bandgap. Both electrons and holes are confined in the material with the smaller bandgap and recombine through direct transitions. An example of this structure is the band alignment formed between InAs/GaAs and GaSb/AlSb.

### 2.3.4.2   Type-II heterojunction

As represented in Figure 2.8(b), type-II heterojunction (also called staggered configuration) is formed when the bandgap of one material is at higher energy than that in the second material or oppositely when the bandgap of one material is at lower energy than that in the second material. This means that electron and hole carriers are confined into different layers when the values of conduction and valence band offsets have the same signs. Therefore, recombination occurs via spatially indirect transitions due to the spatial separation of the carriers. Examples of this heterojunction type are the band alignment formed between InAs/InAsSb, GaSb/GaAs, and InAs/AlSb.

However, if the value of the valence band offsets is greater than the bandgap energy of one of the materials, so that the valence band energy of one material is greater than the conduction band energy of the other material, then a ''broken gap'' type-II band structure (also known as type-III) is created, as depicted in Figure 2.8(c). Examples of this structure are the band alignment formed between InAs/GaSb and InAs/InSb.

|  | (a) | (b) | (c) |
|---|---|---|---|
|  | Type-I | Type-II<br>(staggered configuration) | Type-II<br>(broken gap) |
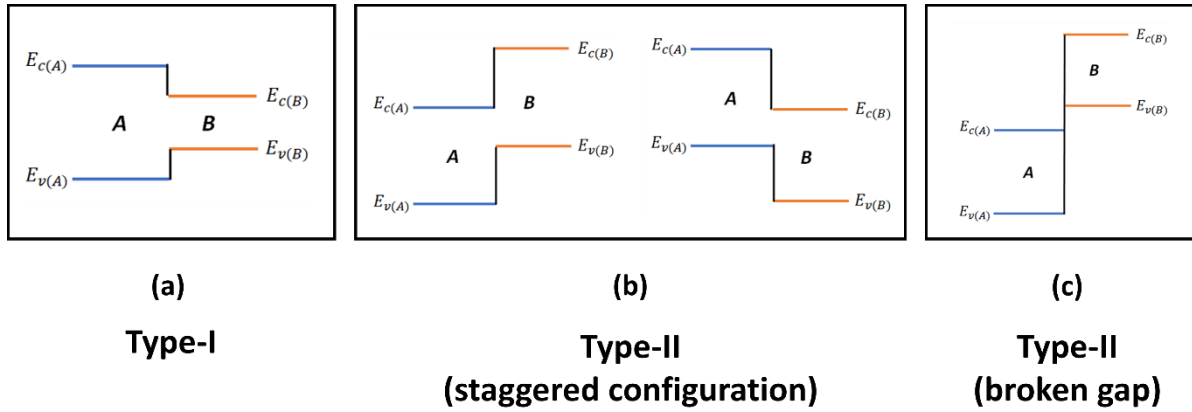
Figure 2.8: classification of band alignments at heterojunctions: (a) type-I, (b) type-II, is also called staggered heterojunction, and (c) type-II or type-III, it is called straddling or broken gap heterojunction.

## 2.4    Strained layers epitaxy

When a layer of semiconductor material is grown on top of another layer with dissimilar lattice constants, a built-in strain will be introduced into the structure as a result of the mismatch in lattice constants. Hence, this leads to structural defects (crystal defects) in the material.

There are two types of strain; one is called compressive strain, which occurs when the epitaxial layer's lattice constant is larger than the substrate ($a_{epilayer} > a_{substrate}$). This compressive strain decreases the lattice constant perpendicular to the growth direction while increasing it along the growth direction, as depicted in Figure 2.9(a-c). If the lattice constant of the epitaxial layer is smaller in comparison with the substrate ($a_{epilayer} < a_{substrate}$), then a tensile strain will occur, which increases the lattice constant perpendicular to the growth direction and reduces it in the growth direction, as shown in Figure 2.9(d-f). Therefore, if there is a considerable lattice mismatch, the dislocation of atoms and dangling bonds will occur in the material system. However, it is possible to grow structures with different material systems having different lattice constants with a particular condition provided that:

$$If\ d_l < d_C \qquad\qquad (2.17)$$

where $d_l$ is the thickness of the epitaxial layer, and $d_c$ is the critical thickness. A structure with free defects could be grown if this condition is satisfied. This critical thickness is given by an empirical relation as follows:

$$d_C \cong \frac{a_s}{2\,|\,\epsilon\,|} \quad ; \quad where \;\; \epsilon = \frac{a_l - a_s}{a_l} \tag{2.18}$$

where $\epsilon$ is called the lattice mismatch parameter in which $a_l$ and $a_s$ are the lattice constants of the epilayers and substrate, respectively. Therefore, when $\epsilon = 0$, this leads to that $a_l$ will be equal to $a_s$ means that it is a perfect lattice-matched structure. Nevertheless, if $\epsilon \neq 0$, this results in $a_l \neq a_s$; therefore, $\epsilon$ is the lattice parameter measure.
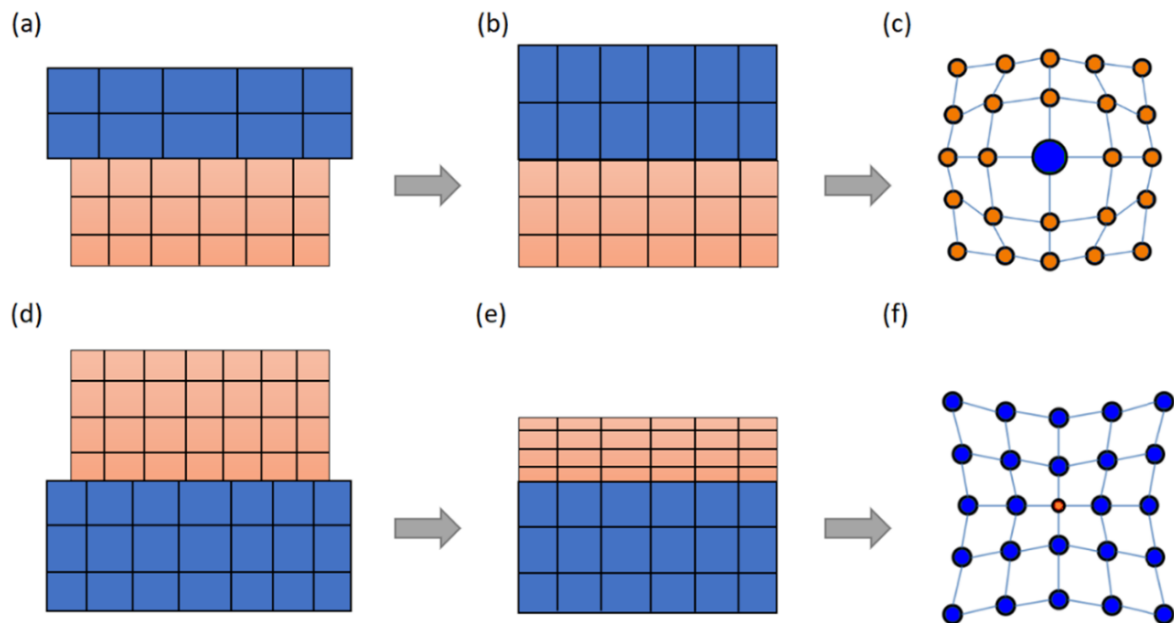


Figure 2.9: Schematic diagram represents (a) deposition of the semiconductor layer with a greater lattice constant (blue region) than the substrate (orange region), (b) the greater lattice constant of the deposited material is compressed perpendicular to the growth direction and stretched in the growth direction, (c) formation of compressive strain due to this type of growth process, (d) a deposited layer with a smaller lattice constant (orange region) than the substrate (blue region), (e) the smaller lattice constant of the deposited material is stretched perpendicular to the growth direction and squashed in the growth direction, and (f) formation of tensile strain in the structure due to this growth process.

## 2.4.1  Critical thickness

The critical thickness is the thickness of the grown epitaxial layer before it relaxes back to its natural lattice constant. Beyond this critical thickness, strain builds up and forms structural

dislocations. Hence, several attempts were established to calculate the critical thickness at the IF between two materials. The first calculation was carried out by Frank and Van der Merwe [40] using the following equation:

$$h_C \cong \frac{1}{8\pi^2} \left( \frac{1-v}{1+v} \right) \frac{a_0}{f} \qquad (2.19)$$

where $h_C$ is the critical thickness, $a_0$ is the substrate lattice constant, $f$ is the lattice mismatch, and $v$ is Poisson's ratio which is equal to $C_{12}/(C_{11} + C_{12})$, where $C_{11}$ and $C_{12}$ are referred to as the epilayer elastic constants. This expression was further expanded and developed by Matthews and Blakeslee [41], where $b$ is the Burgers vector magnitude, using the following expression:

$$h_C \cong \left( \frac{b}{f} \right) \left[ \frac{1}{4\pi(1+v)} \right] \left[ \ln \left( \frac{h_C}{b} \right) + 1 \right] \qquad (2.20)$$

Another development of this expression was done by People and Bean [42], where the formation of dislocations was considered to occur within the layer at the IF alternative to the edge. In this case, thus, the following equation was proposed where $a(x)$ is the epilayer lattice constant:

$$h_C \cong \left( \frac{1-v}{1+v} \right) \left( \frac{b^2}{16\pi\sqrt{2a(x)f^2}} \right) \left[ \ln \left( \frac{h_C}{b} \right) \right] \qquad (2.21)$$

## 2.4.2 Formation of defects

Defects might occur within the lattice structures during the growth of semiconductor materials. Distortion of the lattice structure's atomic arrangement is denoted as crystal defects. Defects in the structure can be classified into two categories based on dimensionality. These are zero-dimensional or point defects and one-dimensional or line defects. These are described in detail in this section.

### 2.4.2.1  Point defects

Defects might occur during the growth of semiconductor materials. The one-dimensional defect is called a point defect. This point defect consists of only one atom, surrounded by a perfect lattice. The formation of these point defects in the semiconductor materials might affect the optical and electrical properties of the devices. Figure 2.10 depicts different types of crystal point defects that may occur during growth. These point defects include vacancy, interstitial, and substitutional defects.

Vacancy defects are defined as when an atom is missing from the lattice structure due to high growth temperature. At high temperatures, it is stated that due to atoms' high surface mobility, they start moving from their site, leaving behind an empty lattice space. These vacancy defects can be classified into two sets. The first set is called a Schottky defect in which the atoms leave their position and transfer to the crystal surface, whereas if the atoms vacate their site and transfer to an interstitial site in the structure, this is called a Frenkel defect.

Interstitial defects occur in the lattice structure when an atom is in a non-equipped lattice site within the crystal. In the meantime, if an extra atom is involved, this type of interstitial defect is called a self-interstitial defect.

A substitutional defect is an atom different from the lattice composition that substitutes the original atom site. It can be noted that the vacancies and self-interstitial defects are classified as intrinsic point defects because no extra atoms are involved. In contrast, the substitutional and interstitial defects are classified as extrinsic point defects since additional atoms are encompassed.
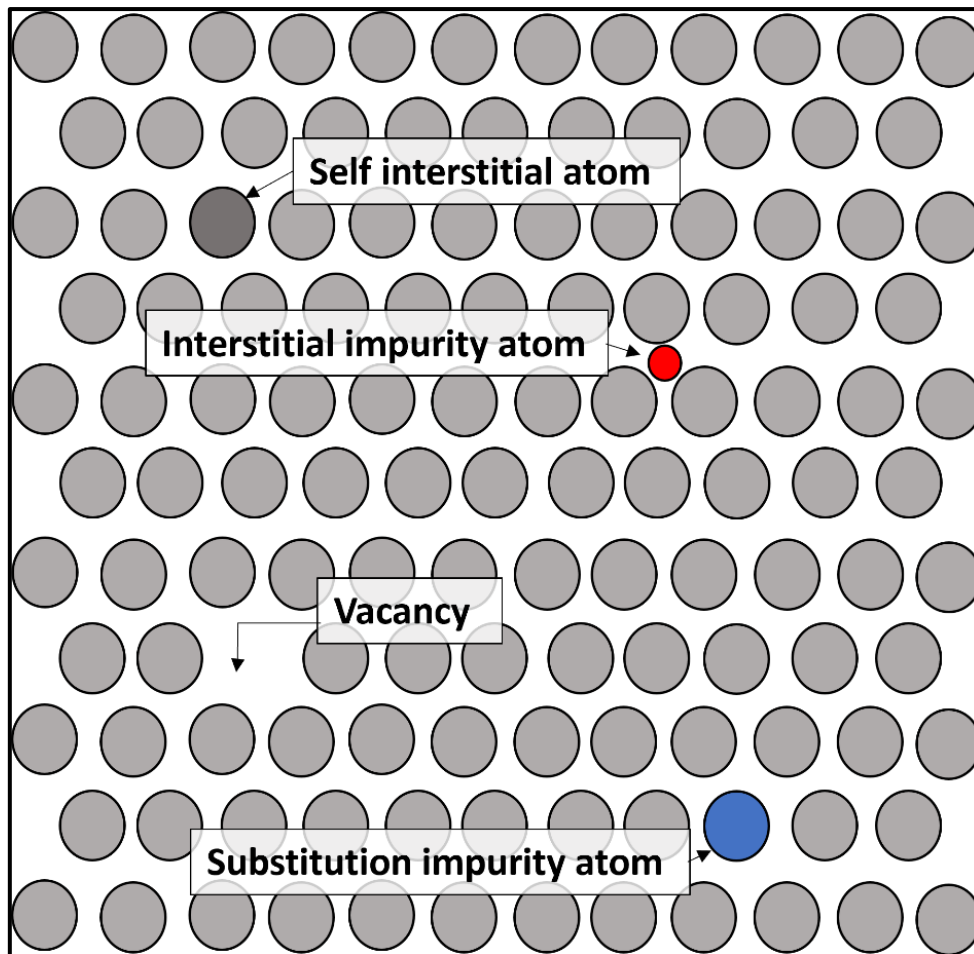
Figure 2.10: Schematic diagram represents different types of point defects that typically form within the crystal structure.

### 2.4.2.2 Line defects

Material dislocations are abrupt changes in the periodic structure of atoms along a dislocation line. These dislocations occur mainly owing to the misalignment of atoms in a crystal lattice. These can occur because of the introduction of impurities or the formation of strain, which can consequently affect the lattice structure. There are two primary categories of dislocations: edge and screw dislocations, as shown in Figure 2.11.

Edge dislocations are formed when a plane of atoms terminates in the centre of a crystal. The adjacent planes are not linear but curve around the edge of the terminating plane so that the crystal structure on either side is precisely ordered. If the misalignment shifts a block of ions gradually upwards or downwards, causing a screw-like deformation, then a screw dislocation is formed in the structure.
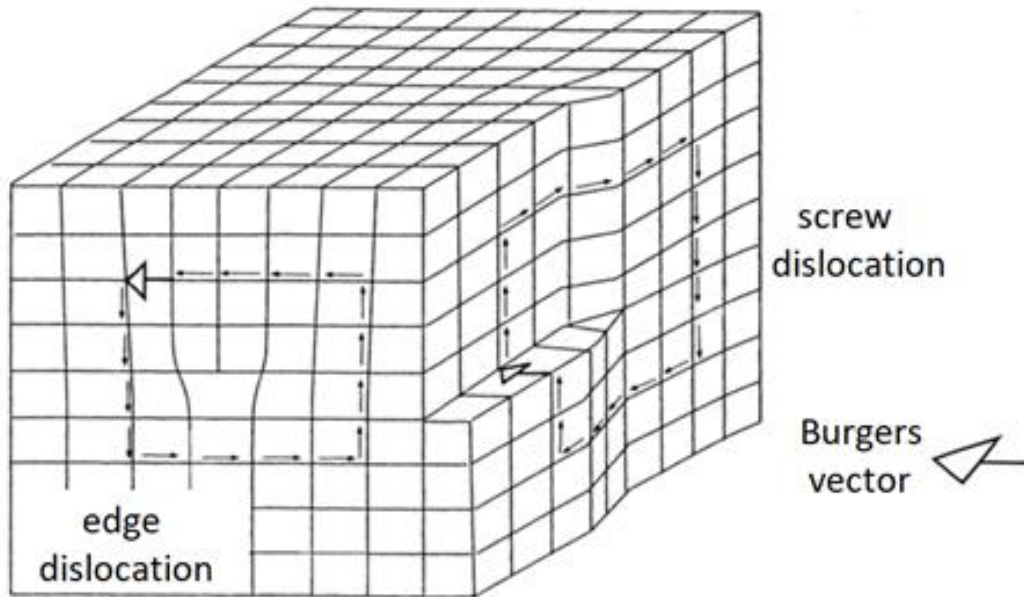
Figure 2.11: Schematic diagram shows two types of dislocations in a crystal lattice structure. These are edge and screw dislocations. The figure is adapted from reference [43].

### 2.4.3 Strain effect on the band structure

The band structure of a QW with no strained effect is represented in Figure 2.12(a). However, when strain is introduced in the structure, the bandgap energy of the materials is affected. As seen from Figure 2.12(b-c), when strain is formed in the structure, the bandgap energy changes either increases or decreases depending on the type of strain, namely tension or compression [44].

In the case of tensile strain, as depicted in Figure 2.12(b), the bandgap energy decreases, and the heavy hole (HH) and light hole (LH) valence bands are split due to this effect which creates an anisotropic band structure. Besides that, the LH band is shifted up from the HH band. In contrast, when the material is under compressive strain, as represented in Figure 2.12(c), the bandgap energy increases, and the valence band splitting is experienced, opposite to the tensile strain, such that the HH is now the highest band.
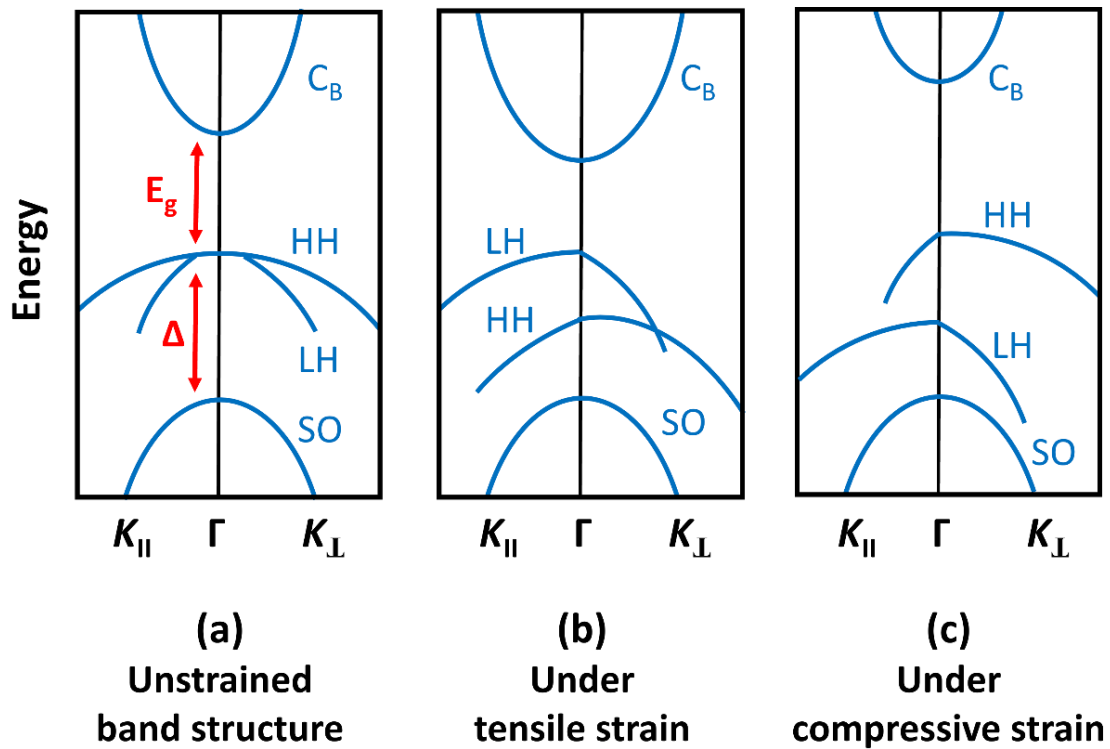
Figure 2.12: Schematic diagram shows the strain effect on the band structure of a material system (a) no-strain is introduced into the structure, (b) tensile strain is formed into the structure, and (c) compressive strain is introduced into the structure. The figure is reproduced from reference [44].

## 2.5    Classification of infrared detectors

A detector is a device that converts the energy of incident radiation, typically into an electrical signal. IR detectors can be classified in terms of their cut-off wavelength. For a specific IR spectral band, different material systems and IR detectors are designed to span the required IR spectral band. Besides the wavelength requirement, IR detectors are mainly grouped into thermal and photon detectors. This section briefly overviews different types of IR detectors and their operation principles. More detailed information on IR detectors and the history behind IR detection can be found in references [15], [45], [46].

### 2.5.1   Thermal detectors

There have been extensive investigations for IR detection utilising thermal detector technologies due to their simplicity, low cost, broad responsivity, and room temperature operation. Nowadays, the demanding technology is mainly based on MCT/HgCdTe detectors,

an II-VI compound. Figure 2.13 shows a typical thermal IR detector that absorbs IR incident radiation to change the material's temperature; consequently, this thermal change produces electrical power. The IR detector is attached to the heat sink via a thermal insulator and a substrate. The signal is independent of the photonic nature of the incident radiation.
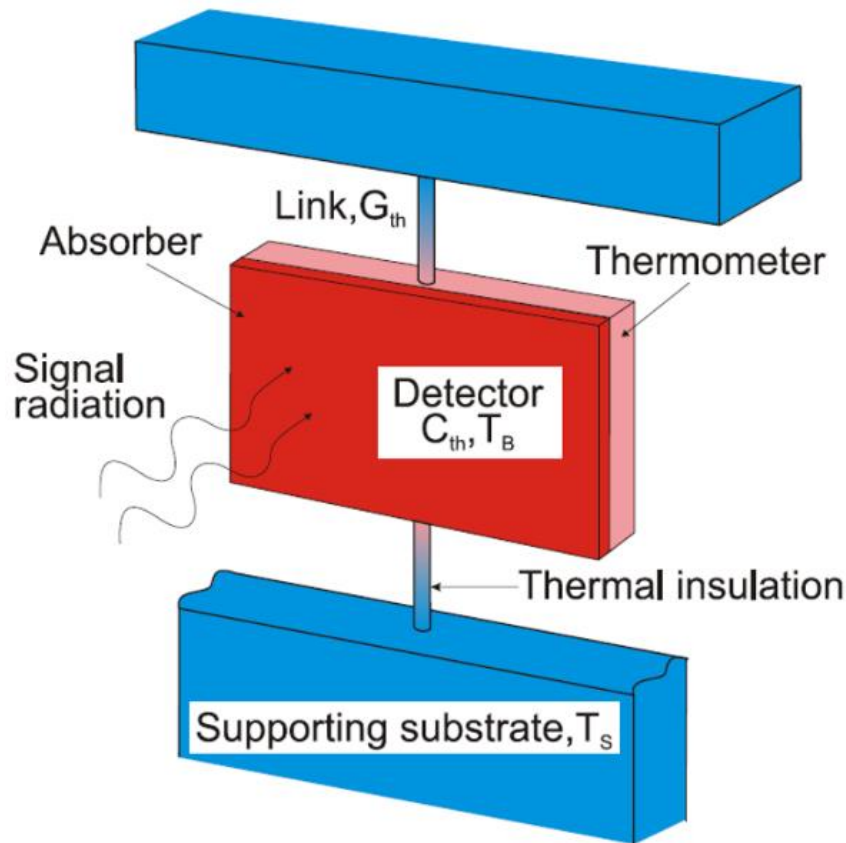


Figure 2.13: Schematic of a typical thermal detector. The figure is adapted from reference [47].

Consequently, thermal effects do not rely on the wavelength where the spectral response is flat and wide, which differs from photon detectors, as shown in Figure 2.14. There are different types of thermal detectors: bolometers, pyroelectric, thermocouples, thermopiles, and pneumatic. For more detailed information, the reader is guided to the following reference [47]. Thermal detectors' specific detectivity (D*) typically ranges between $10^8$ and $10^9$ cm.Hz$^{1/2}$/W at a low frequency of approximately 10 Hz and room temperature operation, but the detectivity decreases significantly with increasing the frequency [48]. These detectors have several drawbacks, including lower responsivity speed and sensitivity compared to photon detectors.
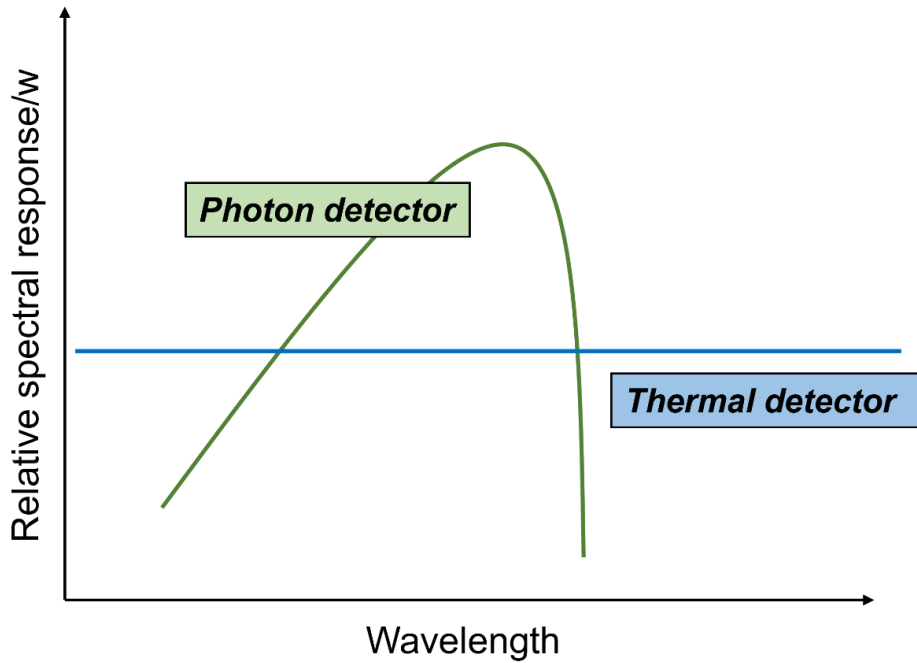
Figure 2.14: Schematic diagram represents the relative spectral response for a photon and thermal detector.

## 2.5.2  Photon detectors

Photon detectors are another type of IR detector with the highest theoretical performance limit, high responsivity, and excellent SNR [45]. Photon detectors differ from thermal detectors as they do not have a flat and broad spectral response, as already shown in Figure 2.14. They generally require a cryogenic cooling system to operate at high temperatures. In a photon detector, IR radiation is absorbed when the energy of IR photons is higher than that of the detector's bandgap energy, which allows carriers to be excited from the valence band to the conduction band. Photon detectors are subdivided into two major groups: photoconductive (PC) and photovoltaic (PV) detectors.

### 2.5.2.1  Photoconductive detectors

In photon detectors, the photogenerated electron-hole pairs, created by the absorption of IR radiation, are collected at the contact regions with the aid of an externally applied voltage to prevent recombination. The overall flow of current via the detector increases due to the presence of photocurrent, which is produced by the absorption process as the conductivity of the detector increases. A schematic diagram of a typical PC detector is represented in Figure

2.15, and the current can be seen as an applied voltage across the resistance. As can be seen, a PC detector is typically made with a semiconductor which includes doping and ohmic contacts at both sides in which the conductance changes with the absorption of photons. The photogenerated current can be typically evaluated using the following formula:

$$I_{photo} = q\eta w l \emptyset_s g_{photo} \qquad (2.22)$$

where $q$ is the electron charge, $\eta$ is the quantum efficiency, $w$ is the width, $l$ is the length of the photoconductive detector, $\phi_s$ is the density of the incident photon flux, and $g_{photo}$ is the gain of the photoconductor.
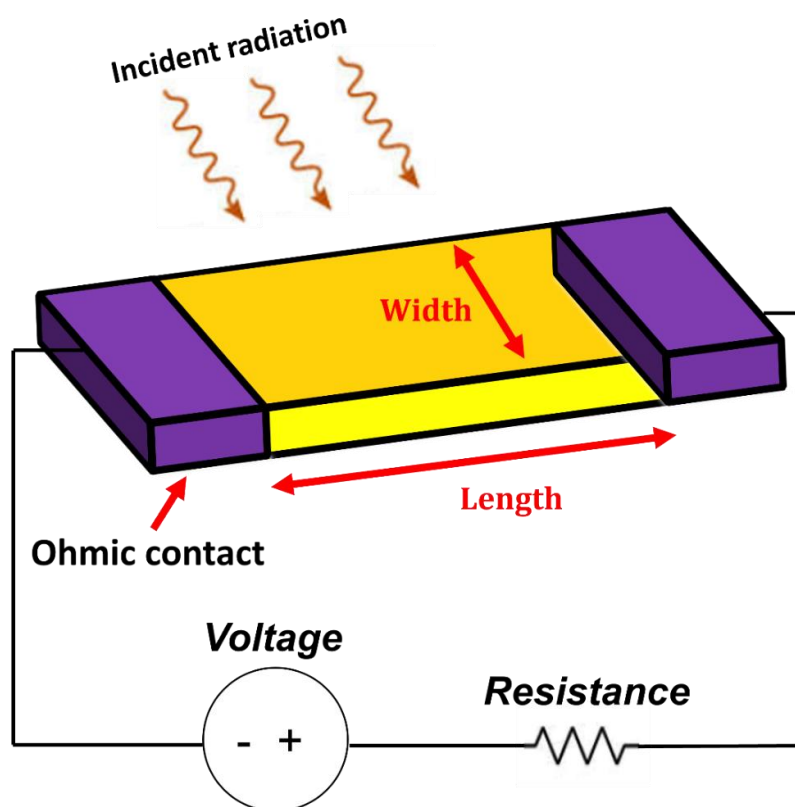


Figure 2.15: Schematic diagram shows a typical PC detector with a semiconductor material and contacts at both ends connected to a voltage source.

### 2.5.2.2  Photovoltaic detectors

In the case of photovoltaic detectors, the photoexcited electron-hole pairs get collected by the contacts through a built-in electric field generated in a *p-n* junction. A typical PV detector and principle of operation are depicted in Figure 2.16. The *p-n* junction comprises *p*-type and

*n*-type semiconductors, which can be homojunction or heterojunction, depending on the *p*-type and *n*-type semiconductors if they are the same materials or not, the majority hole carriers in the *p*-type region and the majority electron carriers in the *n*-type region forms a depletion region at the *p-n* junction. Consequently, a built-in electric field is produced at the junction. In the reverse bias operation, the photogenerated free carriers sweep to the inverse side of the junction due to the built-in electric field. Then, these carriers produce photocurrent, contributing to the reverse current. The photocurrent in PV detectors can be assessed as follows:

$$I_{photo} = q\eta Al\emptyset_s \tag{2.23}$$

where *q* is the electron charge, $\eta$ is the quantum efficiency, *A* is the diode area, and $\phi_s$ is the incident photon flux density. To obtain high-performance conditions, the dark current of the diode must be lower than the photogenerated current. Figure 2.17 shows a typical I-V curve of the diode with and without light illumination.
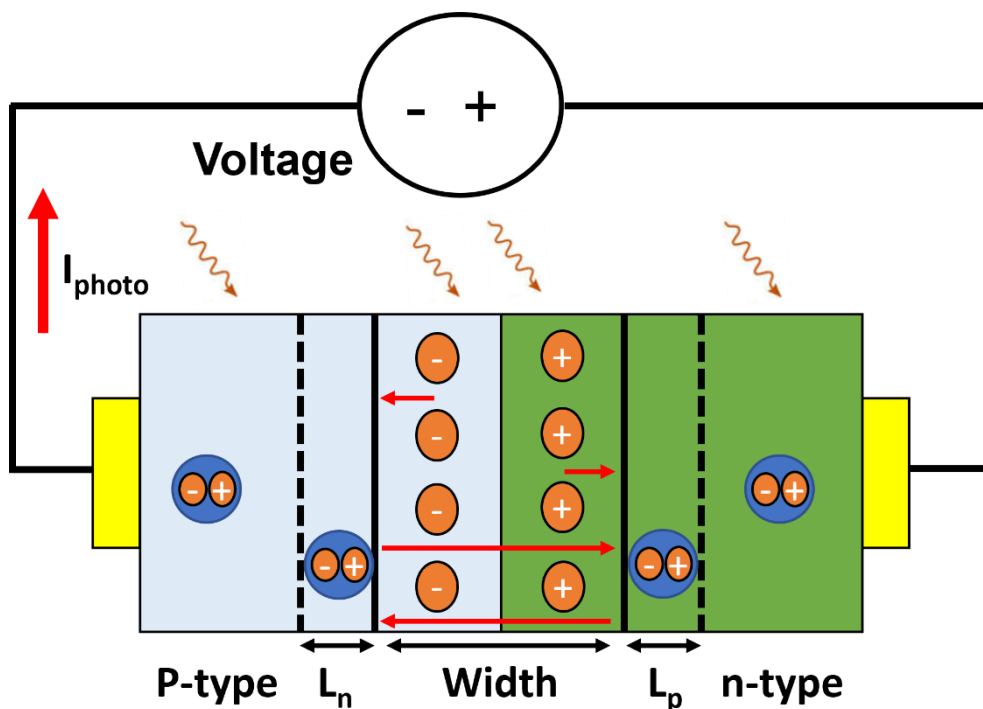


Figure 2.16: Schematic diagram represents the operation of a PV detector in a p-n junction. $L_n$ and $L_p$ are the minority carrier diffusion lengths.

Compared with PC detectors, PV detectors, including p-n and p-i-n heterostructures, are more favourable due to the low power consumption required for collecting photogenerated carriers, as they only need a low level of reverse bias operation.
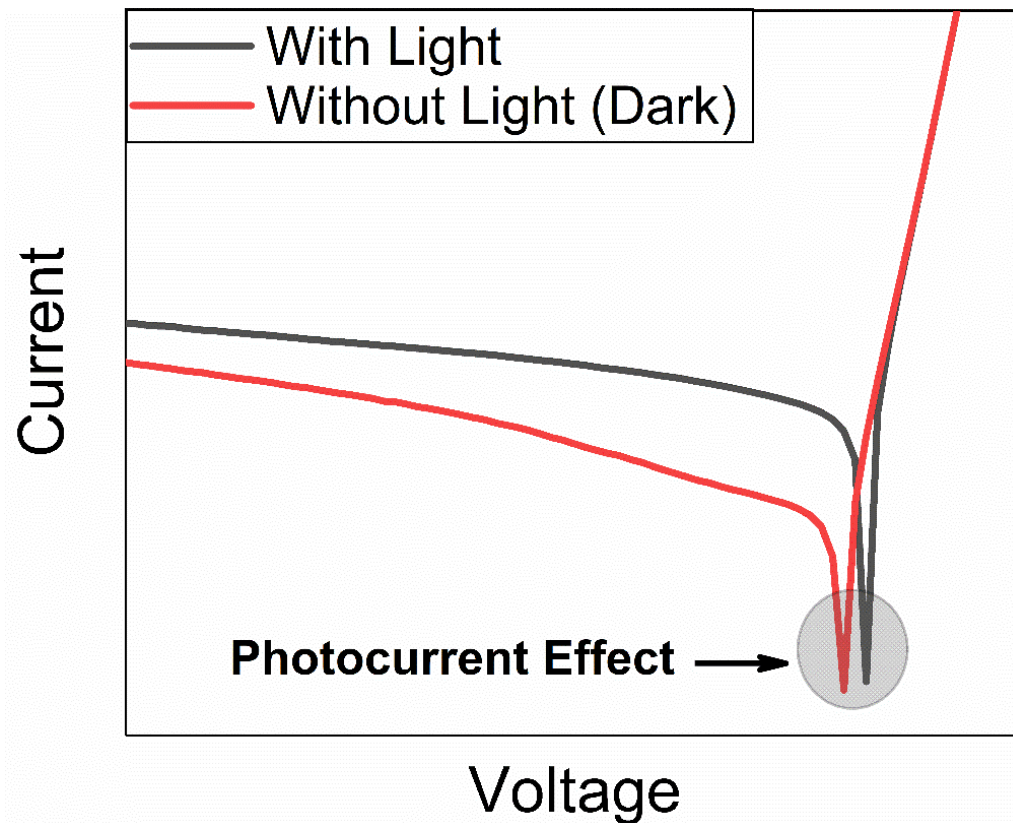


Figure 2.17: A typical current-voltage (I-V) characteristic for a semiconductor diode with and without light illumination with photocurrent effect.

### 2.5.2.3  Bandgap modification detectors

Due to the shortcomings of the bulk-based detectors, research has been carried out to search for alternative materials. Consequently, a structure with energy states for excitation called quantum well (QW) or superlattice (SL) was realised. Depending on the band structure alignment, type-I is commonly known as a quantum well-infrared photodetector (QWIP), and T2SL photodetector is a promising technology for IR detection applications. In the case of QWIPs, GaAs/AlGaAs, a typical material system, is a narrow bandgap semiconductor material sandwiched between large bandgap semiconductors to create a QW. Therefore, this leads to forming subbands localised in specific energy levels inside the QW, as shown in Figure 2.18.

The carriers on these subbands can be excited to the upper subbands and then tunnel through continuum states. The absorption process can also transmit them directly from the subbands to the continuum states.
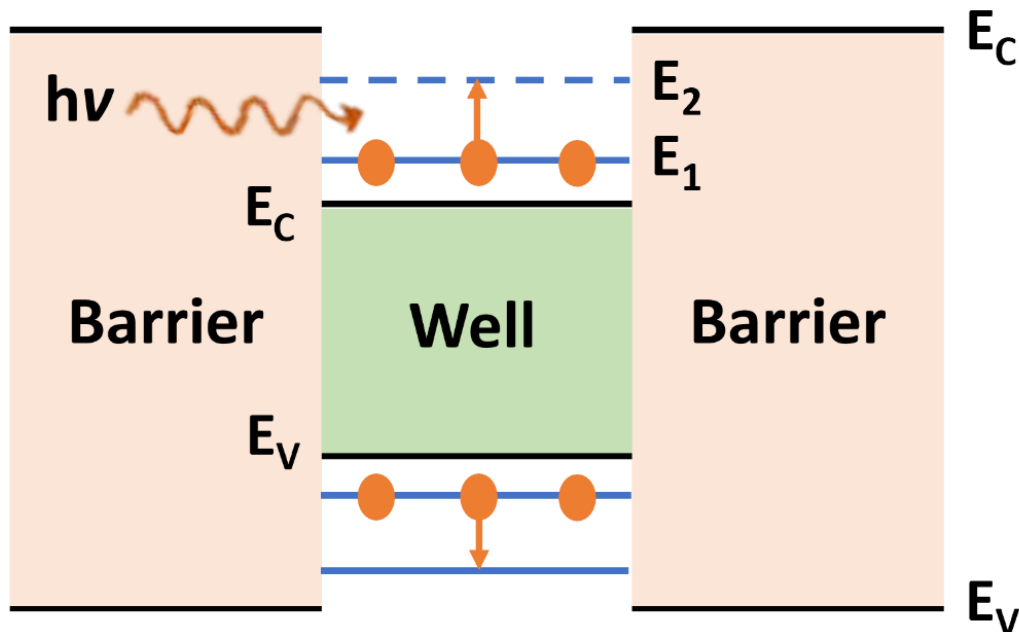


Figure 2.18: A diagram illustrates the subbands of the optical transition of carriers in QWIPs. This figure is a redrawn version from reference [49].

The contacts then collect the photoexcited carriers owing to the external bias, which increases the current flow within the detector, as depicted in Figure 2.19. The energy difference between the first two localised energy states determines the operational wavelength of QWIPs. Hence, the bandgap energy of QWIPs can be modified by adjusting the dimensional or compositional parameters of the barrier and QW. Although QWIPs have many advantages, including low cost of growth and fabrication, high uniformity, high yield, bandgap tunability, and dual-band or dual-colour detection, they still suffer from very low quantum efficiency, which is reported to be around 15% in the MWIR spectral range [17], preventing them from being a considerable alternative to the current state-of-the-art MCT technology.
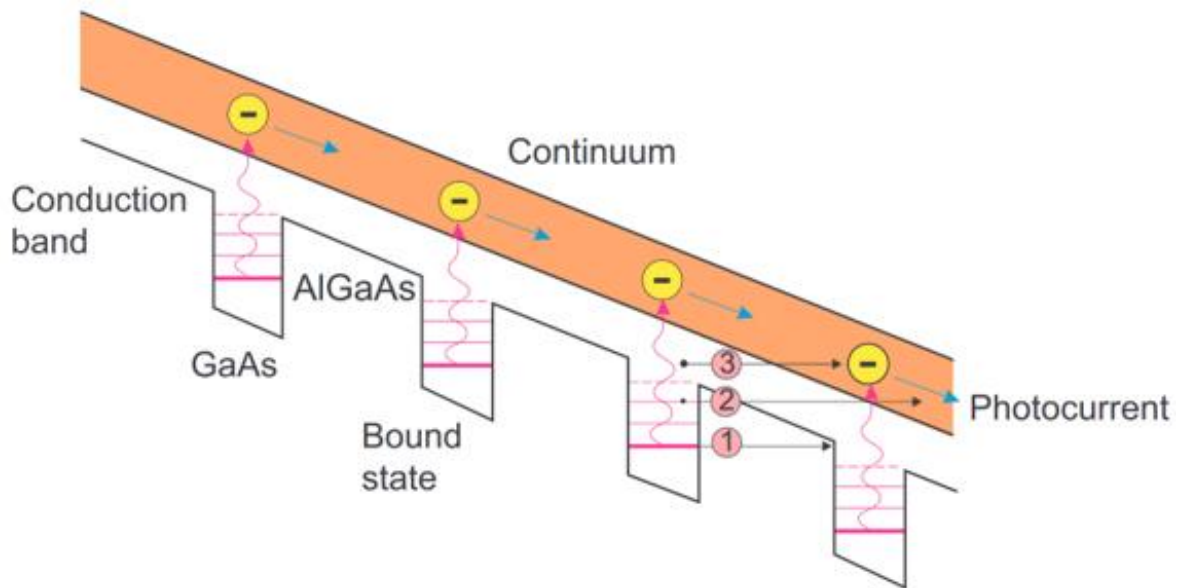
Figure 2.19: The conduction band of GaAs/AlGaAs QWIPs under bias operation. The figure is adapted from reference [47].

### 2.5.2.4  Type-II superlattice detectors

MCT has become the preferred material for IR photodetection over the last few decades due to its high-performance level and wavelength tunability. Nevertheless, MCT-based MWIR detectors necessitate cryogenic cooling, which, coupled with different fabrication challenges, has prompted the search for alternative materials. Manufacturers have pursued HOT devices, which eliminate the requirement for cumbersome cooling systems, in an effort to reduce SWaP requirements. The T2SL detectors are the emerging and competitive technologies to MCT thanks to their promising advantages, including bandgap energy flexibility, low dark current, high quantum efficiency, availability of lattice-matched substrate, and low growth and fabrication costs.

A superlattice (SL) is a one-dimensional periodic heterostructure consisting of two or more alternating atomic layers. The SL layers are atomically thin, typically in the range of 5-20 atomic monolayers (MLs). The SL structure is advantageous to achieve a narrow bandgap to attain a particular cut-off wavelength, from SWIR to VLWIR spectral band, required for specific applications [50], [51]. Moreover, it is known that the formation of strained SL layers leads to breaking the degeneracy of HH and LH in the valence band, indicating a possibility of suppressed non-radiative Auger recombination processes that dominate in bulk materials

33

[23], [24], [25]. Due to these promising fundamental material properties, research has been concentrated on the design, growth, and fabrication of T2SL, including single-pixel and focal plane array (FPA) detectors.

The alignment of the band heterostructure of InAs and GaSb, as depicted in Figure 2.20, confers T2SL with a desirable characteristic. The 6.1 Å group family of binary compound semiconductors consist of InAs, GaSb, and AlSb. The band structure configuration depends on the conduction, valence band offsets, and electron affinity. As an illustration, type-II heterojunction (broken gap) is formed between the InAs and GaSb layers because of the variations in conduction and valence band offsets ($\Delta E_c$ and $\Delta E_v$) and the electron affinities of each material. Herein, the conduction band ($C_B$) of InAs materials is located at a lower energy level than the valence band ($V_B$) of the GaSb material. This kind of heterostructure configuration leads to the spatial separation of electrons and holes in the conduction and valence bands of the InAs and GaSb materials, respectively. Another possible heterojunction configuration is the band alignment formed between AlSb and GaSb materials. This type of configuration is called a type-I heterojunction. In this case, the smaller bandgap material (GaSb) is sandwiched between the wide bandgap material (AlSb). Note that electron and hole carriers are confined to each layer.

Moreover, since the minor lattice mismatch between the materials of the 6.1 Å group family (III-V materials with lattice constants close to 6.1 Å), the T2SL heterostructure offers the tuneability of bandgap and corresponding wavelength required for a combination of dissimilar materials, thereby permitting device designs optimised for enhanced performance in optoelectronic applications. Therefore, the ideal SL could be any combination of InAs, GaSb, and AlSb binaries (or their alloys) comprising the 6.1 Å family. The notable characteristics of T2SLs have led to several proposed theoretical advancements compared to the current state-of-the-art MCT detectors. Grein et al. [52] and Youngdale et al. [53] demonstrated less non-radiative Auger recombination in T2SLs than in MCT. The adaptability offered by the 6.1 Å family has also been utilised in designing and developing innovative barrier designs capable of reducing the dark current and enhancing the device's performance.

**Temperature = 0 K**

Energy

AlSb  $C_B$

$\Delta E_C = 0.49$ eV

GaSb

$E_g = 0.81$ eV

$E_g = 1.70$ eV

$\Delta E = 0.15$ eV

$\Delta E_V = 0.40$ eV

InAs

$\Delta E_V = 0.56$ eV

$E_g = 0.41$ eV

$V_B$
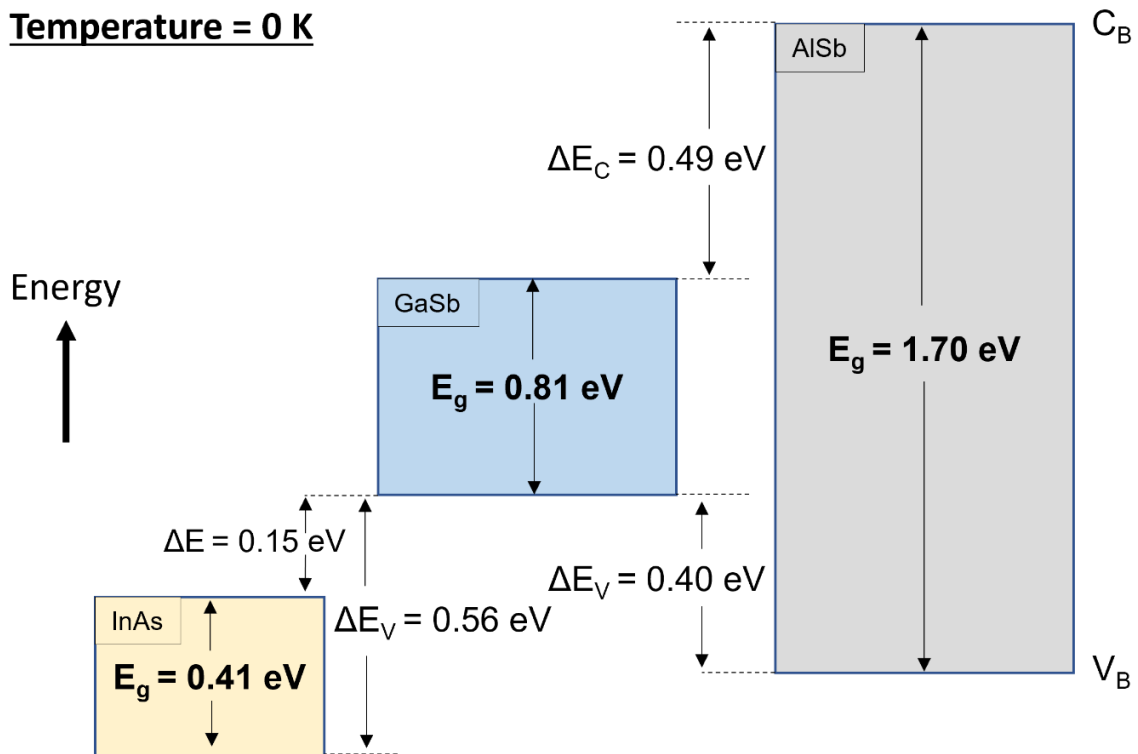
Figure 2.20: The band heterostructure alignment of the 6.1 Å group family of III-V semiconductors, such as InAs, GaSb, and AlSb at a temperature of 0 K.

Another desirable characteristic of the T2SLs is the capability of bandgap energy modification. Figure 2.21 depicts the band alignment of the type-II InAs/GaSb material system. Combining the two materials into a periodic stack or SL produces a series of QWs with spatially separated electrons and holes. The electrons are confined to the InAs layer and holes to the GaSb layer. This is important because it increases the interaction between adjacent QWs, and that interaction gives rise to these highlighted minibands. Consequently, the effective bandgap energy of the bulk material is now defined as the difference between the first electron miniband to the first HH miniband. This is an attractive property where the bandgap energy can be tuned by changing the layer thickness of InAs and GaSb materials. This is a highly desirable characteristic for IR detectors with a narrow bandgap, as the cut-off wavelength can be tailored to be the exact wavelength range required for any specific application. Another advantage of using the SL structure is that the electron effective mass ($m_e$) does not depend on the SL bandgap energy [22], [54], which differs from bulk semiconductor materials, resulting in lower mobility and hence, lower tunnelling current.
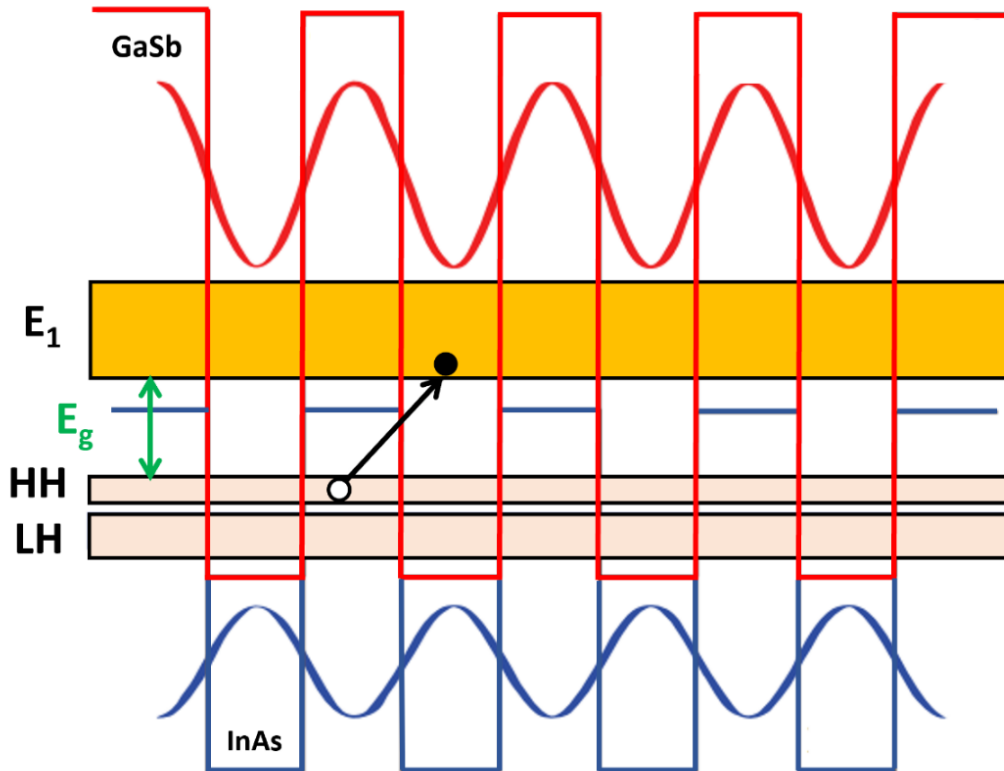
Figure 2.21: The band heterostructure alignment of type-II InAs/GaSb material system. The effective bandgap energy of the SL (highlighted in green) is herein calculated as the difference between the first electron and HH minibands in the conduction and valence bands, respectively. The figure is a reproduced version from reference [55].

The material benefits of III-V compound semiconductors over MCT contain greater robustness, lower defect density, and suppression of tunnelling currents owing to larger effective masses. T2SLs also offer manufacturing benefits compared to MCT, such as operability, homogeneity, stability, producibility, and cost-effectiveness for FPA applications. Not only these, but also T2SLs can be grown on lattice-matched GaSb substrates, which become currently available in 2-, 3-, 4-, and 6-inch diameters.

## 2.6    Figures of merit for infrared detectors

As SWaP reductions are primarily a result of performance enhancements, it is instructive to describe the figures of merit utilised to assess the performance level of the detector. The figures of merit presented herein are effective for assessing and comparing the performance level of IR devices [56].

### 2.6.1  Dark current

The dark current is the current flow via the detector without light. Therefore, this will create a false signal as no form of detection can be observed by the device. Fortunately, the surface current can be minimised in a semiconductor material during fabrication by applying passivation layers, allowing for the detection of lower power signals. There are different sources of dark current observed in IR detectors, such as generation-recombination (G-R), diffusion, trap-assisted tunnelling (TAT), band-to-band tunnelling (BTB), and shunt currents [12]. These are described in the following sections.

#### 2.6.1.1  Generation-recombination current

The generation recombination current ($I_{G-R}$) occurs in semiconductor devices due to defects formed in the depletion region, named Shockley Read Hall (SRH) centres. Additional energy levels are provided due to the defects in the semiconductor material's mid-gap, which allow carriers to be both thermally excited and recombined. In the case of reverse bias, the G-R current can be expressed using the following equation [57]:

$$I_{G-R} = \frac{qAn_iW_{dep}V}{(V_{bi} - V)\tau_{G-R}} \ for \ V < 0 \qquad (2.24)$$

where $A$ is the device area, $W_{dep}$ is the width of the depletion region, $V$ is the applied voltage to the junction, $V_{bi}$ is the built-in voltage of the device, $n_i$ is the intrinsic carrier concentration, $q$ is the charge of electrons, and $\tau_{G-R}$ denotes the generation-recombination lifetime of carriers in the depletion region. The width of the depletion region can be obtained using the following equation [57]:

$$W_{dep} = \sqrt{\frac{2\varepsilon_0\varepsilon_s(N_a + N_d)(V_{bi} - V)}{qN_aN_d}} \qquad (2.25)$$

where $\varepsilon_0$, $\varepsilon_s$, $N_a$, and $N_d$ are the free space permittivity, static dielectric constant, acceptor carrier concentration (*p*-type doping concentration), and donor carrier concentration (*n*-type

doping concentration), respectively. The intrinsic carrier concentration ($n_i$) can be obtained using the following expression [58]:

$$n_i = \sqrt{N_C N_V}\, exp\left(-\frac{E_g}{2K_B T}\right); \quad \begin{cases} N_C = 2\sqrt[3]{\dfrac{K_B T m_e}{2\pi\hbar^2}} \\[3mm] N_V = 2\sqrt[3]{\dfrac{K_B T m_h}{2\pi\hbar^2}} \end{cases} \qquad (2.26)$$

where $N_C$ and $N_V$ are the effective density of states in the conduction and valence bands, respectively; $E_g$ is the bandgap energy of the semiconductor material, $K_B$ is Boltzmann constant, $T$ is the temperature, $m_e$ is the electron effective mass, $m_h$ is the hole effective mass, and $\hbar$ is the reduced Planck's constant which $\hbar=h/2\pi$.

### 2.6.1.2 Diffusion current

The diffusion current component is mainly dominated by the carriers (electrons and holes), which diffuse at the junction from one side to the other. Minority carriers typically diffuse from high to low concentrations. This diffusion current mechanism appears to be temperature-dependent and can be expressed as follows [57]:

$$I_{Diff} = \frac{qAn_i^2}{N_d}\sqrt{\frac{K_B T \mu_h}{q\tau_h}}\, tanh\frac{d}{L_h}\left[exp\left(\frac{qV}{K_B T}\right)-1\right] \qquad (2.27)$$

where $\mu_e$ and $\mu_h$ are the carrier's mobility which are electrons and holes, $\tau_e$ and $\tau_h$ are the carrier's lifetime of electrons and holes, $d$ is the thickness of the active region, and $L_h$ is the hole diffusion length.

### 2.6.1.3 Trap-assisted tunnelling current

The trap-assisted tunnelling current ($I_{TAT}$) arises when minority carriers tunnel from one side to another at the junction. This tunnelling mechanism is additionally created with the help of trap states presented in the depletion region of the device due to the formation of defects or impurities in the material. This type of dark current can be calculated using this equation [59]:

$$I_{TAT} = \frac{\pi^2 q^2 A m_e M^2 N_T (V_{bi} - V)}{h^3 (E_g - E_T)} exp\left(-\frac{8\pi\sqrt{2m_e}\sqrt[3]{(E_g - E_T)}}{3qhE_{max}}\right) \quad (2.28)$$

where $E_{max}$ is the maximum electric field across the depletion region, $M$ is the matrix element related to the trap potential, $N_T$ is the density of trap states, and $E_T$ is the energy of trap centres. The maximum electric field across the depletion region can be calculated as follows:

$$E_{max} = \sqrt{\frac{2qN_d(V_{bi} - V)}{\varepsilon_0 \varepsilon_s}} \quad (2.29)$$

### 2.6.1.4 Band-to-band tunnelling current

The band-to-band tunnelling current ($I_{BTB}$) mechanism dominates at high reverse bias. In this case, carriers tunnel from the valence band of the device to the conduction band. This type of dark current relies mainly on the applied voltage and the electric field in the depletion region of the device. The BTB tunnelling current is calculated using the following equation [39]:

$$I_{BTB} = \frac{\sqrt{2m_e}q^3 AEV}{4\pi^2 \hbar^2 \sqrt{E_g}} exp\left(-\frac{4\sqrt{2m_e}\sqrt[3]{E_g}}{3qE\hbar}\right) \quad (2.30)$$

### 2.6.1.5 Shunt current

The ohmic shunt current commonly occurs in the diode due to the formation of native oxides, usually created on the mesa sidewalls through the etching process, acting as good conductors. This source of current can be expressed using Ohm's law:

$$I_{Shunt} = \frac{V}{R_{Shunt}} \quad (2.31)$$

where $R_{shunt}$ is the diode shunt resistance, and $I_{shunt}$ is the shunt current.

### 2.6.2 Responsivity

The spectral response of the photodetector is defined as the ratio of the produced photocurrent or photovoltage to the input optical power which can be expressed as follows:

$$R_i = \frac{I_{ph}}{P_{in}} \quad OR \quad R_V = \frac{V_{ph}}{P_{in}} \tag{2.32}$$

where $R_i$ is the photodetector's current responsivity, $R_V$ is the photoreactor's voltage responsivity, $I_{ph}$ is the photocurrent, $V_{ph}$ is the photovoltage, and $P_{in}$ is the input optical power. The responsivity measurement can be carried out with a Fourier transform infrared spectrometer (FTIR) system using a broadband IR source to collect the photodetector's relative response.

### 2.6.3 Quantum efficiency

The optical performance of the photodetector is assessed by the quantum efficiency (QE), defined as the conversion of the incident photons into electron-hole pairs. The QE can be evaluated from the responsivity measurement using the following equation:

$$QE = \frac{1.24 \, R_i}{\lambda} \tag{2.33}$$

where $R_i$ is the photodetector's responsivity and $\lambda$ is the cut-off wavelength.

### 2.6.4 Noise

There are different types of noise which might exist in devices. One of these is Johnson and Shot noise which is called white noise. These types of noise are frequency independent. On the other hand, $1/f$ noise is another noise mechanism which is mainly frequency dependent. These noise mechanisms are discussed below.

### 2.6.4.1 Johnson noise (thermal noise)

Johnson noise is associated with the thermal transition of electronic charges and can be expressed using the following equation:

$$\langle i^2_{Johnson-noise} \rangle = \frac{4K_B T}{R} \Delta f \qquad (2.34)$$

where $K_B$ is Boltzmann constant, $T$ is the temperature, $R$ is the resistance, and $\Delta f$ is the bandwidth.

### 2.6.4.2 Shot noise

Shot noise is associated with the quantisation of electronic charges and photons, and it can be described using the following equation:

$$\langle i^2_{Shot-noise} \rangle = 2qI\Delta f \qquad (2.35)$$

where $q$ is the charge of electrons, and $I$ is the photodetector's current.

### 2.6.4.3 (I/f) noise

This form of noise depends predominantly on frequency. This type of noise is inversely proportional to the frequency, meaning that this noise mechanism becomes dominant in the low-frequency range.

## 2.6.5 Detectivity

For the photodetector's detectivity evaluation, the signal of the photodetector and its noise are to be considered, and they are important parameters. Detectivity can be defined as the inverse of the photodetector noise equivalent power (NEP). As its name suggests, NEP is the ratio of the generated signal to the input power. The photodetector's detectivity, however, is affected by the bandwidth and device area measurement. Therefore, a specific term called specific detectivity ($D^*$) was proposed by Jones [60] in which the detectivity of the device is normalised to the device area ($A$) and bandwidth ($\Delta f$) utilising the following equation:

$$D^* = \frac{\sqrt{\Delta f . A}}{NEP} \qquad (2.36)$$

This specific detectivity term can also be expressed as follows:

$$D^* = \frac{R_i}{\sqrt{\frac{4K_B T}{RA} + 2qJ}} \qquad (2.37)$$

where $R_i$ is the photodetector responsivity, $RA$ is the resistance-area product, and $J$ is the dark current density.

$$D^* = \qquad 42$$

# Chapter 3: Motivation and Literature Review of the State-of-Art Type-II Superlattices

This chapter briefly overviews the developments of IR detectors and the emergence of T2SLs (Sections 3.1 and 3.2). It discusses the fundamental material properties of T2SLs, including bandgap energy (Section 3.3.1), minority carrier lifetime (Section 3.3.2), and absorption coefficient (Section 3.3.3). A comprehensive literature review is also presented to compare the performance levels of MWIR detectors based on T2SL and MCT materials, including quantum efficiency (Section 3.4.1), dark current density (Section 3.4.2), and differential resistance-area product (Section 3.4.3). The chapter also presents recent technological advancements in IR detection, including barrier detectors (Section 3.5.1) and quantum cascade detectors (Section 3.5.2). The chapter concludes by discussing the motivation behind the current research work (Section 3.6). The main aim and objectives of the current research are also emphasised (Section 3.7).

## 3.1    A brief history of infrared detectors

IR detection was first discovered in 1800 due to research conducted by the astronomer Frederick William Herschel [61]. Herschel began developing the idea of IR radiation while investigating the spectrum of sunlight with an optical prism. In 1821, Thomas Johan Seebeck discovered the thermoelectric effect [62], in which he examined the junction behaviour of electrically conductive materials. In 1829, Leopoldo Nobili [62] began to develop an initial thermopile by connecting numbers of Seebeck thermocouples to convert thermal energy into electrical energy.

Around 1833, Leopoldo Nobili and Macedonio Melloni [62] adjusted the thermopile utilising Bismuth (Bi) and Antimony (Sb). The modified thermopile comprised a series of SbBi thermal couples capable of producing a high measurable output to detect the heat emitted from a person approximately nine metres away. This was the most common detector used for IR radiation owing to its effectiveness.

In 1873, the photoconductivity effect was discovered by Willoughby Smith [63]. Smith undertook his experiments with selenium (Se) used as an insulator for underwater cables. IR detection was then moved into a new stage with the discovery and development of bolometers by Samuel Langley in 1880 [64]. The bolometers are used to measure the power of incident electromagnetic radiation through the heat of temperature-dependent material electrical resistance. In 1917, Theodore Willard Case [65] discovered the photoconductivity effect of thallium sulphur ($TI_2S$) to create the initial IR PC. This type of PC was then used to investigate fog-like atmosphere conditions for military purposes, but the results were limited.

Since then, modern IR photon detectors have emerged and accelerated with the Second World War. Advances in narrow bandgap semiconductor materials such as InSb and mercury cadmium telluride (MCT/HgCdTe) have allowed for the development of high-performance IR photon detectors. During the 1960s, a wide range of semiconductor alloys with narrow bandgaps was developed from distinct semiconductor groups: III-V (InSb and InAsSb) and II-VI (HgCdTe, MCT) [15], and their spectral response could be modified. The MCT covers up to the VLWIR (30 μm) range making this semiconductor alloy the best choice for a wide range of IR detectors. Due to its low dielectric constant and variable bandgap, MCT has been studied for high-speed applications because it offers a diverse spectrum for SWIR to VLWIR IR detector designs.

Even though MCT detectors dominate the market due to their superior optical and electrical performance, MCT has several shortcomings, such as high material toxicity of Hg and Cd [13], poor uniformity [14], and high costs of growth and fabrication [14]. Due to those limitations involved with the MCT, research activities are being undertaken to search for alternative material systems. Hence, T2SL detectors have become a competitive technology to the current state-of-art MCT because of its superior material qualities, which are significantly different from bulk semiconductors, such as flexibility of bandgap engineering enabling wavelength spanning from SWIR to VLWIR spectral bands [12], reduction of Auger non-radiative recombination arising from the spatial separation of electrons and holes [23], [24], [25], reduction in the tunnelling current caused by the larger electron effective mass leading to lower mobility [22]. In addition, T2SL benefits from several intrinsic properties such as excellent material uniformity over large areas, structural stability due to strong chemical

bonds [26], [27], low growth and fabrication costs [28], and availability of lattice-matched substrates [28].

## 3.2    Historical perspective of type-II superlattice infrared detectors

Since its discovery in the late 1970s, T2SL has been the research focus. The first theoretical investigation and proposal of the new IR detector technology known as ''superlattice'' was realized by Esaki and Tsu in 1970 [66] and Sai-Halasz et al. in 1977 [19]. This was also followed by the first experimental demonstration of InAs/GaSb T2SL by Sakaki et al. in 1978 [67]. The ''Ga-based'' InAs/GaSb T2SL was then proposed for IR imaging by Smith and Mailhiot in 1987 [20]. In 1996, the first high-performance detector based on InAs/GaInSb T2SL was reported by Johnson et al. [21]. Since then, T2SL has received extensive interest due to its favourable material properties. This has allowed the emergence of another competitive material system called ''Ga-free'' InAs/InAs$_{1-x}$Sb$_x$ SL. The InAs/InAsSb SL was initially demonstrated by Biefeld et al. in 1994 and 1995 with the incorporation of low antimony (Sb) content (below 20%) to cover the MWIR spectral band, grown by metal-organic chemical vapour deposition (MOCVD) on InAs substrates and molecular beam epitaxy (MBE) on GaAs substrates [68], [69]. This was followed by the first report on MWIR InAs/InAsSb lasers with a continuous-wave operation, revealed by Zhang [70], demonstrating their suitability for IR emitters. Over the past 20 years, significant advancements have been made in developing device designs to improve the performance level of MWIR T2SL detectors.

Figure 3.1 depicts a five-decade overview of research interests in Ga-based InAs/GaSb T2SL and Ga-free InAs/InAsSb T2SL between 1970 and 2020. As can be seen, since the initial conception of SL in the 1970s, there has been an increase in research publications, although fewer published research articles concentrated on Ga-free T2SL (5.7%) than Ga-based T2SL (10.7%). Between 1991 and 2000, the number of published research articles in Ga-free T2SL increased by 37.7% compared to Ga-based T2SL (19.04%). In contrast, significant progress was made in developing IR detectors between 2001 and 2010, with a greater emphasis on Ga-based T2SL (31.45%) versus Ga-free T2SL (9%). Over the past decade, Ga-free T2SL (47.5%) and Ga-based T2SL (38.7%) have attracted many researchers due to advancements in MBE and MOCVD growth technologies and detector designs. Consequently, using each T2SL

material system offers particular merits and demerits. Table 3.1 summarises the pros and cons of the Ga-based T2SL and Ga-free T2SL material systems.
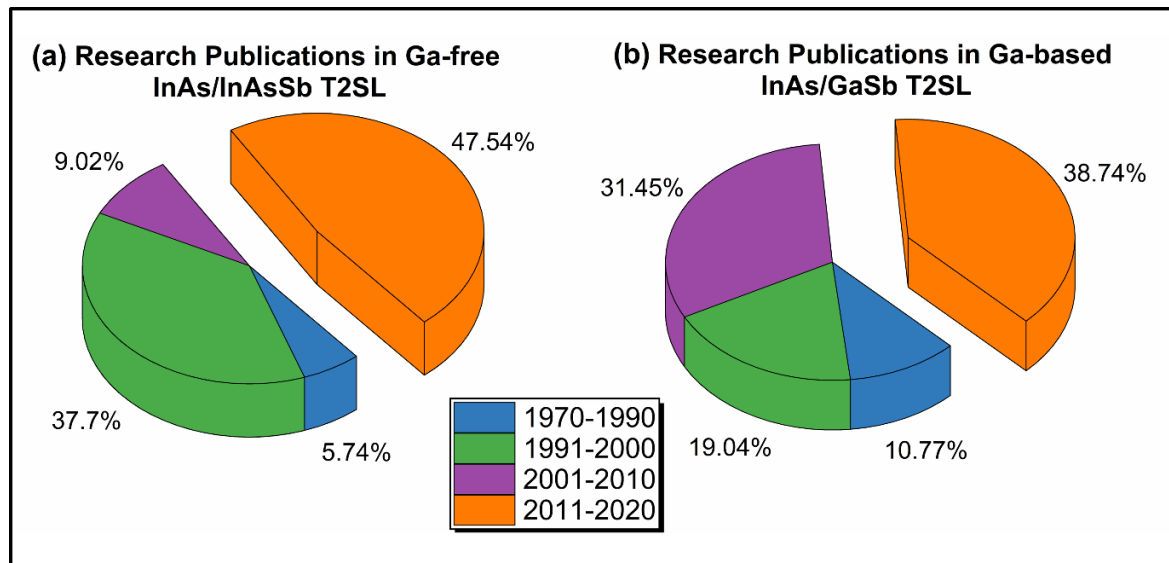


Figure 3.1: A summary of published research articles (in proportions) for both (a) Ga-free InAs/InAsSb and (b) Ga-based InAs/GaSb T2SLs over the past 50 years. Web of Science search employing the terms ''InAs/InAsSb and InAs/GaSb Type-II Superlattices'' in the titles, subjects, abstracts, and keywords.

Given the importance of these two emerging technologies, a thorough literature review is required to compare the materials' properties and device performance with the current state-of-art MCT technology. Because this thesis focuses on developing a Ga-based InAs/GaSb T2SL material system, the review will specifically discuss this material and its device performance compared to other competing materials, such as Ga-free InAs/InAsSb T2SL and MCT.

Table 3.1: A summary of the pros and cons of the Ga-based InAs/GaSb and Ga-free InAs/InAsSb T2SL material systems.

| Material System | Pros | Reference | Cons | Reference |
|---|---|---|---|---|
| InAs/GaSb T2SL | Stronger optical absorption coefficient | [71], [72] | Shorter minority carrier lifetime in the MWIR regime, typically between 140 ns and 800 ns at 77 K | [73], [74] |
| | Larger conduction and valence band offsets leading to lower tunnelling current | [14] | More difficult to grow as four shutters (In, As, Ga, and Sb) must be controlled during growth | [75] |
| | Wider range of cut-off wavelengths can be tuned to cover the SWIR to VLWIR spectrum | [76] | At the SL IFs, sensitivity to elemental intermixing is high | [77], [75], [78], [79] |
| | | | Limited by SRH because of the presence of Ga-component in the GaSb material | [80] |
| InAs/InAsSb T2SL | Longer minority carrier lifetime in the MWIR region, typically from 1.8 μs to 9 μs at 77 K | [81], [82] | Weaker optical absorption coefficient, particularly at longer wavelengths resulting in lower quantum efficiency | [72], [83], [84] |
| | Less complicated growth scheme since solely one shutter (As or Sb) needs control during growth | [85], [14] | More challenging vertical hole transport, particularly at longer wavelengths | [84], [86], [87] |

| | More tolerant to defects, as defects are mainly localised above the conduction band edge | [88] | Smaller conduction and valence band offsets leading to increased tunnelling current | [14] |
|---|---|---|---|---|
| | | | Strong dependence of quantum efficiency on the carrier diffusion length, particularly at longer wavelengths; lower quantum efficiency is caused by shorter diffusion length | [72], [89] |
| | | | Prone to Sb segregation at the SL IFs | [90], [91], [92] |

## 3.3 Fundamentals material properties of type-II superlattice

The binary compound semiconductors used in the T2SL structures are explained in this section. It provides the basic material properties of the InAs/GaSb T2SL, such as bandgap energy (Section 3.3.1), minority carrier lifetime (Section 3.3.2), and absorption coefficient (Section 3.3.3).

### 3.3.1 Bandgap energy

Figure 3.2 depicts the bandgap energy of III-V semiconductor materials (including InAs, InSb, GaSb, GaAs, AlSb, and AlAs) as a function of lattice parameters. As can be seen, these binary materials have specific bandgap energies (cut-off wavelengths). For instance, InSb is a binary semiconductor material with a fixed bandgap energy corresponding to a 5.5 µm cut-off wavelength at 80 K. Although InSb detectors offer high quantum efficiency along with excellent uniformity and high pixel operability [93], [94], [95], InSb-based detectors can only be utilised in the MWIR spectral range, and it can only be operated at a low-temperature range which limits its application for uncooled IR imaging systems [16]. In contrast, the bandgap energy of the $InAs_{1-x}Sb_x$ bulk material system, which is the narrowest (approximately 0.08 eV) among all III-V semiconductors at 0 K, can be tuned to cover the MWIR and LWIR spectral regions by merely altering the Sb concentration.

Nonetheless, there is no available lattice-matched substrate for InAsSb, especially at higher Sb concentrations, which increases the possibility of threading dislocations (TDs) and dark current. InAsSb also suffers from a high rate of Auger non-radiative recombination and high tunnelling current due to its reduced effective mass, which depends on the bandgap energy of bulk materials. Due to these limitations of bulk materials, an alternative material system such as SLs is being investigated. As previously mentioned, the primary advantage of using such a material system is the adaptability of bandgap energy and the corresponding wavelength while maintaining a lattice-matched substrate and reducing TDs.
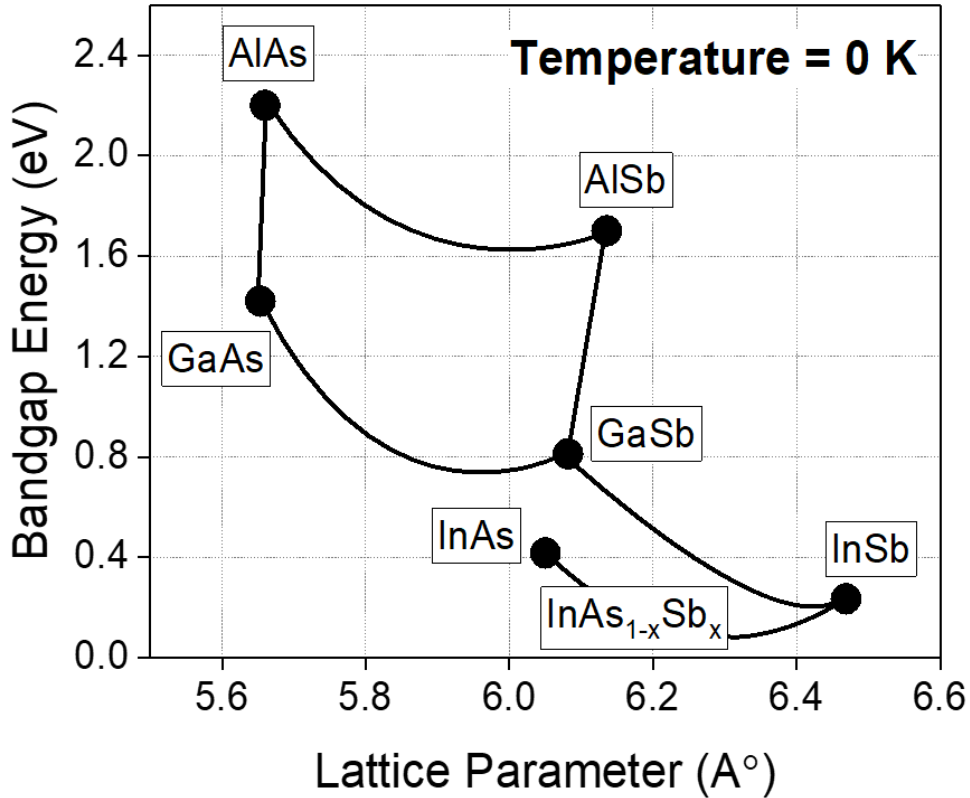
Figure 3.2: Bandgap energy versus lattice parameter of several III-V semiconductor materials, including InAs, InSb, GaSb, GaAs, AlAs, and AlSb at a temperature of 0 K.

### 3.3.2 Minority carrier lifetime

The minority carrier (MC) lifetime is an important optical property of the T2SL material, as it directly influences the dark current as expressed by Equation 2.27, detectivity, and operating temperature of T2SL detectors. The MC lifetime of the detectors depends on the diffusion length as expressed by:

$$L = \sqrt{D}\tau \qquad (3.1)$$

where $L$ is the diffusion length of the MC lifetime, $D$ is the diffusion coefficient, and $\tau$ is the MC lifetime. The effect of MC lifetime and the diffusion length on the performance of the T2SL detector is discussed later in Section 3.4.1. Several recombination processes influence the MC lifetime in the T2SL. These are radiative or non-radiative recombination, such as Auger and

50

Shockley-Read-Hall (SRH). Radiative recombination occurs in a direct bandgap semiconductor material when an electron in the conduction band recombines with a hole in the valence band and produces light (photon). However, non-radiative recombination occurs when electrons and holes recombine; they might not generate a photon. Alternatively, the energy produced is transferred to vibrate the lattice atoms meaning that energy is converted into phonons. Each of these recombination mechanisms has its lifetime ($\tau$), and it is significantly temperature dependent, and the total lifetime can be described as follows:

$$\frac{1}{\tau} = \frac{1}{\tau_{Rad}} + \frac{1}{\tau_{Aug}} + \frac{1}{\tau_{SRH}}$$

(3.2)

where $\tau_{Rad}$, $\tau_{Aug}$, and $\tau_{SRH}$ refer to the corresponding lifetimes of radiative, Auger, and Shockley-Read-Hall recombination processes, respectively. The temperature-dependent MC lifetime measurement is adequate for determining the dominant recombination mechanism in the T2SL material [96]. In 2013, Höglund et al. [82] performed the MC lifetime temperature-dependent measurements of Ga-free T2SL between 77 and 250 K. This study reported that the radiative recombination process was dominant in the temperature range from 77 to 200 K, and the MC lifetimes noticeably increased from 1.8 to 2.8 µs. In contrast, the MC lifetimes were limited to Auger recombination above 200 K since this type of recombination dominated the process at this temperature range. The Auger recombination of MWIR Ga-free T2SL was reported to be almost an order of magnitude lower than the MCT material system [97]. The Auger recombination was shown to be reduced by modifying the electronic band structure, including layer thickness, composition, and coherent strain. The intrinsic properties of the materials, including absorption spectrum, band structure, and carrier density, can also determine the BTB radiative and Auger non-radiative recombination.

On the contrary, SRH non-radiative recombination occurs due to the formation of intentional or unintentional dopants; as a result, the recombination occurs through defects (trap levels take place in the bandgap of the material). The formation of these defects occurs typically during growth caused by the internal strain, impurities, or TDs in the structure. In the case of Ga-based T2SL, it was reported that the MC lifetimes decrease over the temperature range between 11 and 100 K, which could be attributed to the influence of carrier localisation and

the substantial contribution from SRH non-radiative recombination active centres. For more information about the carrier localisation effect on MC lifetimes and device performance of T2SL, the reader is guided to the following papers [98], [99], [100].

Several authors have measured the MC lifetimes of Ga-based and Ga-free T2SL materials. The MC lifetimes of MWIR Ga-based T2SL are significantly shorter (100 ns at 100 K [101] and typically in the range of 30-100 ns at 77 K [81], [82], [101], [102], [103]) than that of Ga-free T2SL (10 μs at 77 K) [102]. The existence of the Ga-component in the InAs/GaSb T2SL material is believed to contribute to the creation of native defects, which ultimately deteriorates the device's performance [80]. Figure 3.3 depicts the MC lifetimes of III-V compound semiconductors, including InSb, GaSb, InAs, InAs/GaSb T2SL, InAs/InAsSb T2SL and II-VI MCT material systems. This figure provides a summary of the reported MC lifetimes at 77 K in the MWIR region over the past few years, from 2005 until 2020. Data were collected from the following research groups working on Ga-free T2SL [81], [82], [100], [102], [104], [105], [106], [107], [108], [109], [110], [111], Ga-based T2SL [73], [112], [80], [113], [101], [114], [115], [116], binary and ternary compounds of InAs, InSb, GaSb, and InAsSb [80], [81], [105], [117], [118], [119], [120], [121], [122], and MCT [123], [124], [125], [126], [100], [104]. As can be observed, although the MCT material has the longest MC lifetime (close to 59 μs), the Ga-free InAs/InAsSb T2SL has roughly comparable lifetimes. This is followed by InAs, InSb, and InAsSb bulk materials with remarkably longer MC lifetimes than GaSb material. Among all other compounds, the Ga-based InAs/GaSb T2SL material system consistently has the shortest MC lifetime, generally ≤ 100 ns. This is due to SRH non-radiative recombination centres caused by the presence of Ga component in the GaSb material, as it has been reported that defects are located in the mid-gap of the InAs/GaSb T2SL as opposed to the Ga-free material system, where defects are localised above the conduction band edge. It should also be noted that as the lifetime directly impacts the diffusion current of the T2SL devices based on $I_{diff} \sim \tau^{-1}$, the performance of diffusion-limited Ga-free T2SL devices is theoretically projected to surpass the Ga-based T2SL devices significantly; however, this has not been practically recognised yet.

Figure 3.3: An overview of the accumulated values of MC lifetimes at 77 K over the last few years for III-V compound semiconductors including InAs, InSb, GaSb, InAs/GaSb T2SL, InAs/InAsSb T2SL, and II-VI MCT.

### 3.3.3 Absorption coefficient

Another important optical property of semiconductor materials is the absorption coefficient. It is well known that absorption of incident photons occurs when their energy is greater than or equal to the bandgap energy of the materials ($E \geq E_g$). In contrast, photon transmission occurs when the incident photons are smaller than the bandgap energy of the material ($E < E_g$). Considering an incident photon with intensity ($I$) passing at some depth through a semiconductor material ($x$). The intensity of the photons varies with distance, and this can be described using the fowling equations:

$$-\frac{dI(X)}{dx} = \alpha I(x) \qquad\qquad (3.3)$$

$$I(x) = I_0 exp^{-(\alpha x)} \qquad\qquad (3.4)$$

where $\alpha$ is the absorption coefficient with the unit of $cm^{-1}$. The absorption coefficient mainly depends on the energy and corresponding wavelength of the incident photons and the semiconductor material property. As Equation (3.4) expresses, the photon intensity exponentially decreases with the material depth or thickness increase.

Klipstein et al. [72] conducted theoretical and experimental work to compare the absorption coefficients of the Ga-based and Ga-free T2SLs. For a realistic comparison, this study designed both materials to have similar cut-off wavelengths, around 4.5 µm at 77 K. Figure 3.4 depicts the absorption coefficients of the Ga-based and Ga-free T2SLs as a function of wavelength at 77 K. As observed, the absorption coefficient of the Ga-based T2SL is slightly stronger (> 0.2 $µm^{-1}$) in comparison with the Ga-free T2SL (< 0.2 $µm^{-1}$) near the cut-off wavelength of the photodetectors. It is believed that the lower absorption coefficient could be attributed to the more negligible conduction and valance band offsets in the Ga-free T2SL in comparison to the Ga-based T2SL, which increases the tunnelling mechanism of e-h carriers, thereby decreasing the absorption coefficient and QE performance.

The layer thickness, number of periods, and Sb composition in Ga-free T2SL typically influence the absorption coefficient of T2SL. Several studies have shown that increasing the absorption layer of the T2SL affects the QE performance. For instance, Katayama et al. [127] performed a theoretical analysis of three InAs/GaSb T2SL *pin* structures with different thicknesses of absorption layers (1.5, 3, 5, and 10 µm). It was revealed that the 10 µm thick absorber layer attained the highest QE of around 65% at a 4.5 µm cut-off wavelength. In contrast, the 1.5 µm thin absorber layer achieved the lowest value of QE of approximately 28%. Another investigation by Letka et al. [128] showed the effect of increasing the periodic thickness of MWIR InAs/InAsSb T2SL on the absorption coefficients while preserving the exact absorption layer thickness of 0.7 µm. The absorption coefficients were higher with increasing the T2SL periodic thickness, particularly near the cut-off wavelengths of the devices.
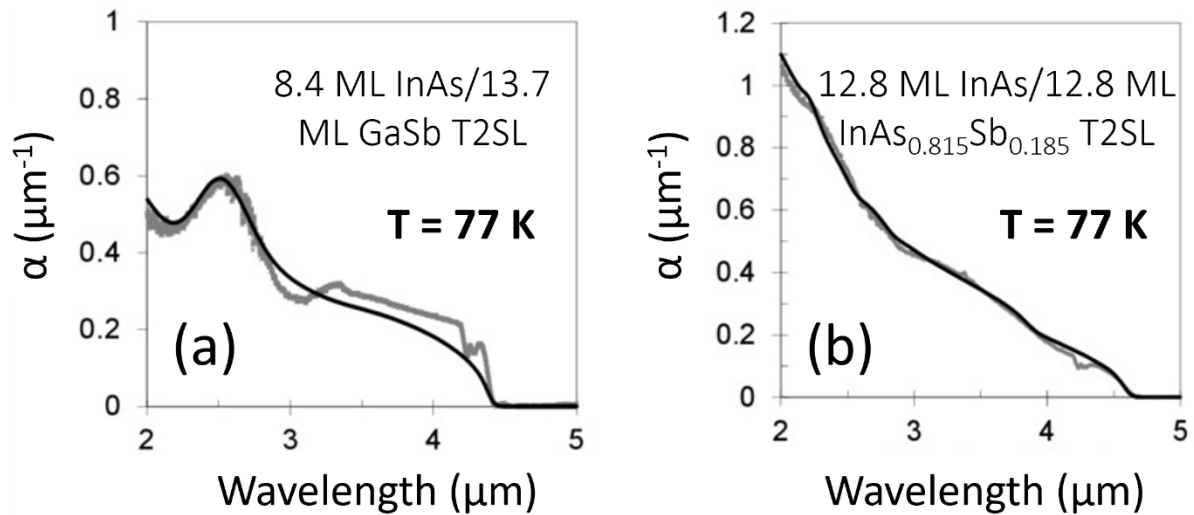
Figure 3.4: Theoretical (black line) and experimental (grey line) results of the absorption coefficient versus the detector cut-off wavelength at 77 K for (a) Ga-based and (b) Ga-free T2SLs. The figure is reproduced from reference [72].

A study by Flatté et al. [129] reported the effect of modifying the Sb compositions in InAs/InAsSb T2SL from 20 to 40% on the absorption coefficient. It was found that by increasing the Sb contents between 20 and 25%, the absorption coefficients noticeably increased. In contrast, the absorption coefficients became insensitive to the variations with higher Sb compositions in the InAs/InAsSb T2SL. It is argued that the variations in the absorption coefficients are possibly owing to the changes in the conduction and valence band offsets whilst changing the Sb compositions in the InAs/InAsSb T2SL material.

## 3.4    Performance comparison of type-II superlattice

This section compares the device's electrical performance of InAs/GaSb T2SL, InAs/InAsSb T2SL, and the most advanced MCT. This comprises the performance of quantum efficiency (Section 3.4.1), dark current density (Section 3.4.2), and differential resistance area-product (Section 3.4.3).

### 3.4.1  Quantum efficiency

The QE of any semiconductor device is critical. The conversion of incident photons (input light) into output power is called QE. Two primary QE terms necessitate differentiation. These are

internal quantum efficiency (IQE) and external quantum efficiency (EQE). The IQE is the ratio of the number of electron-hole (e-h) pairs or charge carriers collected to the number of photons of a given energy that shine from outside and are absorbed by the device. In contrast, the EQE is the ratio of the number of charge carriers collected by the device to the number of photons of a given energy that shine on the device from outside (incident photons). As expressed by Equation (2.33), the QE is inversely proportional to the cut-off wavelength of the detector. It is indicated that the QE performance of T2SL detectors can be improved by increasing the thickness of the absorber layer or by applying an anti-reflection (AR) coating. However, the primary technological issue with T2SL detector fabrication is the difficulty in growing a high-quality thick absorption layer that can improve QE performance. The challenge associated with the critical thickness originating from the internal strain of the SL can deteriorate the material quality while increasing the thickness of the constituent layers. This problem results from the minor lattice mismatch between the InAs and GaSb layers. The internal strain energy in the SL structure increases due to the growth of non-lattice-matched layers of two materials on top of one another. This strain energy will subsequently increase until a certain critical thickness is attained. At this point, the formation of TDs and defects becomes energetically advantageous.

The MC diffusion length also influences the performance of MWIR T2SLs via the collection efficiency [14]. It is commonly accepted that for a detector to achieve a high QE, the thickness of its absorption layer must be equal to or greater than the desired cut-off wavelength. The MC diffusion length should be considered when increasing the absorber layer thickness of T2SL because increasing the absorber layer thickness beyond the diffusion length may not improve the device's efficacy. This is because the photogenerated carrier collection is impossible when the absorption layer thickness exceeds the detector's carrier diffusion length. It has been reported that the diffusion length for MCT is around 20 μm, implying no trade-off between absorption and collection efficiency. As a result, MCT detectors with thick active regions frequently achieve high QE performance, typically around 80% at 77 K [14]. The absorption thickness and diffusion length limitation for T2SLs can be overcome using a multi-stage detector called quantum cascade infrared photodetector (QCIRPD) design, which will be discussed briefly in Section 3.5.2.

Figure 3.5 depicts the overall QE performance of the emerging Ga-containing and Ga-free T2SL detectors with different absorber layer thicknesses, designs, doping concentrations, and bias operations at a temperature of 77 K. Data were herein collected from various research groups that are working on the developments of this kind of material system including Ga-free T2SL [130], [131], [132], [133], [134], [135], [136], [137] and Ga-containing T2SL [114], [138], [139], [140], [141], [142], [143], [144], [145], [146], [147], [148], [149], [150] on GaSb substrates.
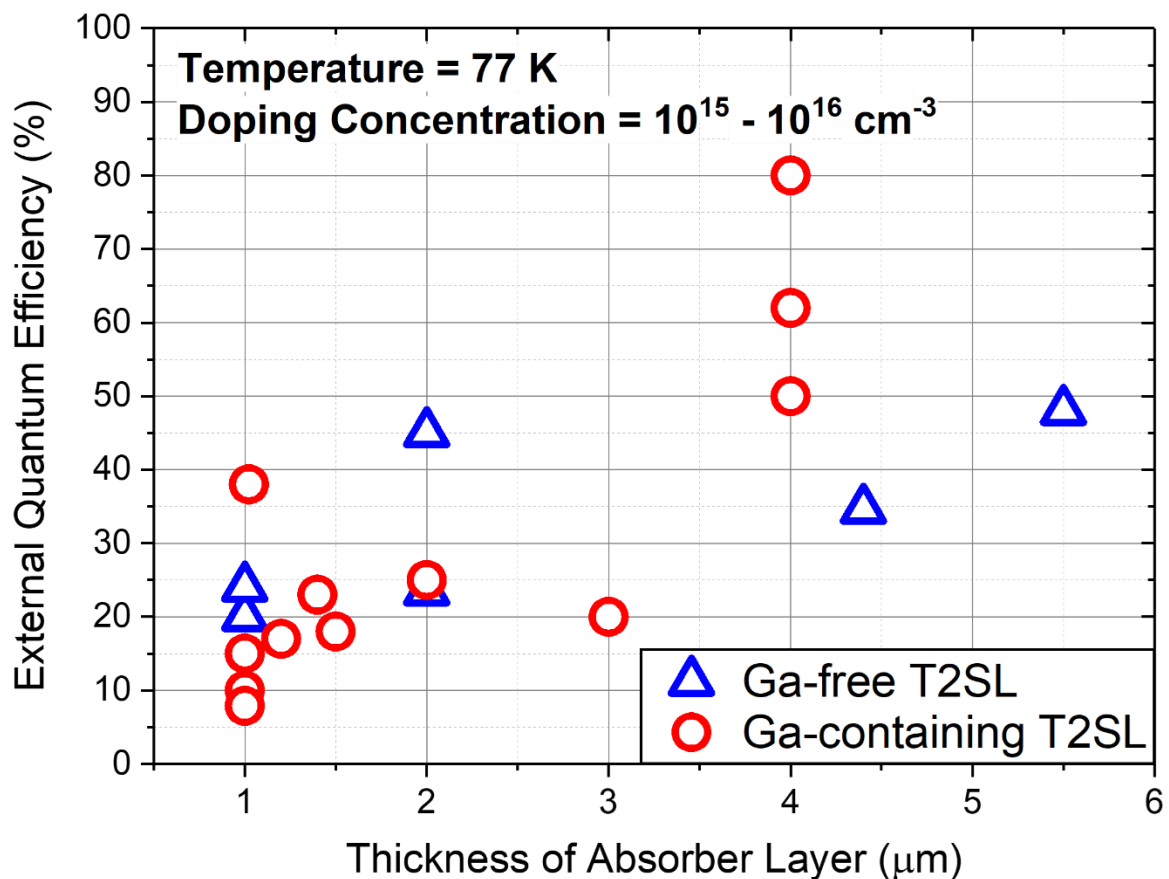


Figure 3.5: Accumulated values of EQE as a function of absorber layer thickness for Ga-free and Ga-containing T2SL detectors at 77 K.

As can be observed, the QE performance depends on the absorption layer thickness; therefore, the QE of the detectors improves substantially when the absorption layer thickness is increased; however, as previously demonstrated, the diffusion length parameter must be considered. It is also evident that the EQE for both Ga-free and Ga-containing T2SL detectors generally ranges between 10%, with thinner active regions, and reaches 60%, with increasing the thickness of the T2SL active regions. The best-performing T2SL device is reported by Chen

et al. [150], where the QE of the InAs/GaSb *pin* T2SL detector was around 80% at a 4.6 μm cut-off wavelength. Similarly, the EQE for both material systems at HOT of 150 K is depicted in Figure 3.6. Data herein were collected from the following research groups, including Ga-free T2SL [151], [137], [132], [152], [153], [154], [155], [156] and Ga-containing T2SL [157], [158], [159], [114], [160], [161]. T2SLs with barrier and non-barrier structures are compared to demonstrate the effect of T2SL design on EQE performance. The advantages of these novel barrier designs will be briefly discussed later in Section 3.5.1. The EQE for T2SL detectors at 150 K is roughly between 25 and 60%. While the EQE of T2SLs appears to be temperature-dependent, the literature contains contradictory arguments regarding MC diffusion length's temperature dependence. Rogalski et al. [162] presumed that the diffusion length reduces at elevated temperatures, possibly as a result of the decreased MC lifetime implied by the well know $T^{-1/2}$ dependence of SRH lifetimes. In contrast, several works revealed that the diffusion length is directly proportional to the temperature. Klipstein et al. [163] demonstrated that the lateral diffusion length changes linearly from 6.3 to 11 μm over the temperatures between 78 and 130 K. This also agrees well with the temperature dependence of diffusion coefficient (*D*) as described by:

$$D = \frac{K_B T}{e} \mu \tag{3.5}$$

where $K_B$ is the Boltzmann constant, *T* is the temperature, and *μ* is the mobility. It should be noted that Equation (3.5) can only be used to calculate the lateral diffusion length, not the vertical diffusion length, which primarily influences the detector performance. Taghipour et al. [116] have recently utilised the electron-beam induced current (EBIC) technique to determine the vertical diffusion length of InAs/GaSb T2SL over the temperature range of 80 to 170 K. It was found that the diffusion length is almost constant at around 1.5 μm between 80 and 140 K and then increases significantly to 4.5 μm at 170 K. This study suggests that by paying attention to the T2SL design and diffusion length parameter, the QE of the T2SL can be improved even further. It is also important to note that the background doping concentration (intrinsic carrier concentration – $n_i$) affects the MC lifetime and hence the QE of T2SL detectors. It was found that when the doping concentration of the T2SL active region is increased, the QE of the detectors decreases, possibly due to a decreased MC diffusion length

[164]. This suggests that the intrinsic carrier concentration scales inversely with the MC lifetime ($n_i \sim \tau^{-1}$) [82]. The reader is directed to the following references for more detailed information on the impact of carrier doping concentration on MC lifetime [165], [166], [167], [168].
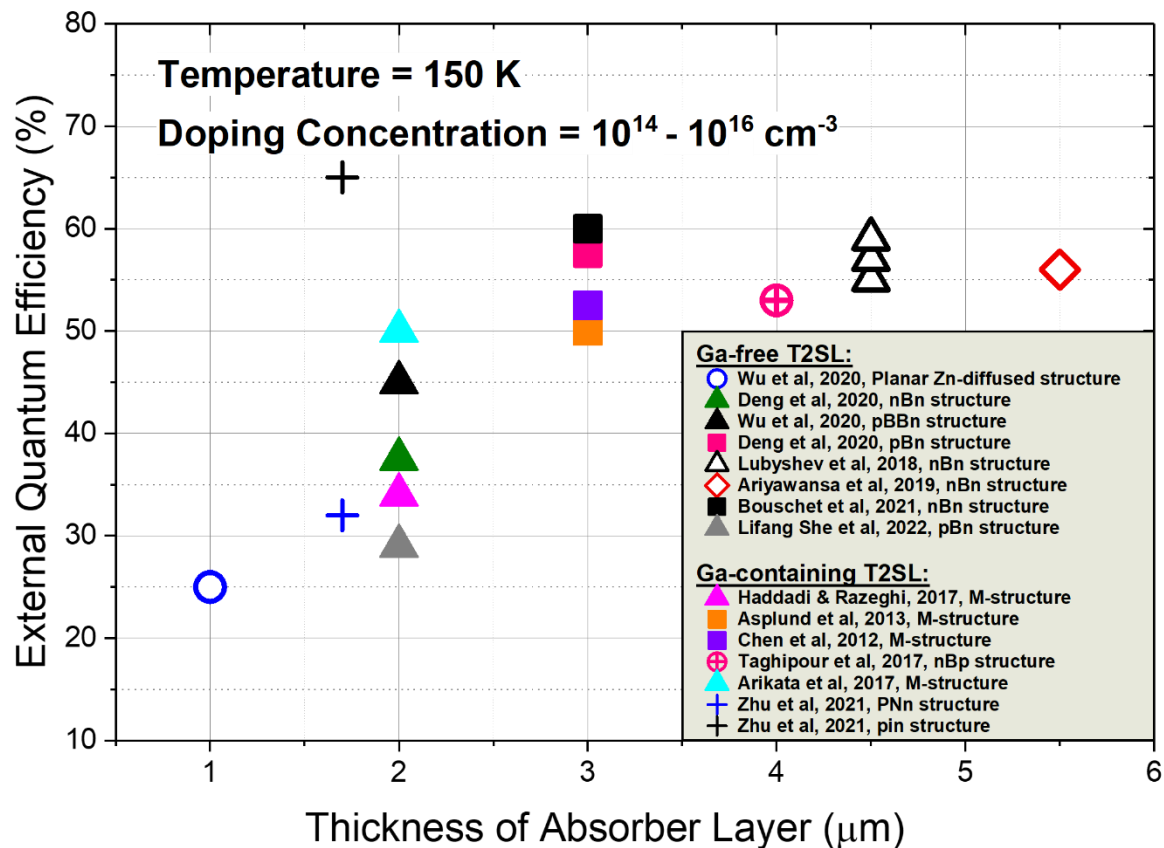


Figure 3.6: Collected values of EQE as a function of absorber layer thickness for Ga-free and Ga-containing T2SL detectors at HOT of 150 K.

### 3.4.2 Dark current density

The dark current is a crucial figure of merit for the devices. Despite the anticipated technological and theoretical benefits of T2SLs, the practical efficacy of T2SL detectors has not yet reached that of bulk MCT detectors. The origins of dark current must be investigated in order to comprehend the reasons for the high dark current demonstrated by the T2SL detectors. Overall, the dark current of narrow bandgap semiconductors can be differentiated into ''bulk'' and ''surface'' currents as expressed by the following equation:

$$J = \frac{I}{A} = \frac{(I_B + I_S)}{A} = J_B + J_S \left(\frac{P}{A}\right) \tag{3.6}$$

where $I_B$ and $I_S$ are the bulk and surface currents, $J_B$ and $J_S$ ate the bulk and surface current densities, and $P/A$ is the ratio of the device mesa perimeter to the area. The most significant ''bulk'' dark currents are (i) G-R current related to the SRH process in the depletion region of the detector and (ii) thermally produced diffusion current associated with the intrinsic properties of the material. As explained earlier, the SRH G-R process is dominant in InAs/GaSb T2SL owing to the presence of the Ga-component, which is responsible for the native defects, limiting the MC lifetime and increasing the dark current of T2SL devices [55]. Since the MC lifetime directly affects the diffusion current of T2SL detectors according to $I_{diff} \sim \tau^{-1}$, diffusion-limited Ga-free T2SL detectors are supposed to perform significantly better than their counterpart Ga-based T2SL detectors due to the longer MC lifetime. However, this has not been realised yet.

In contrast, the ''surface'' dark current is related to the surface states in the junction. It is understood that during the pixel (mesa) isolation process, termination of the periodic crystal structure occurs abruptly, creating unsatisfied (dangling) chemical bonds at the semiconductor-air IF, which are responsible for generating surface states within the bandgap and anchoring the Fermi level. To illustrate, surface states occur due to abrupt discontinuity of the lattice structure at the surface, in which many localised energy states or generation-recombination centres might be introduced. On the contrary, interface states are localised states near the interface and within the forbidden band. Interface traps introduce energy states within the semiconductor bandgap, cause the Fermi level to be pinned near the mid-gap, and enhance surface leakage currents [169]. The surface states can affect the junction current at the surface, resulting in higher dark current and probably lower photocurrent due to shorter lifetimes/diffusion lengths. Thus, to improve overall device performance, surface passivation should be developed for the T2SL InAs/GaSb material system to terminate the dangling bonds at the semiconductor interface. In addition, etch by-products, surface contaminants resulting from the fabrication process, and differential etching generate additional interfacial states contributing to the dark current. Fortunately, the surface-related

current can be efficiently minimised using various passivation processes discussed in Section 3.6.2

The dark current density of state-of-the-art T2SL detectors is still substantially higher than that of bulk MCT detectors in the MWIR range, as shown in Figure 3.7. ''Rule 07'' is an empirical expression established in 2007 and updated in 2010 which shows the best performing diffusion-limited dark current densities of planar *p-n* MCT detectors manufactured at Teledyne Imaging Sensors (TIS) and operated at a temperature above 77 K [170, p. 07]. Figure 3.7 accumulates the reported dark current density of Ga-containing and Ga-free T2SL detectors at 77 K. The data in the figure was collected from the literature as these T2SL devices were fabricated by various research groups, as summarised in Table 3.2. It should be noted that these consist of different designs of T2SLs, including barrier and non-barrier structures, doping concentration, bias operation, absorber thickness, and periods.
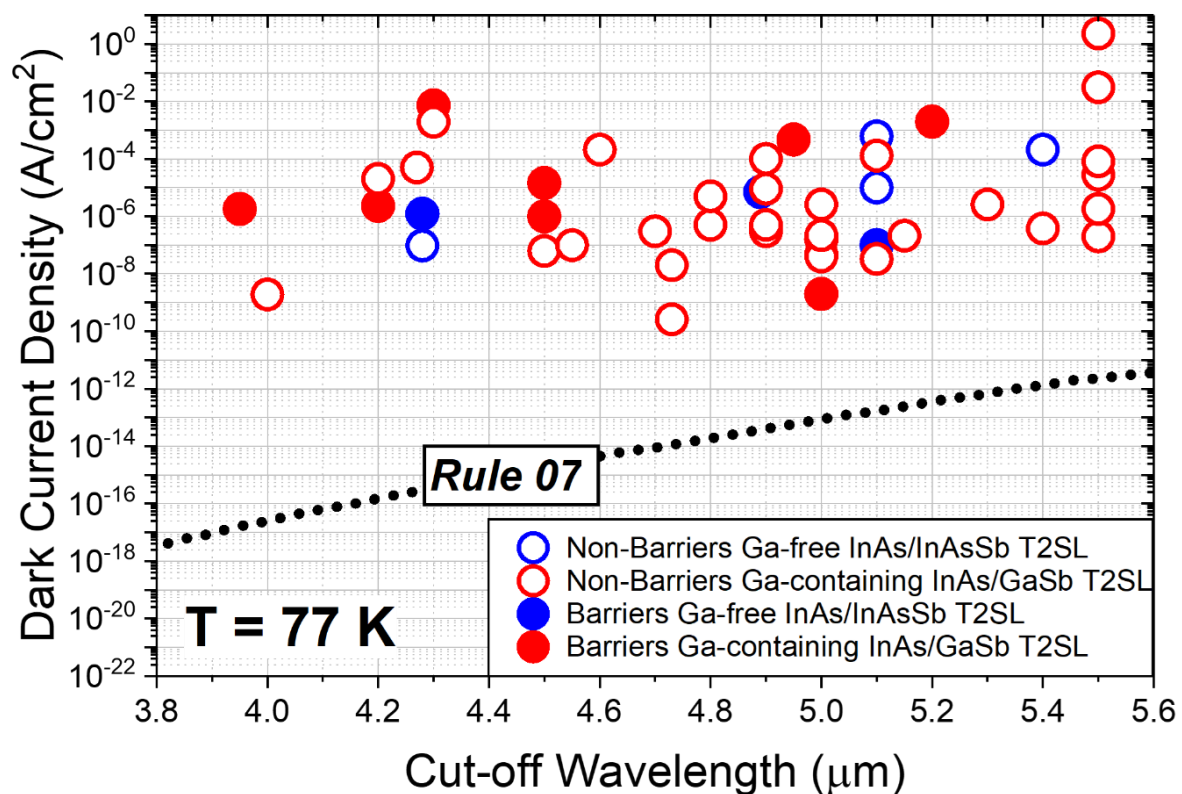


Figure 3.7: Accumulated values of dark current density versus cut-off wavelength for Ga-containing and Ga-free T2SL detectors compared with MCT's ''Rule 07'' at a low temperature of 77 K.

Figure 3.7 demonstrates that the dark current density of T2SLs is typically four to five orders of magnitude greater than that of MCT's ''Rule 07''. As can be seen, the research studies of Ga-free (barrier and non-barrier-based) T2SL are limited compared to their Ga-containing counterparts. The majority of dark current densities of the barriers and non-barriers Ga-containing and Ga-free T2SL detectors are roughly in the range between $10^{-4}$ and $10^{-8}$ A/cm$^2$ (with some higher and lower outliers). So far, the best-performing T2SL detector was reported by Schmidt et al. [171] in 2017, employing a $P^+N^-$ design with a cut-off wavelength of 4.73 μm attained at 77 K. A very low dark current density of $2.6 \times 10^{-10}$ A/cm$^2$ was obtained under an applied voltage of 100 mV.

Table 3.2: The development of InAs/GaSb and InAs/InAsSb T2SLs is the focus of numerous international research groups.

| Research Group | Interest/Focus | Reference |
|---|---|---|
| Centre for Quantum Devices (CQD) at the Northwestern University, the USA | Ga-containing and Ga-free T2SLs | [131], [132], [148], [153], [159], [172], [173], [174], [175], [176], [177], [178], [179], [180], [181] |
| State Key Laboratory for Superlattices and Microstructures, Institute of Semiconductors, Chinese Academy of Sciences, China | Ga-containing T2SLs | [182], [183], [184] |
| Synergetic Innovation Centre of Quantum Information and Quantum Physics; University of Science and Technology of China | Ga-containing and Ga-free T2SLs | [133], [134], [185] |
| Kunming Institute of Physics, University of Technology, China | Ga-containing T2SLs | [186] |
| Centre of Materials Science and Optoelectronics Engineering, University of Chinese Academy of Sciences, China | | [152], [154], [156] |

| | | |
|---|---|---|
| Agency of Defence Development, Republic of Korea | Ga-free T2SLs | [187] |
| Jet Propulsion Laboratory (JPL) at the National Aeronautics and Space Administration (NASA), the USA | | [76], [111], [130], [188], [189] |
| Montpelier in France | Ga-containing and Ga-free T2SLs | [96], [110], [141], [143], [144], [145], [155], [190], [191], [192], [193], [194], [195] |
| Arizona State University (ASU) in the USA | Ga-free T2SLs | [151] |
| Centre for High Technology Materials, University of New Mexico | Ga-containing T2SLs | [114], [138], [139], [140], [142], [146], [196], [197] |
| Fraunhofer Institute for Applied Solid State Physics in Germany | | [171], [198], [199] |
| Institute of Applied Physics, Military University of Technology, Poland | Ga-containing and Ga-free T2SLs | [200] |
| ShanghaiTech University in China | | [149], [161], [201], [202] |
| Key Laboratory of Infrared Imaging Materials and Detectors, Shanghai Institute of Technical Physics, Chinese Academy of Sciences in China | Ga-containing T2SLs | [150], [203] |
| IRnova in Sweden | | [145] |
| Department of Physics, Chonnam National University, Korea | | [204], [205] |
| Department of Physics, Middle East Technical University, Turkey | | [206, p. 3], [207] |

Figure 3.8 depicts the dark current density of the T2SL detectors at a HOT of 150 K. Due to incorporating these barrier layers into the T2SL structure, the dark current density of barrier-based T2SL detectors has largely reached the performance level of MCT's ''Rule 07''. These barrier layers help reducing or even eliminating the contribution of G-R SRH-related dark current. The current density is generally around two orders of magnitude to a few times Rule 07. So far, the lowest reported dark current density of $8 \times 10^{-7}$ A/cm$^2$ was obtained with a Ga-free barrier structure at 4.5 μm cut-off wavelength and under an applied voltage of -100 mV at 150 K [187], which is only six times ''Rule 07'' of the MCT.
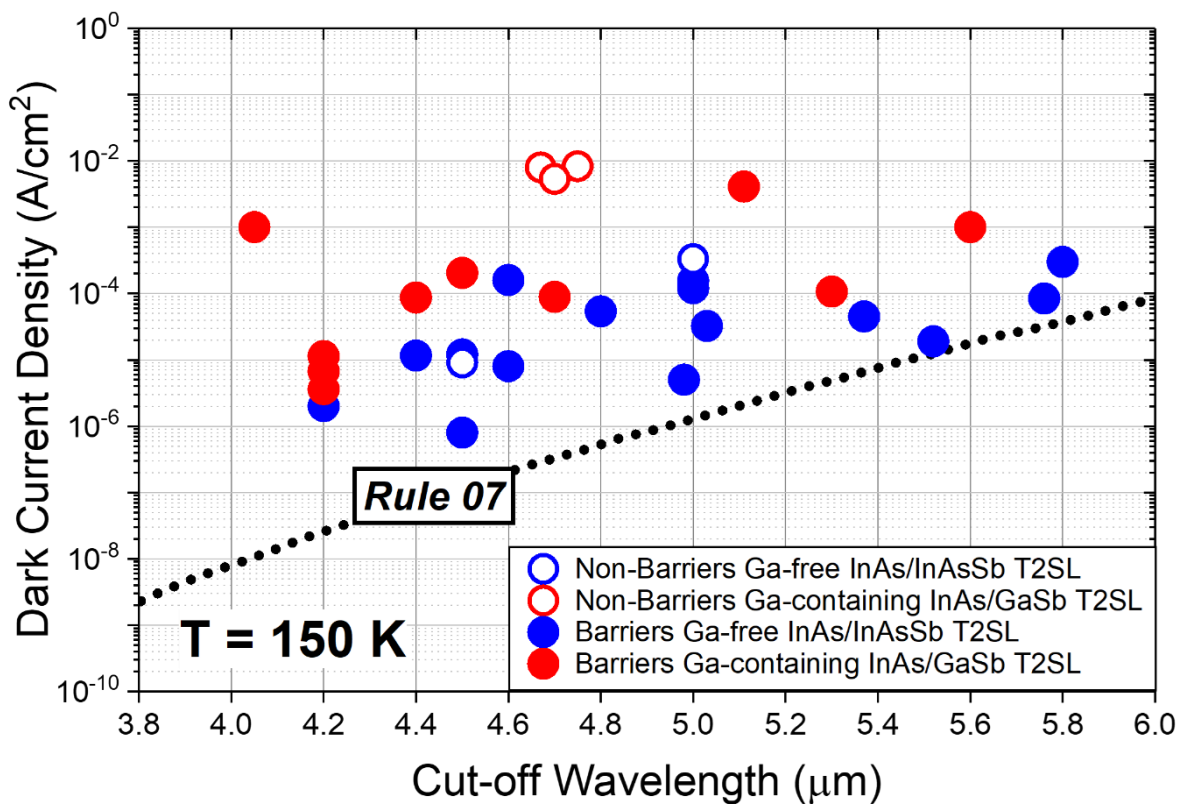


Figure 3.8: Accumulated values of dark current density as a function of cut-off wavelength for Ga-containing and Ga-free T2SL detectors compared with MCT's ''Rule 07'' at HOT of 150 K.

### 3.4.3 Differential resistance-area product

Differential resistance area-product ($R_dA$) is an essential figure of merit of a PV detector and can be evaluated using the following expression:

$$R_0 A = \left( \frac{\partial J_{dark}}{\partial V} \right)^{-1} \tag{3.7}$$

where $R_0$ is the resistance at zero-voltage, and $J_{dark}$ is the dark current density. $R_dA$ refers to the dynamic resistance area-product, and it is used for barrier detectors where an applied voltage is needed to attain an appropriate spectral response. Figure 3.9 depicts the $R_dA$ product of T2SL detectors compared to ''Rule 07'' at room temperature. Data in the plot were collected from different research groups, including MCT [200], Ga-free T2SL [208], [209], [210], [211], and Ga-based T2SL [96], [197], [200], [212] detectors. Generally, the $R_dA$ performance of T2SL detectors is noticeably close to the performance level of the current state-of-the-art MCT detectors at room temperature operation.
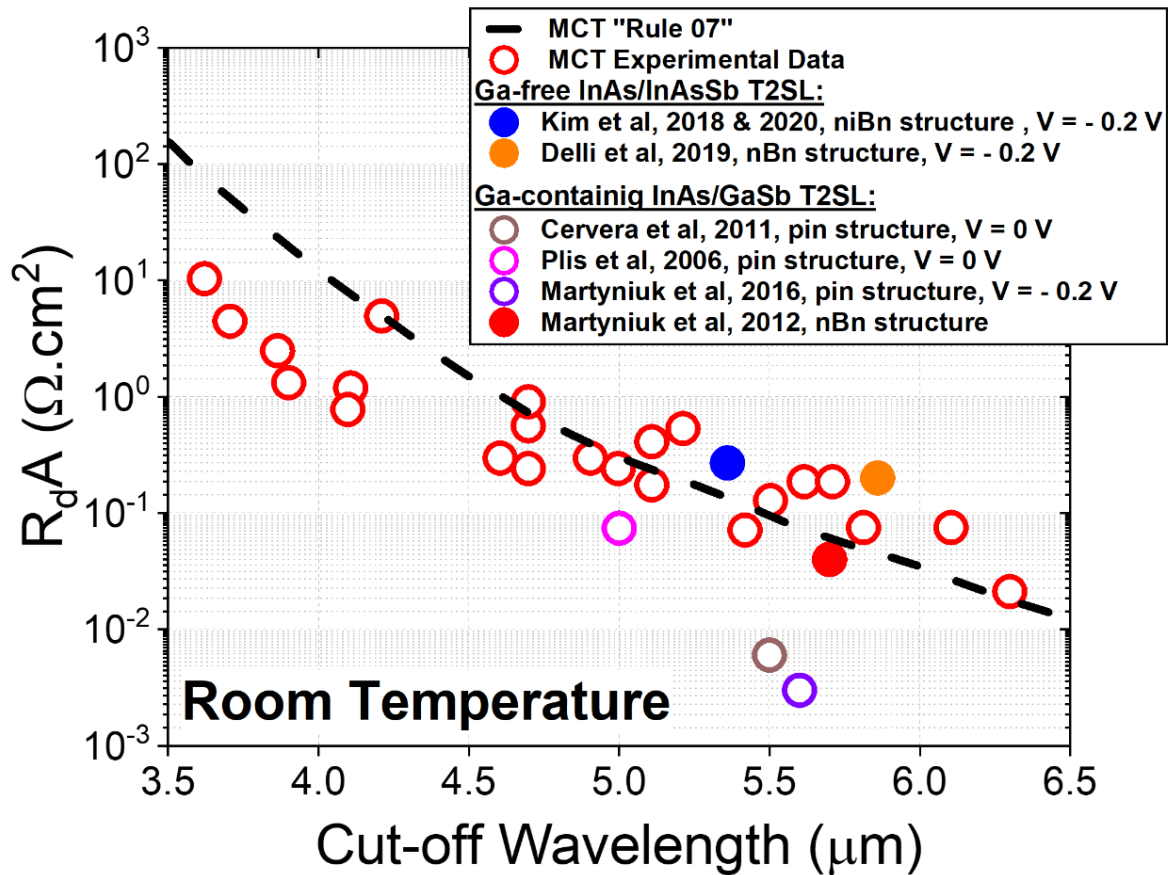
Figure 3.9: Accumulated values of differential resistance area-product of InAs/GaSb T2SL, InAs/InAsSb T2SL, and MCT detectors at room temperature operation.

## 3.5    Advancements in infrared type-II superlattice technologies

Due to the promising advantages of T2SLs in recognising HOT detection, several advances in IR detection technologies have been made to circumvent the requirements for cryogenic cooling and fulfil the need for SWaP application. This section briefly discusses novel technologies and future approaches to HOT IR detection, such as incorporating barrier detectors (Section 3.5.1) and QCIRPDs (Section 3.5.2).

### 3.5.1   Barrier infrared photodetectors

The HOT application is eventually realized through the use of detectors with a unipolar barrier structure, such as *nBn*, which typically consists of a thin *n*-type region, a wide bandgap unipolar barrier layer that forms a barrier for electrons but not holes, and an *n*-type absorber

region. The first barrier structure-based *nBn* was established in 2006 by Maimon and Wicks [213], where they successfully demonstrated a reduction in the dark current of the *nBn* devices. In their work, InAs or InAsSb bulk material was utilised as an *n*-type absorber region and a wide bandgap barrier layer was employed between the top contact and the absorber region, as shown in Figure 3.10(a). The incorporation of the barrier layer acts as a blocking layer for the majority of carriers and allows confining of the electric field into the barrier layer instead of the active region. The *nBn* structure has two major benefits over the conventional *pin* structure. (i) the dark current density of the *nBn* detector is lower than that of the *pin* detector at the same operating temperature, and (ii) the *nBn* structure can operate at a higher temperature than the *pin* structure at the same dark current density, as depicted in Figure 3.10(b).

In a *pin* junction, the SRH G-R mechanism efficiently occurs in the depletion region, where the mid-gap traps are activated. Particularly, the SRH G-R becomes dominant at low temperatures (below 200 K), which is found to be the main contribution to the dark current [213]. In the barrier structure, the SRH process occurs over the wide bandgap of the barrier material leading to a significant reduction in the SRH process. Alternatively, the diffusion current dominates the dark current for the barrier devices. The G-R current related to the SRH process and diffusion current can be calculated as follow:

$$J_{SRH} \; \alpha \; n_i \exp\left(\frac{-E_g}{2K_B T}\right) \tag{3.8}$$

$$J_{diff} \; \alpha \; n_i^2 \exp\left(\frac{-E_g}{K_B T}\right) \tag{3.9}$$

where $J_{SRH}$ and $J_{diff}$ are the Shockley-Read-Hall and diffusion current density, respectively, $E_g$ is the bandgap energy, $K_B$ is the Boltzmann constant, $T$ is the temperature, and $n_i$ is the doping concentration.

Since Maimon and Wicks' invention of the barrier structure, extensive research has been conducted to enhance the design and performance of T2SL detectors. Hence, various T2SL barrier designs have been extensively developed by many research groups such as *nBn* [139],

[146], [214], [215], [137], [174], [190], *pBn* [154], [173], and *nBp* [114], [138], [216]. In 2007, the CQDs group led by Razeghi developed an M-barrier-based structure [217].
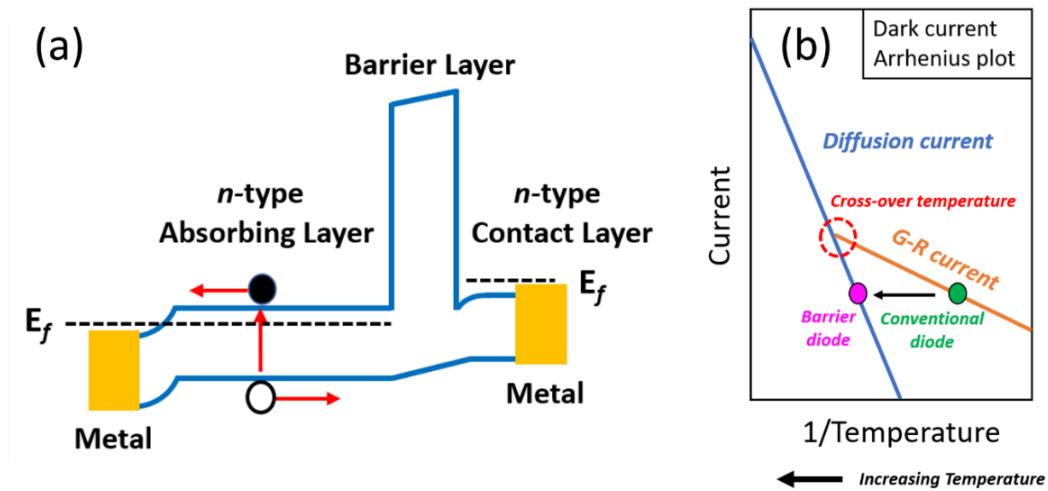


Figure 3.10: (a) Schematic view of incorporating a barrier structure under an applied voltage and (b) representation of dark current (Arrhenius plot) depicting the dark current temperature dependence in a conventional and barrier diode structure.

The M-structure consists of a thin AlSb barrier layer placed in the centre of the GaSb layer inside the InAs/GaSb T2SL region to block electrons in the conduction band and produce a double QW for holes in the valence band. Figure 3.11 represents the M-structure, emphasising the eponymous ''M'' shape. The main advantage of using this structure is to suppress the tunnelling current of the detector and achieve HOT performance.
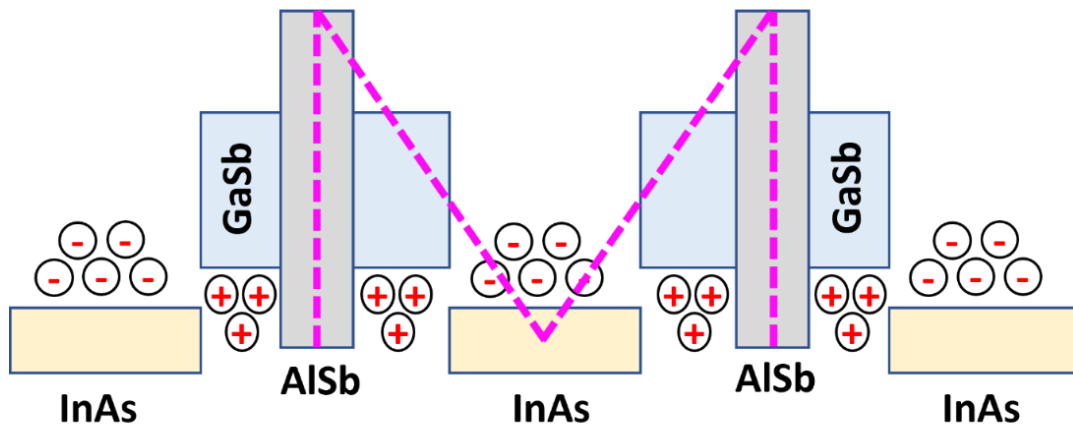
Figure 3.11: Schematic diagram of the InAs/AlSb/GaSb T2SL (M-structure) proposed by Razeghi's group at the CQDs.

### 3.5.2 Quantum cascade infrared photodetectors

QCIRPDs are multistage IR detectors proposed to enhance the QE and attain HOT with a low SNR. As discussed in Section 3.4.1, the detector's QE can be improved by increasing the absorber layer's thickness. However, the carrier diffusion length limits the QE of a conventional photodiode. Consequently, the diffusion length factor must be taken into account when increasing the absorber thickness since increasing the thickness of the absorber layer beyond the carrier diffusion length may not result in the desired parameters improvement. To overcome this issue, each absorber layer in the QCIPDs is engineered to be ultimately shorter than the diffusion length to allow the collection of photogenerated carriers.

The QCIPDs are classified into two groups (i) inter-band quantum cascade infrared photodetectors (IB-QCIRPDs) and (ii) inter-subband quantum cascade infrared photodetectors (IS-QCIRPDs). The IB-QCIPD with multi-absorber layers based on Ga-containing InAs/Ga(In)Sb is schematically shown in Figure 3.12. As can be seen, there are various regions, and each region has its mechanism. Zone (1) is the excitation zone (absorbing layer), where electrons are excited from the valence band to the conduction band through the absorption of photons. Zone (2), the intraband relaxation zone, has electron and hole barriers consisting of digitally graded AlSb/GaSb MQW barriers for electrons and InAs/AlSb MQW barriers for holes. In this region, electrons are transported, and holes are confined to zones (1) and (3). In zone (3), the inter-band tunnelling region, electrons return to the valence band of the absorbing layer through the tunnelling effect.
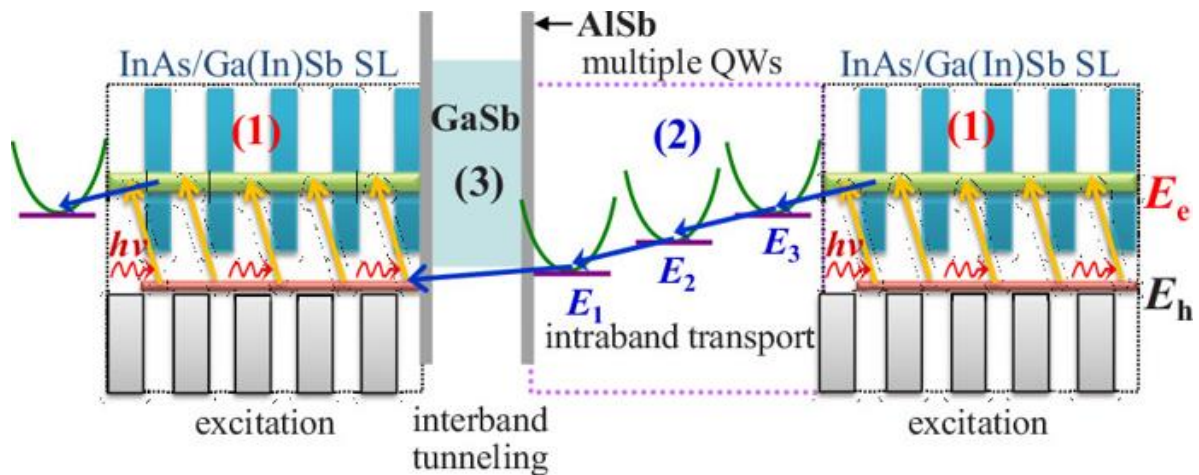
Figure 3.12: Schematic diagram of an InAs/AlSb/GaInSb T2SL IB-QCIPD. The figure is adapted from reference [218].

## 3.6 Challenges addressed in this research work

Given the existing difference between the presently possible performance levels of MWIR T2SLs and those of MCT, this research aims to develop approaches for bringing MWIR T2SLs' performance closer to their theoretically attainable levels. To enhance the material quality and device performance, the growth and fabrication of T2SLs are the main research areas. Sections 3.6.1 and 3.6.2 discuss the growth and fabrication aspects of T2SLs, which open a research path for the current work.

### 3.6.1 Epitaxial growth

The -0.6% lattice mismatch between InAs and GaSb, leading to an internal interfacial strain that restricts material quality and device thickness, is one of the most significant challenges to enhancing the performance of InAs/GaSb T2SLs. Consequently, the nature and sharpness of the interfacial elements have become a subject of extensive research. There are no common cations or anions in the InAs/GaSb heterostructure, which may lead to the formation of numerous interfacial components, including InSb-like, GaAs-like, or a combination of InAs and GaAs, resulting in ternary or quaternary interfacial intermixing [78], [219], issues like In and Sb segregation [79], [220], or IF-diffusion of atoms [221]. As group-V and group-III change at the IF due to atomic kinetic energy and the effect of growth temperature, both GaAs-like and InSb-like IFs can form, as depicted schematically in Figure 3.13. When GaAs-like IFs are

formed, the average lattice constant of the SL reduces even further, resulting in an increase in the tensile strain in the SL. In contrast to the formation of the InSb-like IFs, the average lattice constant of the SL would increase slightly, partially compensating for the strain in the SL. Thus, there are many reports on GaAs-like [222], [223], [224], [225], InSb-like [195], [226], [227], [228], [229], [230], [231], and ternary/quaternary [231], [232] IFs, which have demonstrated promising results for enhanced device performance.
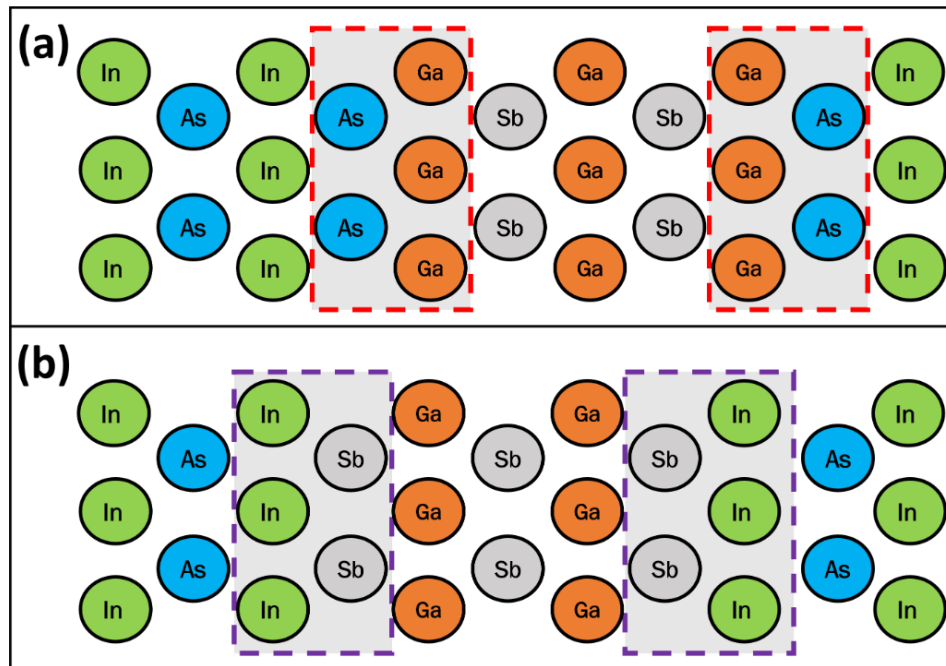


Figure 3.13: Schematic of possible formation of (a) GaAs-like or (b) InSb-like IFs in InAs/GaSb T2SL heterostructure.

The InSb IF is the most popular scheme because it provides strain compensation, enhancing the device's efficacy [233]. This is due to the +6.3% lattice mismatch between InSb and GaSb, which acts in opposition to the -0.6% lattice mismatch between InAs and GaSb, as depicted schematically in Figure 3.14. Theoretically, strain compensation can be accomplished by selecting an InSb IF thickness that is approximately 10% of the total InAs thickness. In addition, the InSb IF maintains the type-II band alignment of the T2SL, which is advantageous in terms of both structural and optical quality. It is also comparatively straightforward to realise by means of migration-enhanced epitaxy (MEE) or conventional MBE growth techniques. However, multiple studies on T2SLs with InSb IFs have shown superior optical quality despite the overall inferior structural quality in comparison with T2SLs with other IF schemes [234], [235]. To comprehend why this is the case, it is necessary to compare the optical and structural

properties of InAs/GaSb T2SLs with and without InSb IFs. Therefore, this is the first objective of the current research, which is presented in Section 3.7.1.
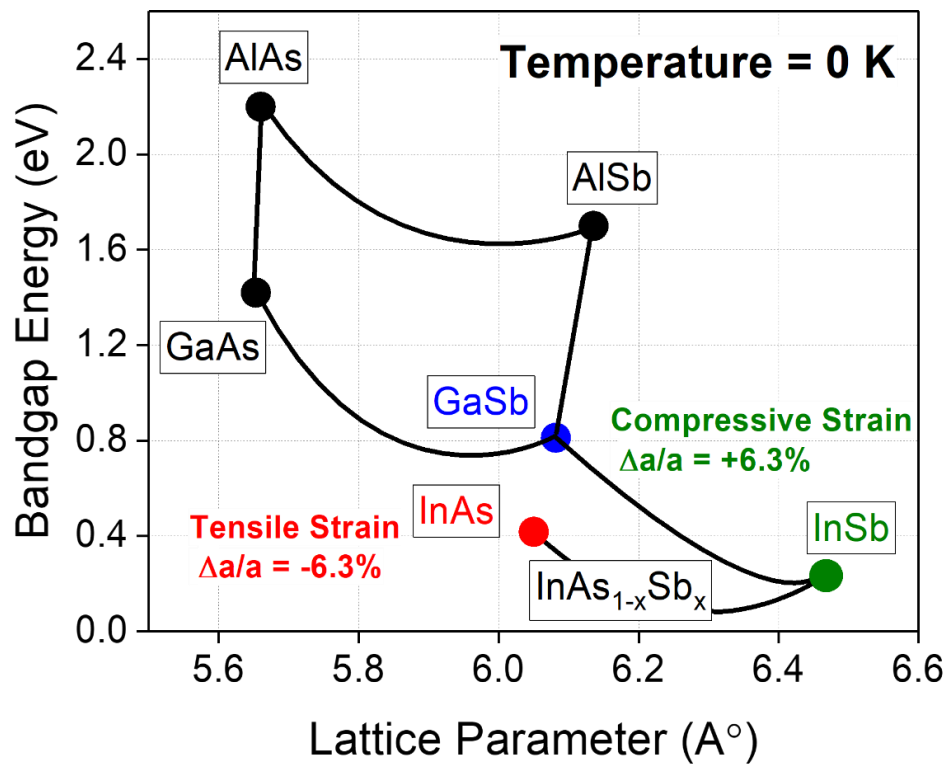


Figure 3.14: The bandgap energy and lattice parameters for selected III-V semiconductors. The lattice mismatch of InAs and GaSb is highlighted in green and red, depending on the strain.

### 3.6.2 Device fabrication

The fabrication of T2SL-based devices has been an active area of study, but no widely adopted standard processes exist. As discussed below, mesa etching and passivation are critical areas of development required for the fabrication of T2SLs. For a detector component to be effective, the signals from distinct pixels must be distinguishable. Even though some research has been recently carried out to accomplish this via diffusion doping [132], [135], [136], [172], [236], [237], [238], [239], most processes use some type of etching to create mesas. It is understood that the etching process is the final step to isolating pixels after the photolithography and metallisation steps. Etching can be commonly realised using two main approaches: wet etch and dry etch processes. Wet etching employs chemical solutions, whereas dry etching uses plasmas. Therefore, selecting the most desirable etching method, depending on the designs and features of the devices, is critical. It is also essential to choose

the most suitable method that is desirable to control the etching depth. Both wet and dry etching methods are viable options for forming mesa of InAs/GaSb T2SL single pixels and FPAs. Chemical wet etching procedures are straightforward, cost-effective, and induce negligible surface degradation [240]. However, they can generate contamination or residues and form concave sidewalls. Free Sb is hypothesised to form on surfaces during wet etching, thereby facilitating the formation of current paths on those surfaces. Due to its anisotropic characteristics, inductively coupled plasma (ICP) dry etching, which utilises a high density of active discharges, is an appealing technique for fabricating semiconductors. Table 3.3 summarises the advantages and disadvantages of the wet and dry etching approach.

This thesis utilised the dry etching approach to enhance the dark current compared to the outcomes obtained from the wet etching method. In order to create an array, it is necessary to use pixels that are small in size and have a small space between them. Dry etching is used to precisely control the verticality of the mesa sides. But in this thesis, initial results on the dry etching were inferior to the wet etching results. The dark current can experience significant deterioration as a result of the ion bombardments that occur during dry etching. In order to enhance it further, a hybrid approach involving both wet and dry etching is employed to refine the sidewalls, and an optimum recipe should enhance the dark current. Hence, further optimisation of the process will be required, which can be the future work.

Table 3.3: A summary of the wet and dry etching approach [30], [31], [55], [241], [242], [243].

| Etching Approach | Advantages | Disadvantages |
|---|---|---|
| Wet etch | Lower cost | Uncontrollable |
| | Easier to implement | Lower fill factor |
| | Higher etching rate | Unavoidable tendency to undercut |
| | Higher throughput | |
| | Better selectivity for most materials | Isotropic profile |
| | | Damage to the substrate |
| | Smaller number of broken chemical bonds | Inadequate for the definition of a small feature size < 1 μm |
| | Reduction of free carriers | Wafer/sample contamination |

| Dry etch | Vertical (anisotropic) profile | Higher cost |
|---|---|---|
| | Increased etch uniformity | Harder to implement (to control gas mixtures) |
| | Much smoother sidewalls | Lower throughput |
| | Higher fill factor | Poorer selectivity |
| | Controllable | Potential damage to the wafer/sample surface caused by ICP ion bombardment |
| | Reproducible | |
| | Suitable for the definition of a small feature size < 100 nm | |

Wet etching process typically requires immersing the sample in a solution including an acidic etchant, such as citric ($C_6H_8O_7$) or phosphoric acid ($H_3PO_4$) for T2SLs, and an oxidising agent, such as hydrogen peroxide ($H_2O_2$). The chemical solution is therefore customed for each material. For example, etchants based on "inorganic" hydrochloric acid (HCl) and $H_3PO_4$ and "organic" $C_6H_8O_7$ are commonly used to etch InAs/GaSb T2SLs [194], [216], [244], [245], [246], [247]. Various acidic etchants have been investigated in literature and used to etch InAs-based materials. As an illustration, it is found that the $C_6H_8O_7$-based solution can selectively etch the InAs against GaSb materials [248]. In contrast, an HCl-based solution is found to be very selective and cannot etch InAs materials [249]. Therefore, correctly selecting the wet chemical etchants is critical to etching the InAs/GaSb T2SLs since the two binary compound semiconductors have different physical and chemical properties. It is also vital to note that surface leakage currents are typically caused by surface inhomogeneity, which is attributed to the selective properties of these chemical solutions. In addition, T2SL devices exhibit a significant surface leakage current on the mesa surfaces, which can be attributed to the presence of dangling bonds and impurities. Therefore, in order to mitigate the surface leakage current, various research groups have developed different passivation techniques. These methods include the use of ammonium sulphide [169] to passivate the surface, the deposition of a polyimide layer [250] on etched sidewalls, the overgrowth of a wide bandgap material [251] across the surface, and electrochemical sulphur passivation [252]. The experimental environment, such as temperature, pressure, humidity, and the kinetic etch of each chemical etchant, which is extremely sensitive to the amount of each component present in the solution, are also essential factors that can influence the wet etching process.

The main advantage of the wet etching scheme is the accessibility and low cost of the required tools and materials. Nevertheless, the resulting etch profile will be either isotropic or crystallographic, as shown in Figure 3.15(a-b). This indicates that the etching follows the crystal planes of the semiconductor or a combination of both. This firstly implies that the fill factor of the pixels will be extremely low and, hence, incompatible with the closely manufactured pixels of FPAs. Secondly, due to the isotropic or crystallographic nature of this etching procedure, the homogeneity of the resulting etch profiles is likely to be low, with various pixels or planes etching at varying rates. Consequently, the primary difficulty of this method is the high degree of undercut induced by etchant chemical reactions.

Due to the challenges associated with the wet etching approach, this has led researchers to implement dry etching to realise high-performance detectors. Plasmas with high energies are typically accelerated towards the sample's surface during the dry etching. Chemical etchant gases (such as $BCl_3$) evaporate the semiconductor material using a chemical process, and physical etchant gases (such as Ar) literally remove the desired material. In this case, a plasma source is usually utilised where the ICP reactive ion etching (RIE) process is performed inside a high vacuum chamber with the introduction of gases, including chlorine-based gases ($Cl_2$, $SiCl_4$, $BCl_3$) or methane-based gas ($CH_4$) combined with an inert gas such as Argon (Ar) [241], [242], [253], [254]. Chlorine-based gases are usually preferable compared to the methine-based gas due to the higher volatility of the reactive products (Ga and Sb chlorides), faster etching rates (based on the use of the chlorine gas), and smoother surface morphologies [31], [241], [242]. Ar gas (ions) is used to aid in the desorption of reactive products produced by ion bombardment during dry etching. However, the primary obstacle with the chlorine-based plasma etching is the formation of indium chlorides ($InCl_x$) on the etched surface of the mesa sidewalls. Moreover, the difference in InAs and GaSb etching rates, specifically with an asymmetrical layer thickness of superlattice, is also problematic. Hence, to overcome those issues, the temperature of the dry-etched surface and the power of ion bombardment needs to be elevated [242]. The resulting dry etch profile will be anisotropic, as depicted in Figure 3.15(c). It is favourable for most high-performance applications and is required for FPA fabrication because of its fill factor. Likewise, the dry etching approach is controllable and homogeneous across the wafer when adequately optimised.

A combination of the two approaches is also common in T2SLs, in which the mesas are created using a dry etch, and the surface damage is cleaned using a wet etch approach. Recently, Zhou et al. [255] used a combination of dry and wet etching processes. Chlorine-based plasma etching chemistry was combined with citric acid-based solutions. The advantage of using the wet etch process followed by the dry etch is to eliminate the damage caused by the ICP and ion bombardment during the dry etch process.
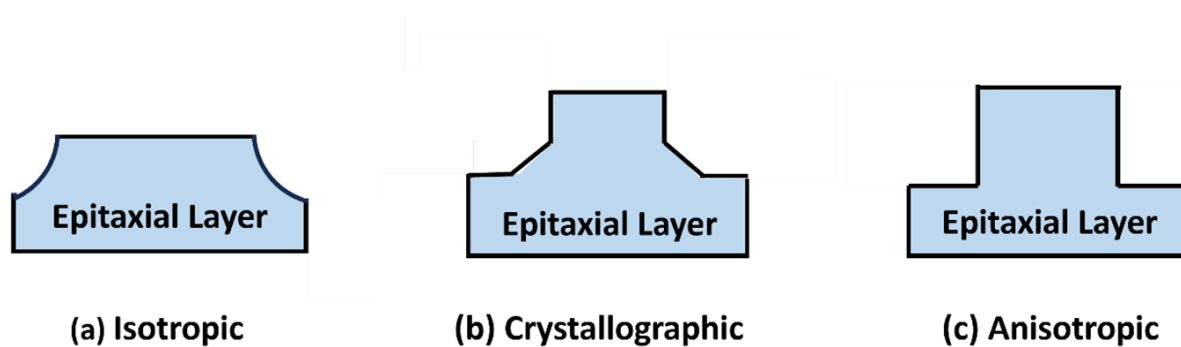


Figure 3.15: Schematic of possible mesa etching profile (a) isotropic, (b) crystallographic, and (c) anisotropic.

The fabrication process of T2SL is challenging because of the complexity of the structure, which consists of a few microns thick SL region composed of InAs and GaSb layers and additional InSb or GaAs as an interfacial layer. The primary issue with the fabrication of T2SL material becomes crucial during the pixel isolation process (etching process). Dangling bonds usually originate at exposed device sidewalls after the mesa isolation process, forming IF states in the T2SL bandgap and contributing to increased surface leakage current. In addition, undesirable native oxides typically form during the etching process, influencing the device's performance. Following the etching process, diffusion of oxygen to the surface of the exposed sidewalls and formation of native oxides may occur through the following processes:

$$2InAs + 3O_2 \rightarrow In_2O_3 + As_2O_3 \qquad \text{(3.10)}$$

$$2GaSb + 3O_2 \rightarrow Ga_2O_3 + Sb_2O_3 \qquad \text{(3.11)}$$

$$In_2O_3 + As_2O_3 \rightarrow 2InAsO_3 \qquad \text{(3.12)}$$
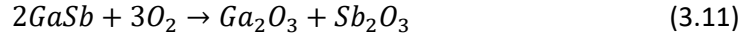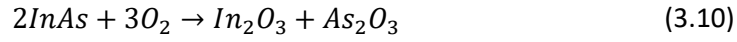
These oxidation processes are common, and the resulting native oxides are excellent electrical conductors, resulting in a high surface dark current. Because of their narrow bandgap, (V)LWIR detectors face an extra challenge. As a result, several conventional passivation approaches were used on the semiconductor surface to reduce surface current by encapsulating the T2SL device sidewalls in a relatively thick layer. Depending on the material, passivation can be divided into several categories: dielectric passivation, organic deposition, chalcogenide passivation, and electrochemical passivation.

The dielectric passivation is the most implemented scheme, which typically uses plasma-enhanced chemical vapour deposition (PECVD) to deposit materials, such as silicon oxide ($SiO_2$) [256], [257], [258], [259], silicon nitride ($Si_3N_4$) [205], [260], or aluminium oxide ($Al_2O_3$) [206, p. 3], [261]. Recently, the deposition of $Al_2O_3$ by atomic layer deposition (ALD) has been proposed as an efficient method of passivation due to its favourable Gibbs free energy resulting in the preferred formation of $Al_2O_3$ over In, Ga, As and Sb oxides. Specht et al. [262] have shown that $Al_2O_3$ passivation decreases the dark current in InAs/GaSb LWIR T2SLs by an order of magnitude. Perimeter-to-area (P/A) analysis is indicative of the reduction in the surface-related component of the dark current. Moreover, Salihoglu et al. [263], [207] have shown that $Al_2O_3$ passivation is more efficient for MWIR InAs/GaSb T2SLs compared to typical methods, such as $SiO_2$, $TiO_2$, $HfO_2$, ZnO, and $Si_3N_4$, by few orders of magnitude in some cases. Although this type of passivation is effective, it has several drawbacks in producing high-quality, low-fixed, and interfacial charges density dielectrics at process temperatures considerably lower compared to the growth temperature of InAs/GaSb T2SL [55]. In addition, the existence of native fixed charges in the dielectric passivation layer may enhance or worsen the device's performance [264].

T2SL passivation with organic elements, polyimides or photoresists is also an alternative approach to dielectric passivation [265], [266], [267]. SU-8 is commonly the most applied polyimide negative photoresist to a T2SL mesa sidewall which can be physically applied using the same steps of applying any photoresist (spin-coating, soft baking, exposure, and developing) to shield the mesa sidewalls from ambient air. This method is advantageous as it is fast and does not require costly equipment for implementation. Photoresists are typically deposited at room temperature and can be used as a protection layer for T2SL devices with various operating wavelengths. The significant benefit of this method is its ease of use rather than its quality since it is universally accepted that chemical passivation is a more efficient option than physical protection from ambient air.

Chalcogenide passivation or sulphurisation is another passivation method in which Sulphur (S) atoms are used to satisfy dangling bonds on the surface of semiconductors. Sulphur-based passivation, in which a covalently bonded sulphur layer protects the outer group-III and group-V atoms, has been demonstrated to be successful and is frequently employed in conjunction with a dielectric layer [268], [269]. The easiest sulphurisation method is to immerse the sample in aqueous solution of ammonium sulphide [169], [270]. The advantage of using this passivation method is that it does not require any additional step of oxide removal since the native oxides are etched by $(NH_4)OH$ formed in water solution of ammonium sulphide. Thioacetamide (TAM, $C_2H_5NS$) [271] and octadecanethiol (ODT, $CH_3[CH_2]_{17}SH$) [272] treatments have also been used to provide more stable bonds between Sulphur and T2SL constituent elements (In, Ga, As, and Sb).

The electrochemical passivation (ECP) process is a new sulphurisation method used to saturate the dangling bonds with Sulphur through electrolysis in S-containing solution. Herein, chemical decomposition is produced by passing an electric current through a solution containing ions. Although this method is sufficient, deposition of the Sulphur layer through ECP might oxidise quickly, and hence additional encapsulation layer is needed. Several research groups have tried a combined approach for the T2SL detectors' passivation in recent years. For example, chemical and physical passivation layers have been shown to be more effective in reducing leakage current. Hao et al. [268] have reported that the anodic sulphide passivation followed by PECVD of the $SiO_2$ layer has reduced the dark current density and improved the detector performance. Zhang et al. [40] have also noticed that the anodic oxide

or anodic fluoride passivation in combination with zinc sulphide has enhanced the detector performance. DeCuir Jr. et al. [273] discovered that the sulphide chemical passivation coated by the SU-8 photoresist impedes the formation of native surface oxides, fulfils dangling bonds, and offers the stability of passivation over a long time.

Epitaxial overgrowth of a wide-bandgap material has been shown to help reduce or suppress surface leakage current [251], [274]. This procedure is effective for T2SLs owing to the large band offset between the active region and the wide bandgap semiconductor, which brings about carrier depletion near the IF. The benefit of this approach over dielectric deposition is that the common Fermi level between the two materials may be adjusted by doping the region of the wide-bandgap material. To minimise the surface leakage current, reticulated shallow etch mesa isolation (RSEMI) and heterostructure designs are employed instead of chemical passivation [275], [276]. This method makes use of barrier designs such as the *nBn*, which only etch the n-top contact. Etching via the barrier layer of such a device would be adequate for pixel isolation. In this manner, the unetched absorber region does not affect the surface current. Considering the above discussion of T2SLs fabrication, this has also opened a research route for the present work. Sections 3.7.2 and 3.7.3 discuss the second and third objectives of this thesis.

## 3.7    Aim and objectives of the current research

The development and optimisation of growth schemes, fabrication, and characterisation capabilities for T2SL detectors are critical objectives in the pursuit of the primary goal. As discussed, one of the most promising strategies for improving the crystalline quality and detector performance of MWIR T2SLs is to grow InAs/GaSb T2SLs with an interfacial layer that can compensate for the internal strain during growth. In this way, developing T2SLs with superior crystalline quality enables the fabrication of single-pixel detectors with high-performance levels. The objectives, methods, and thesis chapters which discuss the current study are summarised in Table 3.4. As per the table, three objectives have been established to satisfy the main aim of this research, as stated previously in Section 3.6, which are discussed in the following sections.

### 3.7.1 Growth and characterisation of InAs/GaSb T2SLs using different interfacial schemes

It is believed that one of the most promising ways for T2SLs to outperform the MCT is via overcoming the growth difficulties of utilising the InSb IF scheme. The incorporation of an intentional strain compensating InSb IF layer is found to enhance the performance of T2SL detectors [233]. Unfortunately, there is a paucity of detailed characterisation studies that correlate the quality of this approach, so the mechanisms by which this enhancement is accomplished remain obscure. In order to achieve the first objective of this research, the purpose is to conduct a comprehensive characterisation study to ascertain the effect of interfacial schemes on the structural and optical properties of MWIR InAs/GaSb T2SLs. It is hoped that this study can be then utilised to optimise future device designs and enhance the detector's performance.

### 3.7.2 Fabrication of InAs/GaSb T2SLs using different etching methods

Another critical aspect that requires investigation is the fabrication of T2SLs with ultimately high-performance devices. Consequently, the second objective of this research project is to fabricate MWIR InAs/GaSb T2SLs using various etching techniques (including wet and dry etching methods, a combination of both, and surface protection). The efficacy of the etching approach on device performance is also studied using I-V characterisation measurements.

### 3.7.3 Fabrication process developments of Sb-based using alternative wet etching recipes

The third objective of the current research is the optimisation process developments of wet etching using alternative recipes. It involves studies of other recipes alternative to HF-based solutions. Recipes including phosphoric, sulphuric, hydrochloric, and citric acid solutions are explored. The electrical performance of the devices is also examined by I-V characterisation.

Table 3.4: A summary of the main objectives and approaches used for the current research project.

| Section | Objective | Approach | Thesis Chapter |
|---|---|---|---|
| 3.7.1 | Determining the effect of InAs/GaSb T2SL IF growth schemes on the structural and optical properties of the samples | Growth and characterisation of InAs/GaSb T2SL samples using different IF schemes | Chapter 5 |
| 3.7.2 | Optimising the InAs/GaSb T2SL fabrication process via wet etching, dry etching, and surface protection techniques and studying their efficacy on the device's performance | Fabrication of InAs/GaSb T2SL using wet etch approach, namely HF acid, and investigating alternative dry etch and wet etch methods and surface passivation | Chapter 6 |
| 3.7.3 | Optimising the wet etching process of Sb-based materials towards fabricating high-performance T2SLs | Investigation of alternative wet etching recipes/processes, including phosphoric, sulphuric, citric, and hydrochloric (HCl) acids | Chapter 7 |

# Chapter 4: Experimental and Theoretical Methods

## 4.1    Introduction

This chapter provides a detailed description of the experimental and theoretical work and the tools used in this research project. Experimentally, after the growth of materials by an MBE reactor, various characterisation techniques were used to characterise them. The structural properties of as-grown materials were studied by X-ray diffraction (XRD), scanning electron microscopy (SEM), and transmission electron microscopy (TEM) measurements. To evaluate the surface morphology of the grown samples, they were imaged and characterised by atomic force microscopy (AFM). Photoluminescence (PL) measurements were also utilised to determine the bandgap energy of the as-grown materials and to evaluate the optical properties of the materials that are essentially associated with the electronic properties of the processed devices.

After materials characterisation, single-pixel devices were fabricated inside the clean room (CR), and the electrical performance of the fabricated devices was studied by current-voltage (I-V) and capacitance-voltage (C-V) measurements. Theoretically, Nextnano software was then employed to simulate the band structure of the grown samples and other T2SLs to extract the bandgap energy. Lastly, Mathematica and Silvaco ATLAS software were utilised to simulate the I-V characteristics of the fabricated devices and compare them with the experimental results.

Figure 4.1 is a schematic of the experimental and theoretical methods used in this research project and their applications. Figure 4.2 represents the entire T2SL process layout from growth to device fabrication and characterisations.
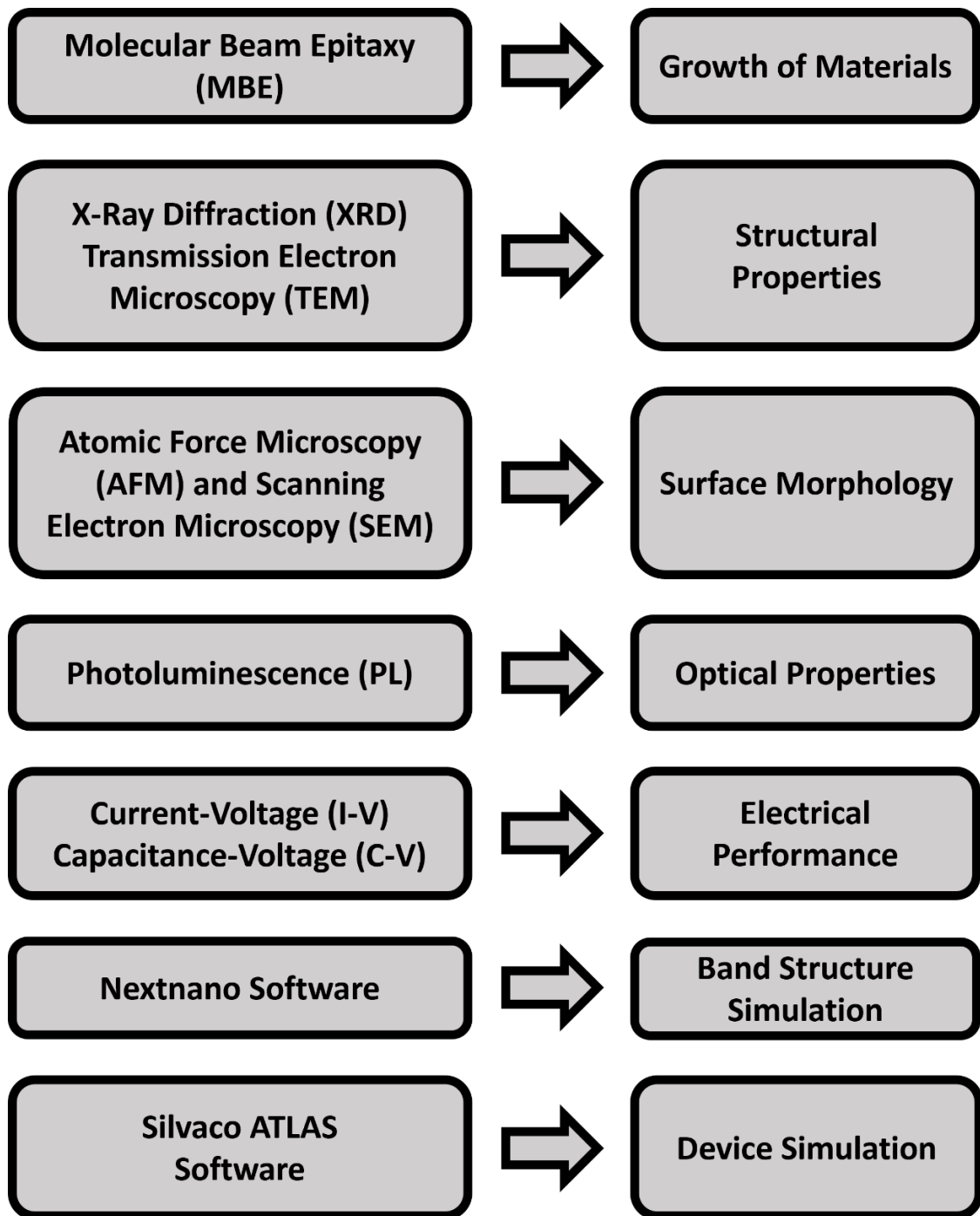
Figure 4.1: Experimental and theoretical methods and the information attained from each technique.

```
┌─────────────────────────┐
│   Materials growth by   │
│    Molecular Beam       │
│     Epitaxy (MBE)       │
└─────────────────────────┘
             │
             ▼
┌─────────────────────────┐
│       Materials         │
│    characterisation     │
└─────────────────────────┘
             │
             ▼
┌─────────────────────────┐
│    Device fabrication   │
└─────────────────────────┘
             │
             ▼
┌─────────────────────────┐
│    Device electrical    │
│    characterisation     │
└─────────────────────────┘
```
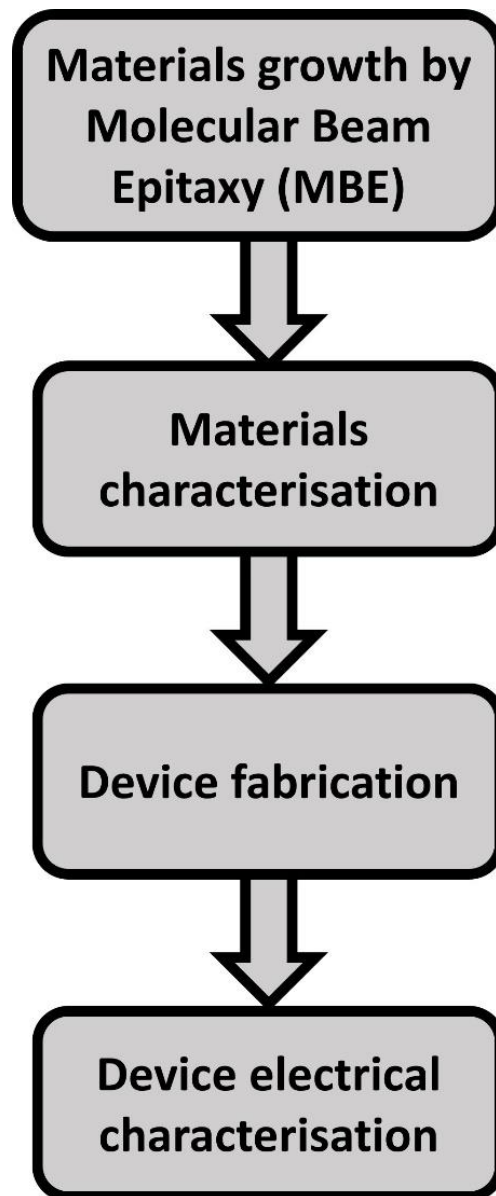
Figure 4.2: Schematic representation of the whole T2SL process layout.

## 4.2   Material growth

InAs/GaSb T2SL, material and device structures were grown utilising a combination of group III-V components. The growth of T2SL materials was performed using a modern growth technology called MBE, as it helps to grow very thin films with the advantage of controlled layer thickness and composition with great uniformity. Figure 4.3 depicts an InAs/GaSb T2SL reference sample grown by the MBE reactor.
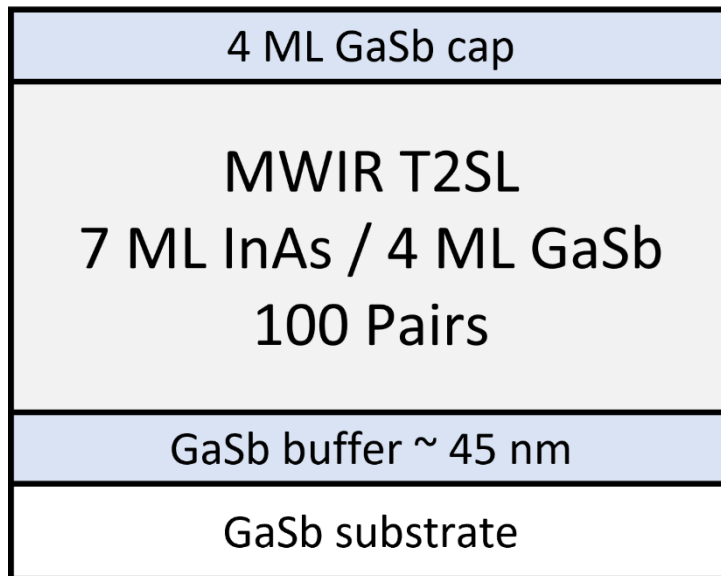
Figure 4.3: Schematic of an InAs/GaSb T2SL reference sample grown by the MBE reactor.

MBE is an epitaxial procedure used for the deposition of thin films of single crystals, which utilises an ultra-high vacuum (UHV) environment to generate high-purity epitaxial structures. The MBE takes advantage of a low growth rate (1 ML per second), enabling the growth of very defined and well-controlled layer thickness and composition. Figure 4.4 depicts a basic schematic of an MBE reactor with the critical elements identified.

In a UHV chamber, thin epitaxial films were crystallised through the interactions of thermal-energy molecular or atomic beams of the components and a substrate preserved at a HOT, typically at a temperature of a few hundred Kelvin. By choosing the evaporation rates of the proper sources, which determine the relative arrival rates of the components, it is possible to control the composition of the epitaxial layer. If the growth rate is slow enough, the impinging species will travel over the surface of the semiconductor to guarantee homogeneous epitaxial layer deposition. Complex structures, such as T2SLs, are grown by periodically pausing and resuming deposition by opening and closing mechanical shutters. In order to attain the ML accuracy required to precisely and consistently form the QWs of the T2SL, in situ monitoring and exact control of the MBE growth procedure are necessary. Over the past decade, several research activities have been conducted to demonstrate the growth of T2SLs employing MOCVD technology, which has the benefit of higher throughput and lower costs [175], [277]. Nevertheless, because the melting point and equilibrium vapour pressure of InSb are low,

which are needed for the InSb IFs frequently used in Ga-containing T2SLs, the majority of these reports pertain to the Ga-free T2SL counterpart.
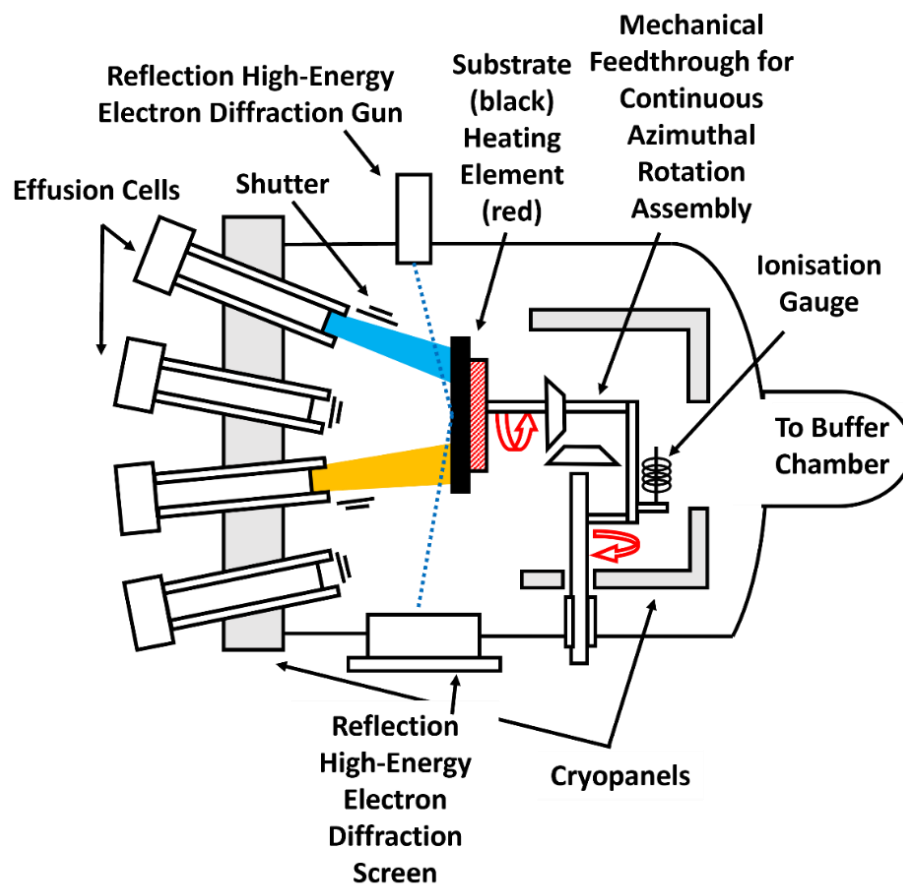


Figure 4.4: Basic schematic of an MBE reactor with the essential parts labelling the growth chamber surrounded by material effusion cells and shutters, substrate and heating source, feedthrough for CAR assembly, ionisation gauge, RHEED gun and screen for growth process monitoring.

Huang et al. [278] have recently demonstrated the growth of InAs/GaSb T2SLs by MOCVD employing GaAs-like interfacial layers, but this method has not been commonly investigated or reproduced. Thus, MBE is currently the only method appropriate for developing high-performance T2SL structures. As depicted in Figure 4.4, the MBE machine typically comprises important elements discussed underneath.

- Load lock

The load lock is utilised to transport materials into and out of the key chambers without compromising their vacuum. The chamber includes a compact volume so that the backing pump can rapidly attain the required pressure ($10^{-8}$ Torr).

- Preparation chamber

The preparation chamber is where the first outgassing occurs. The materials are then moved from the preparation chamber to the growth chamber. The chamber is outfitted with an ion pump, enabling it to obtain pressures comparable to the growth chamber ($10^{-10}$ Torr).

- Growth chamber

The growth chamber is the primary compartment of the MBE reactor where epitaxial growth occurs. Due to the chamber's size, a vacuum operation of $10^{-11}$ Torr is required, which necessitates the operation of a turbopump, ion pump, and cryopump.

- Feedthrough for continuous azimuthal rotation assembly

The substrate and heating element are outfitted with a continuous azimuthal rotation (CAR) assembly that is capable of approximately 150 rotations per minute. Thus, the surface homogeneity of the epitaxial layer is increased.

- Effusion cells

In an inert crucible, the Knudsen-effusion cells contain the source materials in a condensed state. A resistance-heated source is utilised to heat the crucible to the required temperature for evaporation so as to produce molecular beams. The temperature is regulated by means of a thermocouple. Numerous contemporary designs employ a ''dual filament'' setup in which distinct thermocouples heat the cell's base and tip, thereby enhancing the uniformity of the grown films. The shutters are accompanied by these cells to be turned on and off during growth.

- Reflection high-energy electron diffraction

The MBE reactor has a considerable advantage over other epitaxial growth techniques because it is conducted in a high vacuum environment. This enables surface-sensitive in-situ characterisation techniques such as reflection high-energy electron diffraction (RHEED). This technique enables a great degree of control over the epitaxial deposition. As stated previously, this benefit allows the development of complicated designs such as T2SLs. RHEED is the most

significant of the in-situ investigation methods because it enables the observation of the MBE growth process's dynamic nature. An electron beam with a high energy of 3 to 10 keV is typically directed towards the sample surface at a particular angle. This assures that the beam's penetration is restricted to the atomic layers closest to the surface. These electrons are then scattered by the crystal structure of the sample's surface and strike a phosphor screen positioned on the opposite side of the chamber. The roughness and atomic configuration of the sample surface determine the RHEED signal intensity. If the surface is rough, many electrons will scatter and not be detected by the phosphor screen. In contrast, the RHEED signal will be very strong if the sample surface is atomically flat. Consequently, it is possible to determine the layer-by-layer deposition of the epitaxial film using the RHEED signal oscillations.

## 4.3    Material characterisation

After the growth of the materials, the following step is the materials characterisation. A variety of material characterisation measurements were undertaken to examine the quality of the grown structures. A set of measurements, including XRD, AFM, TEM, SEM, and PL, are described in detail in the following sections.

### 4.3.1  X-ray diffraction

XRD is a non-destructive method used for the determination of the structural properties of the as-grown thin crystalline films. High-resolution X-ray diffraction (HR-XRD) is technical instrumentation that can characterise the materials and analyse the epitaxially grown layers. It is utilised to obtain more information about the lattice mismatch, strain effect, composition, and layer thickness. Semiconductor materials are periodic structures with a lattice spacing in the order of angstroms (Å). The main principle of XRD is that X-ray beams interact with electrons in matter and get scattered in different directions by the atomic electrons. Hence, when the X-ray beam incident is oriented directly to a sample, beam diffraction occurs by the crystal owing to the X-ray wavelength, which is on the same length scale as the inter-atomic spacing and lattice parameter values. A detector then collects the diffracted beams (patterns) to record the angles and intensities. Figure 4.5 shows a typical XRD setup used to characterise the materials.
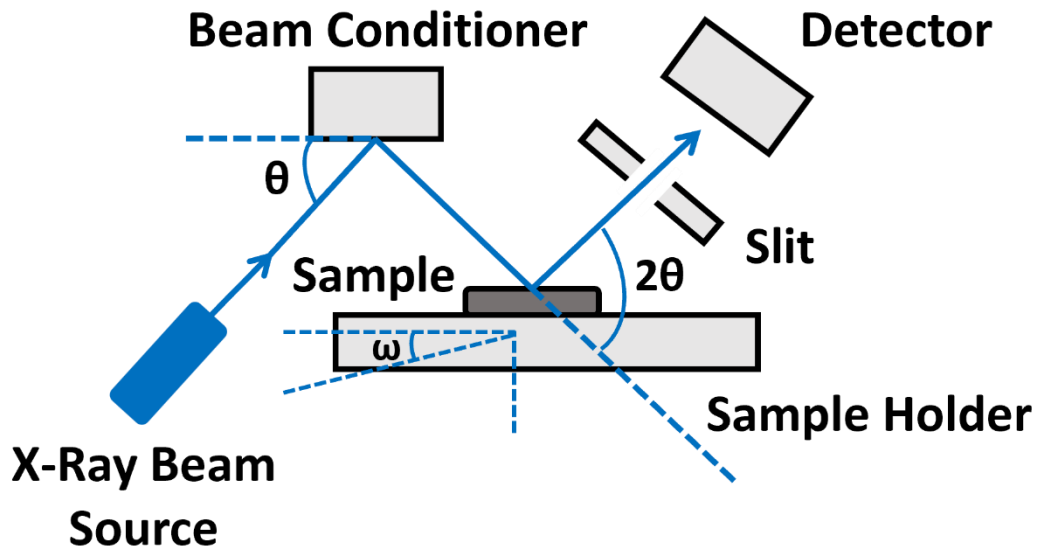
Figure 4.5: Schematic of a typical XRD scanning tool to measure X-ray diffraction from the materials.

To observe X-ray diffraction from a crystalline lattice, the Bragg condition (Derivation of Bragg's law and explanation on how to examine XRD from a SL can be found in Appendix A) must be met based on the following equation:

$$2d_{hkl}\sin(\theta_d) = n\,\lambda \qquad\qquad (4.1)$$

where $d_{hkl}$ denotes the distance between the lattice plane with $h$, $k$, and $l$ being the Miller indices, $n$ is an integer that is related to the order of diffracted beams (satellite peaks), $\theta_d$ is the angle of the diffracted beam, and $\lambda$ is the X-ray wavelength which is equal to around 0.15406 nm. The Bragg condition mainly relies on the angle of the incident X-ray beam as it enters the crystal lattice and the direction in which the diffracted beam exits the lattice, as shown in Figure 4.6.
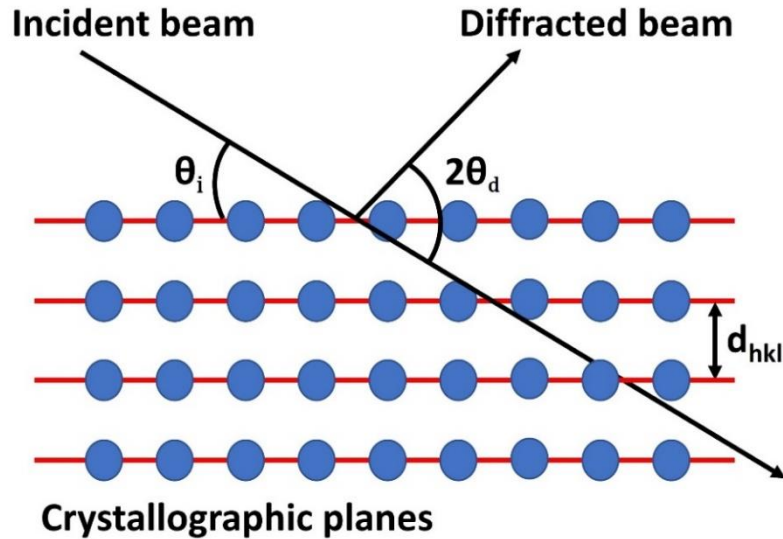
Figure 4.6: Schematic shows the diffraction of the X-ray beam in the crystal lattice. Symbols $\theta_i$ and $\theta_d$ are the angles of incident and diffracted X-ray beams, respectively, and $d$ denotes the distance between the lattice plane.

In cubic structures, the distance of the lattice can be expressed in terms of the lattice constant of the crystal as follows:

$$\frac{1}{d_{hkl}^2} = \frac{h^2 + k^2 + l^2}{a^2} \tag{4.2}$$

The following information can be obtained from the XRD spectrum to determine the lattice mismatch, periodic thickness, and full width at half maximum (FWHM).

- A substrate lattice parameter and the T2SL average lattice parameter

The lattice parameter of the substrate (here it is the GaSb substrate) can be evaluated from the XRD scan using Equations (4.1) and (4.2):

$$a = \frac{2n\lambda}{\sin(\theta)} \tag{4.3}$$

where $n$ is equal to one, $\lambda$ is the X-ray wavelength that is known already, and $\theta$ is the angle that can be directly obtained from the XRD patterns. Similarly, the T2SL average lattice

parameter can be determined utilising Equation (4.3) with the angle now corresponding to the T2SL zeroth-order peak (SL$_0$).

- Determination of strain (lattice mismatch) between the substrate and the T2SL epitaxial layers

To determine the lattice mismatch between the substrate and the T2SL-grown epitaxial layers, the following equation can be used:

$$\frac{\Delta a}{a} = \frac{a_{SL} - a_{substrate}}{a_{substrate}} = \frac{\sin(\theta_{SL_0} - \theta_{GaSb})}{a_{GaSb}}$$ (4.4)

where $a$ is the lattice constants for the superlattice and GaSb substrate, and $\theta$ is the diffraction angles of the GaSb substrate and zeroth-order peak of the superlattice.

- Determination of periodic thickness of the T2SL

The T2SL periodic thickness can be estimated using Bragg's Equation shown in (4.1). From the XRD scan, the periodic thickness of the T2SL sample is calculated from the slope of the linear fitting of the diffracted beam order (satellite peaks order, $n$) as a function of the 2 sin ($\theta_d$).

- Evaluation of full width at half maximum of the T2SL

The FWHM is a qualitative approach to providing information about the crystalline quality of the structure. Narrow and symmetrical SL satellite peaks with FWHM in the order between 18 and 25 arcsecs are indicative of perfectly ordered structures with compositionally abrupt IFs. In contrast, broad and asymmetrical SL satellite peaks with FWHM in the order of 55-65 imply a change of periodic thickness and growth defects formed at the SL IFs. Gaussian or Voigt fitting is typically used to fit the FWHM of the first-order satellite peak of the SL.

### 4.3.2  Atomic force microscopy

AFM is a sufficient tool to prob and investigate ultra-thin tomographic features on the surface of materials utilising a particular tip. AFM is a common surface profile method for micro-and nano-scale topography and can generate very high-resolution images in three dimensions of

the surface of samples and up to atomic resolution. It is also used to provide comprehension of the underlying basis of bonding and interactions in materials in combination with advanced computer-based modelling and simulation techniques, which warrant the expectation of the nature of interlayers [279], [280], [281], [282]. AFM can assess surfaces that might be either electrically conducting or insulating. Small forces can be scanned by a flexible cantilever tip with a minimal mass and a pointed taper. The AFM scan uses a piezoelectric scanner to move the sample on an X, Y, and Z movement stage. The AFM has multiple modes of operation, such as contact, non-contact, and tapping. An AFM digital instrument available at the School of Physics and Engineering was utilised to examine the surface roughness and morphology of the InAs/GaSb T2SL samples. A schematic of a typical AFM setup is represented in Figure 4.7.
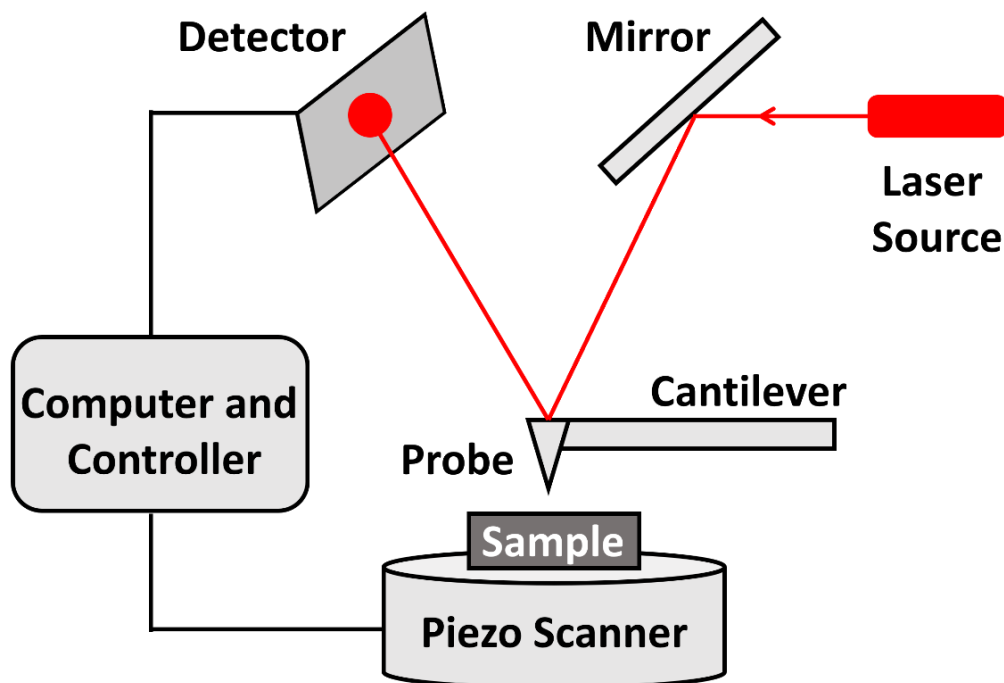


Figure 4.7: Schematic of a typical AFM set-up utilised to characterise the surface morphology of the materials.

### 4.3.3 Optical microscopy

Optical microscopy was used in the research project to determine a high-contrast micrograph of the sample's surface. The fundamental principle of the tool operation is schematically depicted in Figure 4.8. Herein, a source of white light is directed onto a prism by passing it through a polariser. The prism separates the light into two orthogonally polarised beams. An objective directs the two beams onto the surface of the sample, where they are reflected by

92

the prism and recombined. An analyser that is positioned above the prism captures the beams and produces an interference pattern. The resulting image corresponds to the distance between the two separated points on the sample's surface. As a result, changes in colour in the image correlate to changes in slope on the sample's surface. Accessibility and simplicity of use are the main advantages of optical microscopy. In contrast to AFM, large sample areas can be rapidly scanned using this tool, and the setup resolution is appropriate to ascertain the number of surface defects. As with AFM, this method offers information about the substance of the sample but should only be utilised in association with other techniques.
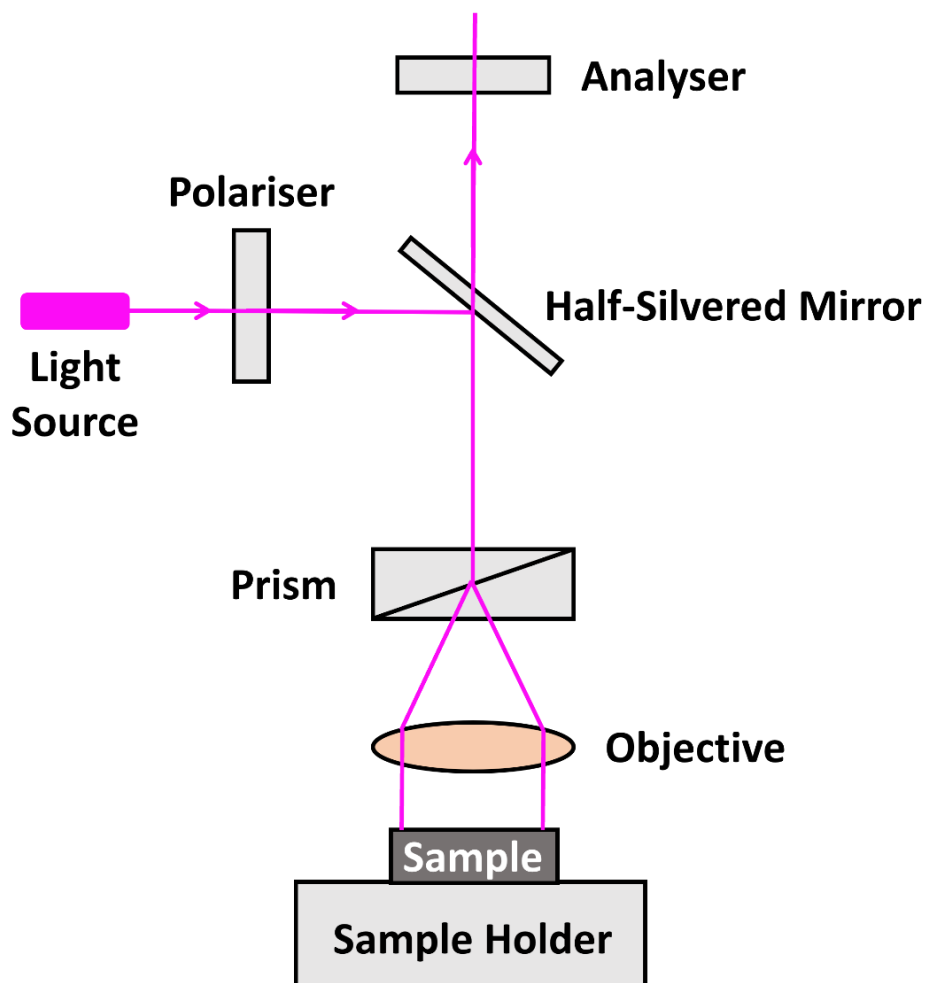
Figure 4.8: Schematic representation of a typical optical microscopy.

### 4.3.4 Scanning electron microscopy

SEM is an important instrument that is employed for the determination of material morphology. Even though optical microscopy is a convenient tool for imaging samples, its

resolution is limited, which is relatively lower when compared to the SEM machine, which provides a high-resolution image. It could sometimes be combined with an energy-dispersive X-ray (EDX) analysis system for determining the elemental composition of the materials. Fundamentally, the SEM consists of a column and specimen chamber operated under a UHV environment. An electron source is located on the top of the column, and its function is to generate electron beams [283]. Electrons as ''particles'' can be accelerated, focussed, and detected. Electrons, as "waves", have shorter wavelengths than visible light and are capable of illuminating a specimen surface to higher resolutions than an optical microscope. The SEM gun can generate electrons that are focused on a small spot and linearly scanned in parallel over the specimen surface. Electrons reflected from the surface can be detected simultaneously by a detector inside the specimen chamber [284].

The SEM typically generates electrons via thermionic, Schottky, or field emission. Acceleration of these electrons can occur due to a high voltage difference between a cathode and an anode, typically around 50 Kev. The SEM system normally operates with a variety of beam cross-sections. These are generated by the electron gun with a diameter of approximately 1 nm to 50 $\mu$m and with current operation in the range of $10^{-6} - 10^{-9}$ mA. The surface of the material can be imaged, and produced images can be analysed using SEM tools and software accompanied with the machine.

Herein, a Phillips model XL-30 SEM tool, available in the clean room at the School of Physics and Astronomy at Cardiff University, is used to examine the structural quality of the materials. Particularly, it was used to determine the mesa sidewalls profile or etching depth during the fabrication process. Also, it helped to evaluate and characterise the surface morphology after mesa etching, photolithography, and metallisation processes. Figure 4.9 shows a typical SEM tool used for the characterisation of the surface morphology of the samples.
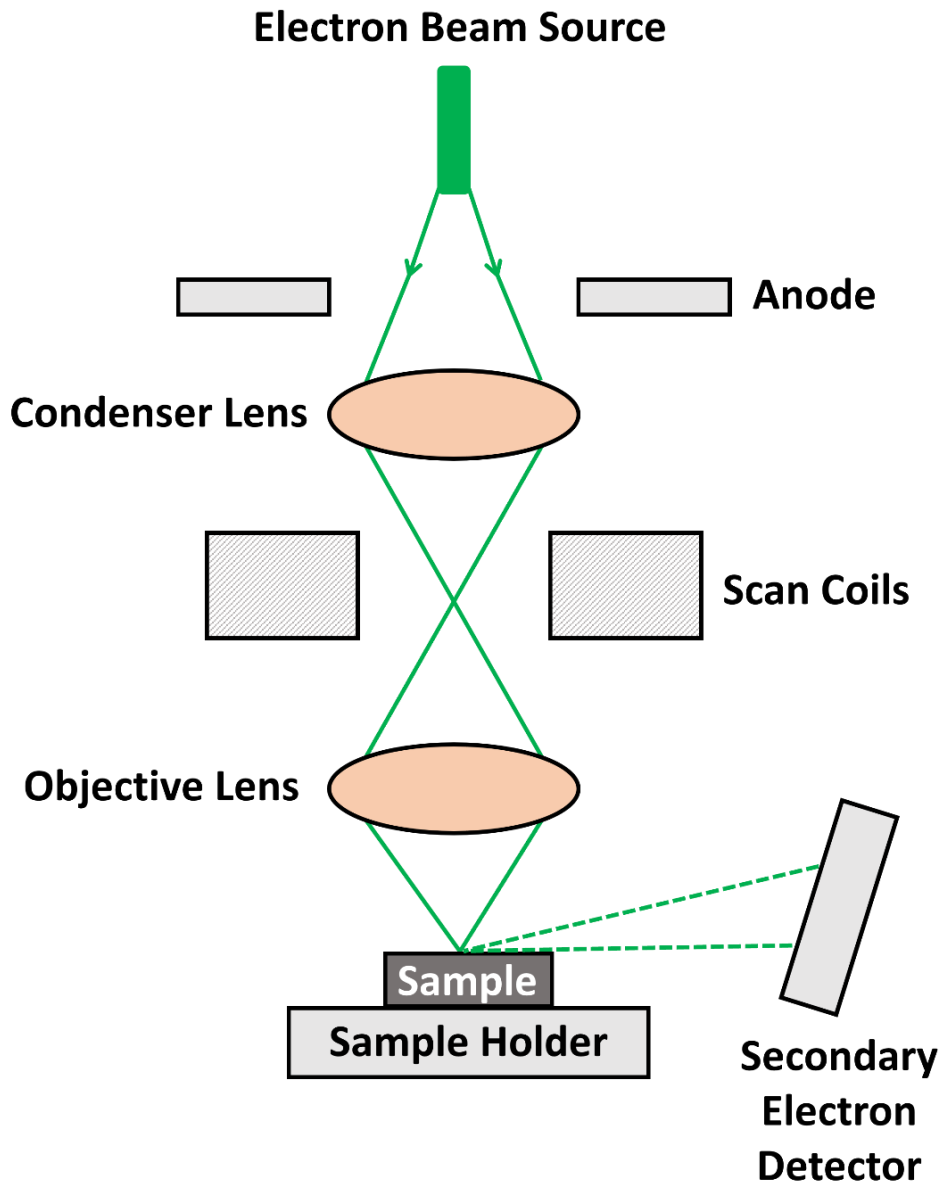
Figure 4.9: Schematic of a typical working principle of a SEM system.

### 4.3.5 Transmission electron microscopy

TEM is an efficient tool that can be utilised to characterise the internal structure of the sample to obtain more details. TEM has the capability to offer much higher-resolution images with even greater magnification compared to optical (light) microscopy. This is due to the lower TEM wavelength, typically around 0.2 nm, compared to a wavelength of around 500 nm used in optical microscopy. Therefore, a lower wavelength of light means more energy in the wave that provides better resolution. There are some differences in terms of the working principles

of electron microscopy with that of light microscopy. In TEM, electron beams are produced upon heating the tungsten filament source in a UHV chamber. Electrons that are generated must be focused through all electromagnetic lenses (when charged with energy turning into a magnetic field which helps to maintain the single electron beam through the vacuum chamber) so that it can reach the sample specimen as a single beam. In this case, high energy, or extra voltage, approximately 20 Kv, is required to help electrons move straight as a single beam to reach the specimen. Another critical parameter is that other positively charged electrodes (anodes) might be necessary to focus the electrons properly towards the sample. Still, mainly the anodes are used in the case of SEM and not in the case of TEM. Herein, an ultra-thin sample is required for electron beams to pass through. Once electron beams reach the ultra-thin sample, heavy atoms absorb more electrons, the light atoms absorb fewer electrons, and the others transmit through the sample. As a result of this variation in absorbance of electrons, an image can be observed as dark and light/grey colour. Once electrons transmit through the sample, a detector detects those high-contrast and better-resolution images generated by electron beams. Figure 4.10 is a schematic depicting the basic working principle of a typical TEM system.

In this work, cross-section preparations of each system were prepared in order to examine the structural properties of Samples A and B using TEM. Sample A was produced as an electron-transparent lamella in a Zeiss Auriga FIB-SEM dual-beam electron microscope utilising a focused ion beam (FIB). In the case of Sample B, a conventional technique for preparing semiconducting material was employed [285]. After grinding, polishing, and dimpling, the cross-section preparation of Sample B was finished by ion-milling in a Gatan 691 Precision Ion Polishing System (PIPS), whose vacuum chamber was previously cooled with $LN_2$. Ultimately, both samples were analysed using TEM techniques on a Thermo Scientific Talos F200X scanning transmission electron microscope (STEM) with an acceleration voltage of 200 kV.
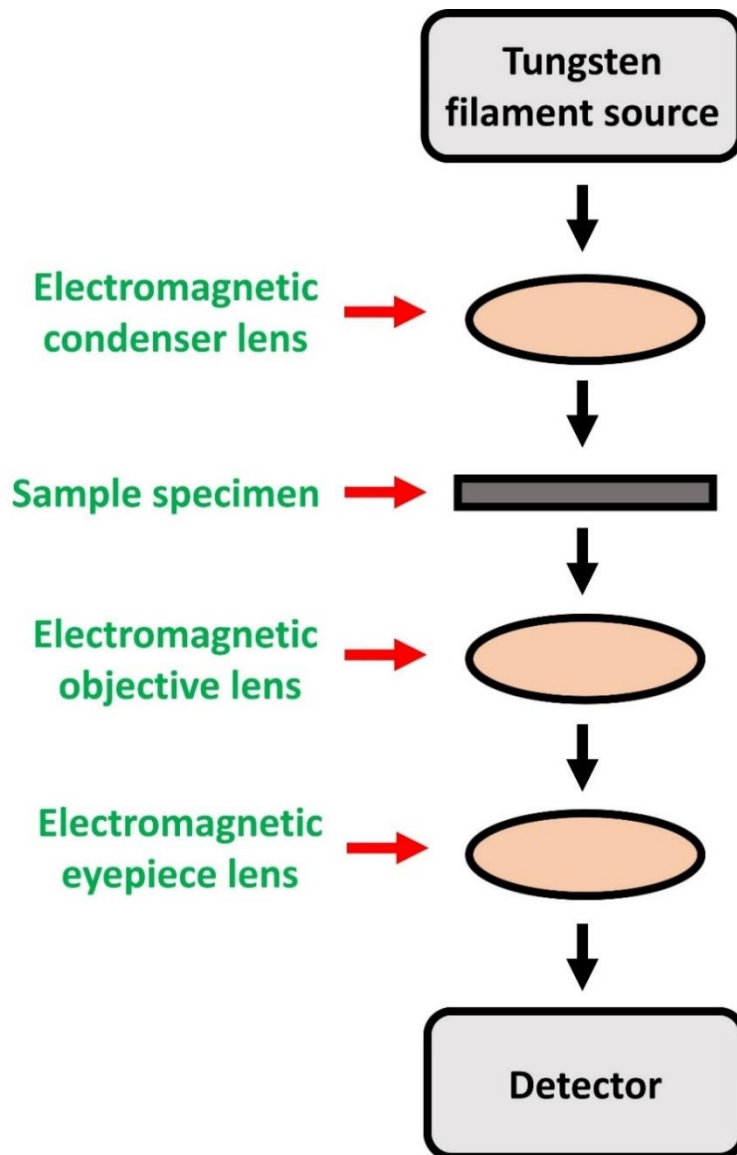
Figure 4.10: Schematic diagram of the basic working principle of a typical TEM system.

### 4.3.6 Energy dispersive X-ray spectroscopy

The elemental composition of the materials can be determined using EDX spectroscopy, which is a non-destructive technique. It can be combined with either SEM or TEM to analyse the sample's surface and bulk. In this case, the atoms in the sample are excited by the electron beam of the SEM or TEM, causing them to emit X-rays with wavelengths characteristic of the atomic structure of the elements in the sample. The X-ray emissions can then be analysed with an energy-dispersive detector to determine the sample's elemental composition.

### 4.3.7 Dektak profiler

The CR employs a DektakXT stylus surface profiler, an innovative tool for measuring the step height of thin and thick films. Besides profiling surface topography and waviness, the DektakXT instrument detects sample roughness in the nanometre range. This instrument has a step-height repeatability of typically less than 0.6 nm.

In principle, the DektakXT profiler performs electromechanical measurements by moving a diamond-tipped stylus across the surface of the sample in accordance with a user-programmed scan length, speed, and force. The stylus is connected to a linear variable differential transformer (LVDT), which generates and processes electrical signals corresponding to the variations of the surface of the sample. These surface variations are saved in a digital file for display and analysis. The Vision64 application is then employed to calculate and present the results of user-chosen analytical functions. These functions are utilised to measure the surface textures and other parameters that characterise the profile date.

### 4.3.8 Photoluminescence

Photoluminescence (PL) measurements investigate the optical properties of the samples. Luminescence is the light emission produced from a material owing to the incident energy application from an external source, such as a laser source. In semiconductors, electron and hole recombination occurs through the luminescence process, resulting in energy production in the form of photons. There are two ways in which this process is produced. These are photoluminescence and electroluminescence (EL), both employed to characterise the optical quality of the grown materials.

PL spectroscopy is a powerful instrument commonly employed to investigate the band structure of semiconductors. PL occurs when an incident photon of energy becomes larger than the bandgap energy of the material. This process excites an electron from the valence band to the conduction band, recombining with the photon emission. The process excites an electron from the valence band to the upper levels of the conduction band as a result of the excess energy in the incident photon. This electron then relaxes close to the conduction band minimum, where it was a finite probability of radiative recombination. Figure 4.11 is a

schematic representation of the PL process in a direct bandgap semiconductor material. Literature examples of PL spectra and transition are shown in Figure B.1 in Appendix B.

The resultant PL profile offers information such as radiative and non-radiative recombination channels. Since the non-radiative recombination channels are largely defect-related, this can provide helpful information on the optical properties of the material. From the PL measurements, useful analyses can be done, including PL intensity, peak position, integrated PL intensity, and FWHM.
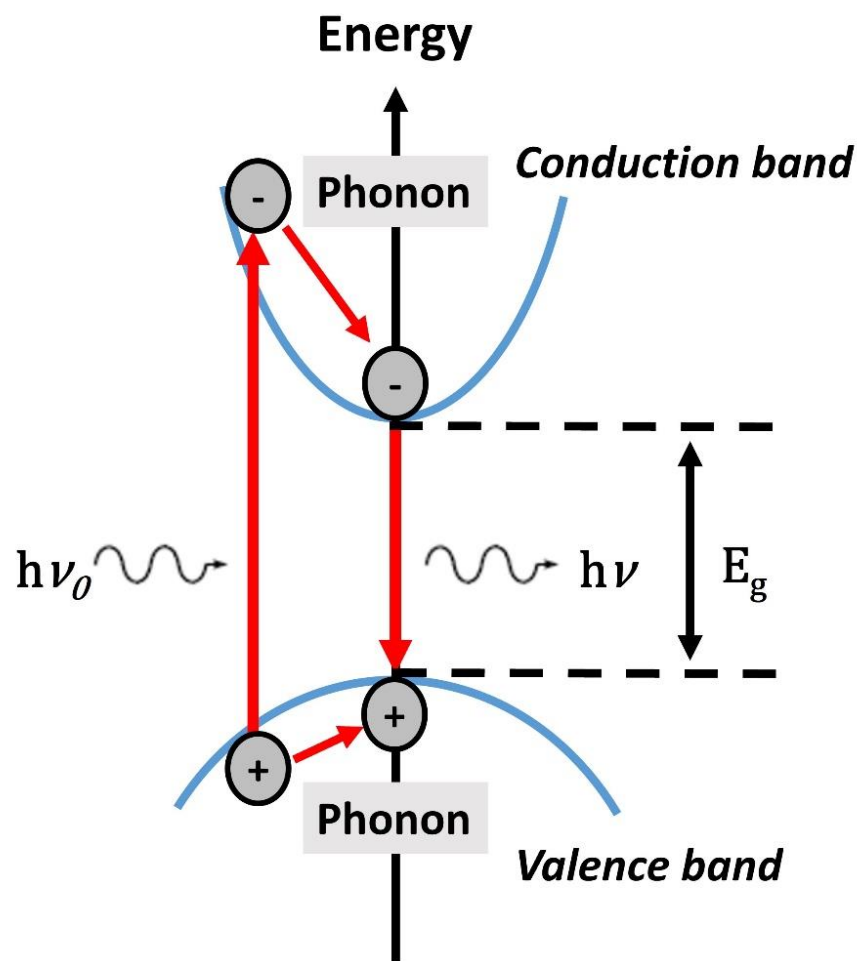


Figure 4.11: Schematic represents the PL process in a direct bandgap semiconductor material.

To access the optical properties of the samples, the PL measurements were conducted in the optics laboratory at the School of Physics and Astronomy at Cardiff University. The samples were mounted onto the sample holder and inserted into a liquid nitrogen ($LN_2$) cooled cryostat equipped with calcium fluoride ($CaF_2$) windows to perform PL measurements at different temperatures and laser powers. A red visible laser diode with a wavelength of 785 nm was

utilised as an excitation power source. A pulse generator was also utilised to modulate the excitation source at a frequency of 20 kHz. A lock-in amplifier was then used to subtract the background signal generated from the system. A Nicolet iS50-R FTIR spectrometer, equipped with a potassium bromide (KBr) beam splitter, was utilised to acquire the PL signals from the samples. A cooled MCT detector then detected the acquired PL signals. A schematic diagram of the PL set-up available in the optics laboratory is depicted in Figure 4.12.
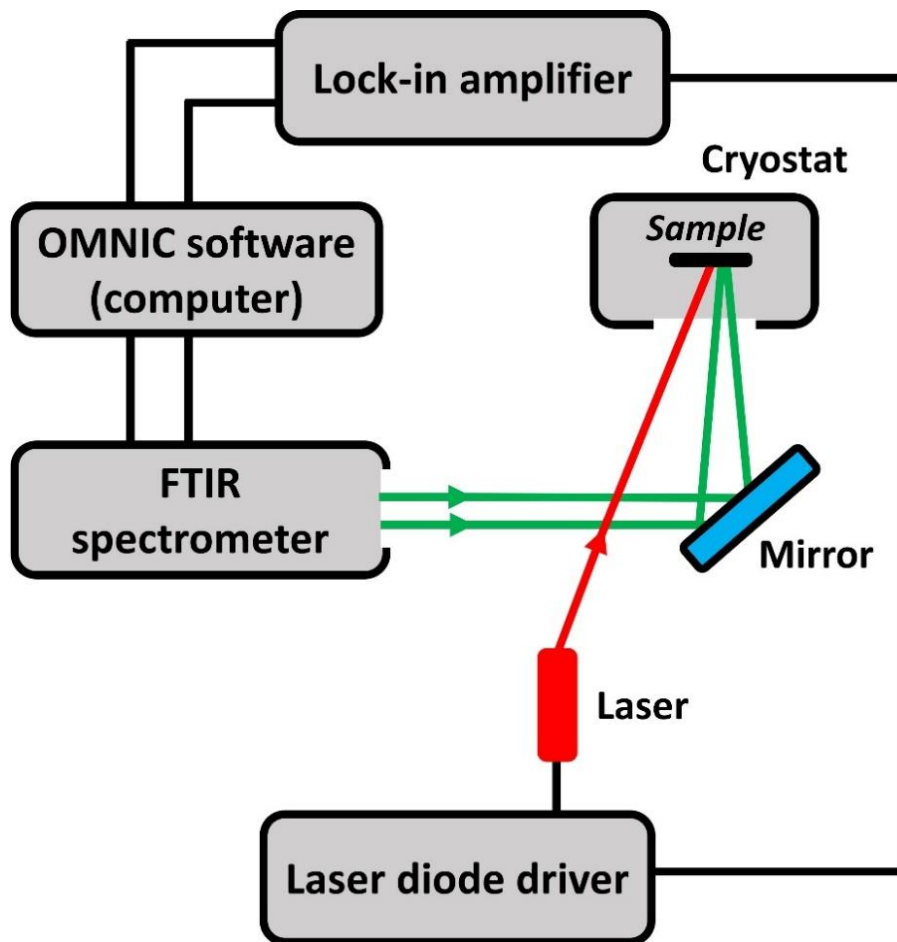


Figure 4.12: Schematic of the PL setup in the optics laboratory at Cardiff University used to perform the PL measurements.

## 4.4    Device fabrication

After materials characterisation, the devices were fabricated at the institute for compound semiconductors (ICS) in the cleanroom (CR) facility in the School of Physics and Astronomy at Cardiff University. Herein, a typical fabrication process of a semiconductor device is described. Figure 4.13 shows a typical *pin* InAs/GaSb T2SL photodiode structure used for fabrication.

Figure 4.14 shows the real equipment used for device fabrication in the clean room, and Figure 4.15 depicts a step-by-step fabrication procedure. This section presents the general process of device fabrication for a semiconductor material. A detailed process of the InAs/GaSb T2SL device fabrication, characterisation, and outcomes is presented in Chapter 6.

| |
|---|
| InAs cap N$^+$ ~1x10$^{18}$ cm$^{-3}$ t ~ 20 nm |
| MWIR T2SL N$^+$ ~1x10$^{18}$ cm$^{-3}$ t ~ 60 nm |
| MWIR T2SL<br>7 ML InAs / 4 ML GaSb<br>n.i.d.<br>t ~ 1 μm |
| MWIR T2SL P$^+$ ~1x10$^{18}$ cm$^{-3}$ t ~ 60 nm |
| GaSb buffer P$^+$ ~1x10$^{18}$ cm$^{-3}$ t ~ 100 nm |
| GaSb P-type substrate |

Figure 4.13: Schematic of a typical InAs/GaSb T2SL pin photodiode structure used in the fabrication process.

**Figure 4.14:** Images of equipment used for device fabrication in the ICS-CR at Cardiff University. Images show (a) wafer/samples scribing stage, (b) wet bench area for samples cleaning and wet etch process, (c-e) photolithography process equipment including spinning of photoresist, soft baking, and exposure respectively, (f) metal deposition step using a physical vapour deposition tool (PVD), and (g) material characterisation machines, including DektakXT surface profiler (top left), Zeiss optical microscopy (top right), and SEM (bottom).
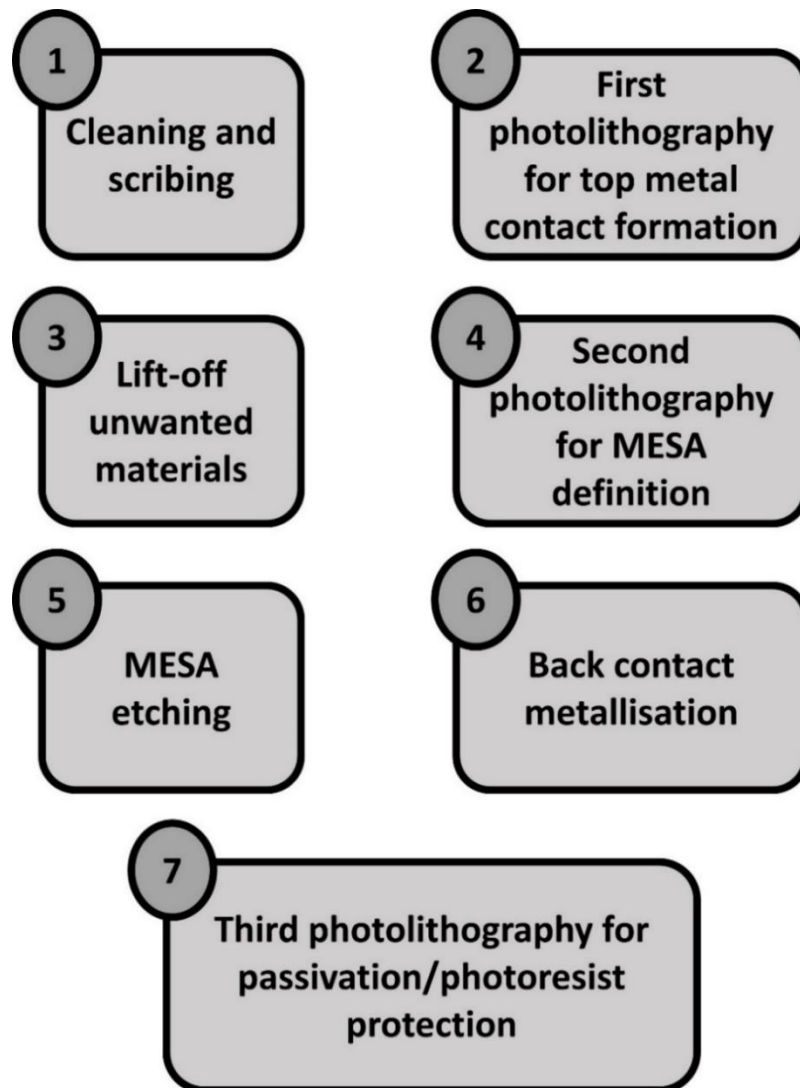
Figure 4.15: A step-by-step device fabrication process.

## 4.4.1 Samples/wafers scribing

Before device fabrication, wafers usually need to be broken up into smaller pieces for processing. It is important to note that when etching is involved with the fabrication process, it is essential to know the direction of a cleavage plane since this impacts the etched channel profile. It is usually revealed by previous cleaves or flats on the wafer; however, if the cleavage plane is unclear, an alternative is to do the following. (i) A slice should be placed on some CR tissues. (ii) Pressure is applied at a wafer edge with a fine point until the slice beaks along a cleavage plane. To produce a piece of material for processing, the size of the pieces required for processing should be known. A diamond scriber makes firm scratches along the edge to determine the size. Then, the sample is clamped between the jaws of a Perspex holder with

the scribed line along the edge of the jaws. Lastly, tap sharply but without undue force on the protruding material with a wooden or plastic rod or tweezers. Figure 4.14(a) shows the necessary equipment to scribe a sample or wafer.

### 4.4.2 Samples cleaning

For sample cleaning, it is critical to clean the sample with solvents between each step to prevent the sample from contamination or residuals caused during the fabrication process. The wet bench area is used in the CR, as shown in Figure 4.14(b). The standard procedure is to soak the sample in acetone, followed by methanol and isopropanol (IPA) for 5 minutes each and then followed by blow-drying with a nitrogen gun. If cleaning is insufficient, the solvents are sometimes placed inside an ultrasonic bath to help the cleaning process and remove residuals.

### 4.4.3 Photolithography

Photolithography is a chemical procedure in which patterns (photomask) are produced utilising a light source. Photolithography is a very advantageous process in which the produced patterns (created structures) can be very small, well-defined, and reproducible. However, the downside of photolithography is that the process is slow, and there is a possibility of contamination, low density, and defects formation. A photolithography mask is required to produce patterns on the device necessary for the photolithography process. Figure 4.16 shows the optical images of the NEWPIN photomask used during the fabrication process. As can be seen, the mask is designed to have six layers with different patterns required for the creation of the photodiode. These patterns are explained underneath.

- Top contact mask

It is designed for the deposition of top contacts. In this mask, the photolithographic UV light is blocked by the gold regions of the photomask, whereas the UV light is passed through the black regions. This mask is designed for the top contact deposition with a positive photoresist and lift-off process. It also has cross and triangular alignment markers, as shown in pink in Figure 4.16(a).

- Mesa mask

This mask creates mesa using a positive photoresist and etching method. In this case, one set of alignment markers is utilised to align the mesas with the deposited top contacts, while the other set is covered by the mask and used in the subsequent stages. Figure 4.16(b) shows the mesa mask in the photomask.

- SU8 mask

This mask is intended for the deposition of a positive photoresist in order to shield the mesa sidewalls from exposure to ambient air. The bottom alignment markers are utilised to properly align the mask to the mesas. Figure 4.16(c) shows the SU8 mask of the photomask.

- Bottom contact mask

This mask, depicted in Figure 4.16(d), is intended for the deposition of bottom contact using a positive photoresist and lift-off process. Both alignment markers can be used to align the mask to the mesas. Since the substrate is conducting, metals were directly deposited on the backside of the sample; hence, this mask was not used in this research project.

- Anti-reflection coating mask

This mask was not used in this research work but is intended for applying an AR coating. Figure 4.16(e) shows this mask of the photomask.

- $Si_3N_4$ mask

This mask is intended to be coated with dielectric passivation. The plan is to deposit the passivation layer over the entire sample surface, and spinning and exposure of a positive photoresist over the desired regions are then performed. The unwanted dielectric materials are then etched away. The mask is aligned to the mesas using both alignment markers. Figure 4.16(f) shows this mask of the photomask.
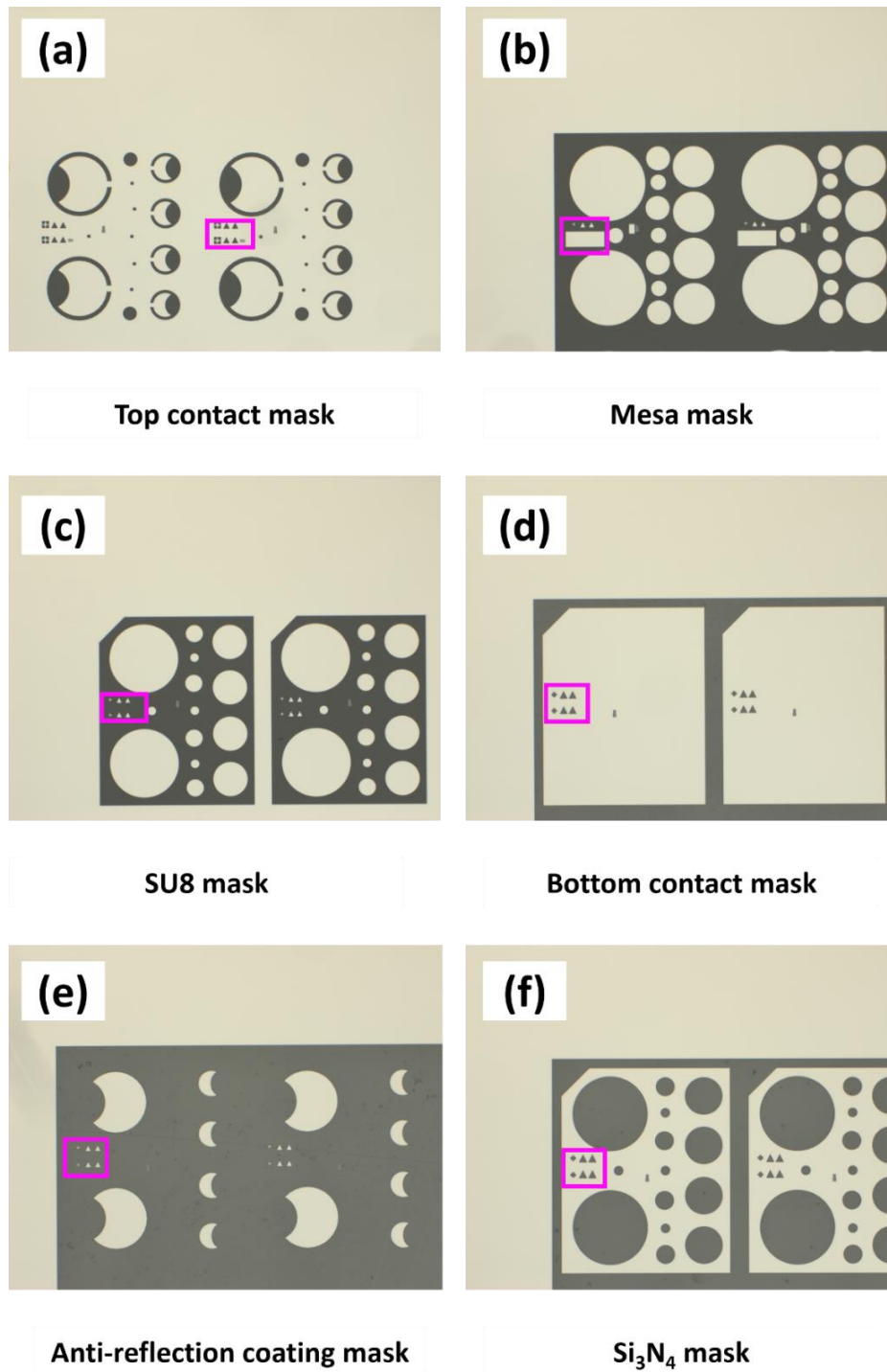
Figure 4.16: Optical images of the NEWPIN photomask used during fabrication. The pink rectangle underlines the alignment markers in each mask of the photomask.

The photolithography process comprises four typical steps: spin-coat of photoresist, soft bake, exposure to UV light, and development. The real photolithography equipment required to proceed with these steps is already depicted in Figure 4.14(c-e). The first step of photolithography is the spin-coat of the photoresist. Two types of photoresists can be

106

proceeded, either negative or positive, as shown in Figure 4.17. This is important because it defines which part of the photomask is remained or is removed. In the case of a positive photoresist, the exposed part with the UV light will be removed. In contrast, if the photoresist is negative, the exposed part to the UV light will remain.
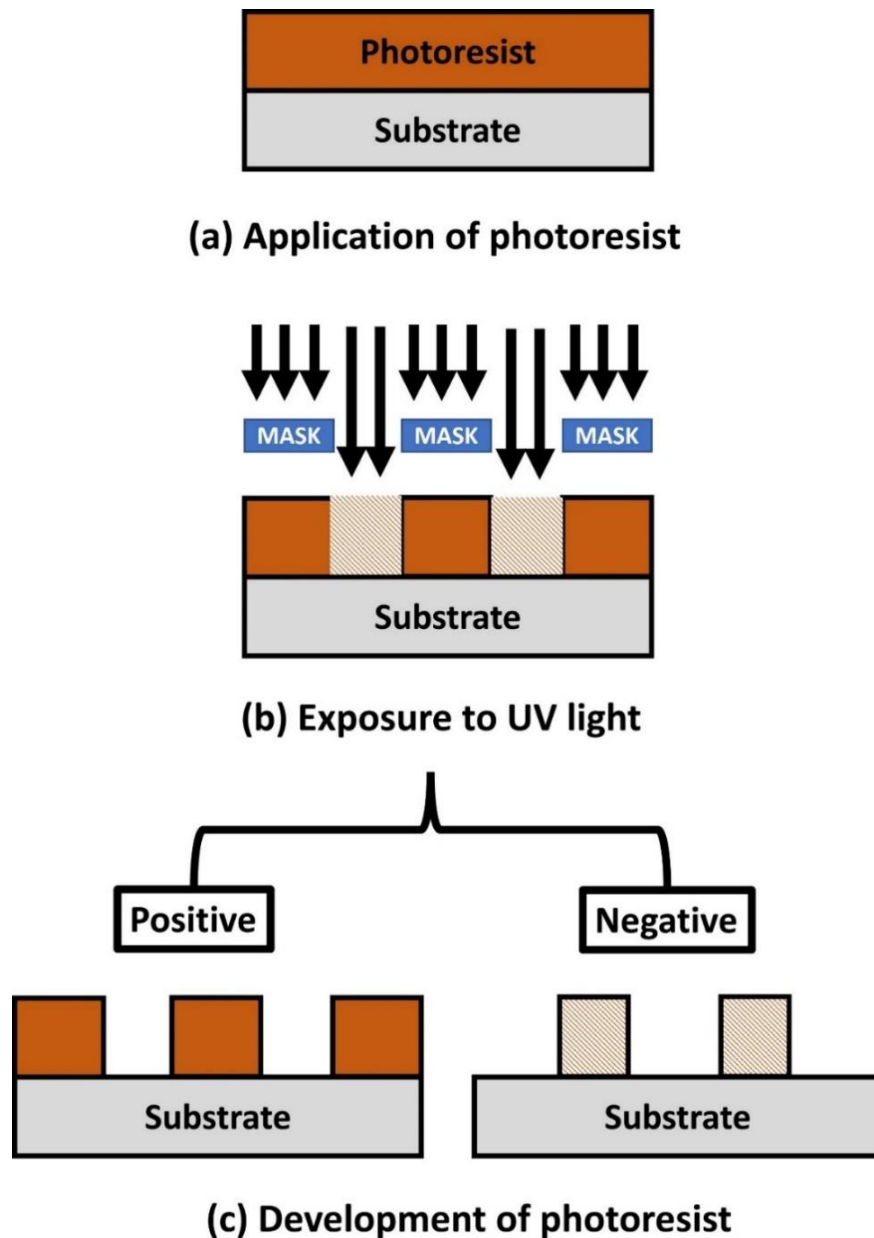


Figure 4.17: Photolithography procedure including (a) application of a photoresist, (b) exposure to UV light, and (c) development of the photoresist.

In terms of applying the photoresist, the sample is placed in the centre of a spinner tool. The sample is stuck into a plastic film to hold it inside the spinner, and a bi-layer positive photoresist is applied over the top surface of the whole sample. The bilayer is used to facilitate

the following lift-off process. The spinner enables the photoresist to thin down to a specific thickness depending on the speed of the spinner. Once the photoresist is applied to the surface of the sample, then the second step is to soft-bake it on a hot plate station. The third step is the exposure of the photomask to the UV light using a mask aligner. The MJB4 mask aligner defines small patterns down to around 1 μm. The sample is placed inside the mask aligner on the sample holder, and the photomask is placed on top of the sample to enable the required patterns to print on the sample through exposure to UV light. The photomask must be held with a vacuum, so the sample does not move during the process. Once the photomask is placed in the correct position, the last step is to expose the sample to UV light. Here, specific goggles should be worn to prevent the eyes from the possible risk encountered by UV radiation. The last step of photolithography is the development of the photoresist. This chemical reaction process enables the exposed photoresist to generate a visible image. The development requires a chemical developer and diluted water (DIW) to finish the chemical reaction. Figure 4.18 depicts the sample after performing the mesa photolithography step.
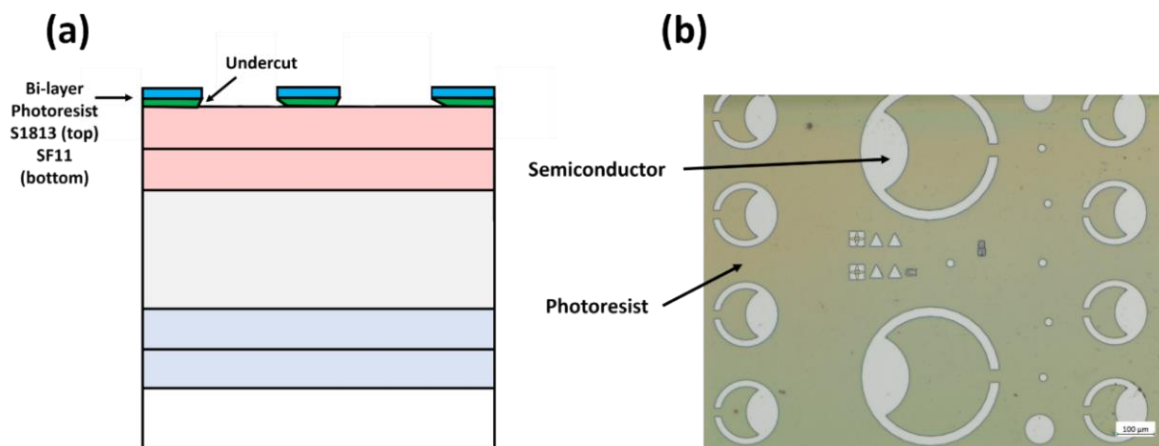


Figure 4.18: (a) Schematic and (b) optical micrograph of the sample after mesa photolithography.

It is worth mentioning that the photolithography process was performed three times during the fabrication procedure. The first process is to define the top contact patterns for the metallisation step using the top contact photomask. The second process is to define mesas for the etching step using the mesa photomask. The third process is to deposit a photoresist as a protection layer using the SU8 photomask. The main difference is the mask alignment, as the first photolithography step does not require specific alignment to the photomask markers. However, during the second photolithography step, both maskers must be completely aligned

with the alignment markers printed during the first photolithography step. Hence, designing different alignment markers around the structure is essential for proper alignment.

### 4.4.4   Metal deposition

The metal deposition is performed by creating a layer of metals to make an ohmic contact with the semiconductor material. The metallisation steps occur twice during the fabrication procedure. During the first photolithography process (top contact definition), metals are deposited to form the top contact for the device. The bottom contact is formed after mesa etching during the second photolithography step. Using a physical vapour deposition (PVD) tool, chrome (Cr) and gold (Au) contacts were deposited on the top side of the sample using the top contact mask in the NEWPIN photomask. A lift-off process of unwanted materials was then performed employing acetone and NPM1165 remover in an ultrasound bath. Figure 4.19 depicts the sample after top contact deposition.



Figure 4.19: (a) Schematic and (b) optical micrograph of the sample after the top contact metallisation step.

The PVD typically occurs when an ionised gas molecule displaces an atom of the materials to form a plasma at an atomic level. The plasma interacts with the atoms of the sample to form a thin layer after striking a material target. Figure 4.20 depicts the PVD machine used in the CR. The PVD machine contains a chamber, and it has a crucible to load an adhesive layer, such as titanium (Ti), platinum (Pt), chrome (Cr), or nickel (Ni), and a boat to load metals, such as gold (Au). Regarding the metallisation process, the sample is mounted on a sample holder and

placed into the chamber where the sample surface faces the heated metals for deposition. Metals are then loaded, for example, Au in a boat, and Cr is heated through a rod. The samples are then mounted to the holder and placed at a short distance of around 30 cm from the boat and crucible. Once all parts are in place, a bell jar is placed over the tool, and the chamber is evacuated to a pressure of around $2\times10^{-2}$ mbar using the roughing pump. The chamber is further evacuated to a pressure of approximately $2\times10^{-6}$ mbar to help maintain a high vacuum environment to enable successful deposition. Once a suitable vacuum is achieved, the current is gradually ramped up to heat the boat first and the rod second, allowing for metal evaporation. Once metals are heated and melted, the shutter is opened for deposition. The shutter is closed after metal deposition, and a specific thickness of deposited metals is achieved by utilising a quartz-crystal monitor. The current is then ramped down gradually to prevent thermal shock to the boat and crucible. After obtaining the desired combination of material and thickness, the PVD chamber must be vented to restore to typical pressure, and within this time, the sample cools down. The resulting deposited layer should be thin and uniform on the sample. A SEM, Zeiss optical microscope and Dektak profiler can be used to inspect and determine the thickness of the deposited layer, as already depicted in Figure 4.14(g).
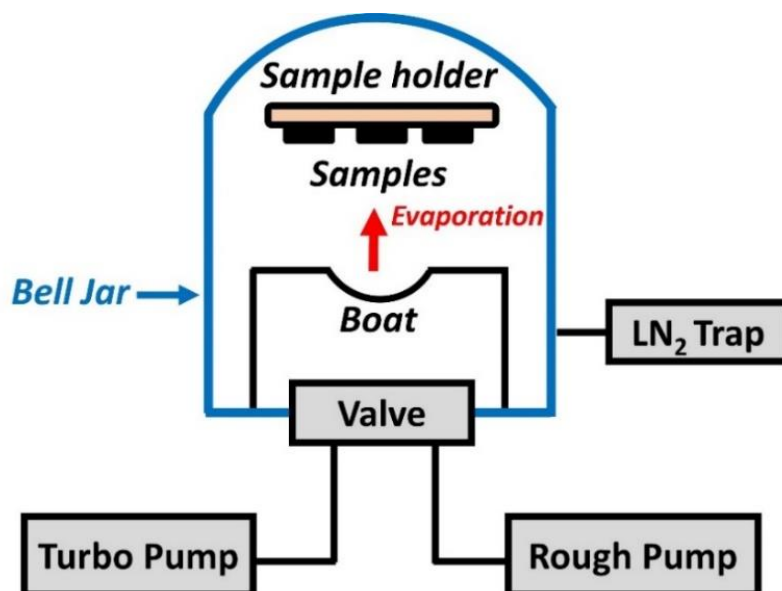


Figure 4.20: Schematic diagram shows the PVD machine used in the CR.

### 4.4.5 Mesa etching

Etching is the final step to isolate mesas after the photolithography and metallisation processes. The etching process is commonly based on chemical reactions that form patterns created by photolithography. There are two approaches to realise mesa etching: wet and dry etch. Herein, the mesa mask of the photomask was used to deposit and pattern a layer of S1813 photoresist. Figure 4.21(a) shows that the sample was etched to around 0.76 μm using HF and citric acid-based wet etchants. The T2SL device was etched in citric acid with HF acid per the following etchant recipe: 40 ml of $H_2O_2$, 40 ml of $C_6H_8O_7$, and 40 μl of HF.

This etching depth was accomplished in about five minutes based on previous calibrations. As can be seen, the etching profile appears isotropic due to the uncountability of the chemicals. Using a two-stage DIW treatment, the chemical reaction was stopped. The sample was then cleaned with acetone and IPA. Figure 4.21(b) depicts the optical image of the sample after mesa etching.
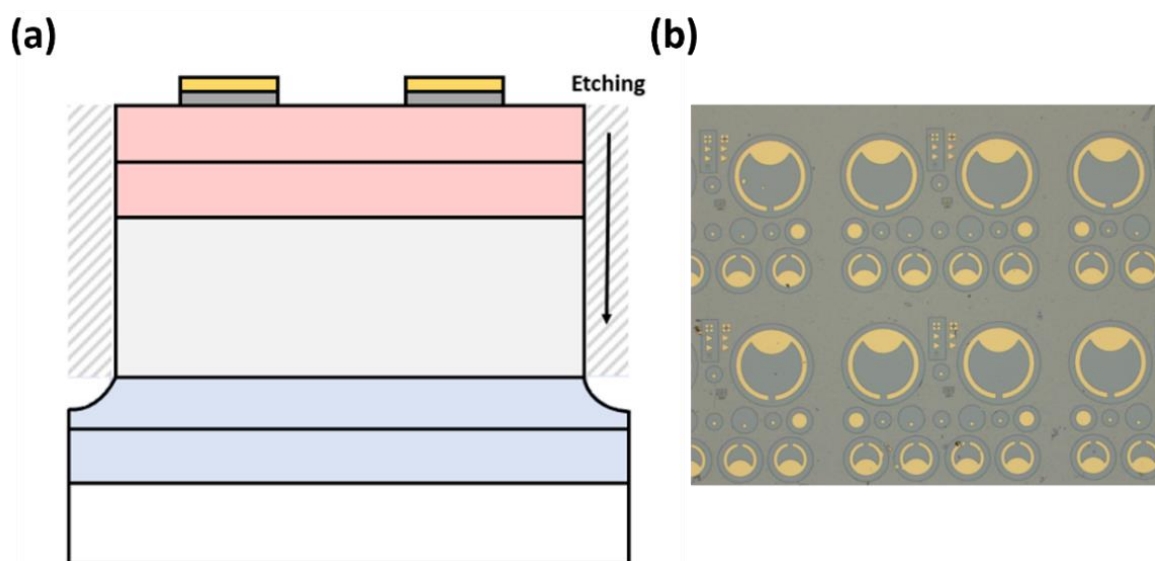


Figure 4.21: (a) Schematic and (b) optical image of the sample after mesa etching.

### 4.4.6 Mesa sidewalls passivation

Using the ''SU8 mask of the photomask'', a layer of S1813 positive photoresist was patterned onto the sample, as depicted in Figure 4.22(a). This layer was then baked at 80 °C for two hours. The bottom contact is the final stage, where the metals were deposited on the backside

of the sample, as shown in the schematic. Figure 4.22(b) is an optical image of the sample after mesa sidewall protection by the photoresist to prevent oxidation from ambient air.
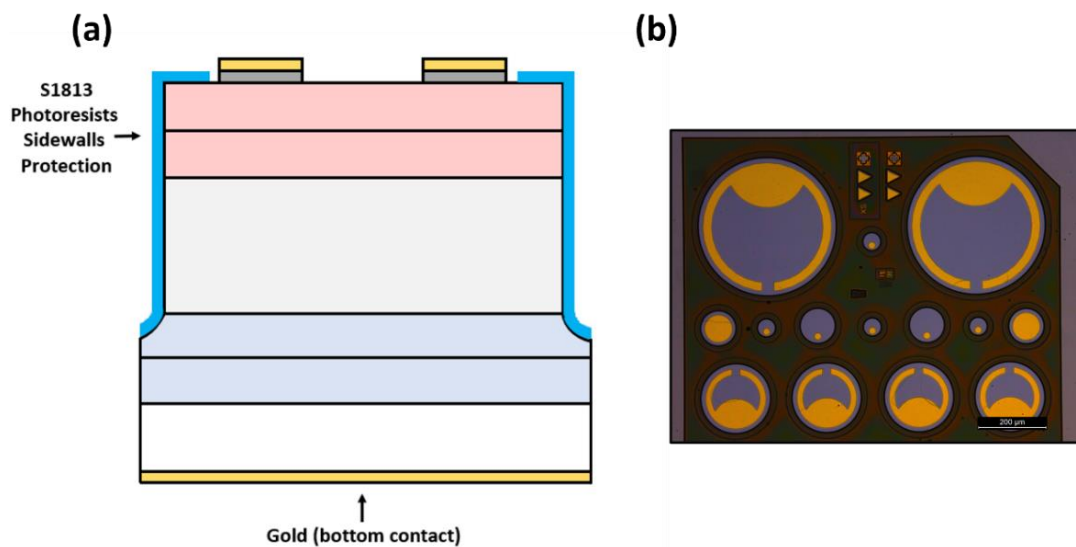


Figure 4.22: (a) Schematic and (b) optical image of the sample after mesa sidewall protection by the photoresist and bottom contact metallisation steps.

## 4.5    Device characterisation

The performance of the fabricated devices was examined in the optics laboratory. The following electrical characterisation techniques were deployed to test their performance: current-voltage (I-V) and capacitance-voltage (C-V) measurements. The electrical characterisation measurements were carried out using a TTPX Lakeshore system cryogenic probe station kit in the optics laboratory, presented schematically in Figure 4.23. The samples were placed on the sample holder and cooled down to 77 K using $LN_2$. Probes are used to make contact with the top and bottom contacts. The sample holder can also serve as a probe for devices with a bottom contact. A voltage is applied between the probes to run the electronic measurements, and a Keysight B1500A semiconductor device analyser measures the corresponding current or capacitance depending on the experiment. The supplied current or capacitance is controlled through the device in small increasing steps, and the resultant voltage is recorded. The device analyser reveals the I-V or C-V characteristics of the measured device in the form of current versus voltage or capacitance versus voltage graphs, respectively. It is worth mentioning that to avoid damaging the device, the current level is set to an upper

limit of around 200 mA, and the voltage is applied from -1 V to + 1 V in steps of 0.01 V. A temperature controller is also utilised to change the temperature measurements from 77 K to room temperature.
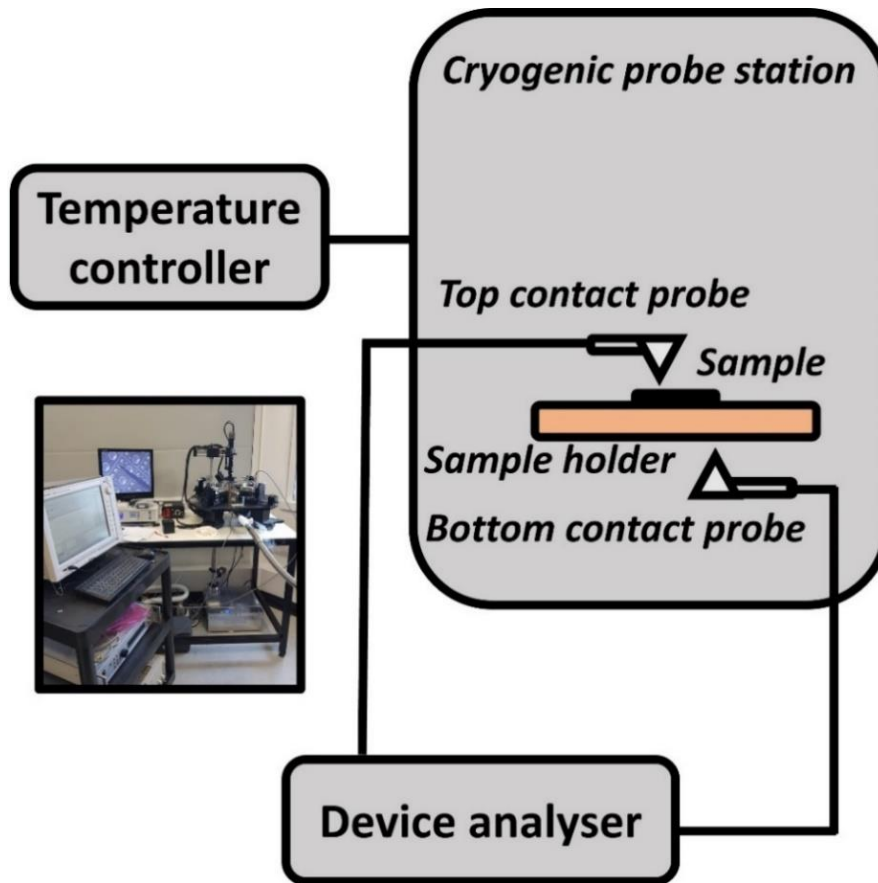


Figure 4.23: Schematic representation of the cryogenic probe station system available in the optics laboratory used to undertake electrical characterisations of the processed devices, including I-V and C-V measurements. An image of an actual experimental setup is included.

## 4.6    Theoretical modelling

To complement the experimental investigations, theoretical modelling was undertaken to simulate the band structure and bandgap energy of the grown materials. Furthermore, device simulation has been conducted to model the electrical performance of the fabricated devices. This section provides a detailed description of the software and methods used for modelling.

### 4.6.1 Band heterostructure simulation

Quantum mechanics is essential to determining the electronic properties of a T2SL. To calculate the global electronic structure of a device, it is thus crucial to solve the Schrödinger equation. Several research studies have utilised microscopic electronic structure techniques, including the pseudopotential [286], [287] or empirical tight-binding model (ETBM) [288], [289], which solve the issue at the atomic level. Nevertheless, because these techniques are computationally expensive and the involved structures span tens of nanometres, the 8-band k.p method described below was employed in this research.

#### 4.6.1.1 k.p theory

The electronic band structure of a bulk semiconductor is often governed by a many-particle Hamiltonian encompassing all electrons and nuclei within a crystal. By considering the atomic cores as immobile and employing a mean field approximation for all interactions involving many particles, the problem can be characterized by a single-particle Schrödinger equation that describes an electron in a completely periodic crystal,

$$\widehat{H}\psi_n(x) = \left[\frac{\hat{p}^2}{2m_0} + V(x)\right]\psi_n(x) = E_n\psi_n(x) \qquad (4.5)$$

where $\hat{p}$ is the momentum operator, $V(x)$ is the resulting band edge profile that incorporates band offsets, band shifts due to strain effect, and the electrostatic potential. The eigenfunctions $\psi_n(x)$ adhere to Bloch's theorem (Derivation of Bloch's theorem can be found in Appendix C) due to the crystal periodicity. i.e. these functions are eigenfunctions of the translation operator with the same eigenvalue, $\widehat{T}_{\mathbf{R}}$, such that,

$$\widehat{T}_{\mathbf{R}}\psi_{n,\mathbf{k}}(x) = e^{(i\mathbf{k}\cdot\mathbf{R})}\psi_{n,\mathbf{k}}(x) \qquad (4.6)$$

By substituting these Bloch functions into the Schrödinger equation stated in Equation (4.5), we obtain the following,

$$\hat{H}(k)u_{n,\mathbf{k}}(x) = \left[\frac{(\hat{p} + \hbar k)^2}{2m_0} + V(x)\right]u_{n,\mathbf{k}}(x) = E_n(\mathbf{k})u_{n,\mathbf{k}}(x) \qquad (4.7)$$

In order to calculate the band structure $E_n(\mathbf{k})$ for the above equation, the k·p approach assumes that most carriers are located near the minima of the conduction band or the maxima of the valence band. Therefore, the k·p technique considers a specific extreme point, $k_0$, at which the energies, $E_n(k_0)$, and Bloch factors, $u_{n,k0}(x)$, are presumed to be already known. The Hamiltonian in Equation (4.7) can be split into constant extremum and k-dependent components, assuming that only wave vectors near the extrema of a limited number of bands are significant. This process yields the subsequent Hamiltonian:

$$\hat{H}'_{\nu\mu} = \hat{H}_{\nu\mu}(\mathbf{k}) + \sum_{\beta \epsilon B} \frac{\hat{H}_{\nu\beta}(\mathbf{k})\hat{H}_{\nu\mu}(\mathbf{k})}{E_\nu(\mathbf{k}_0) - E_\nu(\mathbf{k}_0)} \qquad (4.8)$$

The Hamiltonian specified in Equation (4.8) can be resolved using either a single-band or multi-band method. While the effective mass approximation, also known as the single-band model, is the most straightforward approach, the multi-band models offer greater accuracy. The literature contains reports of numerous k·p models, which primarily vary in the number of bands that are taken into account and the method in which they address strain and spin-orbit interaction [290], [291], [292], [293]. The current study determined that an 8-band k·p model is the most optimal choice for balancing accuracy and computing cost. Thus, we assumed one conduction band and three valence bands. In the context of a multi-band Schrödinger equation, it is necessary to include an additional term, denoted as H$_{SO}$, in order to incorporate the relativistic influence of spin accurately,

$$H_{SO} = \frac{\hbar^2}{4m_0^2, c^2}(\nabla V \times \hat{p}) \cdot \sigma \qquad (4.9)$$

where $\sigma$ is the vector of the Pauli matrices. In accordance with the derivation of Andlauer [294], consequently, the 8-band Hamiltonian can be demonstrated to be,

$$\hat{H}^{8\times8}(k) = \begin{pmatrix} \hat{H}_{ee}^{2\times2}(k) & \hat{H}_{ev}^{2\times6}(k) \\ \hat{H}_{ve}^{6\times2}(k) & \hat{H}_{vv}^{6\times6}(k) \end{pmatrix} \tag{4.10}$$

with

$$\hat{H}_{ee}^{2\times2}(k) = \left( E_c + \sum_{i=1}^{3} k_i A_c k_i \right) \otimes 1^{2\times2} \tag{4.11}$$

and

$$\hat{H}_{ve}^{6\times2}(k) = \begin{pmatrix} -ik_1 P + k_3 B k_2 \\ -ik_2 P + k_1 B k_3 \\ -ik_3 P + k_2 B k_1 \end{pmatrix} \otimes 1^{2\times2} \tag{4.12}$$

the parameter B, associated with the crystal's inversion symmetry, can be assumed to be zero for III/V materials. Reference [295] provides a comprehensive summary defining the necessary k.p parameters.

### 4.6.1.2  Spurious solutions

In the abovementioned approach, spurious solutions such as ghost states, wrong bound states at interfaces, and false oscillatory wave functions create an undesired ambiguity. In the current method, these issues are resolved by meticulously addressing the "remote-band contributions" to the bulk k·p Hamiltonians by establishing an operator ordering that results in self-adjoint Hamiltonians and utilising an up-winding approach to discretise derivatives. To ensure simplicity, we will focus on a 2-band Hamiltonian that encompasses all potential problems for the current subject,

$$\hat{H}^{2\times2}(k) = \begin{pmatrix} E_c + A_c k^2 & iPk \\ -iPk & E_v + A_v k^2 \end{pmatrix} \tag{4.13}$$

In this scenario, the spurious solution of $k^2$ might result in the formation of oscillatory nodes, leading to spurious ghost states. This study circumvents the difficulty by setting $A_c$ to zero and

adjusting certain valence band parameters through rescaling, as Reference [34] suggested. The problematic $k^4$ term is thereby eliminated from the dispersion. Further measures to address the problem of spurious solutions are elaborated upon in more depth in Reference [294].

### 4.6.1.3  Numerical realisation

The physical relations are solved numerically by discretising the partial differential equations and mapping them onto a discrete lattice. This process involves transforming the differential operators into linear algebra problems. The discretisation of the problem is achieved by utilising a box integration finite difference method. The proposed method involves dividing the simulation domain into regular boxes that do not overlap. Each box corresponds to the area surrounding a specific grid node. The box volumes integrate the partial differential equations, yielding an integral equation that is discretised through implementing the finite difference approach outlined in Reference [294]. After discretisation, the partial differential equations are transformed into a complex system of linear or non-linear equations. These systems can, therefore, be solved iteratively employing the conjugate gradient [296], composite step conjugate gradient [297], or biconjugate gradient approaches [298].

### 4.6.1.4  Use of Nextnano software

To engineer the band structure and bandgap energy of a T2SL material system, commercial Nextnano software [299], [300] was implemented. The 8-band k.p method detailed previously has been incorporated into the Nextnano[3] software. This program uses a graphical user interface (GUI) called Nextnanomat that generates input files, runs simulations, and visualises the results. The simulation results can be visualised in the output feature of Nextnanomat, either in the form of graphs or text files. The software has an allocated database of III-V semiconductor alloys with zinc-blende and wurtzite crystal structures [301]. Once the input files are generated, the simulation can be run. The structures considered in this research comprise the InAs, GaSb, and InSb elements and their compounds and alloys. The parameters used for these binary files and the references from which these parameters are taken are listed in Table 4.1.

Table 4.1: List of material parameters of InAs, GaSb, and InSb binaries used in Nextnano³ software framework for calculating k·p band structure. References from which the values are taken are also included.

| Parameter | InAs | GaSb | InSb |
|---|---|---|---|
| Lattice constant $a_0$ (Å) | 6.0583 [302] | 6.0959 [302] | 6.4794 [302] |
| Bandgap energy at 0 K (eV) | 0.410 [302] | 0.812 [302] | 0.240 [302] |
| Varshni parameter $\alpha$ (meV/K) | 0.276 [302] | 0.417 [302] | 0.320 [302] |
| Varshni parameter $\beta$ (K) | 93 [302] | 140 [302] | 170 [302] |
| Conduction band mass $m_c$ (/$m_0$) | 0.022 [71] | 0.042 [71] | 0.135 [302] |
| Luttinger parameter $\gamma_1$ | 19.77 [71] | 11.74 [71] | 34.8 [302] |
| Luttinger parameter $\gamma_2$ | 9.43 [71] | 5.28 [71] | 16.5 [302] |
| Luttinger parameter $\gamma_3$ | 22.2 [71] | 22.4 [71] | 23.3 [302] |
| Spin-orbit splitting $\Delta_0$ (eV) | 832.9 [303] | 884.2 [303] | 684.7 [302] |
| Interband matrix element $E_p$ (eV) | 0.38 [303] | 0.752 [303] | 0.81 [302] |
| Elastic constant $C_{11}$ (GPa) | 832.9 [302] | 884.2 [302] | 684.7 [302] |
| Elastic constant $C_{12}$ (GPa) | 452.6 [302] | 402.6 [302] | 373.5 [302] |
| Elastic constant $C_{44}$ (GPa) | 395.9 [302] | 432.2 [302] | 311.1 [302] |
| Deformation potential CB $a_c$ (eV) | -6.66 [304] | -9.33 [304] | -6.94 [302] |
| Deformation potential VB $a_v$ (eV) | -1 [304] | -1.32 [304] | -0.36 [302] |
| Uniaxial deformation potential b (eV) | -1.8 [302] | -2 [302] | -2 [302] |
| Uniaxial deformation potential d (eV) | -3.6 [302] | -4.7 [302] | -4.7 [302] |
| Valence band offset VBO (eV) | -0.56 [302] | 0 [302] | 0.03 [302] |

The IF matrix element, derived by Klipstein et al. [72] was used in the Nextnano simulation. For a no-atom-in-common interfacial system such as InAs/GaSb, the IF matrix was taken into consideration, which is given by:

$$H_{IF} = \sum_i \delta(z - z_i) \begin{bmatrix} D_s & 0 & 0 & \pi_i\beta \\ 0 & D_X & \pi_i\alpha & 0 \\ 0 & \pi_i\alpha & D_X & 0 \\ \pi_i\beta & 0 & 0 & D_Z \end{bmatrix} \qquad (4.14)$$

where $i$ is the index of the IF at the position $Z_i$ and $\pi_i$ that are either -1 or 1. The IF parameters, $\alpha$ and $\beta$, have been set to 0.2 eV·Å in line with Livneh et al. [71]. The diagonal IF parameters $D_S$, $D_X$, and $D_Z$ should be determined by comparing them with experimental findings. Therefore, the accuracy of this simulation tool can be proven via comparison with the literature of other T2SLs. The following sections provide detailed information regarding the simulation of band structures for Ga-free and Ga-based T2SL structures.

- Ga-free InAs/InAsSb T2SL

The Ga-free InAs/InAsSb T2SL was the initial SL structure evaluated for validation. The previously mentioned 8-band k·p simulation in Nextnano³ was modified to simulate InAs/InAsSb T2SLs with different layer thicknesses and Sb compositions. Because the InAs/InAsSb T2SL is a common-atom SL [305], the diagonal IF parameters ($D_S$, $D_X$, $D_Z$) were assigned to zero in the IF matrix (Equation 4.14). It should be noted that no interfacial layer was assumed between the InAs and InAsSb layers because it was hypothesised that the commonality between the two SL layers would lead to abrupt IFs. Nevertheless, this hypothesis can be tackled based on more recent characterisation studies indicating significant Sb segregation and interfacial atomic intermixing at the SL IFs [91], [306], [92]. Even though this is challenging to determine the extent to which these phenomena occur, their influences could be incorporated into future simulations. Note that the structures were simulated to be lattice-matched to the GaSb substrates, and it was also assumed that no strain was induced into the system. The simulation was set up to output the band edges, wavefunctions, electrons and holes miniband energy levels.

In line with Vegard's law (Equation 4.15), the conduction and valence band energies of the InAsSb material (and any other ternary alloy) are interpolated between the binary alloys InAs and InSb, where $x$ is the Sb content of the material, and $C$ is a bowing parameter whose non-zero value indicates non-linear interpolation:

$$E_{(InAsSb)} = (1 - x)E_{(InAs)} + (x)E_{(InSb)} - C(x)(1 - x)$$ (4.15)

The parameters for the InAs layer are included in the simulation as per Table 4.1. For InAsSb, the bowing parameter for the conduction and valance band energies were set to +0.65 eV and -0.98 eV, respectively, as employed by Keen et al. [307]. The programme is based on a user-modifiable coding script corresponding to the modelled structure. The impacts of varying the layer thicknesses, material compositions, and temperature are observed on the band structure, energy levels, and wavefunction outputs. In addition to being an effective instrument for design, the software provides valuable insight and a practical approach for validating the experimental data. The Nextnano code used to simulate InAs/InAsSb heterostructure is found in Appendix D. The simulation results of the Ga-free T2SL with different layer thicknesses and Sb compositions are also included in Appendix D.

- Ga-based InAs/GaSb T2SL

After simulating the InAs/InAsSb T2SL structures, the data file was used with some modifications in the input values to match the parameters presented in Table 4.1. The parameters for the materials, including InAs, GaSb, and InSb were input in the Nextnanomat file, and the simulations implemented an 8 k·p method. For the case of InAs/GaSb T2SL simulation, Equation (4.14) has also been used and the index ($i$) of the IF at the position $z_i$ and $\pi_i$ takes a value of -1 or 1 at the GaSb-on-InAs and InAs-on-GaSb IFs. Since the InAs/GaSb heterostructure does not have common cations or anions, the diagonal IF parameters ($D_s$, $D_x$, and $D_z$) were selected for best agreement with PL results from T2SL structures reported previously [308]. The IFs were assumed to be InSb-like and had a thickness of 10% of the InAs layer, which was implemented to compensate for the strain. Other IFs included in the simulations of InAs/GaSb T2SL heterostructures were InAsSb and GaInSb. Reference [302] contains the parameters used for InAs, GaSb, and InSb. The linear interpolation between InAs

and InSb was used to derive all other parameters. According to Refaat et al. [309], the bowing parameter for the bandgap energy of GaInSb was set to 0.42 eV. All other parameters were achieved through linear interpolation between GaSb and InSb. Section 5.4 in Chapter 5 reports the simulation results of InAs/GaSb T2SLs with different types of IFs and shows their effects on the bandgap energy and wavefunction overlap.

## 4.6.2 Device simulation

This section provides detailed information regarding the device simulation using Silvaco ATLAS and Mathematica software. The simulation was employed in order to compare its results with the existing I-V experimental data obtained from the InAs/GaSb T2SL devices.

### 4.6.2.1 Silvaco ATLAS software

Modelling devices provides an understanding of their electrical properties even before creating structures. Hence, once the material properties have been established, devices can be simulated via technology computer-aided design (TCAD) Silvaco ATLAS software [310]. Using such software diminishes development costs by visualising the device properties before they are manufactured to optimise their designs. To verify the modelling, several initial modelling was performed. First, for simplicity, a simulation of InAs *pin* and InSb *pin* diode structures was performed and compared to the experimentally reported results by Ray-Ming et al. [311] and Evirgen et al. [93]. Later on, an InAs/GaSb T2SL *pin* photodiode structure found in the paper of Delmas et al. [312] was simulated and compared to the simulation and experimental results. Those initial simulations helped the author verify the results obtained from simulations and check whether the results matched the reported values in the papers. Once they were confirmed, the author went to model the targeted structure.

This commercially available software simulates devices such as *pin* diodes with SL absorption regions [312], [313]. However, one limitation of Silvaco simulation is that the software cannot simulate SLs directly. Still, it can define the SLs as a bulk material, which necessities a clear understanding of the materials parameters. The modelled device was based on a MWIR InAs/GaSb T2SL *pin* photodiode with InAs and GaSb thicknesses of 7 and 4 MLs (7/4 MLs), respectively. Once the structure was defined, the material parameters were specified. For the binaries, InAs and GaSb, the values of the parameters were found from the Silvaco materials

database. The bandgap energy and Varshni parameters of the SLs were found experimentally from the PL measurements. The reduced carrier concentration (background doping) of the SLs was also found from the C-V experimental measurements performed on the photodiode sample. This was extracted from the slope of the linear fitting of the (A/C)$^2$ versus applied bias. Table 4.2 shows the modelling parameters that simulate the InAs/GaSb T2SL *pin* photodiode. Hence, the parameters in Table 4.2 were taken as a weighted average of the SL constituent materials (InAs and GaSb layers). The tunnelling mass ($m_t$) was calculated from the following equation:

$$\frac{1}{m_t} = \frac{1}{m_e} + \frac{1}{m_h}$$

(4.16)

where $m_e$ and $m_h$ are the effective masses of electrons and holes, respectively. This was calculated to be also as a weighted average of the InAs and GaSb in the SL. Lastly, the trap energy level was set to 0.180 eV, as reported in Reference [312]. After specifying all necessary parameters, the MC lifetime was used as a fitting parameter at each temperature. This helped to theoretically estimate the MC lifetime of the MWIR InAs/GaSb T2SL photodiode, which was nearly close to the values reported in the literature. The Silvaco code used to simulate the InAs/GaSb T2SL device can be found in Appendix E.

Table 4.2: Silvaco modelling parameters used to simulate the MWIR InAs/GaSb T2SL pin photodiode.

| Electrical parameters | | Device parameters | |
|---|---|---|---|
| Parameters | Values | Parameters | Values |
| Permittivity | 15.34 $\varepsilon_0$ | p-type doping | $1\times10^{18}$ cm$^{-3}$ |
| Electron affinity ($X$) | 4.73 eV | nid (residual doping) | $9.7\times10^{14}$ cm$^{-3}$ |
| Electron effective mass ($m_e$) | 0.0254 $m_0$ | n-type doping | $1\times10^{18}$ cm$^{-3}$ |
| Hole effective mass ($m_h$) | 0.245 $m_0$ | Absorber thickness | 1 μm |
| Electron mobility ($\mu_e$) | $2.6\times10^4$ cm$^2$/V.s | Mesa diameter | 140 μm |
| Hole mobility ($\mu_h$) | $6.8\times10^2$ cm$^2$/V.s | Mesa area | $1.539\times10^{-4}$ cm$^2$ |

### 4.6.2.2 Mathematica and Origin software

In addition to obtaining more information about the MC lifetimes, the Mathematica software system [314] (modern technical computing), which uses the Wolfram language with a built-in library, is helpful for use in several areas of technical computing, such as symbolic computation, statistics, plotting functions and different types of data, and implementation of algorithms. In this research work, the software was used to solve equations of dark current density and plot functions. Once functions were solved in Mathematica, Origin 2017 software [315] was used to fit and analyse data from Mathematica. Equations (2.24 – 2.31) of dark current density components were employed and solved to model the dark current density. Gopal et al. [57], [316], [317] have precisely modelled the dark current in a T2SL diode to be the total of diffusion, trap-assisted tunnelling, generation-recombination, and shunt currents. After solving equations in Mathematica, data were exported to the origin software for representation as graphs. The Mathematica script used to solve current equations can be found in Appendix F.

# Chapter 5: Effect of Interfacial Growth Schemes on the Structural and Optical Properties of Mid-Wavelength Infrared Type-II InAs/GaSb Superlattices

## 5.1    Introduction

In this chapter, the growth of InAs/GaSb T2SL samples and their structural and optical characteristics are discussed in detail. The structural and optical investigations are critical to determining the quality of the grown structures. An MBE reactor is commonly used to grow strained layer SLs due to the precise control of SL layer thickness and the low growth rate (typically ~1 μm/hour). However, as discussed earlier in Chapter 3, one of the crucial challenges in growing SLs, particularly InAs/GaSb, is that the InAs has a lower lattice parameter than GaSb, introducing dislocations and defects because of internal tensile strain. These issues can be resolved by controlling the interfacial region between the InAs and GaSb layers. Depending on the shutter sequence technique utilised during the growth, this can result in a strain-compensated SL layer with high structural and optical quality. When an InSb IF layer is incorporated at the SL IFs of InAs and GaSb layers, such that the InSb layer (''InSb-like'' IF) or GaAs layer (''GaAs-like'' IF) is formed, the tensile strain in the InAs layers can be compensated by the compressive strain in the InSb layers. Various approaches have been utilised for the insertion of the InSb IF layer between each IF of the SL. One of them is the Sb-for-As exchange shutters method, which involves exposing each SL layer of InAs to Sb soak for a few seconds [75], [141], [232]. Other techniques for the intentional insertion of the InSb layer include the conventional MBE growth procedure in which the In and Sb shutters are turned on at different times [195] and the migration-enhanced epitaxy (MEE) where the In and Sb shutters are opened at the same time [318].

Another challenge with InAs/GaSb T2SL growth is the atomic intermixing at the IF since this material system has no-common atom facilitating the elemental intermixing. The sharpness and atomic intermixing have been active areas of research studies. Various research groups have tried implementing different IF schemes at the SL IFs, including, GaAs-like, InSb-like, or mixed-like IFs. However, the InSb-like IFs appear to be the most widely employed scheme due

to their ability to compensate for the strain. As group-V and group-III are changed at the IFs due to atomic kinetic energy and the effect of growth temperature, there is a possibility for the formation of both GaAs-like and InSb-like IFs. When the GaAs-like IFs are introduced, the average lattice constant of the SL reduces even more, leading to an increase in the tensile strain in the SL. However, when the InSb-like IFs are formed, the SL lattice constant marginally expands, which could partially compensate for the strain in the SL. Therefore, the InSb-like should be efficient for the overall growth of the SL since it can theoretically provide strain compensation leading to enhanced optical quality and improved device performance.

This has motivated the detailed investigation of the effect of implementing the InSb-like IFs on the structural and optical quality of the InAs/GaSb T2SL samples in this work. Herein, the impact of shutter sequence during the growth of InAs/GaSb T2SL samples using two different techniques on the structural, morphological, and optical characteristics are investigated in detail using HR-XRD, AFM, TEM, and PL measurements.

## 5.2    Growth process

Growth of all Ga-based InAs/GaSb T2SL samples described in this research work was performed, at the University of California in Los Angeles (UCLA), on a two-inch p-type (001) oriented GaSb substrate in a Veeco Gen 930 MBE reactor supplied with dual filament SUMO Knudsen effusion cells for Gallium (Ga) and Indium (In) and MARK V valved cracker effusion cells for Arsenic (As) and Antimony (Sb). The growth rates of Ga and In were set to 0.5 and 0.3 ML/s, accordingly. The structure of the samples (Sample A) and (Sample B) comprises a 50 nm thick undoped GaSb buffer layer, followed by 100 pairs of undoped InAs/GaSb T2SL layer and a 4 ML thick undoped GaSb cap layer. The T2SL region consists of 7 MLs of InAs and 4 MLs of GaSb (7/4 MLs InAs/GaSb). The sample structures are schematically depicted in Figure 5.1.
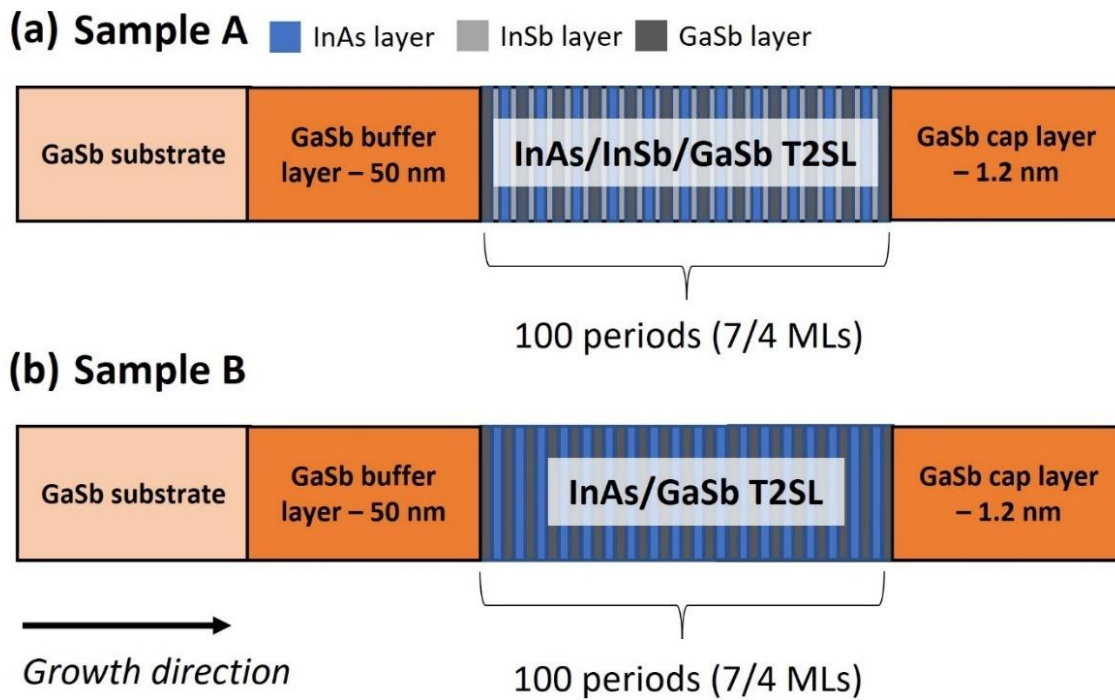
Figure 5.1: Schematic of the sample structures, (a) Sample A and (b) Sample B, using two different techniques.

The shutter sequence procedure utilised during the growth of Samples A and B is shown in Figure 5.2. Note that the Sb flux remained constant during the sample's growth. As seen in Figure 5.2(a), the growth of Sample A was performed by inserting an international InSb IF layer at both SL IFs using the MEE technique. Here, after the growth of the InAs layer, the In shutter was only kept open for 1 second. The In shutter was then turned off, and the Sb shutter was only turned on for 6 seconds to saturate the In surface with Sb. The Ga shutter was then opened to grow the GaSb layer. At the second IF (InAs-on-GaSb IF$_2$), the Sb shutter was opened for additional 6 seconds, and the In shutter was only turned on for another 1 second before the growth of the InAs layer. Sample B was grown differently, with the InAs layer being exposed to an incident Sb flux for 6 seconds to facilitate the Sb-for-As exchange and the formation of InSb bonds at the second IF (the GaSb-on-InAs IF$_1$). Then the Ga shutter was turned on to grow the GaSb layer. Finally, both In and As shutters were kept open to grow the InAs layer, whereas Ga and Sb shutters were turned off at the same time. In this case, the second IF InAs-on-GaSb IF$_2$ was not controlled, as represented in Figure 5.2(b).
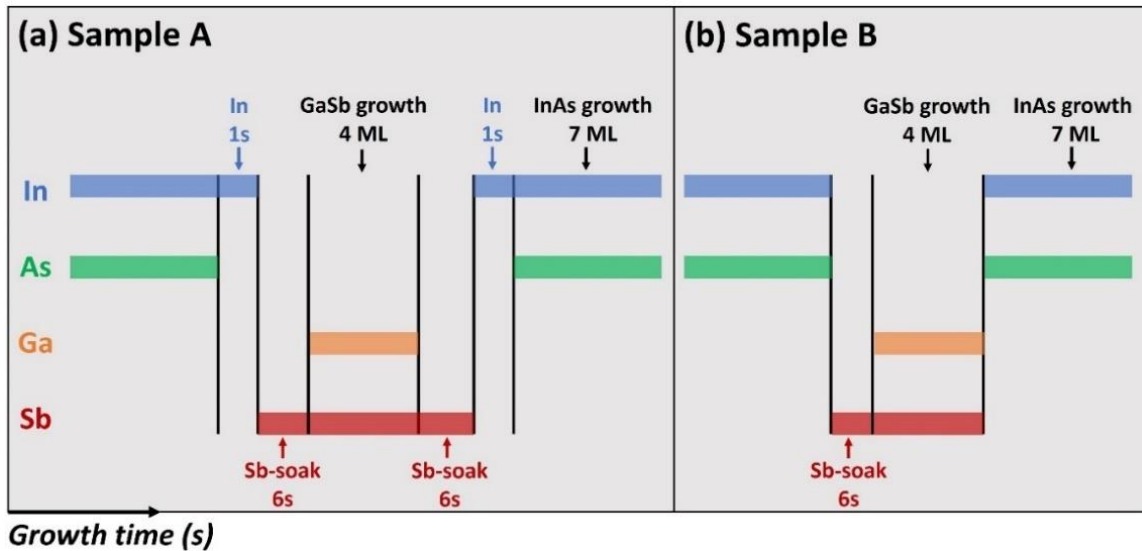
Figure 5.2: Schematic of the shutter sequence during the T2SL growth of Samples A and B.

## 5.3 Material characterisation

Following the growth of the materials, the structural, morphological, and optical quality of the two grown samples is inspected using HR-XRD, AFM, PL, and TEM measurements. Results of material characterisations are provided in the following sections.

### 5.3.1 High-resolution X-ray diffraction

As described previously in Section 4.3.1, HR-XRD is a technical instrument which can be used to characterise the materials and analyse the epitaxial-grown layers. It is utilised to obtain more information about the lattice mismatch, strain effect, composition, and layer thickness determination. In addition, this tool can be used to get information regarding IF roughness and density, which provides a better understanding of the crystalline quality.

Herein, a Bede system was employed to attain HR-XRD ω/2θ scans for the purpose of characterising the grown T2SL Samples A and B. The patterns of the ω/2θ scan around the GaSb (004) reflection for Samples A and B are presented in Figure 5.3. As can be observed, the satellite peaks are sharp, indicating the growth of layers of high crystalline quality, and XRD peaks are visible up to the 2nd-order peaks confirming the growth of periodic superlattice structures. Using Equation (4.4), the strain or lattice mismatch is determined. It is found that the SL layers of Sample A are under a slight compressive strain on the GaSb substrate with a

lattice mismatch (Δa/a) of +0.479%. Although the InSb IF layer was intentionally grown at the SL IFs to achieve a strain-compensated SL, a compressive strain of SL on the GaSb substrate is formed, which is possibly because of the total thick InSb IF layers grown within the SL period. In contrast, a nearly strain-compensated SL layer growth is achieved for Sample B with a lattice mismatch of ~0%. The periodic thickness of the SL was also measured using Equation (4.1). It is found that the periodic thickness is 3.69 and 3.54 nm for Sample A and Sample B, respectively, as shown in Figure 5.4. The difference in the measured thickness of the SL period is due to the deliberate incorporation of InSb IF layers at the SL IFs for Sample A. The measured FWHM at the first order SL satellite peak ($SL_{-1}$) for Sample A and Sample B is approximately 73 and 56 arcsec, respectively, implying that Sample B exhibits a narrower FWHM and suggests a better structural quality than Sample A. Table 5.1 provides a summary of the structural characteristics of Samples A and B.
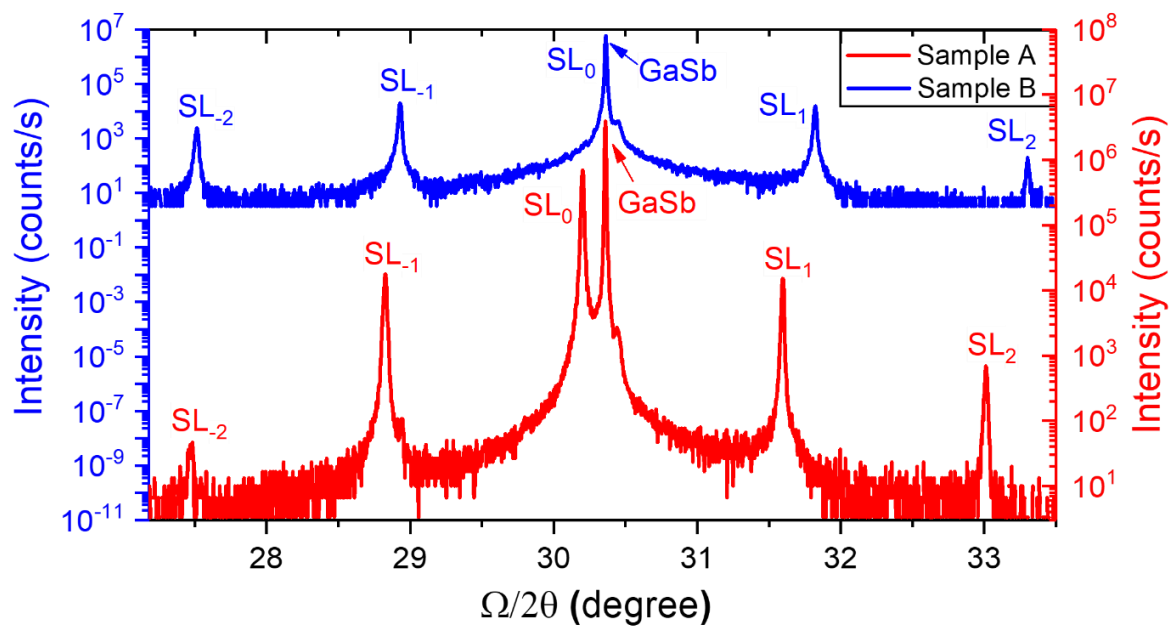


Figure 5.3: XRD spectra of the ω/2θ scan around the GaSb (004) reflection of T2SLs, Sample A and Sample B.
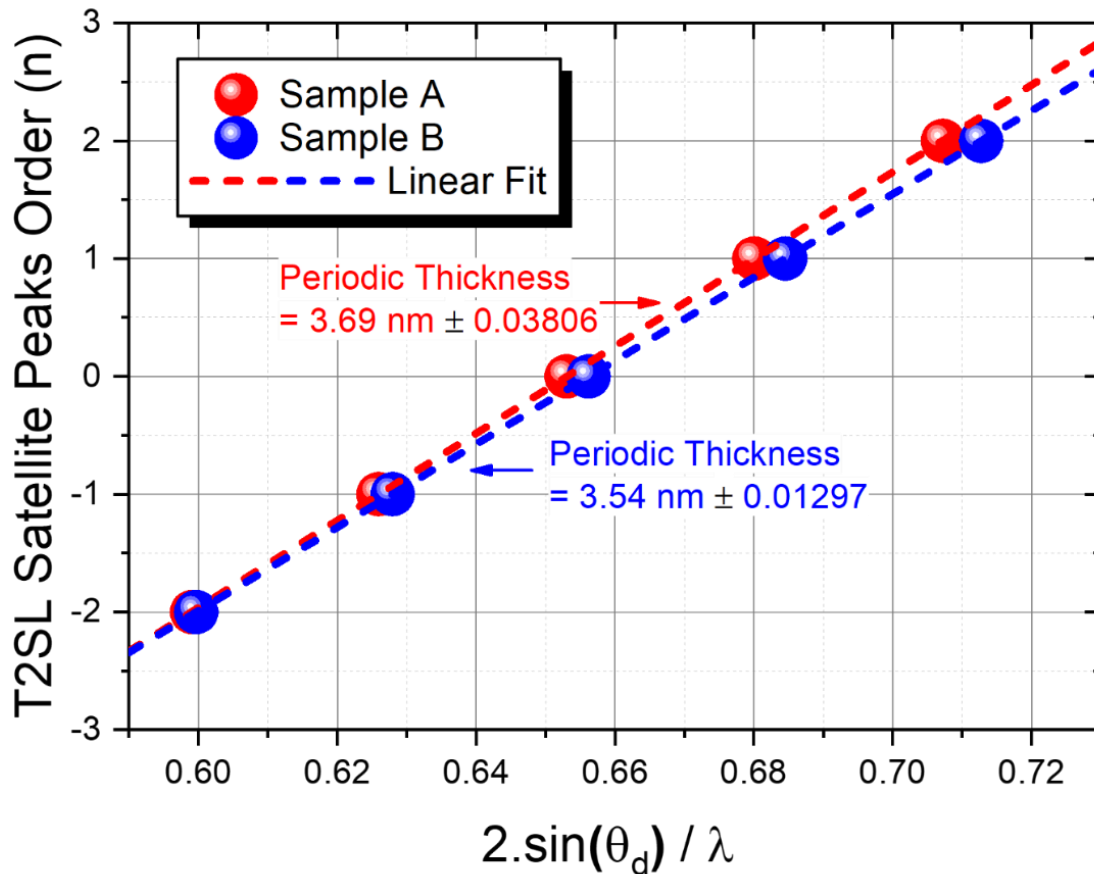
Figure 5.4: Measured T2SLs periodic thickness of Samples A and B from each satellite peaks order (n) versus $2 \sin(\theta_d)/\lambda$.

### 5.3.2 Atomic force microscopy

AFM investigation of the surface morphology of Samples A and B, both scanned over different areas of 2 µm x 2 µm, 4 µm x 4 µm, and 10 µm x 10 µm, are shown in Figure 5.5. The root mean square (RMS) values extracted from the AFM measurements are summarised in Table 5.1. It is observed that the surface roughness is slightly lower for Sample B, suggesting that the surface morphology is relatively smoother than that of Sample A. The AFM characterisation results are consistent with the XRD measurements since the slight mismatch in Sample A may have brought about a minor degradation in material quality, evidenced by slightly larger XRD-FWHM and RMS values as measured by the AFM.

129

## (a) Sample A

2 μm x 2 μm
RMS = 0.209 nm

4 μm x 4 μm
RMS = 0.322 nm

10 μm x 10 μm
RMS = 0.393 nm

## (b) Sample B

2 μm x 2 μm
RMS = 0.193 nm

4 μm x 4 μm
RMS = 0.304 nm
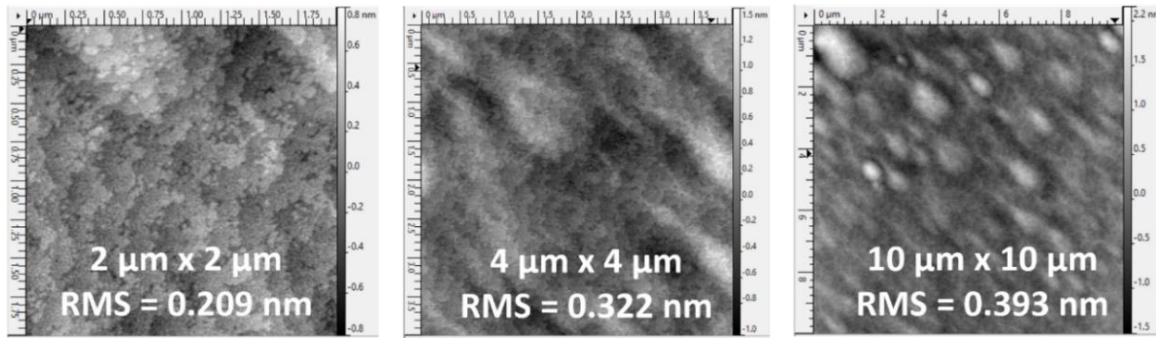
10 μm x 10 μm
RMS = 0.351 nm
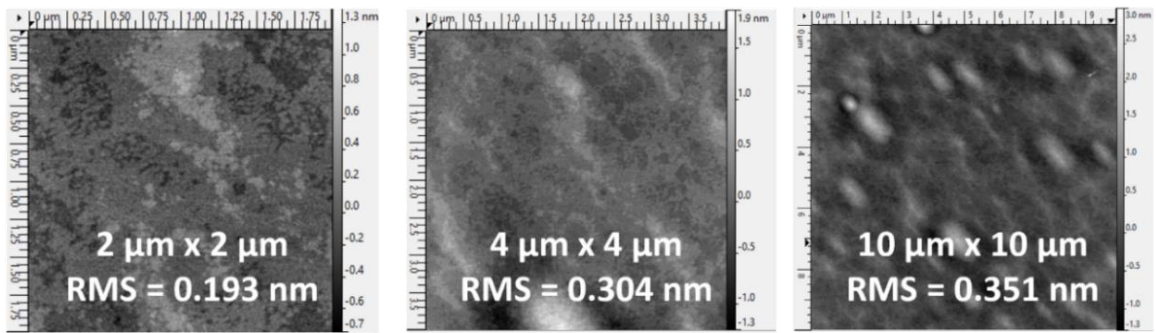
Figure 5.5: AFM measurements scanned over different areas of 2 μm x 2 μm, 4 μm x 4 μm, and 10 μm x 10 μm for (a) Sample A and (b) Sample B.

Table 5.1: A summary of XRD and AFM characteristics of Samples A and B, including lattice mismatch ($\Delta a/a$), full width at half maximum (FWHM), periodic thickness, and root mean square (RMS) values.

| Sample | XRD Characteristics | | | AFM Characteristics | |
|---|---|---|---|---|---|
| | $\Delta a/a$ (%) | FWHM (arcsec) | Periodic thickness (nm) | Scan area ($\mu m^2$) | RMS (nm) |
| Sample A | +0.479 | ~73 | ~3.69 | 2 x 2 | 0.209 ± 0.0001 |
| | | | | 4 x 4 | 0.322 ± 0.0003 |
| | | | | 10 x 10 | 0.393 ± 0.0002 |
| Sample B | ~0 | ~56 | ~3.54 | 2 x 2 | 0.193 ± 0.0003 |
| | | | | 4 x 4 | 0.304 ± 0.0002 |
| | | | | 10 x 10 | 0.351 ± 0.0001 |

### 5.3.3  Photoluminescence

The optical properties of the samples were studied by means of PL measurements. Herein, both temperature and power-dependent characterisation studies were carried out to examine the optical properties of the samples.

#### 5.3.3.1  Temperature-dependent PL measurements

The temperature-dependent PL measurements were carried out to assess the optical quality of Samples A, and B. Herein, PL measurements were undertaken at different temperatures from 77 K to 293 K, and the laser source was fixed to ~50 mW. Figure 5.6(a-b) displays the non-normalised temperature-dependent PL measurements for Samples A and B. As can be seen, a clear PL intensity and dominant PL peak energy were positioned at approximately 5.5 μm (225 meV) and 5.1 μm (243 meV) at 77 K for Samples A and B, respectively. This predominant PL peak energy is related to the SL transition energy from the first electron miniband to the first heavy hole miniband ($e_1$-$hh_1$). It is also clear that Sample A has a stronger PL intensity compared to Sample B, as depicted in Figure 5.6(c), which is possibly due to the intentional incorporation of InSb IF layers (it will be discussed in more detail later). Furthermore, the inclusion of the InSb IF layer, which is a material active in the IR spectrum, still contributes towards a redshift in the optical activity of Sample A, which therefore emits at a longer wavelength compared to Sample B.

It is also visible that the PL peak energy position shifts towards longer wavelengths (lower energy) as the temperature increases. Because of the noise originating from the system during measurements, it is hard to distinguish the peak positions beyond 200 K. For further analysis of the effect of the temperature on PL peak intensity and peak position of the two samples, Figure 5.7 is plotted (The single temperature-dependent PL fittings of Samples A and B are shown in Appendix G). This figure depicts the normalised temperature-dependent PL spectra of both Samples A and B. The dash lines guide the eye drawn to highlight the redshift observed in the PL peak intensity of the two samples. As observed from Figure 5.7, the PL peak position of Sample A is redshifted from 225 to 190 meV, while it is only shifted from 243 to 221 meV for Sample B when temperatures increase from 77 to 293 K.

131
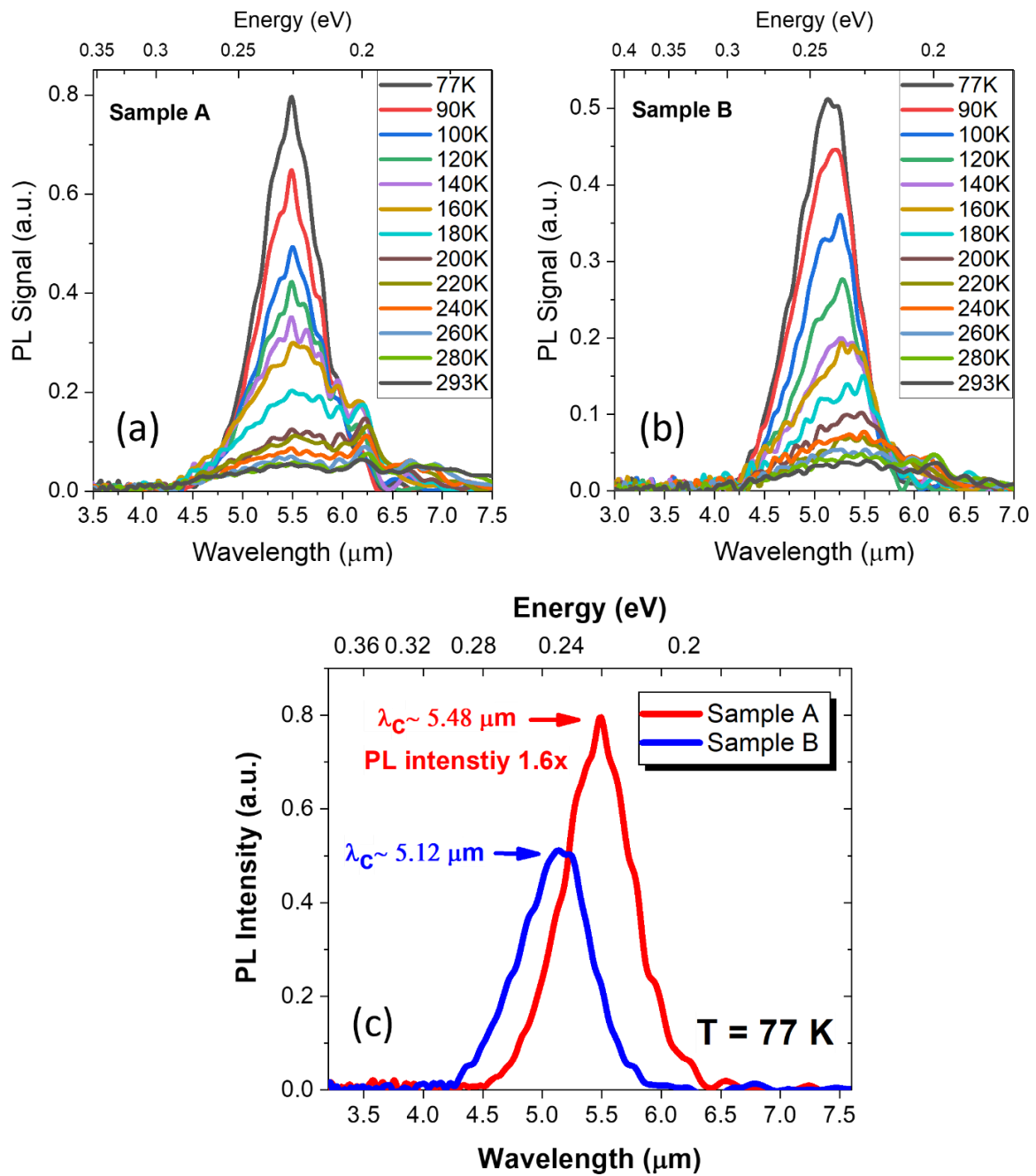
Figure 5.6: (a)-(b) PL measurements undertaken for Sample A and Sample B at different temperatures from 77 to 293 K. (c) A comparison of PL intensity of both samples at 77 K to highlight the PL peak shift and stronger intensity in Sample A.

The observed higher redshift in the PL peak position of Sample A when compared to Sample B is presumably owing to the existence of the overall thick InSb IF layers of Sample A [143], [235] contributing to a reduction in the PL peak energy, which is consistent with a previous report [195].
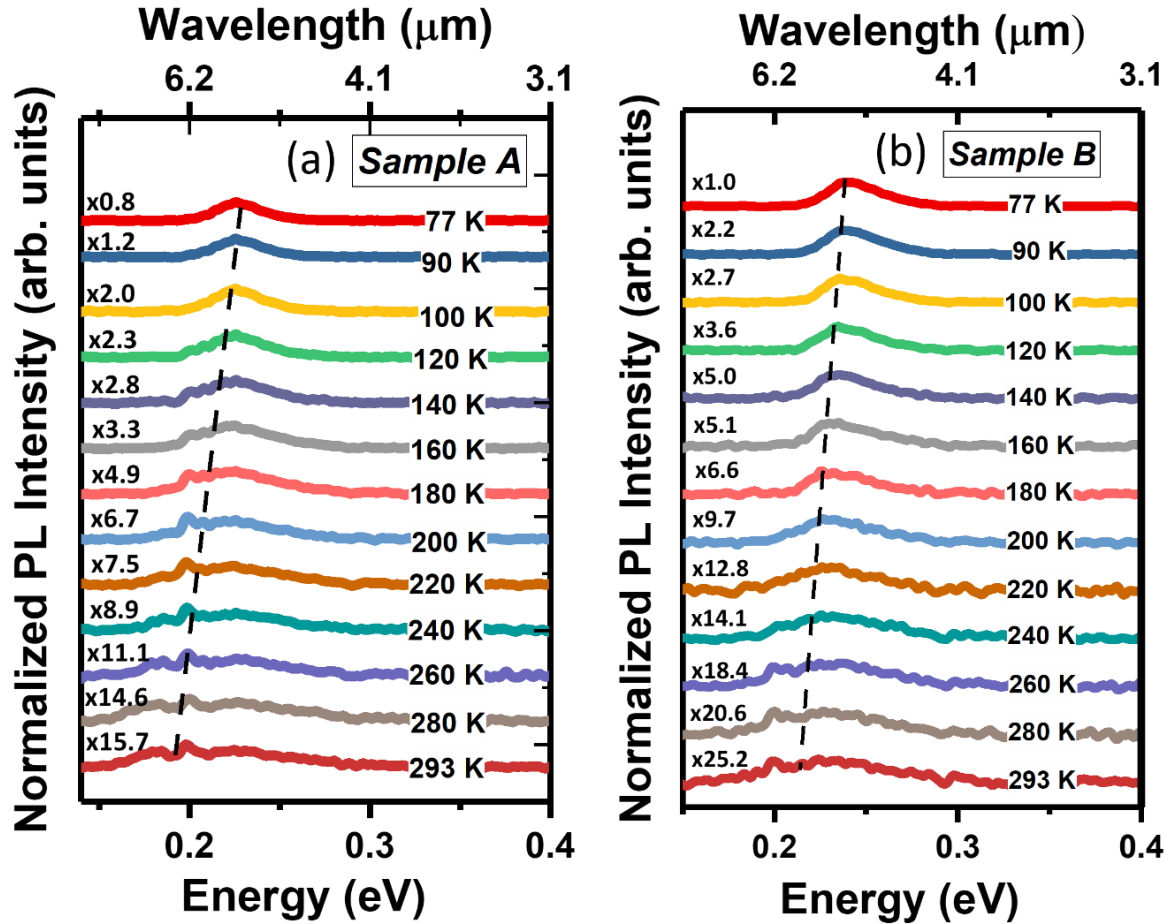
Figure 5.7: Normalised PL spectra versus energy/wavelength at different temperatures from 77 – 293 K of (a) Sample A and (b) Sample B. A dashed guideline is presented in both figures to highlight the shift in the PL peak positions observed from the two samples.

As expected, the PL peak intensity of both samples reduces with increasing temperature from 77 to 293 K, implying the non-radiative recombination may result in strong luminescence quenching [319]. However, in comparison with the rapid thermal quenching of the PL intensity of Sample B, Sample A appears to be less sensitive to temperature variations. It seems that Sample B has a significantly higher thermal quenching rate in the PL intensity than Sample A, with the PL intensity quenched by approximately 1.6x of that in Sample A, confirming the effect of incorporating InSb IF layers at the SL IFs. This, therefore, contributes to minimising the influence of the thermal quenching behaviour of the PL intensity for Sample A. This also demonstrates that a superior optical property of Sample A grown with intentional InSb IF layers at the SL IFs is achieved, which agrees with a previous study [320].

Figure 5.8 depicts the results of a Gaussian fitting analysis employed to derive the integrated PL intensity as a function of temperature. Literature examples of PL signals for T2SLs are shown in Figure B.2 in Appendix B. The thermal quenching of the integrated PL intensity was fitted utilising the non-radiative recombination Arrhenius model [321]:

$$I(T) = \frac{I_0}{1 + A\,e^{\left(\frac{-E_a}{K_B T}\right)}}$$

(5.1)

where $I_0$ is the saturation intensity, $K_B$ is the Boltzmann constant, $A$ is the ratio of non-radiative to radiative recombination probability, and $E_a$ is the activation energy of the non-radiative recombination process. The results are plotted in Figure 5.8, which compares both Samples A and B to a MWIR Ga-free InAs/InAsSb T2SL sample reported in the literature [307], [322]. The Ga-free sample was designed to have a symmetrical layer thickness of 14 nm of InAs and 14 nm of InAsSb with an Sb composition of 13.7%, and it has a cut-off wavelength of around 5.3 μm at 80 K. The fitted parameters are summarised in Table 5.2. The slope gradients are extracted and found to be $3.22 \pm 1.92 \times 10^{-3}$, $3.67 \pm 2.45 \times 10^{-3}$, and $6.00 \pm 7.83 \times 10^{-3}$ for Samples A, B and the Ga-free T2SL respectively. The gradient of the Ga-free T2SL sample is nearly double that of the Ga-containing T2SL Samples A and B for a similar temperature regime, indicating that the two Ga-containing T2SL samples are less responsive to changes in temperature compared to the Ga-free T2SL sample. As previously reported, the high rate of Auger non-radiative recombination may account for the increased sensitivity of the Ga-free T2SL to temperature variations [307].

As seen from Table 5.2, the ratio of non-radiative recombination probability is slightly higher in Sample B compared to Sample A. However, the higher activation energy in Sample A is probably due to the thermal escape energy of excitons from the electron miniband of the SL to the conduction band of the IF InSb layer. This implies that excitons require higher energy to escape from the miniband of the SL to the InSb IF layer in Sample A compared to Sample B, as depicted in Figure 5.9. The extracted activation energies related to the non-radiative recombination process of Sample A is considerably higher $E_a$ (Sample A) = 38.25 meV corresponding to the thermal escape energy of excitons from the electron miniband of the SL to the conduction band of the InSb. Sample B, however, has a relatively lower activation

energy $E_a$ (Sample B) = 28.73 meV, corresponding to the thermal escape energy of excitons from the hole miniband of the SL to the valence band of the GaSb.
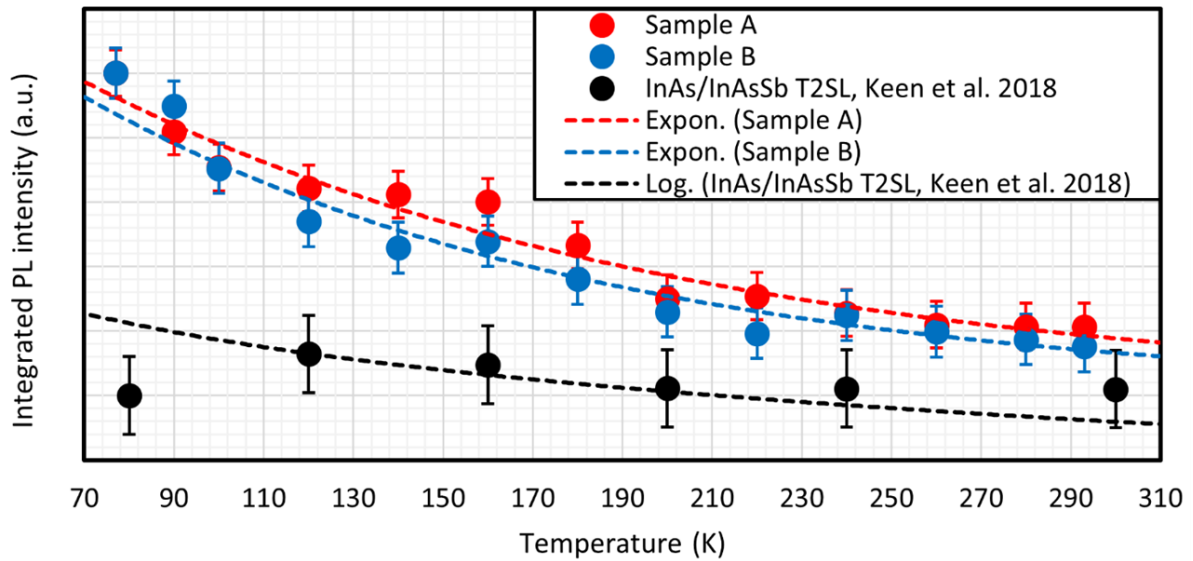


Figure 5.8: Integrated PL intensity as a function of temperature for Samples A and B compared to a MWIR Ga-free InAs/InAsSb T2SL reported in the literature.

Table 5.2: A summary of the parameters extracted from the integrated PL intensity profile.

| Sample | Integrated PL Intensity Parameters | | |
|---|---|---|---|
| | $I_0$ (a.u.) | A (a.u.) | $E_a$ (meV) |
| Sample A | 0.95 ± 0.083 | 15.25 ± 5.974 | 38.25 ± 0.007 |
| Sample B | 1.24 ± 0.166 | 18.32 ± 3.214 | 28.73 ± 0.004 |
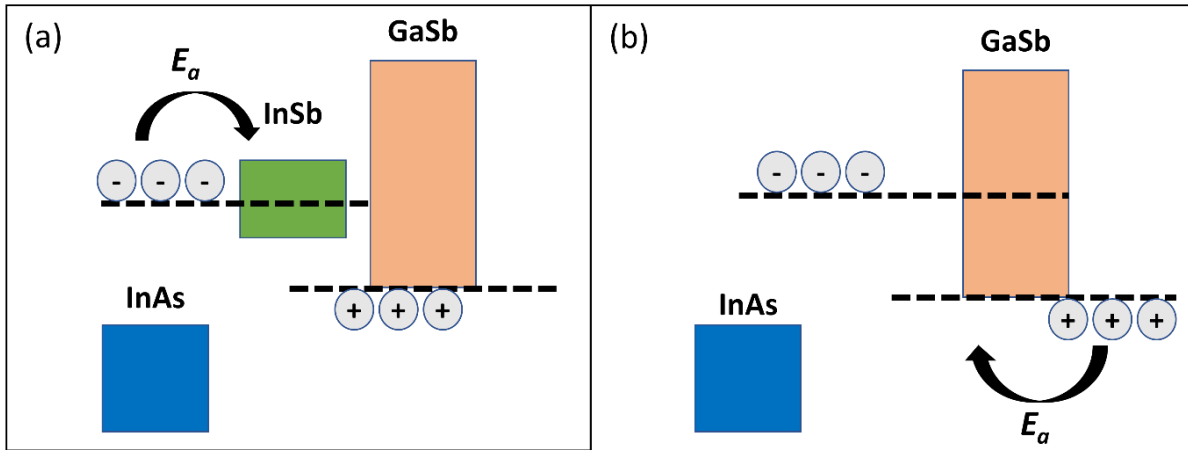
Figure 5.9: Schematic band structures of (a) Sample A with an intentional InSb IF layer at the SL IFs and (b) Sample B without an InSb IF layer.

The temperature-dependent behaviour of the bandgap energy was also fitted utilising the well-known Varshni equation [323]:

$$E_g(\text{T}) = E_g(0\text{ K}) - \frac{\alpha.T^2}{\beta + T}$$

(5.2)

where $E_g(0\text{ K})$ is the bandgap energy at 0 K, $T$ is the temperature, and $\alpha$ and $\beta$ are coefficients and fitting parameters related to the lattice parameter's thermal expansion and Debye temperature, respectively. Here, the value of $\beta$ was 290 and 277 K for Samples A and B, respectively. These $\beta$ values are very close to those reported in the literature [324]. The $\alpha$ values are then found to be 0.162 eV.K$^{-1}$ and 0.171 eV.K$^{-1}$ for Samples A and B, consistent with a previously reported MWIR InAs/GaSb T2SL detector [325]. Figure 5.10 shows the bandgap energy versus temperature for Samples A and B. Sample A is less responsive to temperature variations, which agrees well with what we have found from the normalised PL intensity as a function of bandgap energy in Figure 5.7. A summary of the fitted parameters from the Varshni equation can be found in Table 5.3.
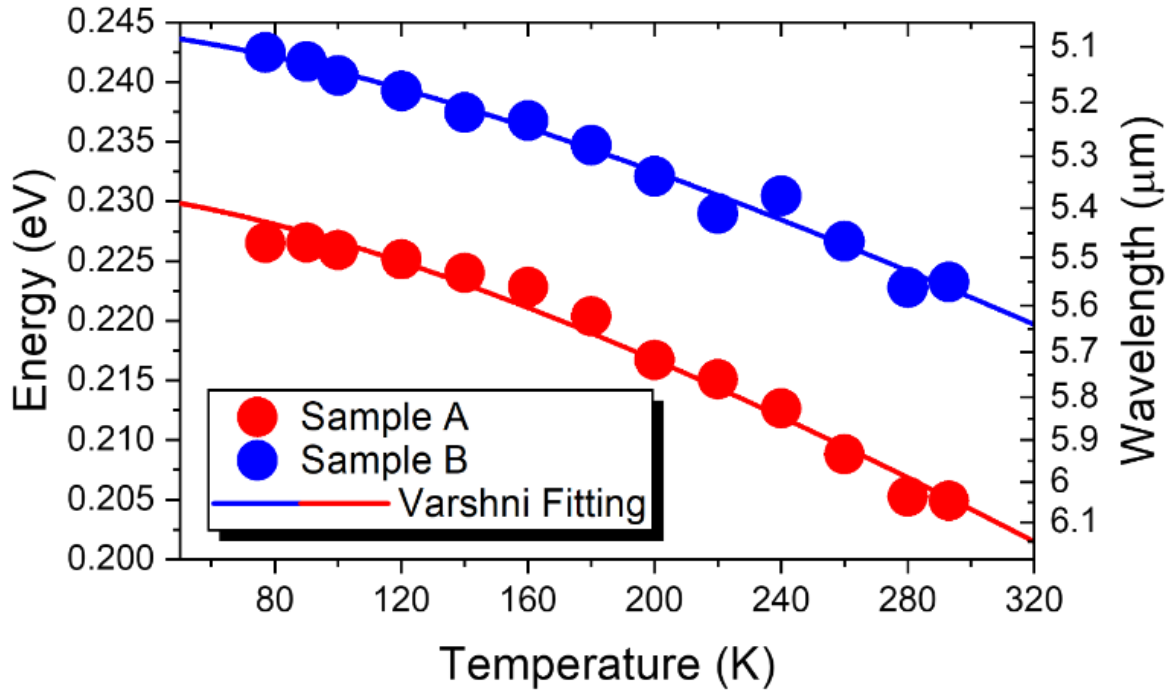
Figure 5.10: Measured bandgap energy versus temperature for Samples A and B. The data were fitted using the Varshni Equation (5.2).

Table 5.3: A summary of the parameters extracted from the fitted data using the Varshni Equation.

| Sample | Maximum PL Intensity (a.u.) | Varshni Parameters | | | |
|---|---|---|---|---|---|
| | | $E_g$ at 0 K (eV) | $\lambda$ at 0 K ($\mu$m) | $\alpha$ (meV/K) | $\beta$ (K) |
| Sample A | 0.795 | 0.231 ± 6.208 | 5.36 | 162 ± 7.229 | 290 ± 0.0 |
| Sample B | 0.511 | 0.244 ± 0.001 | 5.08 | 171 ± 6.237 | 277 ± 0.0 |

Analysis of the FWHM of the PL profile for Samples A and B has also been studied. The FWHM of the PL profile at different temperatures is depicted in Figure 5.11. The FWHM of Sample A is relatively broader compared to that of Sample B, which is attributed to the relatively thick InSb IF layers at the SL IFs. To further analyse these results, the FWHM of the PL profile typically comprises the inhomogeneous part and the temperature homogenous part. The inhomogeneous part is mainly associated with the fluctuations of the QW width, alloy compositions, and IF roughness. The homogeneous part is primarily associated with the

excitons and phonons scattering. The temperature-dependent FWHMs of the samples can be thus modelled by the following expression [326]:

$$\Gamma(T) = \Gamma_i + \frac{\Gamma_c}{e^{\left(\frac{E_{LO}}{K_B T}\right)} - 1} \qquad (5.3)$$

where $\Gamma_i$ is the inhomogeneous broadening of the well width, $\Gamma_c$ is the excitons and phonons coupling strength, $E_{LO}$ is the longitudinal optical phonon energy, and $K_B$ is the Boltzmann constant. It should be noted that the coupling of excitons and the longitudinal optical phonon energy plays an important part in broadening the FWHM. In Figure 5.11, the solid points are the experimental data attained by the Voigt model fitting. The experimental data were fitted using Equation (5.3) and shown as solid line curves. The extracted values of $\Gamma_i$, $\Gamma_c$, and $E_{LO}$ from the fitting are summarised in Table 5.4. As seen from Table 5.4, Sample A has considerably higher fluctuations in the QW width and higher coupling strength of excitons and phonons compared to Sample B. More importantly, the longitudinal optical phonon energy ($E_{LO}$) of both Samples A and B is generally comparable to the reported various binary materials involved in the SLs. It is reported that the $E_{LO}$ values of InSb, GaSb, InAs, and GaAs are 24 meV, 29 meV, 30 meV, and 35 meV, respectively [327]. However, the $E_{Lo}$ values of Sample A appear to be slightly higher (24.36 meV) than that of Sample B (22.85 meV), probably due to the existence of InSb IF layers in Sample A, while Sample B does not contain intentional InSb IFs. $\Gamma_c$ is a characteristic of the excitons and phonons interaction. The interaction of excitons and phonons that influences the PL intensity primarily occurs in the vicinity of the SL IF. Because of the high stress between InSb and SLs, it is more probable that the interfacial phonon mode will increase and that excitons and phonons will interact more strongly. $\Gamma i$ is another important characteristic related to the well width, alloy compositions, and IF roughness which play a key role in the PL FWHM broadening. The fitted values of $\Gamma_i$ for Sample A are slightly higher here than that of Sample B. Therefore, the T2SLs grown without InSb IFs have better lattice and crystalline quality and lower IF roughness, which agrees well with the earlier XRD and AFM measurements. This is also similar to the findings of Wu et al. [328], who found that the T2SLs grown without InSb IFs had better lattice quality than those grown with InSb IFs.
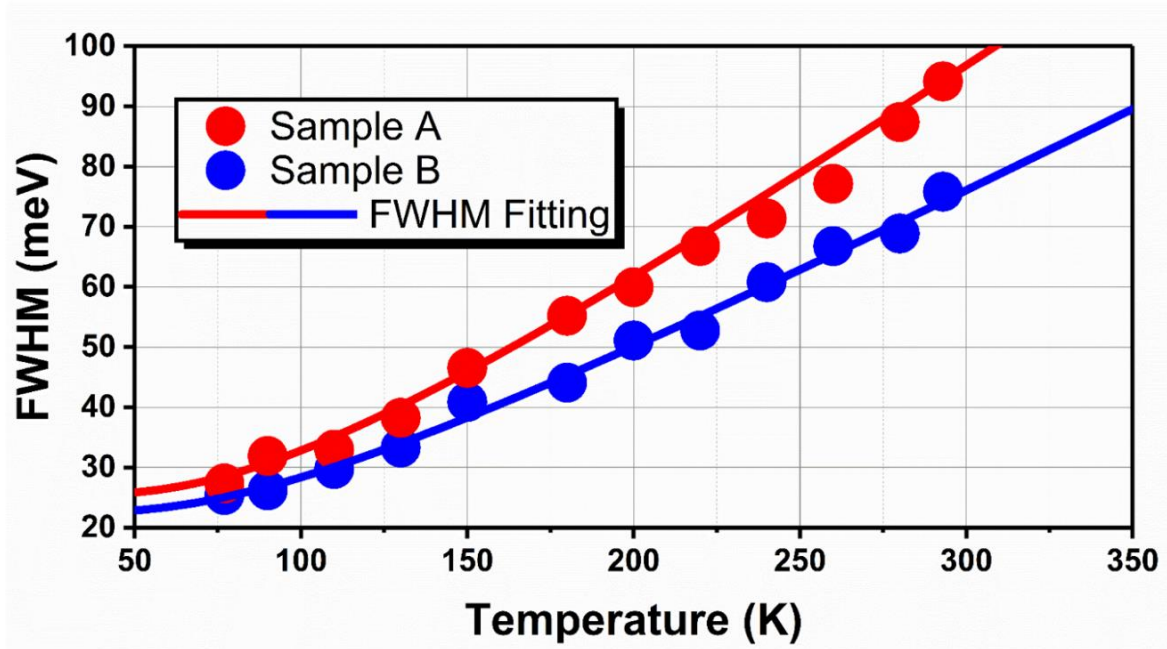
Figure 5.11: Temperature-dependent FWHM of the PL profile of Samples A and B. The solid points are the data attained by the Voigt model fitting, and the solid lines are the fitting curves utilising Equation (5.3).

Table 5.4: A summary of FWHM parameters extracted from the FWHM of the PL spectra.

| Sample | FWHM at 160 K (meV) | FWHM Parameters | | |
|--------|---------------------|-----------------|--------------|------------------|
| | | $\Gamma_i$ (meV) | $\Gamma_c$ (meV) | $E_{LO}$ (meV) |
| Sample A | 49.39 | 25.41 ± 0.002 | 107.56 ± 0.028 | 24.36 ± 0.004 |
| Sample B | 35.90 | 22.54 ± 0.003 | 76.31 ± 0.031 | 22.85 ± 0.002 |

### 5.3.3.2  FITYK analysis of the PL intensity

Figure 5.12 depicts the PL spectra of Samples A and B at 77 K. As can be observed, both samples have shoulders (secondary peaks) around the intense primary emission peak. Using FITYK, an open-source peak fitting software [329], the PL spectra were fitted with seven Gaussian approximations and designated G1, G2, G3, G4, G5, G6, and G7 to determine the origin of these peaks. The strong prominent peak (P1) and the other secondary peaks at higher energies (P2, P3, and P7) and lower energies (P4, P5, and P6) are all assigned. The Gaussian G5, G6, and G7 functions are used to confirm that the observed PL spectra and the generated envelope function are consistent. A literature example of PL fitting to determine the origin of

139

different peaks is shown in Figure B.3 in Appendix B. Table 5.5 provides a summary of the parameters utilised to fit P1, P2, and P3. As can be observed from Figures 5.12(a) and (b), the strongest peak is P1, which corresponds to the first electron and heavy hole miniband transition ($e_1$-$hh_1$) with a FWHM of 27 and 25 meV for Samples A and B, respectively, which agrees with previous works on MWIR InAs/GaSb T2SLs [195], [328].

The maximum PL peak intensity of P1 for Sample A is also observed to be 1.60 times compared to Sample B. It is conceivable that the InSb IF layers of Sample A may have higher As concentrations. Because As has high beam equivalent pressure (BEP), a significant amount of As flux may exist at the growing surface even when the shutter is turned off [203]. As stated by Kim et al. [330], higher As concentrations may result in a more significant lattice disorder. In fact, as inspected by XRD, Sample A has a large compressive strain with a lattice-mismatch with GaSb substrate, which is around +0.479% because of the total thick InSb IF layers. Sample B is almost lattice-matched to the GaSb substrate. As a consequence, it is possible that the greater PL intensity of Sample A is not a result of the higher As concentrations in the InSb IF layers. The T2SL sample grown with InSb IFs employing the MEE technique is known to have stronger luminescence efficiency, which could account for the higher PL peak intensity in Sample A. This is due to the fact that, in the MEE growth mode, cations can migrate longer distances without anions. As a result, the 2-D layer growth mode can be readily obtained more easily [331].

Moreover, a redshift of approximately 15 meV was observed in P1 for Sample A in comparison with Sample B. The origin of the redshift behaviour in P1 for Sample A could be due to the difference in the SL periodic thickness as measured by the XRD (Figure 5.4), a similar phenomenon was also discussed elsewhere [233], or atomic intermixing. This can substantially impact the PL peak energy and the corresponding wavelength. This will be discussed in more detail utilising the TEM measurements in Section 5.3.4 and the band heterostructure simulations in Section 5.4.
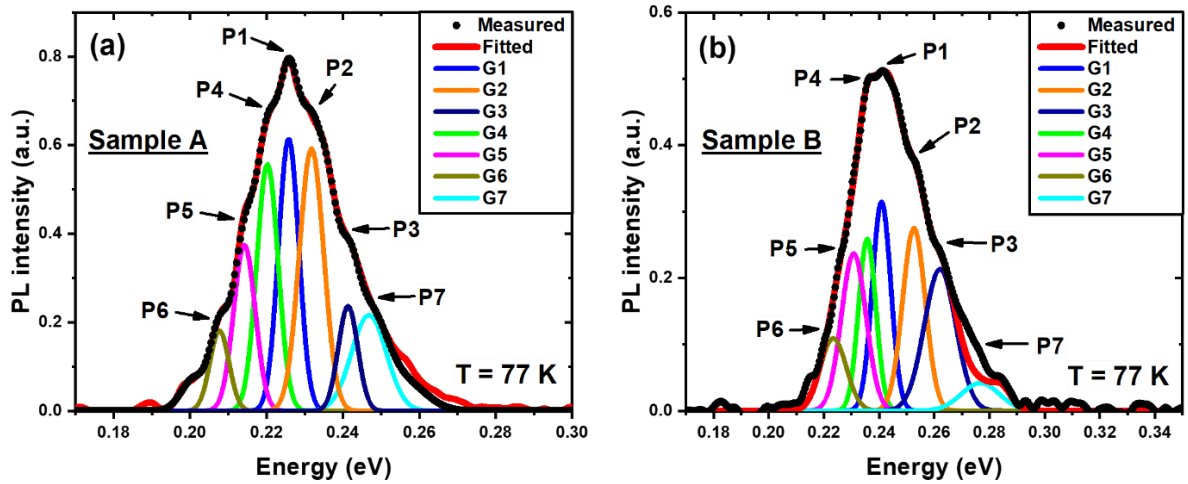
Figure 5.12: PL spectra at 77 K with the Gaussians from P1 to P7 for (a) Sample A and (b) Sample B.

The other secondary peaks (P2 and P3) are not related to the second heavy hole or split-off orbit bands, as these transitions take place at considerably higher energy levels. A possible explanation for the origin of these peaks can be related to Weisbuch et al. [332], who proposed that the creation of one ML thick growth island might be present at the IFs of wells and barriers in the MWQ system, which impacts the confinement energy and, consequently, the PL profile. The presence of growth islands results in uncertainty in the well width, and thus the energy uncertainty for the system can be estimated with the following formula:

$$\Delta E_1 = \Delta L_z \frac{h^2}{4m^* L_z^3} \tag{5.4}$$

where $\Delta E_1$ is the energy uncertainty, $\Delta L_z$ is the well width uncertainty, $h$ is the Planck's constant, $m^*$ is the effective mass, and $L_z$ is the well width. Therefore, taking into account that the well width uncertainty is equal to half of the lattice constant and that the effective mass is a weighted average of the effective masses of the InAs and GaSb, the energy uncertainty is roughly 7.2 meV. Based on this calculation, it appears that the energy uncertainty of the system corresponds well with the differences observed for peaks 1, 2, and 3 (Table 5.5). On average, the energy difference between these peaks is slightly higher in Sample B compared to Sample A, implying that the energy uncertainty is slightly greater for this sample. This is also consistent with the observed XRD peaks, which showed that the overall periodic thickness

and, consequently, the well width are somewhat smaller for Sample B, thereby increasing the energy uncertainty. Moreover, this corresponds well with the results of Ashuach et al. [227] and Kim et al. [220], who observed a significant amount of atomic intermixing and Sb segregation at the IFs of InAs/GaSb T2SLs, particularly with the insertion of InSb IF layer.

The growth temperature is an additional crucial factor that facilitates the diffusion of atoms [79]. Because our InAs/GaSb T2SL samples were grown at a temperature of 410 °C, distributions of In, Ga, and Sb atoms are possible, creating quantum dot (QD) like nanostructures. It has been observed that InGaSb QDs emit at energies comparable to peaks P4-P7, implying the existence of sub-ML QDs at the IFs of the T2SL [333]. Moreover, it has been pointed out that the growth kinetics are favourable for the preferential creation of InGaSb QDs since the diffusion lengths are longer for the In atom compared to the Ga atom.

Table 5.5: A summary of the 77 K PL peak fitting parameters (peak positions, heights, and FWHMs) utilised to fit Gaussian peaks of P1, P2, and P3 for both Samples A and B.

| Sample | Peak Number | Centre (eV) | Height (a.u.) | FWHM (eV) |
|---|---|---|---|---|
| Sample A | P1 | 0.2258 | 0.614 | 0.0273 |
| | P2 | 0.2317 | 0.592 | 0.0075 |
| | P3 | 0.2414 | 0.289 | 0.0066 |
| Sample B | P1 | 0.2408 | 0.314 | 0.0254 |
| | P2 | 0.2526 | 0.275 | 0.0096 |
| | P3 | 0.2620 | 0.213 | 0.0134 |

Figure 5.13(a) and (b) represent the bandgap energy plots as a temperature function for peaks P1, P2, and P3 observed in Samples A and B. The bandgap energy's temperature dependence was determined using the Varshni Equation (5.2). Herein, $\beta$ was also fixed at 270 K, according to previous work [324]. The $\alpha$ values for the prominent peaks P1, P2, and P3 were slightly higher for Sample B when compared to Sample A. Table 5.6 provides a summary of the $\alpha$ values and bandgap energies extracted at 0 K for P1, P2, and P3 for Samples A and B. These $\alpha$

values are comparable to other values reported in the literature [325]. A smaller *α* value implies that the bandgap is less sensitive to changes in temperature, which indicates that Sample A may be ideal for HOT applications [324].
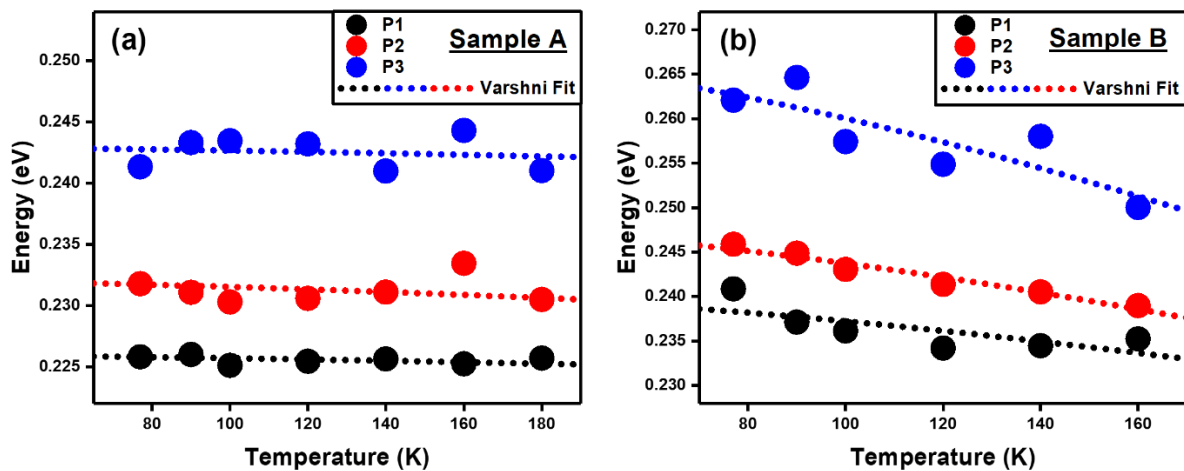


Figure 5.13: The bandgap energy versus temperature and fittings of peaks P1, P2, and P3 for (a) Sample A and (b) Sample B.

Table 5.6: A summary of the α values and bandgap energies derived at 0 K by fittings peaks P1, P2, and P3 to the Varshni Equation.

| Sample | Peak Number | α (eV/K) | $E_g$ at 0 K (eV) |
|---|---|---|---|
| Sample A | P1 | $1.000 \times 10^{-5} \pm 2.985 \times 10^{-5}$ | $0.225 \pm 1.268 \times 10^{-4}$ |
| | P2 | $2.000 \times 10^{-5} \pm 3.463 \times 10^{-5}$ | $0.232 \pm 4.635 \times 10^{-4}$ |
| | P3 | $1.053 \times 10^{-5} \pm 2.968 \times 10^{-5}$ | $0.242 \pm 0.001$ |
| Sample B | P1 | $1.097 \times 10^{-4} \pm 5.258 \times 10^{-5}$ | $0.240 \pm 0.002$ |
| | P2 | $1.588 \times 10^{-4} \pm 1.833 \times 10^{-5}$ | $0.248 \pm 0.006$ |
| | P3 | $2.692 \times 10^{-4} \pm 8.653 \times 10^{-5}$ | $0.267 \pm 0.003$ |

### 5.3.3.3 *Power-dependent PL measurements*

The power-dependent PL measurements were conducted at different excitation laser powers ranging from 10 to 60 mW and at 77 K to investigate the recombination processes that could

occur in the active region of the Ga-containing T2SL samples. Figure 5.14 shows the non-normalised power-dependent PL measurement undertaken for Samples A and B.
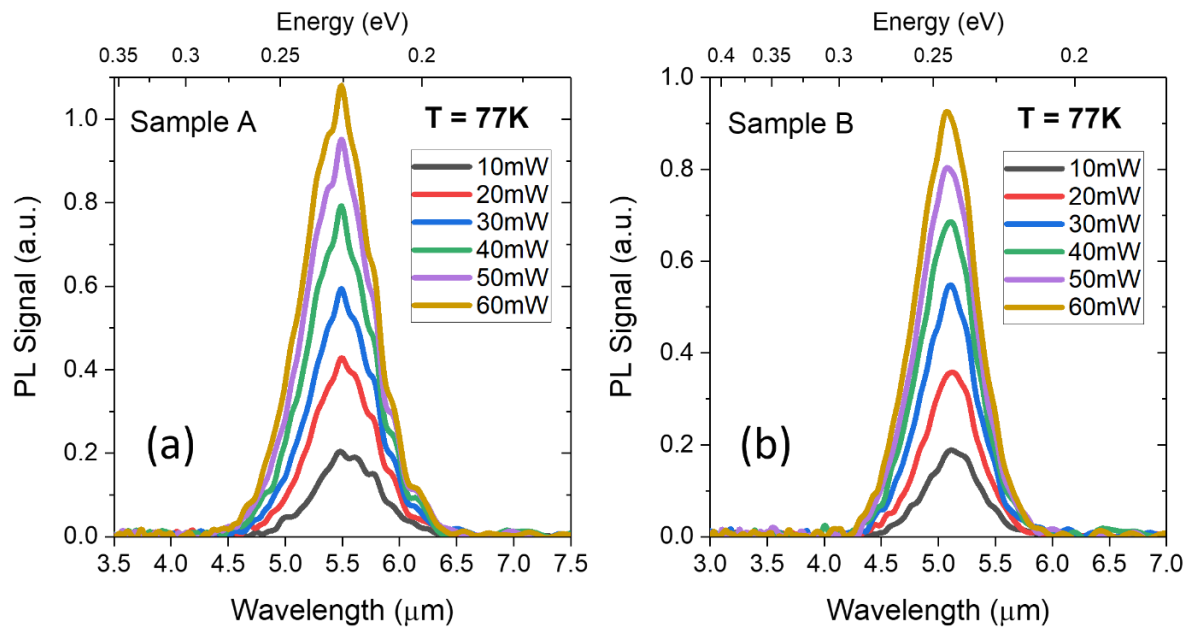


Figure 5.14: non-normalised power-dependent PL spectra undertaken for (a) Sample A and (b) Sample B at different excitation laser power from 10 to 60 mW and 77 K.

Since it is difficult to determine the PL shift from both samples from Figure 5.14, the PL signals were normalised and plotted in Figure 5.15. Herein, after normalisation, it can be observed that both samples exhibit a blue shift in the PL peak, being slightly higher in Sample A when compared to B. By fitting the PL spectra using the Gaussian approximation, the PL peak energy positions, and integrated PL intensity were derived as depicted in Figures 5.16(a) and (b) respectively. As can be observed, the PL peak position of Sample A is blue-shifted from 224.5 meV to 228.3 meV, whereas it is only shifted from 242.4 meV to 245.6 meV when laser power is elevated from 10 to 60 mW at 77 K.

Using the power law relationship $y = a + b.x^c$, the PL peak energy shifting (c) rate was considerably higher for Sample A than for Sample B, as shown in Figure 5.16(a), approximately 271 and 244, respectively. The observed blueshift from both samples could be attributed mainly to the confined carriers' energy shift in the SL's QW [334]. This blueshift behaviour of the power-dependent was also observed from MWIR Ga-free InAs/InAsSb grown on GaSb and Si substrates [211], [335] and Ga-based InAs/GaSb T2SL photodiodes on GaAs and Si substrates [245], [336].
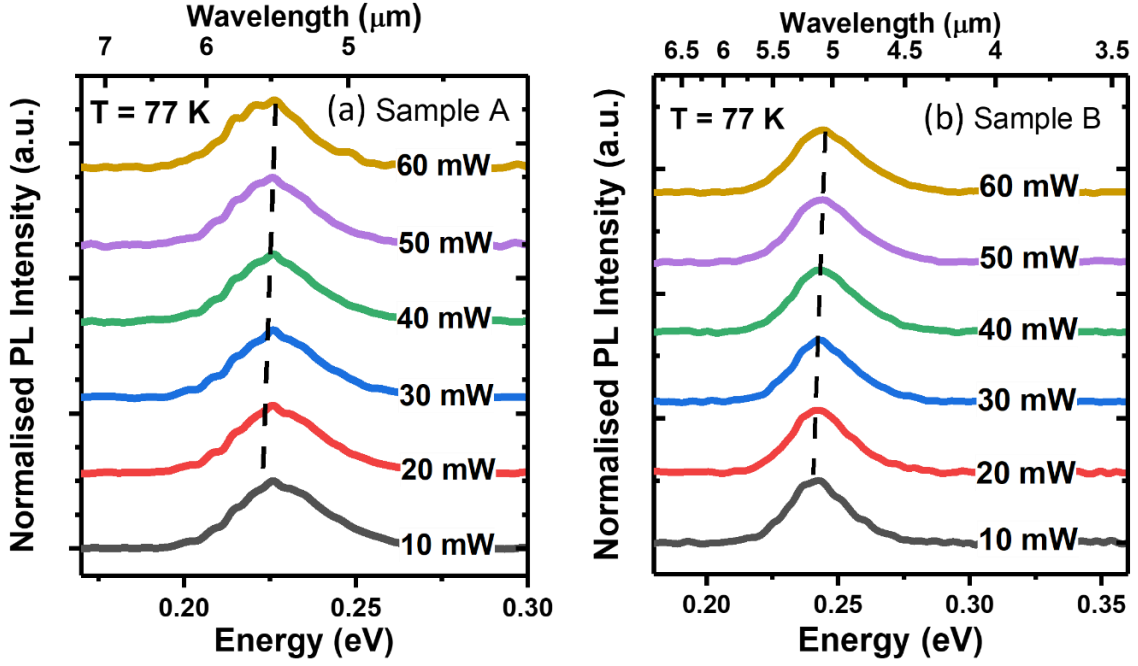
Figure 5.15: Normalised power-dependent PL spectra for (a) Sample A and (b) Sample B. The dash lines are a guideline for eyes to highlight the blue shift observed from both samples as laser excitation power increases.

Lastly, to determine the recombination process occurring in the T2SL region, the integrated PL intensity analysis versus laser power was performed and plotted in Figure 5.16(b) using the power law relationship [337]:

$$I_{PL} = a \, P^{\beta} \qquad\qquad (5.5)$$

where $I_{PL}$ is the integrated PL intensity, $a$ is a constant, $P$ is the laser excitation power, and $\beta$ is the gradient of the slope. The dominant recombination mechanism that occurs in the T2SL active region determines the $\beta$ coefficients. This means that if the extracted $\beta$ coefficient is close to 0.5, then the SRH non-radiative recombination is the main contribution of the recombination mechanism; the $\beta$ value close to 1 indicates that the radiative recombination mechanism is dominant; a value close to 1.5 indicates that the Auger non-radiative recombination dominates the recombination process. Consequently, by fitting the PL peak intensities using Equation (5.5), the extracted $\beta$ values were determined and found to be 0.997 ± 0.027 and 0.942 ± 0.024 for Samples A and B, respectively, as shown in Figure 5.16(b). This result indicates that radiative recombination is the predominant process for both Samples A

and B, which also agrees well with the earlier AFM and temperature-dependent PL spectroscopy observations. This also suggests that Sample A has a superior optical quality compared to Sample B because of the intended incorporation of InSb IF layers at the SL IFs. Interestingly, this result is also well consistent with what was discovered in the temperature-dependent PL investigation, where Sample A appeared to be less sensitive to temperature variations than Sample B. Therefore, these findings suggest that further TEM inspection is required to fully understand the influence of the IF layer incorporation on the optical activity of the samples.
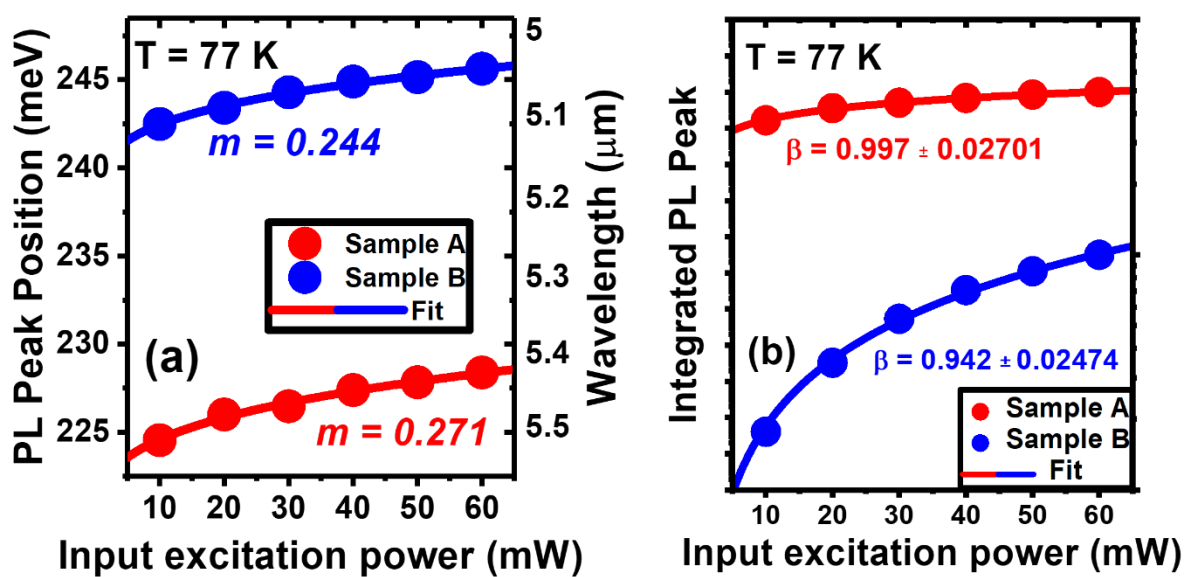


Figure 5.16: (a) PL peak energy and corresponding wavelength positions versus laser power and (b) integrated PL peak intensity versus laser excitation power, and the data fit was implemented to extract the dominant recombination mechanisms for Samples A and B.

### 5.3.4 Transmission electron microscopy

TEM is a useful method for comprehending the behaviour of the samples described in this study because it permits the observation of their nanoscale characteristics and relates them to their macroscopic behaviour. Hence, scanning transmission electron microscopy (STEM) is utilised in this research to investigate atomic intermixing and segregation phenomena in Samples A and B.

Figures 5.17(a-c) and (d-f), respectively, show typical TEM micrographs and selected area electron diffraction (SAED) patterns for both Samples A and B, revealing the crystallinity of the heterostructures at the microscopic scale. The TEM pictures in Figures 5.17(a) and (d) demonstrate that the T2SLs have a homogenous morphology in both samples. A sharp transition from the GaSb buffer to the SLs is also present, which will be validated later by the compositional analysis study of these samples. All the micrographs and diffractograms shown in Figure 5.17 were acquired after tilting the TEM preparations so that one <110> zone axis of the GaSb buffer is parallel to the observing direction. Figures 5.17(b) and (e), which depict SAED patterns acquired around the GaSb region after reaching the zone axis, can be used to confirm this. The observation of cubic materials along this direction is distinguished by the detection of a rhombus-shaped arrangement of reflections, the (002) plane of which can be readily identified in one of the corners for both Samples A and B. Notably, the size of the circles contained in Figures 5.17(a) and (d), implying the approximate areas where the patterns were registered, is not wholly reflective of the real size of the apertures used (they were always the same size). They are only included as an indication of which materials contribute to each pattern. In any case, two noteworthy conclusions can be drawn from these diffractograms. Firstly, both SLs are single-crystalline, as only ordered arrangements of bright reflections can be observed. Secondly, their reflections are structured similarly to those of GaSb when both materials are viewed under identical tilting conditions, verifying that they are epitaxially formed in relation to the buffer layer. Therefore, the following epitaxial relations can be identified in both samples: T2SL [110] || GaSb [110] and T2SL [002] || GaSb [002]. In addition, upon closer inspection of the SL patterns, it is possible to identify a few minor reflections aligned in the direction of growth relative to the brightest ones. Figures 5.17(c) and (f) illustrate and magnify two examples. These reflections are satellite spots, which corroborate the existence of long-period SLs in the context of these systems. As a result, the SL components (for example, InAs or GaSb) contribute to the diffractograms with their own reflection arrangements.
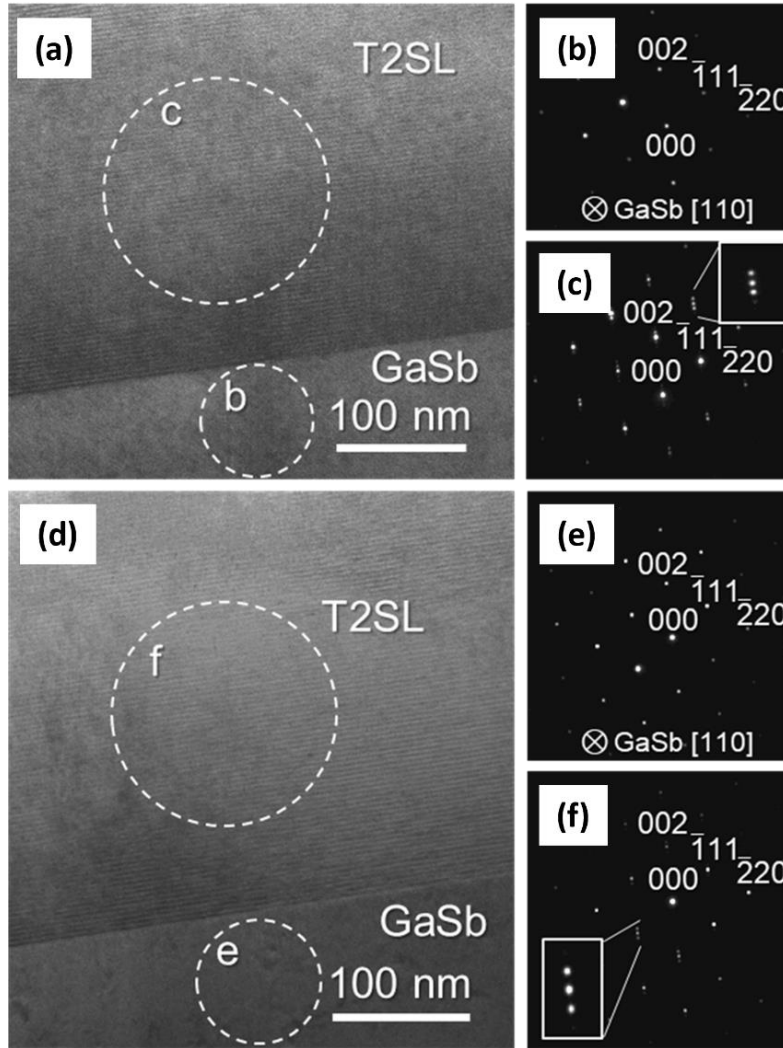
Figure 5.17: In Sample A (a-c) and Sample B (d-f), TEM micrographs were obtained along the [110] GaSb zone axis, as well as SAED patterns from the GaSb buffer and the T2SL.

The SLs were then examined under higher magnification using high-resolution TEM (HR-TEM). Figures 5.18(a) and (b) present two HR-TEM micrographs of the initial layers of the T2SL from Samples A and B, respectively. Some differences between the samples are visible at this magnification and warrant discussion. First of all, although both InAs and GaSb can be identified as the primary constituents in the micrographs of both samples (namely, bright and dark films, correspondingly), the layers in Sample A appear somewhat rougher along their IFs compared to those in Sample B. This observation is consistent with the prior AFM measurements of these samples (shown in Figure 5.5), which demonstrated that the T2SL without deliberate incorporation of InSb IF layers (Sample B) showed to some extent smoother surface compared to the SL with intended InSb IF layers (Sample A). Moreover, the thickness

of each InAs/GaSb period varies between samples. After measuring the GaSb buffer along the [002] direction as a reference and presuming that this material is strain-free ($a_0$ = 6.0959 Å) [278], the lattice spacing for the (002) plane is determined to be 3.048 Å. In these images, the difference with this value along the same direction (measurements not shown) is less than 0.1 Å. As a result, it is reasonable to infer that the period thickness measurements, rounded in Figures 5.18(a) and (b), are accurate enough to conclude that the T2SL in Sample A is generally thicker than that in Sample B. The period thickness values can be determined by dividing the distances shown in both figures by the number of complete SL periods in the yellow rectangles. These distances are calculated using broad intensity derived from rectangle-bounded regions. The number of complete periods is equal to 11 and 9, respectively, for Figures 5.18(a) and (b). This is the maximum number of complete periods conceivable in these micrographs without affecting the accuracy of the intensity profiles and taking into account the limited field of view that such local pictures currently have. Simultaneously, the inaccuracy in averaging the SL period is decreased by a factor of approximately ten in both samples. Thus, after rounding, the resulting average period thickness values for Samples A and B are 3.73 and 3.43 nm, respectively. This trend is consistent with the period thickness values measured earlier (3.69 and 3.54 nm for Samples A and B, respectively, shown in Figure 5.4) and can be explained by the deliberate incorporation of InSb at both IFs of Sample A. Therefore, the average period thickness is greater in this sample than in Sample B, which would be approximately 3.3 nm for a 7/4 InAs/GaSb SL (presuming a single ML would be approximately 0.3 nm thick). For the current study, these HR-TEM measurements disclose apparently coherent thickness values; however, Sample A allows us to conclude that the InSb IF layers must be thicker than anticipated, a feature also noted in the past [235], [338]. Therefore, this excessively thick InSb IF layer appeared to have slightly roughening of the IFs in Sample A and, consequently, a minor reduction in crystalline quality and increased strain [235]. To achieve a lattice-matched InAs/GaSb SL, it is essential to control the thickness of the InSb layer since it is known that progressively thicker InSb IF layers can aid in reducing the lattice mismatch [226]. However, excessively thick InSb IF layers can lead to reduced structural qualities and increased roughness [195], which seems to be the case in Sample A. In contrast, Sample B exhibits sharper transitions between layers and smoother IFs, which will be verified momentarily by the chemical characterisation of these samples. However, it is plausible to hypothesise that some of the rougher areas of Sample A may be associated with

subnanometer regions involving the earlier stated sub-ML QDs. As shown in Figure 5.18(b), these hints are simpler to identify in Sample B due to the deposited smoother layers, which permit the identification of a few short atomic rows at random locations along the IFs. Figure 5.18(a) depicts characteristics that are comparable to those of Sample A. Although it is more difficult to draw definitive conclusions in this instance due to the increased roughness of the SL, the resolution of the available images allows us to measure InAs, InSb, or GaSb. In this regard, a comprehensive characterisation of these sub-ML characteristics is beyond the scope of this research at the present time. Here, at least, we are able to discern local thickness changes in both samples that may be associated with the real presence of nanostructures. Nevertheless, based on the earlier XRD results and analyses (Figures 5.3 and 5.4), it is acceptable to presume that Sample A does not exhibit any substantial variations in material property. In fact, those analyses revealed that the insertion of the InSb IF layers at both IFs resulted in an increase in compressive strain; however, the material degradation was not as pronounced when considering this result alongside others (such as those obtained by PL spectroscopy or AFM measurements) and comparing them to those from Sample B. The FFTs (not shown here) of the regions shown in this figure illustrate the validity of these observations because they enable us to observe the typical behaviour of a properly grown long-period SL that was previously observed by SAED (Figures 5.17(c) and (f)), despite the fact that, based on the comparison of the HR-TEM micrographs of Figure 5.18, Sample A would have a significantly more defective structure compared to Sample B. As a result, in light of the above findings, it is feasible to conclude that the difference in structural properties between these samples is negligible from a structural perspective and in accordance with the aforementioned research. Nevertheless, the addition of the InSb IF layer, which is an IR active material, still contributes toward a redshift in the optical activity of Sample A, which thus emits at a longer wavelength than Sample B. However, its thickness seems insufficient to motivate a significant reduction in crystallinity in Sample A, which was subjected to a substantial compressive strain. At the same time, Sample B was discovered to be nearly lattice-matched despite the absence of intentional InSb at both IFs. This can be explained by the fact that the Sb-soak method chosen for this particular system was suitable, as soaking with this element can also result in a non-zero strain status in other instances [339], which can also occur if InSb is deposited adequately at both IFs [229]. As a result, it is concluded that the growth conditions in Sample A must have been close to optimal to produce a lattice-matched

InAs/InSb/GaSb/InSb T2SL with IR spectrum activity, and this is reflected in the reduced crystalline quality observed at the nanoscopic scale. In addition, it is worth commenting that these results concur with the observations previously reported in this work. Specifically, whereas Sample A reveals enhanced lattice disorder due to AFM-observed characteristics such as higher surface roughness, no lattice defects exist in substantial density throughout its structure, as seen in Figure 5.17. Thus, the increased optical response of Sample A seems to be caused by the presence of atomic intermixing phenomena, as there is no excessive density of nonradiative recombination centres, as Figure 5.17 demonstrates.
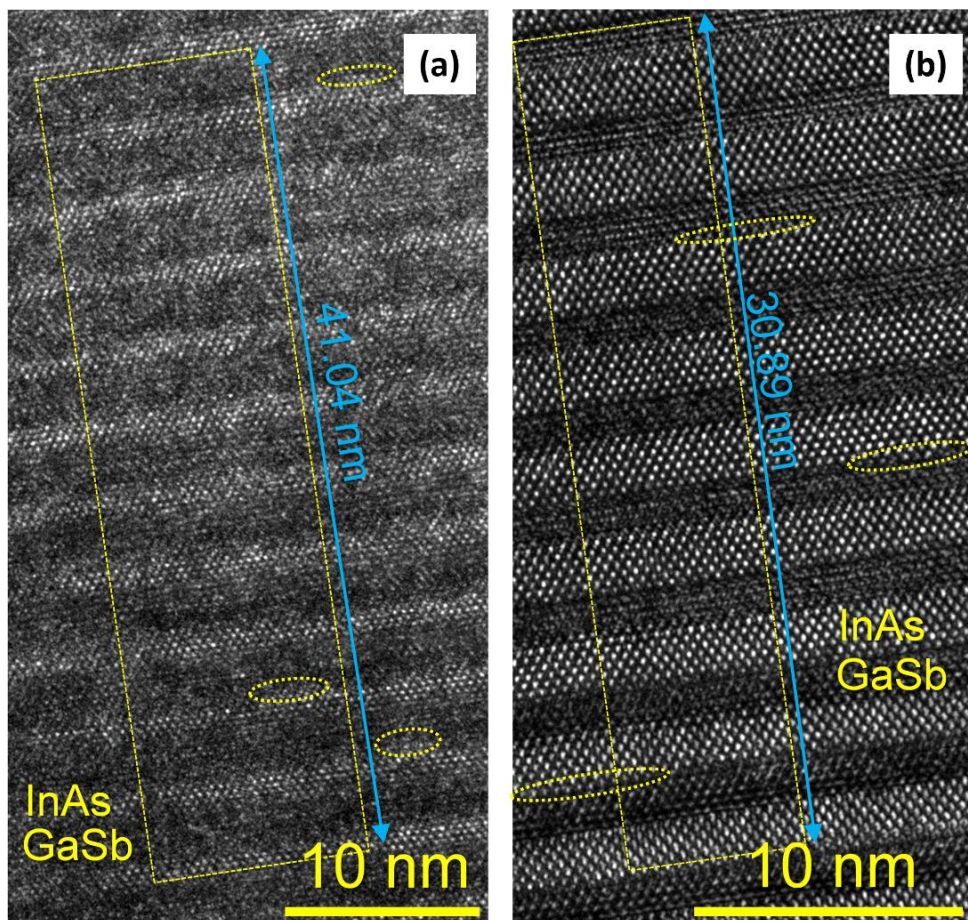


Figure 5.18: HR-TEM micrographs obtained along the [110] GaSb zone axis from about the first bilayers of the T2SL in Samples A (a) and B (b), marked with dotted circles regions with potential sub-ML QDs. The yellow rectangles represent the area across which the SL periods were averaged.

EDX spectroscopy was employed to analyse the composition of these samples at this scale. Figure 5.19 depicts the main results acquired after characterising both Samples A and B. This figure is organised as follows. Firstly, Figures 5.19(a) and (g) display bright-field scanning transmission electron microscopy (BF-STEM) micrographs collected at the T2SL/GaSb region

of each sample. These micrographs already enable us to differentiate atomic columns from the various materials that comprise the heterostructures, and the interpretation of the contrast in the SLs is the same as in the HR-TEM images (namely, brighter layers are InAs, and darker layers are GaSb). The regions shown in these images were scanned by EDX to produce compositional maps, which are depicted in Figures 5.19(b) and (h) for each sample. These maps comprise the mixed signal of the four constituents that were accounted for quantification in these regions: In (green, Figures 5.19(c) and (i)), As (blue, Figures 5.19(d) and (j)), Ga (red, Figures 5.19(e) and (k)), Sb (yellow, Figures 5.19(f) and (l)). These maps indicate the atomic percentage of the represented elements. The combined maps of Figures 5.19(b) and (h) consist of two rectangles with an arrow. The EDX mapping studies within these areas were stable enough (no significant drift or STEM probe contamination issues) to consistently derive integrated atomic percentage profiles along the growth direction beginning with the GaSb buffer. The results are depicted in Figures 5.19(m) and (n) for Samples A and B, respectively. The integrated signal of all the pixels in each segment of these rectangle-shaped regions is represented by one point in each profile, providing a more precise measurement of the areas under investigation. It is worth remarking that further measurements of the periods of both SLs were conducted in Figures 5.19(a) and (g) to verify the consistency of the prior HR-TEM findings. Herein, by employing the EDX maps as guides, up to six complete SL periods could be fitted inside the yellow rectangles roughly included in each micrograph to attain (using the same calculations as in Figure 5.18) average period rounded values of 3.80 and 3.54 nm for Samples A and B, correspondingly, which corroborate the validity of the earlier experiments. Both micrographs, maps, and profiles enable identifying the stacking material sequences predicted in each sample. Nonetheless, comparing Samples A and B in this context shows some other distinctions regarding their compositional behaviour. Firstly, the four constituents of interest appear to be generally more dispersed across the T2SL in Sample A because each map includes more diffuse signals compared to those in Sample B. This property is further reinforced in the case of In and Sb by the deliberate incorporation of InSb IF layers in this sample, which would therefore spread out In/Sb signals across the T2SL. Regarding Ga and As (although this characteristic would also include In and Sb), their evidently more dispersed existence across Sample A may be explained by contemplating the significantly rougher interfacial layers in this sample. This characteristic may have resulted in material projections along the observation direction, implying that contributions from any of these

components are more probable at the IFs. The occurrence of this phenomenon might be explained by supposing that when the STEM probe reaches the components in these areas and scans the next layer, the intensity signals for all of the elements in these regions decline and rise more gently than in Sample B. As a result, there would seem to be compositional differences in the areas across subsequent layers. Nevertheless, given the findings presented so far (specifically, PL and HR-TEM), it is more logical to assume that these apparently roughness-related projections are mostly connected to the presence of compositional variations at the IFs (namely, via intermixing effects). In any case, when the combined maps (namely, Figures 5.19(b) and (h)) are compared again, it is plausible to conclude that, aside from this topic and taking into account both the existence of the InSb layers and the primary qualitative value of these EDX maps, the chemical composition of both SLs is comparable. Although the IFs in Sample B are sharper and the elemental distributions appear more uniform, the similarity in the composition profiles of both heterostructures agrees with the other findings provided in this study and helps to clarify the discrepancies identified between the samples. For instance, the existence of InSb is verified in Sample A, which explicates the redshift in its optical activity, as measured by the PL spectroscopy depicted in Figure 5.6(c), as well as the higher degree of intermixing found along the IFs in the current STEM study. In contrast, although Sample B has sharper IFs and a SL with somewhat superior structural quality compared to Sample A, it is noteworthy that one of the IFs (namely, InAs-on-GaSb) was not regulated during the epitaxial growth. As a result, intermixing occurrences at that IFs are more possible, though, as Figure 5.19 indicates, such difficulties appear to have occurred more often in Sample A. Despite the fact that covering both IFs of the SL with InSb may alleviate In/Sb segregation, provided a proper shutter sequencing is chosen [229]. Our findings are consistent with previous studies in which the use of InSb resulted in greater intermixing occurrences. In Sample B, given that the IF mentioned above is more likely to demonstrate more extended intermixing occurrences compared to the GaSb-on-InAs IF in line with a previous report [79] (although it is worth remarking that the other IF can also be the most intermixed one) [221], one would assume that Sample B is more likely to be influenced by this phenomenon at least in one IF than Sample A, although Sample A is more commonly impacted by these compositional heterogeneities. In any case, the purpose of potential future experiments is to examine these IFs under a higher magnification to verify these hypotheses in greater detail. Nonetheless, it is worth remarking that Figures 5.19(m) and (n) show the

variations in growth strategies used for each sample. First, as shown in Figure 5.19(m), for Sample A, In/As and Ga/Sb peaks are distributed reasonably symmetrically along the growth direction with respect to their maxima and minima, as expected given the deposition process used for this SL (namely, GaSb/InSb/InAs/InSb). In contrast, in Sample B, as depicted in Figure 5.19(n), the In peaks are somewhat shifted to the right relative to the As peaks, indicating that the GaSb-on-InAs IF contains more In, which seems to coincide with the Sb-for-As exchange growth strategy chosen for this SL. In any case, the lack of control over the growth of one IF in Sample B indicates that there is a greater possibility of other interfacial constituents forming between InAs and GaSb as a consequence of intermixing, a problem that has been previously observed and examined in InAs/GaSb SLs grown in dissimilar configurations and that may provide certain benefits (for example, the modification of bandgap energy, as Sample A demonstrates) [79], [219], [225], [340]. Given our earlier results, these intermixing phenomena are not predicted to occur extensively across either IF of Sample B's heterostructure compared to Sample A. However, it is acceptable to assume that the possible occurrence of this problem in certain areas of the SL cannot be fully ignored. As a result, it is possible to conclude that Samples A and B have extremely comparable qualities in the end. Still, the former has the additional benefit of displaying optical activity at a longer wavelength than the latter.
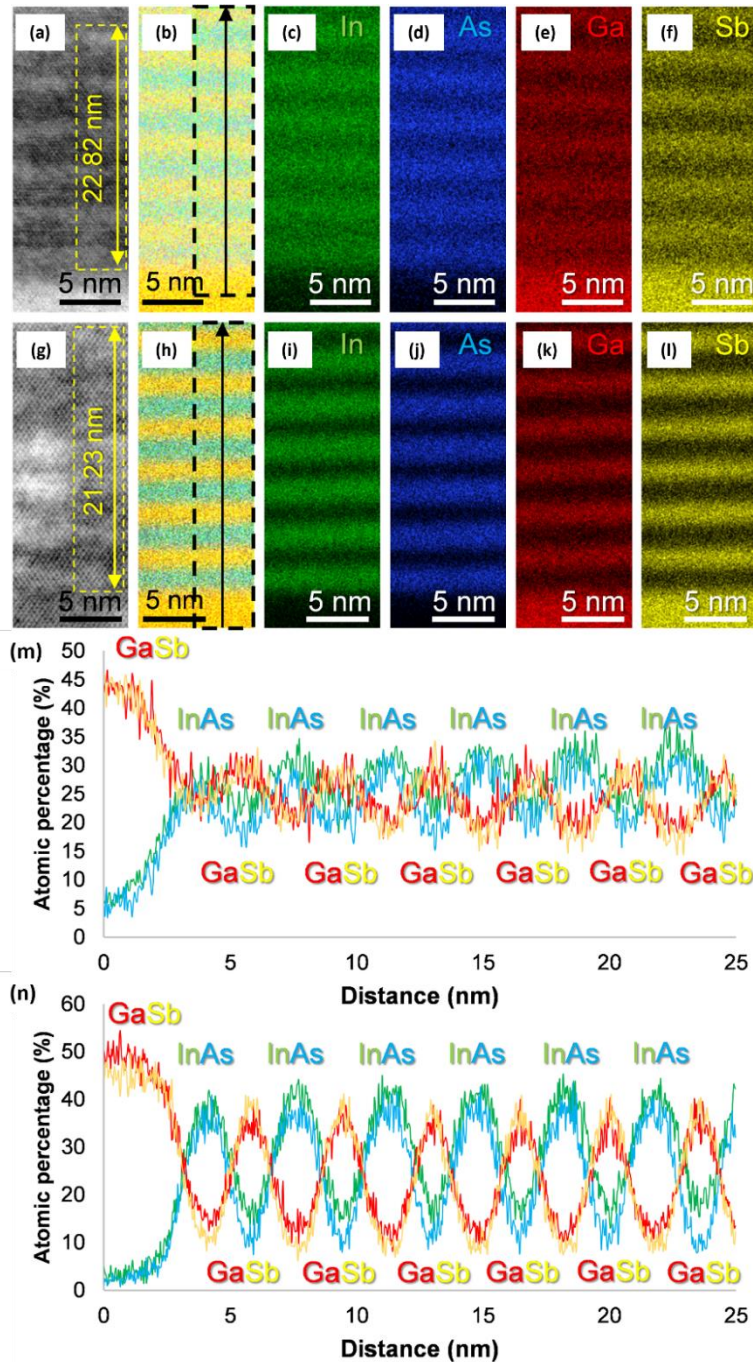
Figure 5.19: For Samples A and B, respectively: BF-STEM micrographs from the GaSb/T2SL region including areas with measurements of SL periods (a, g), combined In-As-Ga-Sb signals atomic percentage EDX map (b, h), individual maps by In (c, i), As (d, j), Ga (e, k) and Sb (f, l) and integrated atomic percentage profiles along the region marked in the combined signal maps (m, n).

## 5.4 Band heterostructure simulation

As observed previously in Figure 5.6(c) and despite exhibiting a more significant degree of structural inhomogeneity (as observed by the TEM and XRD measurements), Sample A shows

a stronger PL peak intensity than Sample B. This finding seems contradictory since material inhomogeneity is expected to degrade a semiconductor's optical quality due to the increasing existence of non-radiative defect centres. However, this supports the results of Zhang et al. [234], who observed that when comparing T2SLs with InSb-like and mixed-like IFs, the InSb-like IFs were demonstrated to offer a higher PL response while exhibiting a larger structural inhomogeneity as evaluated by XRD. Due to the lack of common cations or anions in the InAs/GaSb heterostructure, it is feasible to explain the high probability of atomic intermixing and/or segregation employing band structure simulations of intermixing in a T2SL material system. As a result, band heterostructure simulations were conducted to gain a deeper understanding of the effect of atomic intermixing and segregation at the T2SL IFs on the PL intensity.

Herein, an 8-band k·p solver, employed in the Nextnano$^3$ software [300], was utilised to model the band structure of a 7 ML InAs/ 1 ML InSb/ 4 ML GaSb/ 1 ML InSb T2SL with different forms of intermixing. One manifestation of the intermixing present in Sample A is that the binary InAs and GaSb layers seem to include small quantities of other components, such as Sb or In. Moreover, this feature seems to occur more commonly at the IFs of the T2SL. Based on these speculations, six scenarios (S1-S6) were simulated where various possibilities of IFs were assumed, explaining the influence of different types of atomic intermixing on the optical properties of the T2SL. All the simulations were conducted at a temperature of 77 K. In light of the aforementioned observations, we postulated that a T2SL with no intermixing of 7 ML InAs/ 1 ML InSb/ 4 ML GaSb/ 1 ML InAs (S1) is one possible scenario. Furthermore, other potential scenarios involving intermixing were proposed as follows: 7 ML $InAs_{0.97}Sb_{0.03}$/ 1 ML InSb/ 4 ML GaSb/ 1 ML InSb T2SL (S2); 7 ML $InAs_{0.97}Sb_{0.03}$/ 1 ML InSb/ 4 ML $Ga_{0.97}In_{0.03}Sb$/ 1 ML InSb T2SL (S3); 5 ML InAs/ 1 ML $InAs_{0.93}Sb_{0.07}$/ 1 ML InSb/ 1 ML $Ga_{0.93}In_{0.07}Sb$/ 2 ML GaSb/ 1 ML $Ga_{0.93}In_{0.07}Sb$/ 1 ML InSb/ 1 ML $InAs_{0.93}Sb_{0.07}$ T2SL (S4); 5 ML InAs/ 1 ML $InAs_{0.93}Sb_{0.07}$/ 1 ML InSb/ 1 ML $Ga_{0.93}In_{0.07}Sb$/ 2 ML GaSb/ 1 ML $Ga_{0.07}In_{0.93}Sb$/ 1 ML InSb/ 1 ML $InAs_{0.07}Sb_{0.93}$ T2SL (S5); and 5 ML $InAs_{0.97}Sb_{0.03}$/ 1 ML $InAs_{0.93}Sb_{0.07}$/ 1 ML InSb/ 1 ML $Ga_{0.93}In_{0.07}Sb$/ 2 ML $Ga_{0.97}In_{0.03}Sb$/ 2 ML $Ga_{0.07}In_{0.93}Sb$/ 1 ML InSb/ 1 ML $InAs_{0.07}Sb_{0.93}$ T2SL (S6). The simulation results are presented in Figures 5.20 (a-f) for scenarios S1 to S6. Table 5.7 also includes the extracted parameters.
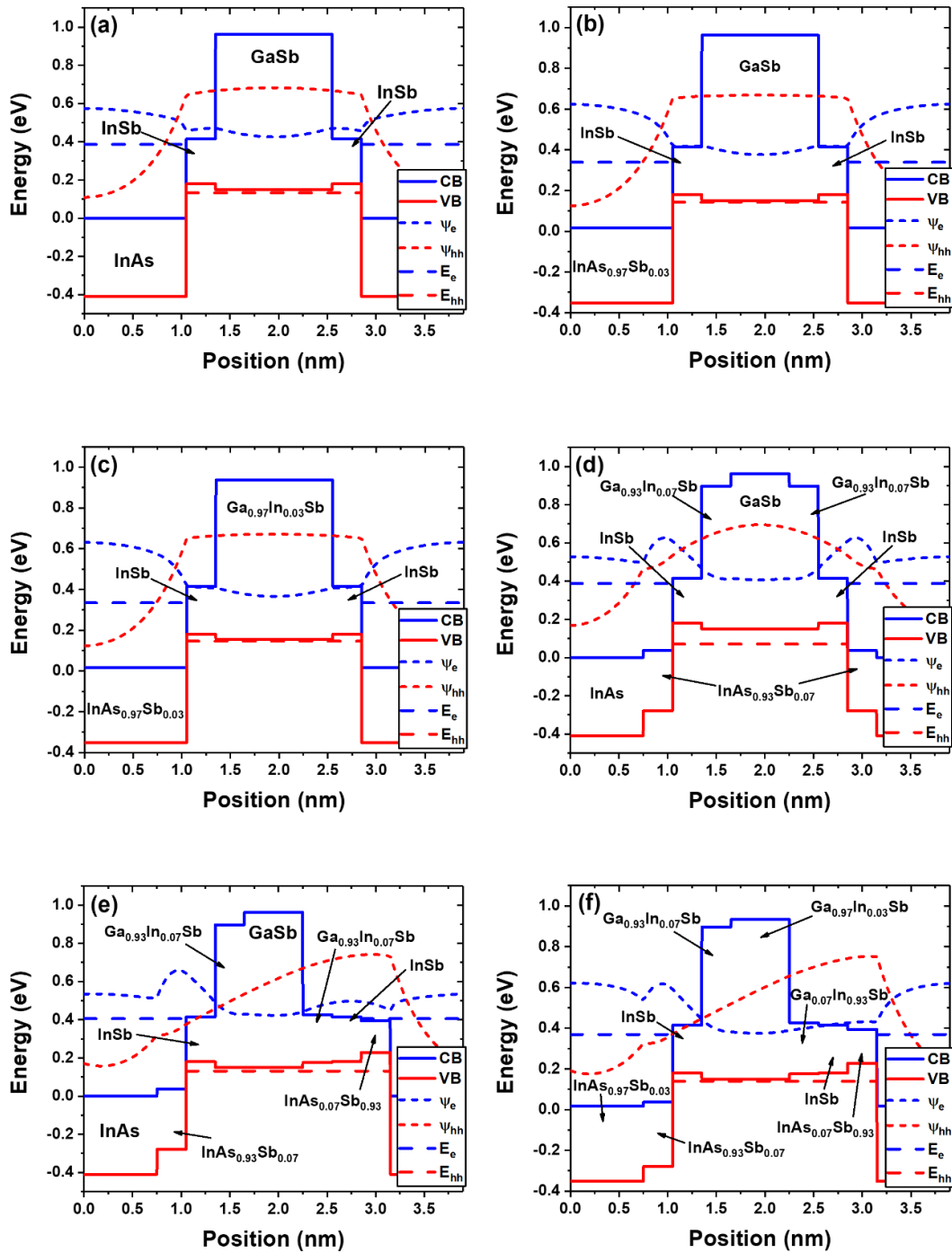
Figure 5.20: (a)-(f) The simulated band heterostructure and wavefunction overlap in the presumed scenarios S1-S6.

Figures 5.20(b) and (c) show that both Sb and In incorporations in the InAs and GaSb layers decrease the wavefunction overlap, thereby reducing the optical response of the T2SL. However, Figures 5.20(d) and (e) show that when the intermixing is limited to Sb or In incorporation at the InSb IF, both the electron and hole wavefunctions at the IF increase, which

157

has the effect of increasing the overall wavefunction overlap. When Figures 5.20(a) and (f) are compared, it seems that the positive impact of interfacial intermixing outweighs the negative influence of Sb or In incorporation. Indeed, this is determined by the relative magnitudes of these occurrences. Thus, it can be claimed that intermixing may enhance the optical response of most T2SL samples as long as the formation of non-radiative defect centres is not too severe (for example, by the existence of a large density of lattice defects in the heterostructure) [341]. Figure 5.20(f) depicts a possible scenario involving both types of intermixing. This modelled scenario (S6) has a bandgap energy comparable to Sample A at 77 K but a larger wavefunction overlap than if its IFs were entirely sharp, as presented in Figure 5.20(a). Comparing scenarios S1 and S6 in Table 5.7 also suggests that intermixing will likely decrease the bandgap energy of the T2SL, thereby increasing its cut-off wavelength. These simulation outcomes are consistent with the results of TEM and PL measurements. Sample A, which exhibits increased intermixing, demonstrates a longer cut-off wavelength and a more prominent PL peak intensity. Consequently, it appears that the increased optical response of Sample A can be attributed to the presence of intermixing occurrences, as there is no excessive density of non-radiative recombination centres, as Figure 5.17 proves.

Table 5.7: The following values were retrieved from band heterostructure simulations of assumptions made to predict various atomic intermixing or segregation situations in S1-S6.

| Scenario | Intermixing | Bandgap Energy (eV) | Wavefunction Overlap (%) |
|----------|-------------|---------------------|--------------------------|
| S1 | None | 0.253 | 56.2 |
| S2 | Sb incorporation | 0.191 | 52.2 |
| S3 | Sb and In incorporation | 0.188 | 51.2 |
| S4 | Symmetrical interfacial intermixing | 0.318 | 65.6 |
| S5 | Asymmetrical interfacial intermixing | 0.275 | 62.4 |
| S6 | A combination of S3 and S5 | 0.230 | 57.8 |

## 5.5    Summary

The influence of using two different interfacial growth schemes on the structural and optical quality of the T2SL samples has been investigated through XRD, AFM, PL, and TEM measurements. Sample A, with an intended InSb IF layer, exhibits a larger compressive strain than Sample B, which has a nearly lattice-matched T2SL to the GaSb substrate but no deliberate InSb IFs. AFM measurements revealed that Sample A has a rougher surface roughness compared to a smother roughness in Sample B, possibly due to the overall thick-grown InSb interfacial layers in Sample A.

PL spectroscopy revealed that Sample A possesses a more substantial optical property than Sample B. Moreover, the radiative recombination is marginally stronger in Sample A with a substantially higher PL peak intensity than in Sample B. The higher luminescence efficiency could be attributed to the effect of the MEE growth mode. In the MEE growth mode, the cations can migrate longer distances without anions; therefore, 2-D layer growth can be more easily attained. The origin of the various peaks observed in the T2SL samples was investigated, and it was determined that the prominent peaks are associated with the SL transition. In contrast, the secondary peaks are related to 2-D growth islands or sub-MLs of QDs at the IFs. In addition, the FWHM profile of the temperature-dependent PL measurements reveals that Sample A has considerably higher fluctuations in the QW width and higher coupling strength of excitons and phonons than Sample B, indicating that T2SLs grown without InSb IFs have superior lattice and crystalline quality as well as reduced IF roughness.

TEM investigations were also conducted to confirm the findings of XRD, AFM, and PL measurements. It was demonstrated that the morphology of the two T2SLs samples is homogeneous. Both SLs show single-crystalline because only ordered configurations of bright reflections can be observed. Furthermore, the T2SLs were proven to be epitaxially formed with respect to the buffer layer, and the insertion of the InSb interfacial layers at both IFs did actually raise the compressive strain in Sample A, although the material degradation was not considerable. It was also discovered that the IFs in Sample A are rougher than in Sample B, suggesting an enhanced probability of interfacial atomic intermixing and segregation, which is also well consistent with the XRD and AFM measurements.

Band heterostructure simulations were also carried out to thoroughly comprehend the TEM and PL measurements' observations and investigate the effect of atomic intermixing and segregation on the PL intensity in a T2SL material system. It was discovered that atomic intermixing and segregation alter the bandgap energy of the T2SL and affect the wavefunction overlap, which substantially affects the optical properties of the structures. This concludes that in light of these structural and optical characterisation results, it is anticipated that high material property can be attained by optimising the growth conditions while paying attention to the IFs to improve the structural and optical characteristics of the T2SL heterostructures.

# Chapter 6: Fabrication and Electrical Characterisations of Mid-Wavelength Infrared Type-II InAs/GaSb Superlattices

This chapter details the process of fabricating 7/4 MLs of InAs/GaSb T2SL (Sample C) using an HF-based wet etching method (abbreviated as Sample C1) after the growth of *pin* photodiode structure based on the growth method of Sample B. Upon completion of the device fabrication, electrical measurements and analyses were undertaken to examine the performance of the devices including I-V and C-V. The development of fabrication methods of T2SLs, including dry etching (abbreviated as Sample C2) and a combination of both dry and wet etching + surface passivation processes (abbreviated as Sample C3), are also described and discussed in this chapter.

## 6.1    Photodiode structure and XRD characteristics

A *pin* detector structure with an intrinsic absorber region comparable to the structure of Sample B was grown employing the same growth conditions presented previously in Chapter 5. Herein, the photodiode structure was grown on a *p*-type GaSb substrate which consists of a 60-nm thick heavily *n*+-type doped ($N_d$ ~ $1x10^{18}$ cm$^{-3}$) top contact, a 1-μm thick non-intentionally doped *i*-absorber region, and a 60-nm thick heavily *p*+-type doped ($N_d$ ~ $1x10^{18}$ cm$^{-3}$) bottom contact. The whole *pin* structure has the same superlattice design, which was grown to have 7/4 MLs of InAs/GaSb SL but with different SL periods. Then, the *pin* photodiode was capped and buffered with a 20-nm thick heavily *n*+-type doped ($N_d$ ~ $1x10^{18}$ cm$^{-3}$) InAs layer and a 100-nm thick heavily *p*+-type doped ($N_d$ ~ $1x10^{18}$ cm$^{-3}$) layer. A schematic of the *pin* photodiode structure is depicted in Figure 6.1.
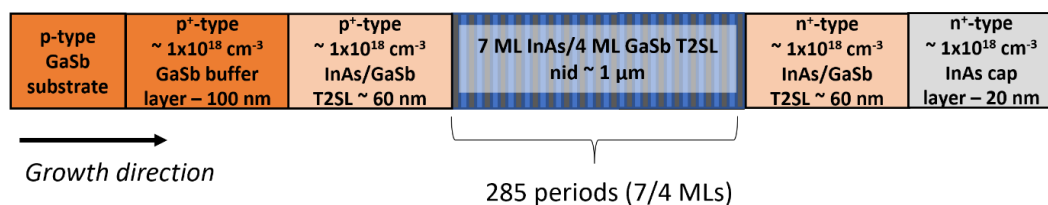


Figure 6.1: Schematic of the InAs/GaSb T2SL pin photodiode structure used for fabrication (Sample C).

Figure 6.2(a) displays the measured XRD scan from Sample C, and Figure 6.2(b) depicts the estimated periodic thickness. As can be seen, the XRD peaks of the T2SL up to the second-order peaks are sharp and visible. The measured periodic thickness of the SL of Sample C is found to be around 3.48 nm with a FWHM at the $SL_{-1}$ below 145 arcsec. The lattice mismatch was determined to be nearly 0% which is below 50 arcsec.
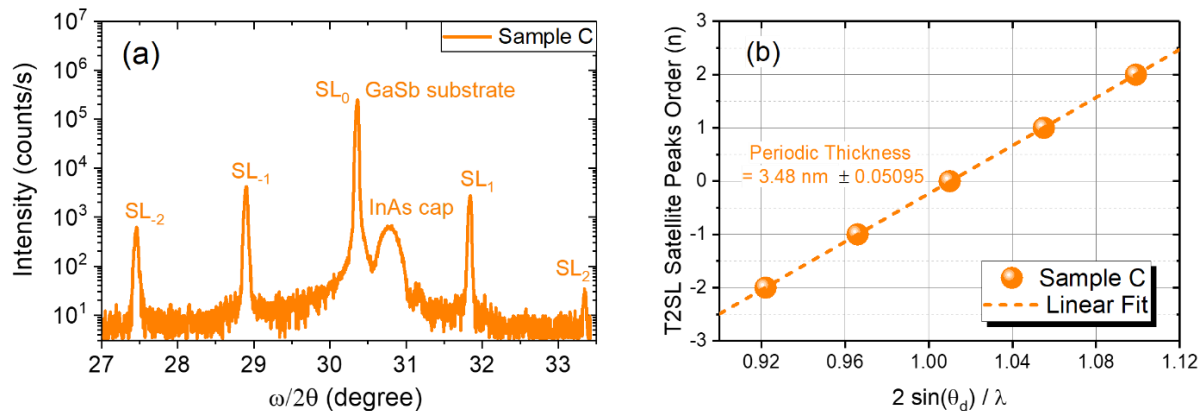


Figure 6.2: (a) XRD scan and (b) measured periodic thickness of the T2SL photodiode (Sample C).

## 6.2    Device fabrication using the wet etching method

Following the growth of a *pin* photodiode structure, the sample was then processed for fabrication at the ICS-CR facility in the School of Physics and Astronomy at Cardiff University. Herein, conventional photolithography and wet etching processes, as described in Chapter 4, were carried out to fabricate single-pixel devices with mesa diameters varying from 90 to 440 µm. The fabrication stages using the wet etching method are summarised in Table 6.1. In summary, the fabrication process comprises three primary photolithography steps. The first, second, and third photolithography steps are for the top contact formation, mesa definition, and mesa sidewall protection. For more descriptive details, Figure 6.3 depicts the process flow of the fabrication steps using a wet etching approach for Sample C1. Figure 6.4 shows the optical microscope images of the completed device fabrication, and Figure 6.5 depicts the final outcome of the fabricated device after mounting it onto a TO-8 header ready for testing. A schematic of the final fabricated *pin* devices with the current path and SEM image therein is depicted in Figure 6.6(a-b), respectively.

Table 6.1: A summary of the wet etching method used to fabricate the MWIR InAs/GaSb T2SL at the ICS CR at Cardiff University.

| Stage | Experimental Procedure | Equipment Used | Chemicals and Materials | Descriptive Detail |
|---|---|---|---|---|
| 1 | Preparation and cleaving | Scriber | None | InAs/GaSb T2SL MWIR samples were cut into small sizes of 1 cm x 1 cm |
| 2 | Cleaning | Wet bench area: chemical materials | Acetone, Methanol, and Isopropanol (IPA) | Samples were immersed in Acetone, Methanol, and IPA for 5 minutes each to clean the surface. Then, they were dried using a nitrogen gun |
| 3 | Top-contact definition: first photolithography | Nano booth: spin coater and hot plate | PMGISF11 and S1813SP15 positive photoresists | Bilayer photoresists were spun-coated on the surface of the samples. Firstly, the SF11 photoresist was applied to the surface of the samples by a spin coater (spinning parameters: 5000 rpm/20 seconds), followed by baking on a hot plate for 10 minutes at 97 °C. Secondly, the S1813 photoresist was then applied on the surface by a spin coater (spinning parameters: 6000 rpm/45 seconds), followed by baking on a hot plate for 5 minutes at 80 °C |
| | | MJB3 mask aligner, mixed area photolithography mask | None | Samples were then exposed to UV light for 7 seconds through the top contact design of the photolithography mask |

| Stage | Experimental Procedure | Equipment Used | Chemicals and Materials | Descriptive Detail |
|-------|------------------------|----------------|-------------------------|--------------------|
| | | Wet bench | MF319 developer and Deionised water (DIW) | MF319 developer and DIW were prepared with a ratio of (1 ml: 30 ml). Samples were immersed in the developer for 15 seconds, then rinsed quickly in DIW for 1 second and DIW for 40 seconds. Blow drying was then performed using a nitrogen gun. These steps were performed to remove the damaged photoresist |
| 4 | Metal top-contact formation | Physical vapour deposition (PVD) | Gold (Au) wire and Chrome (Cr) rod | 20-nm and 200-nm thick layers of Cr and Au, respectively, were deposited on the surface of the samples using a thermal evaporator |
| 5 | Metals lift-off | Wet bench area | Acetone, NPM1165 remover, IPA, and DIW | Samples deposited were immersed in Acetone for 10 minutes, followed by them being immersed in a NPM 1165 remover for also 10 minutes to remove the SF11 photoresist, and then dipped in IPA and DIW for 5 minutes each to clean the surface |

| Stage | Experimental Procedure | Equipment Used | Chemicals and Materials | Descriptive Detail |
|-------|------------------------|----------------|-------------------------|--------------------|
| 6 | Mesa preparation: second photolithography | Nano booth: spin coater and hot plate | S1813SP15 photoresist | The S1813 photoresist was spun coated on the surface of the samples using a spin coater (parameters used for spinning were 6000 rpm/45 seconds) and followed by baking them in a hot plate for 3 minutes at a temperature of 97 °C |
| | | Nano booth: MJB4 mask aligner and mixed area photolithography mask | None | Samples were exposed to UV light for 8 seconds through the Mesa design of the photolithography mask |
| | | Wet bench area | MF319 developer | Samples were then immersed in MF319 developer for 15 seconds, then rinsed quickly in DIW for 1 second and rinsed again in DIW for 40 seconds. Blow drying was then made using a nitrogen gun. Then, samples were soft-baked on a hot plate for 3 minutes at 97 °C |

| Stage | Experimental Procedure | Equipment Used | Chemicals and Materials | Descriptive Detail |
|---|---|---|---|---|
| 7 | Mesa etching | Wet bench area: chemical materials/solutions and DEKTAK system | Hydrogen peroxide ($H_2O_2$), citric acid ($C_6H_8O_7$), hydrofluoric acid (HF) | 40 ml of $H_2O_2$, 40 ml of $C_6H_8O_7$, and 40 µl of HF were mixed. The etch rate was determined using a DEKTAK system to measure the etch depth via the etch profile. The etch rate was about 0.76 µm/5 min. To etch and reach the desired depth, the etching was performed up to the GaSb buffer layer of the samples |
| 8 | S1813 photoresist removal after wet etching | Wet bench area | Acetone, 1165 remover, and IPA | The etched samples were immersed in Acetone for 5 minutes, then immersed in a 1165 remover for another 5 minutes, and then immersed in Acetone and IPA for 5 minutes until the photoresist was removed. A blow drying with a nitrogen gun was also made to clean the samples |
| 9 | Mesa sidewalls protection: third photolithography and hard bake | Nano booth: spin coater and hot plate | S1813SP15 photoresist | The S1813 photoresist was spun coated on the surface of the samples using a spin coater (parameters used for spinning were 6000 rpm/45 seconds) and followed by baking them in a hot plate for 3 minutes at a temperature of 97 °C |

| Stage | Experimental Procedure | Equipment Used | Chemicals and Materials | Descriptive Detail |
|-------|------------------------|----------------|-------------------------|---------------------|
| | | Nano booth: MJB4 mask aligner and mixed area photolithography mask | None | Samples were exposed to UV light for 8 seconds through the SU-8 design of the photolithography mask |
| | | Wet bench area | MF319 developer | Samples were then immersed in MF319 developer for 15 seconds, then rinsed quickly in DIW for 1 second and rinsed again in DIW for 40 seconds. Blow drying was then made using a nitrogen gun. Then, samples were soft-baked on a hot plate for 3 minutes at a 97 °C |
| | | Hard bake | Oven | Samples were then baked in an oven for 2 hours at 80 °C. After which, samples were cleaned in Acetone and IPA solvents |
| 10 | Metal bottom-contact formation | PVD | Au and Cr | 20-nm and 200-nm thick layers of Cr and Au, respectively, were deposited on the backside of the samples using the thermal evaporator |

| Stage | Experimental Procedure | Equipment Used | Chemicals and Materials | Descriptive Detail |
|-------|------------------------|----------------|-------------------------|--------------------|
| 11 | Mounting | TO-8 header | Epoxy | The sample was mounted onto a TO-8 header containing 12 pins for electrical contacts. This was performed by pasting an epoxy on the surface of the TO-8 header to make a sufficient adhesion |
| 12 | Wire-bonding | Wire-bonder | Silver wire | The sample contacts were connected to the header pins |
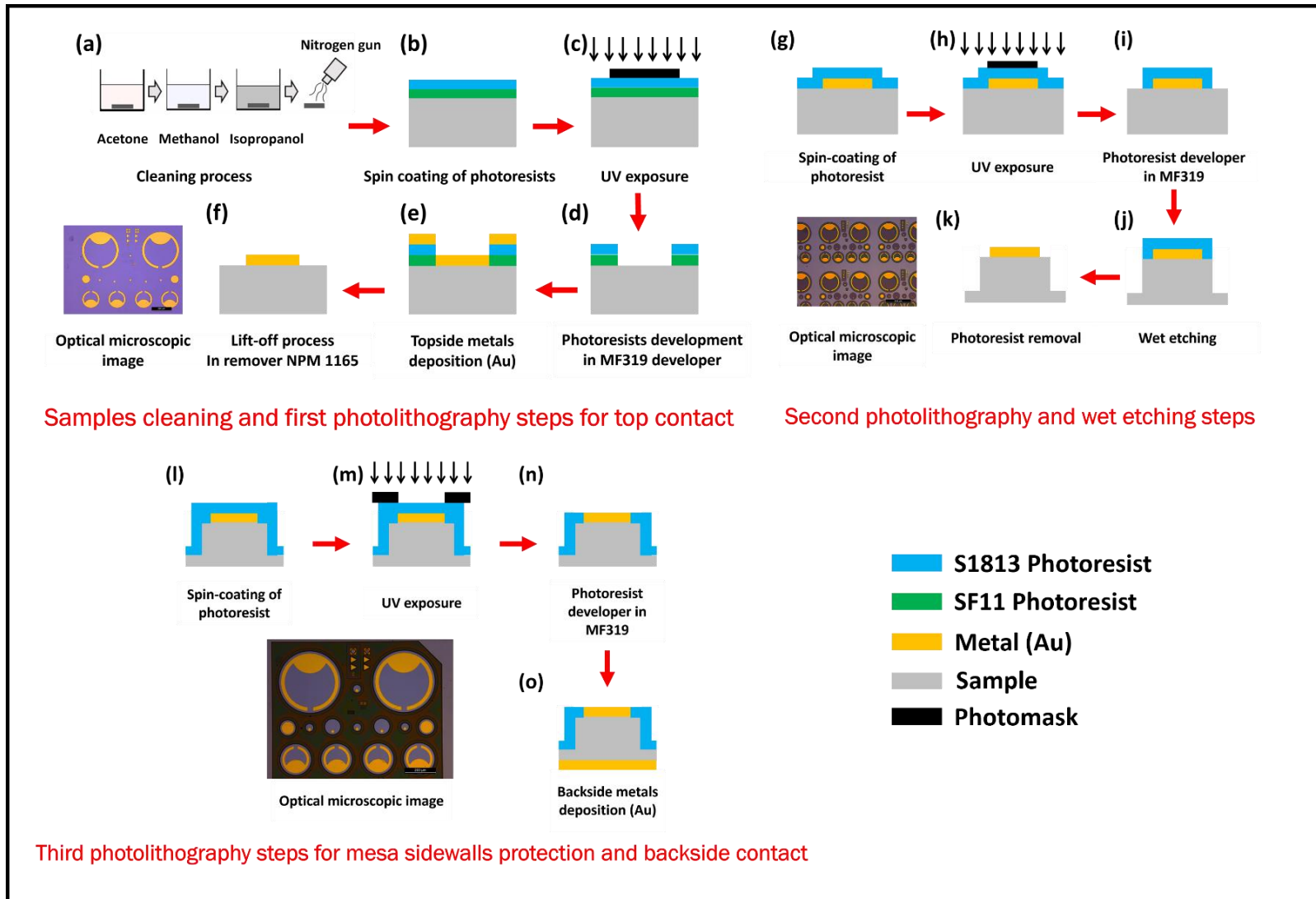
Figure 6.3: Process flow of the InAs/GaSb T2SL sample fabrication using the wet etching approach.
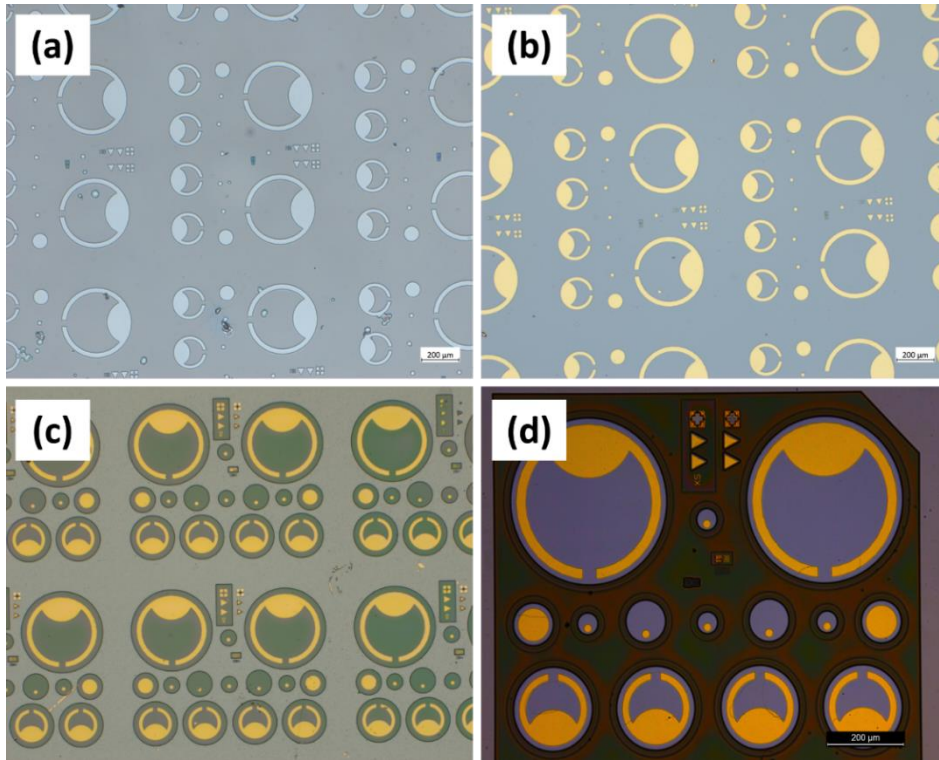
Figure 6.4: Optical microscope images of the fabricated InAs/GaSb T2SL devices with various mesa sizes ranging from 90 μm to 440 μm. (a) The sample after top-contact definition: first photolithography (stage 3), (b) The sample after metallisation and lift-off of unwanted metal and photoresist (stages 4-5), (c) The sample after wet etching and removal of photoresist (stages 6-8), and (d) The final fabricated photodiode after applying a photoresist for mesa sidewall protection from ambient air (stage 9).
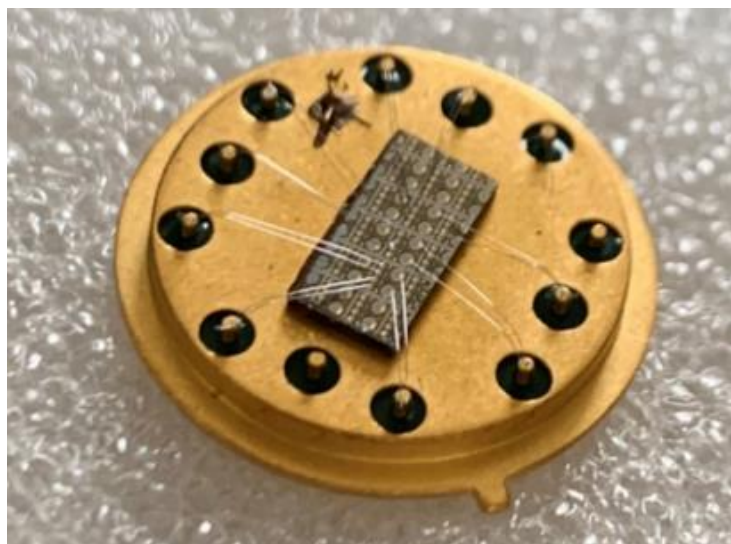


Figure 6.5: The final fabrication outcomes of a single-pixel InAs/GaSb T2SL device, mounted onto a TO8-header and wire bonded ready for testing via electrical measurements.
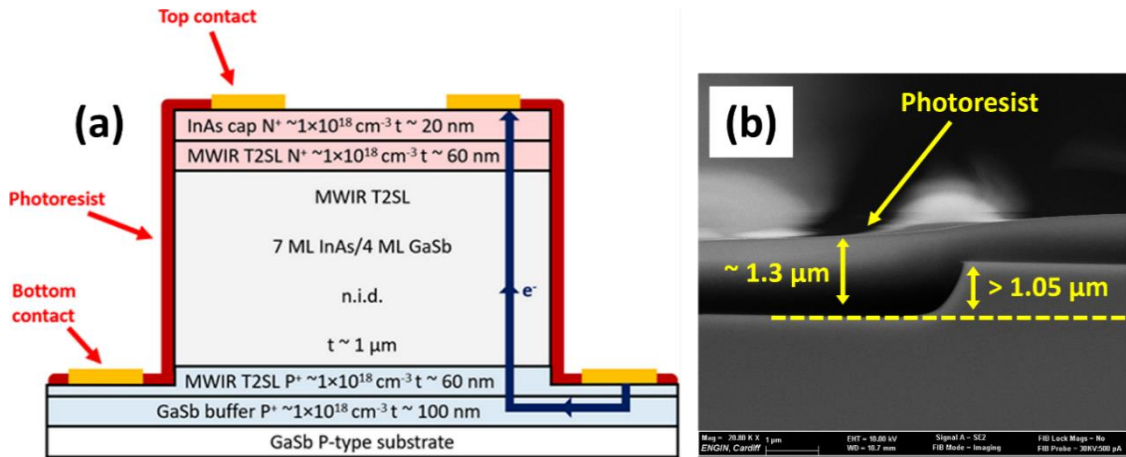
Figure 6.6: (a) Schematic of the fabricated InAs/GaSb T2SL device. The blue arrow highlights the flow of electrons. (b) cross-sectional SEM image was taken from the fabricated photodiode after applying a photoresist as a protective layer to block the mesa sidewalls from ambient air.

## 6.3    Device electrical performance

After the T2SL photodiode fabrication with different mesa diameters ranging from 90 to 440 μm, they were characterised using a LN$_2$ cooled cryogenic probe station system available at the optics laboratory at the School of Physics and Astronomy, Cardiff University. The measurements were conducted at different temperatures and biases to access the I-V and C-V characteristics.

### 6.3.1   Current-voltage measurements

To assess the electrical performance of the fabricated devices, I-V measurements were undertaken at a wide range of temperatures ranging from 77 to 300 K and at an applied bias ranging from +0.3 to -1 V. Figure 6.7(a) depicts the dark current density characteristics (J = I/A, where A is the device area) of the photodiode with a mesa diameter of 240 μm. As can be seen, the dark current density increases with increasing temperatures from 77 to 300 K. The lowest value of the dark current density of 5x10$^{-6}$ A/cm$^2$ is achieved at an applied bias of -100 mV and 77 K. In contrast, it increases significantly to 7 A/cm$^2$ at 300 K and under the same applied bias. It can also be seen that the J-V characteristics are shifted towards the forward bias region at a lower temperature range between 77 and 100 K, possibly due to the effect of photocurrent presented in the cryogenic probe station.

From the J-V plot, the $R_dA$ is derived, where $R_0$ is the resistance of the photodiode at zero bias via the second derivative of the J-V plot, as expressed earlier by Equation (3.7). Figure 6.7(b) shows that the highest $R_0A$ product of $6 \times 10^4$ $\Omega.cm^2$ is achieved at 77 K, whereas it drops dramatically to approximately 0.017 $\Omega.cm^2$ at 300 K.
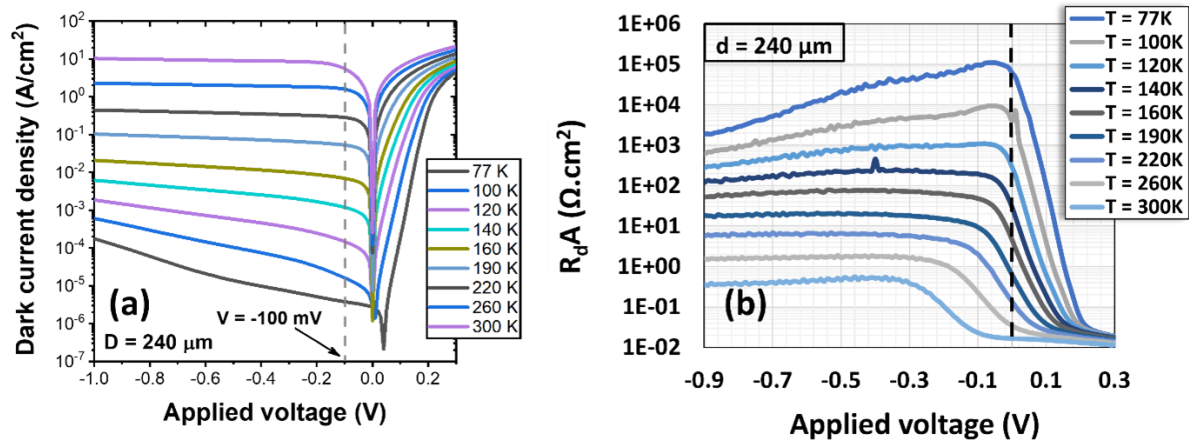


Figure 6.7: (a) Dark current density and (b) differential resistance-area product ($R_0A$) versus the applied voltage of the fabricated T2SL using HF-based etchants (Sample C1) with a mesa diameter of 240 μm performed at temperatures between 77 and 300 K.

To understand the dominant dark current mechanisms for the photodiode, an Arrhenius plot (Figure 6.8) depicts the dark current density as a function of temperature and at a bias operation of -100 mV. In Figure 6.8, data between 77 and 110 K were excluded from the fitting regime due to the effect of photocurrent. Only data from 120 to 300 K were included in the fitting regime. Data from 136 to 120 K were fitted using the generation-recombination current (Equation 3.8), whereas data above 136 K were fitted based on the diffusion current (Equation 3.9). The fittings show that the photodiode is dominated by diffusion and G-R currents above and below 136 K, respectively. The extracted activation energy of the diffusion current is found to be 191.2 meV, slightly lower than the measured bandgap energy from the PL (~243 meV). In contrast, the extracted activation energy of the generation recombination current is around 125.7 meV, almost half of the measured bandgap energy (~121.5 meV). At a lower temperature range between 77 and 100 K, the photodiode is dominated by a combination of surface leakage and tunnelling currents.
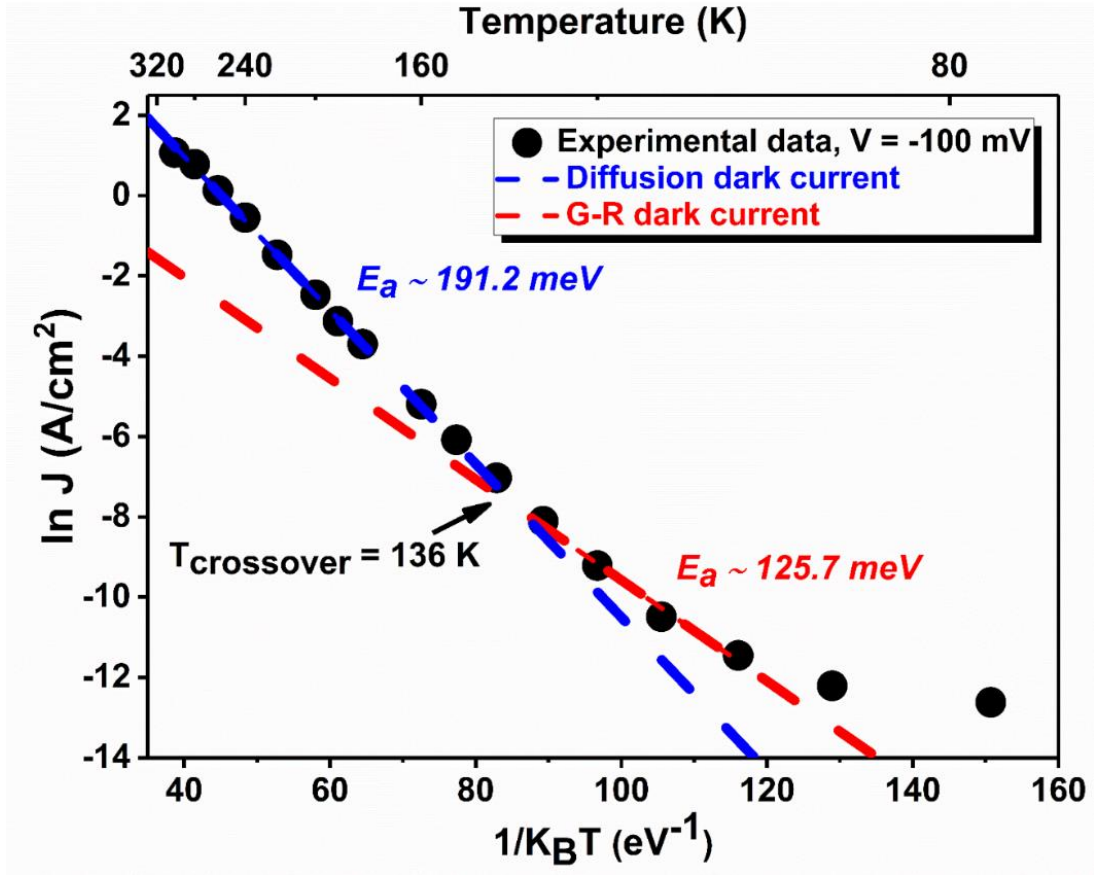
Figure 6.8: Dark current density versus inverse temperature (Arrhenius plot) to extract the dominant dark current mechanisms for the T2SL photodiode (Sample C1) at an applied bias of -100 mV.

To study the main contribution of dark current density at low temperatures, the differential resistance-area product at zero bias ($R_0A$) for four different photodiode sizes (440, 240, 140, and 90 µm) at 77 K is plotted against the applied voltage as depicted in the inset of Figure 6.9. As can be seen, the $R_0A$ has a relatively similar value for all photodiodes, which is around $6 \times 10^4$ $\Omega.cm^2$. Figure 6.9 depicts the inverse $R_0A$ as a function of the perimeter-to-area ratio of the photodiode mesa sizes. To evaluate the contribution of dark current, one can use the following equation:

$$\frac{1}{R_0A} = \frac{1}{R_s} \times \left(\frac{P}{A}\right) + \frac{1}{(R_0A)_{Bulk}}$$

(6.1)

where $R_S$ and $R_0A_{Bulk}$ are the surface and bulk resistivities, respectively, and ($P/A$) is the device perimeter-to-area ratio.
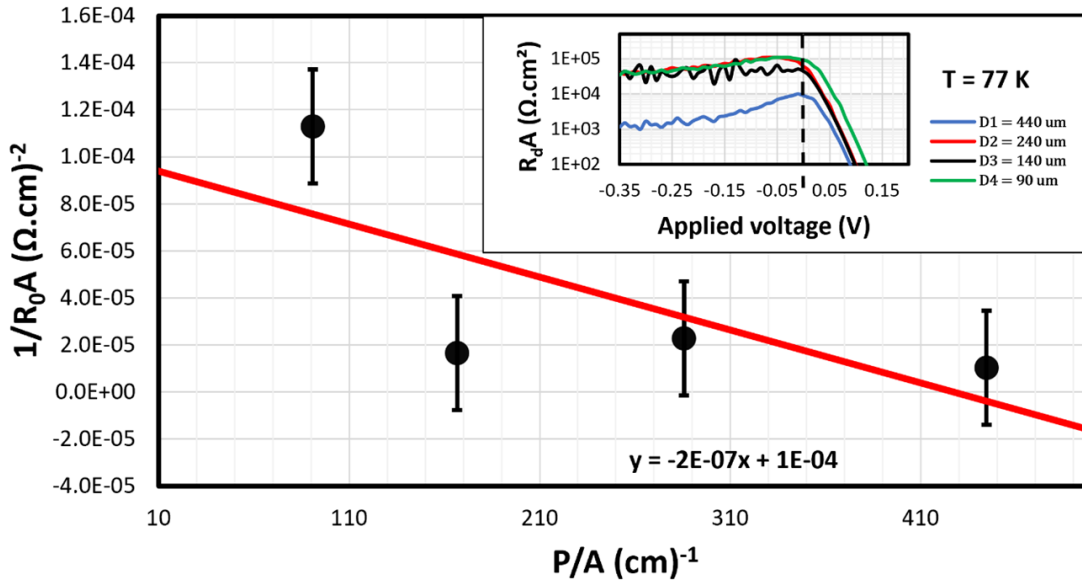
Figure 6.9: Inverse $R_0A$ as a function of the P/A ratio of the photodiodes (Sample C1). The inset shows $R_dA$ versus applied voltage at 77 K on photodiodes with different mesa diameters (440, 240, 140, and 90 μm).

From the linear fitting of $1/R_0A$ as a function of *P/A* of the four devices, the bulk resistivity ($R_0A_{Bulk}$) and surface resistivity ($R_S$) were evaluated and found to be $1\times10^4$ $\Omega.cm^2$ and $5\times10^6$ $\Omega.cm$ accordingly. The deduced $R_0A_{Bulk}$ is nearly equivalent to or even less than the measured $R_0A_{Surface}$, indicating that both surface and bulk leakage currents strongly influence the dark current, which limits the device performance. This also agrees with the previous observation that the shunt and G-R currents dominate at a low applied voltage of around -100 mV. The shunt current usually occurs due to the native oxides produced on the mesa sidewalls during etching. In contrast, the G-R current is associated with the physical defects in the depletion region acting as SRH non-radiative recombination centres. This suggests that further optimisation of the etching process is required to achieve high uniformity and minimise the influence of surface leakage current by applying surface passivation. Furthermore, the bulk leakage current can be minimised by enhancing the device structure using a barrier design and controlling the shutter sequences during growth to possibly prevent G-R current and related SRH defects.

### 6.3.2 Capacitance-voltage measurements

To further test the device performance, C-V measurements were carried out at different temperatures ranging from 100 to 150 K and at a frequency of 1 MHz on a photodiode with a

mesa diameter of 240 μm, as shown in Figure 6.10(a). The reduced carrier concentration or the background doping ($N_{red}$) can be extracted from the C-V measurements using the following equation:

$$\left(\frac{A}{C(V)}\right)^2 = \frac{2V_d}{q\varepsilon_r\varepsilon_0 N_{red}} - \frac{2}{q\varepsilon_r\varepsilon_0 N_{red}}V \qquad (6.2)$$

where $A$ is the device area, $V_d$ is the built-in potential voltage, $q$ is the electron charge, $V$ is the applied voltage, and $\varepsilon_r$ and $\varepsilon_0$ are the relative dielectric permittivity of the material (taken equal to 15.4) and vacuum permittivity, respectively. Thus, the residual doping concentration $N_{res}$ was extracted from the slope of $(A/c)^2$ versus the applied voltage at a temperature of 100 K, as depicted in Figure 6.10(b). The $N_{res}$ extracted from the slope was found to be $9.98 \times 10^{14}$ cm$^{-3}$, which is consistent with values reported for the same periodic composition and thickness [312], [318].
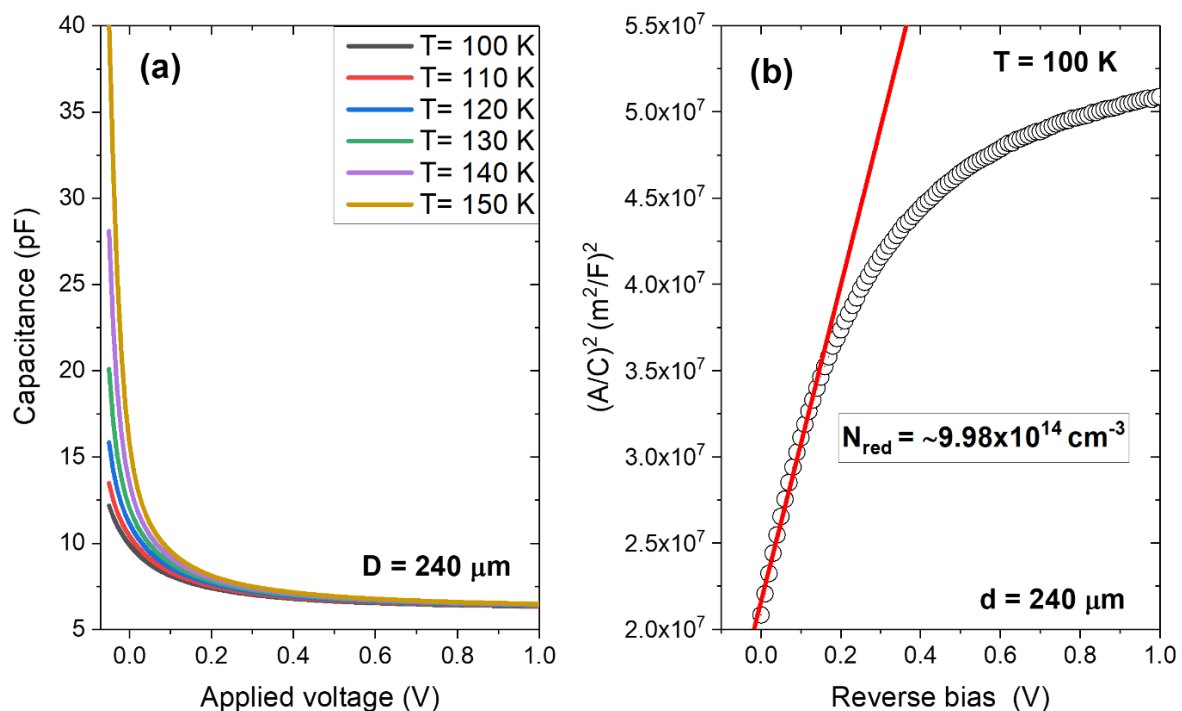


Figure 6.10: (a) Capacitance-voltage characteristics measured for the photodiode (Sample C1) with a mesa diameter of 240 μm at temperatures from 110 to 150 K and (b) the corresponding $(A/c)^2$ as a function of applied voltage.

## 6.4 Device modelling

The J-V modelling was performed using Mathematica software to verify the I-V experimental results. The MC lifetime was also extracted from the Silvaco ATLAS modelling.

### 6.4.1 Current density-voltage modelling

J-V modelling at temperatures of 110 K, 200 K, and 300 K was performed using Mathematica software, as described in Section 4.6.2, to assess the device performance further. Modelling at 77 K was not practicable owing to the insufficient shielding of the probe station and the influence of photocurrent. The dark current density in a T2SL photodiode has been accurately modelled by Gopal et al. [57], [316], [317] to be the total of diffusion, trap-assisted tunnelling, generation-recombination, and shunt currents. The data were fitted using Equations (2.24 – 2.31), as shown in Figure 6.11. As can be seen, this model matches with the data except for a slight variation at higher bias which may be ascribed to the band-to-band tunnelling current, which is not addressed here. Figure 6.11(b) shows that at a relatively low temperature of 110 K, G-R dominates the current at a low applied bias. Still, TAT is the dominant current when the applied bias is increased above ~0.2 V. Nevertheless, at higher operating temperatures of 200 K and 300 K, the contribution of diffusion current is dominant at low applied bias ~50 mV, as depicted in Figures 6.11(c-d). This finding is consistent with previous reports on comparable G-R-restricted devices at low temperatures [342], [343]. The substantial contribution of the shunt current may be attributable to the absence of efficient passivation, despite the fact that the mesa sidewalls were shielded by a photoresist.
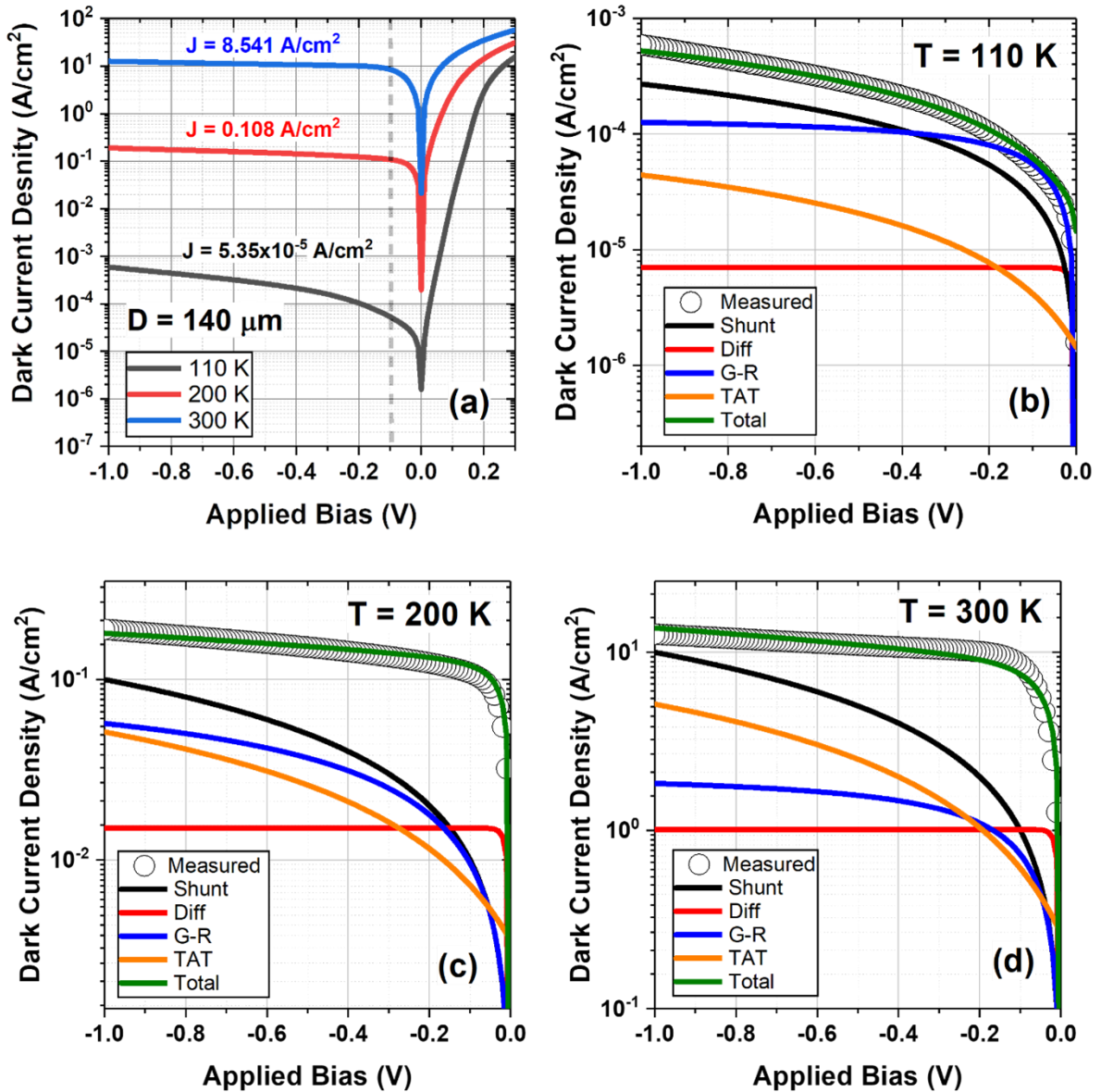
Figure 6.11: (a) Measured dark current density versus applied bias characteristics of the HF-based wet etched devices with a mesa diameter of 140 μm (Sample C1) at temperatures of 110 K, 200 K, and 300 K. Modelled dark current density under applied bias at temperatures of (b) 110 K, (c) 200 K, and (d) 300 K.

## 6.4.2 Minority carrier lifetime extraction

To extract the MC lifetime for the MWIR T2SL photodiode, Silvaco ATLAS software was used. As previously mentioned in Chapter 4 and Table 4.2, all parameters were entered in the simulation file. Figure 6.12 is the plot at which the J-V was simulated at various temperatures between 77 and 240 K for a photodiode with a mesa diameter of 140 μm.
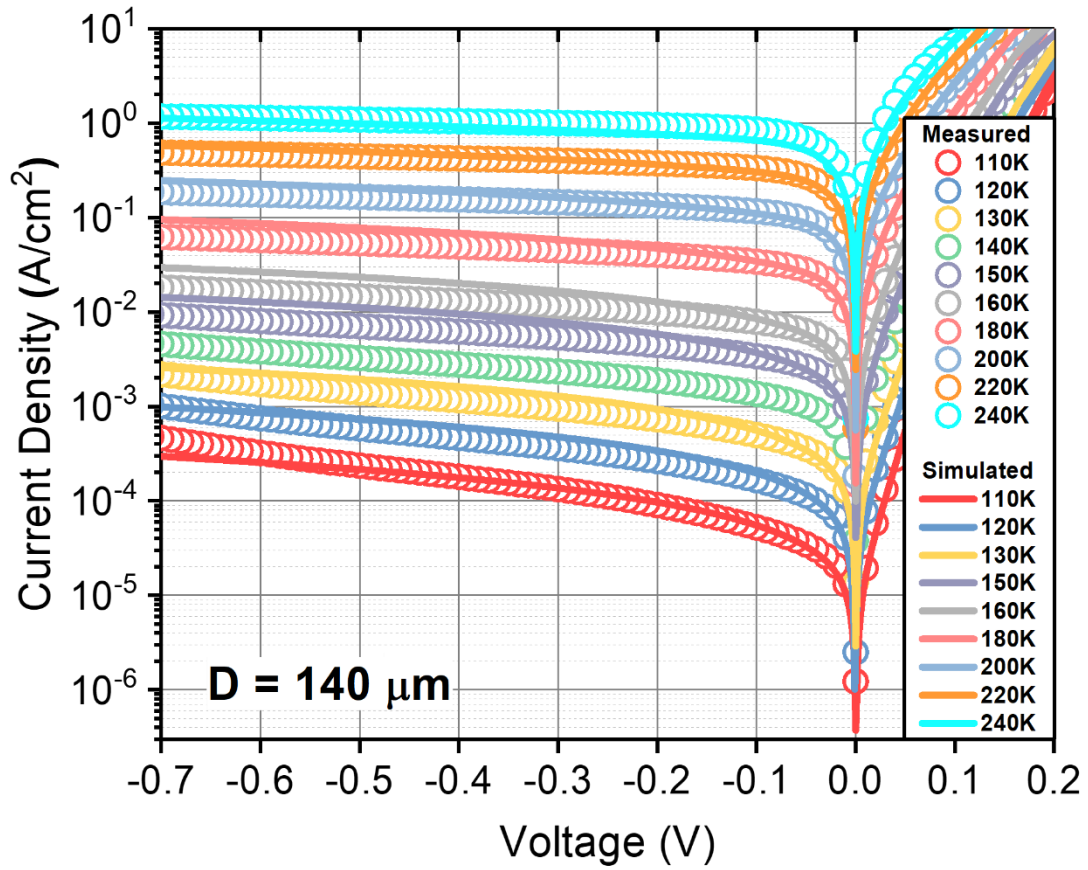
Figure 6.12: Modelled J-V data at temperatures from 110 to 240 K using Silvaco ATLAS software for the device with a diameter of 140 μm.

From the J-V simulated data in Figure 6.12, the MC lifetime was extracted and fitted according to the following equation:

$$\tau_{SRH} \; \alpha \; \frac{1}{T^{\frac{1}{2}}}$$

(6.3)

where $\tau_{SRH}$ is the Shockley-Read-Hall lifetime, and $T$ is the temperature. The estimated MC lifetimes are shown in Figure 6.13. As can be seen, the MC lifetime at 77 K is found to be around 63 ns, which is very close to the reported MC lifetime measured for MWIR InAs/GaSb T2SLs at 77 K [73], [165], [344].
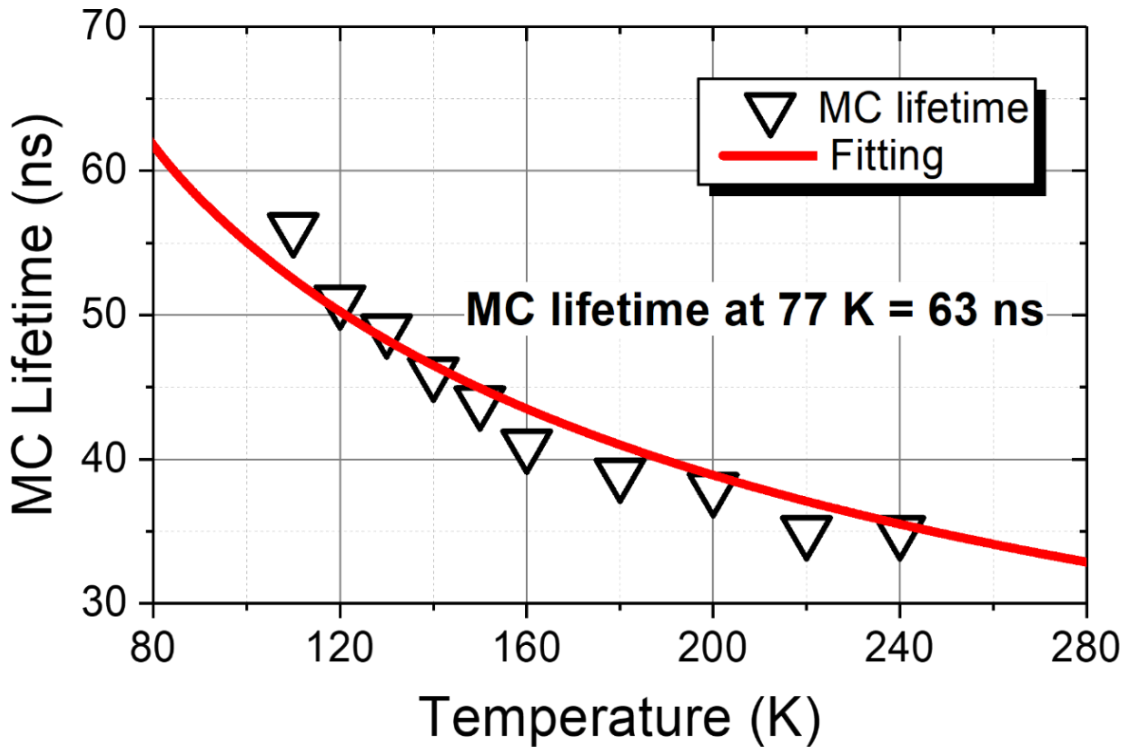
Figure 6.13: Extracted MC lifetime from the simulation and fitted using the SRH lifetime Equation 6.3.

Figure 6.14 depicts the MC lifetimes for III-V semiconductor materials (including InAs, GaSb, InSb, InAsSb, InAs/GaSb T2SL, and InAs/InAsSb T2SL) and II-VI MCT material over the last 15 years at a temperature of 77 K. Data in the figure were accumulated from the following research groups working on Ga-free T2SL [81], [82], [100], [102], [104], [105], [106], [107], [108], [109], [110], [111], Ga-based T2SL [73], [112], [80], [113], [101], [114], [115], [116], binary and ternary compounds of InAs, InSb, GaSb, and InAsSb [80], [81], [105], [117], [118], [119], [120], [121], [122], and MCT [123], [124], [125], [126], [100], [104]. For reference, the MC lifetime of the InAs/GaSb T2SL *pin* photodiode fabricated at Cardiff University is also included. As can be seen, the MC lifetime of our fabricated InAs/GaSb T2SL *pin* photodiode is comparable to other T2SL values reported in the literature.
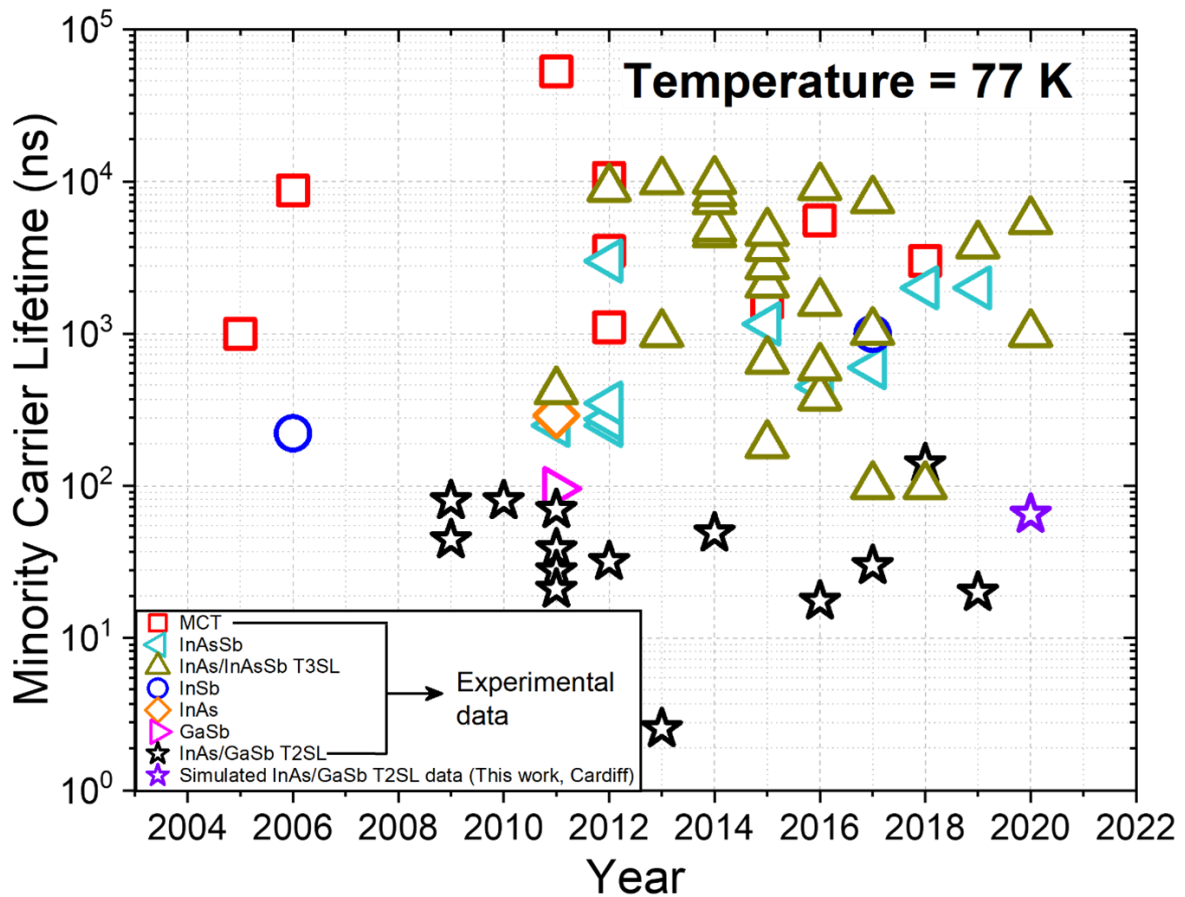
Figure 6.14: A summary of the collected experimental values of MC lifetimes at 77 K over the last few years for III-V compound semiconductors including InAs, InSb, GaSb, InAs/GaSb T2SL, InAs/InAsSb T2SL, and II-VI MCT. Our simulated (theoretical) data at Cardiff is also included for reference.

## 6.5 Development process of device fabrication

In this section, the fabrication process was developed by realising single-pixel T2SL detectors utilising dry etched (Sample C2) and a combination of dry and wet etched techniques and mesa sidewall protection (Sample C3). Different etching techniques were investigated to fabricate MWIR InAs/GaSb T2SL detectors. In this section, an alternative dry etch and a combination of dry and wet etch methods were utilised to fabricate the devices and compare them with the reference devices using the wet etching method, as reported in Section 6.3.1. The dry etching method is investigated using $BCl_3$ and Ar. Furthermore, a combination of dry and wet etch methods was experimented with utilising a sulphuric acid-based solution immediately followed by surface protection.

### 6.5.1  The realisation of mesas via the dry etching method

The dry etching process was performed as an alternative method to improve the device's performance. As discussed previously in Section 3.6.2, the dry etch has an anisotropic profile with better directionality. Not only that, but it also benefits from the etch rate's controllability. Herein, ICP was used to etch the T2SL and reactive ion gas to etch the $Si_3N_4$ hard mask, which was applied on the surface of the samples before starting the process employing a physical enhanced chemical vapour deposition (PECVD) technique, which was performed at Bristol University. A detailed description of the CR steps and procedures used to fabricate the samples using the dry etching approach is summarised in Table 6.2.

In summary, a conventional photolithography process was also used to fabricate devices with diameters between 90 and 440 µm. A 200-nm thick $Si_3N_4$ hard mask/layer was applied on the surface of the samples to prevent damaging samples during the dry etching process. The final steps were the etching process, in which the RIE approach was utilised to etch the $Si_3N_4$ mask, and the ICP etching was used to etch the SLs. It should be noted that the sidewalls were not protected with any polymers. The process flow for fabricating T2SL samples using a dry etching approach (Sample C2) is schematically depicted in Figure 6.15.

### 6.5.2  The realisation of mesas via combined dry and wet etching methods

Herein, additional steps were performed for combining dry and wet etch methods for Sample C3. Upon the completion of the dry-etched sample, it was then submerged in a sulphuric acid-based etchant to clean the mesa sidewalls and prevent the damage caused by the dry etch process. Before wet etching, the surface of the sample was spun-coated with an S1813 PR, soft-baked, exposed, and developed using the same parameters as in Table 6.1. Afterwards, the sample was immersed in $H_2SO_4$:$H_2O_2$:$H_2O$ with a ratio of 1:8:80 for three seconds. After which, the sidewalls of the sample were promptly protected with an S1813 PR to prevent oxidising the surface from ambient air.

Table 6.2: A summary of the dry etch fabrication process used to etch the MWIR InAs/GaSb T2SL sample.

| Stage | Experimental Procedure | Equipment Used | Chemicals and Materials | Descriptive Details |
|---|---|---|---|---|
| 1 | Preparation and cleaving | Scriber | None | InAs/GaSb T2SL MWIR samples were cut into small sizes of 1 cm x 1 cm |
| 2 | Cleaning | Wet bench area: chemical materials | Acetone, Methanol, and IPA | Samples were immersed in Acetone, Methanol, and IPA for 5 minutes each to clean the surface. Then, they were dried using a nitrogen gun |
| 3 | Application of $Si_3N_4$ thin layer | PECVD | $Si_3N_4$ material | A thin $Si_3N_4$ layer of around 200 nm was applied on the surface of the samples as a hard mask. The PECVD tool was used to coat the layer. This step was performed at Bristol University since this capability is not currently available at the CR at Cardiff University |
| 4 | Cleaning | Wet bench area: chemical materials | Acetone, Methanol, and IPA | Samples were immersed in Acetone, Methanol, and IPA for 5 minutes each to clean the surface. Then, they were dried using a nitrogen gun |

| 5 | Edge bead removal (EBR) and Si$_3$N$_4$ definition: first photolithography | Nano booth: spin coater and hot plate | Ti-prime and AZ-10XT positive photoresists | Bilayer photoresists were spun-coated on the surface of the samples. Firstly, the Ti-prime adhesive layer was applied to the surface of the samples by a spin coater (spinning parameters: 3000 rpm/20 seconds), followed by baking on a hot plate for 2 minutes at a temperature of 97 °C. Secondly, the AZ-10XT photoresist was applied on the surface by a spin coater (spinning parameters: 4000 rpm/45 seconds), followed by baking on a hot plate for 2 minutes at 97 °C |
|---|---|---|---|---|
| | | MJB4 mask aligner, EBR and mixed-area photolithography masks | None | To remove the photoresist at the edges, Samples were first exposed to UV light for 49 seconds through the EBR mask (this mask covers the median area of the samples and only exposes the photoresist at the edges to prevent air gap) |
| | | Wet bench | AZ-400K developer and DIW | AZ-400K developer and DIW were prepared at a ratio of (1 ml: 40 ml). Samples were immersed in the developer for 2 minutes, then rinsed quickly in DIW for 1 second and DIW for 40 seconds. Blow drying was then performed using a nitrogen gun. These steps were performed to remove the damaged photoresist at the edges |

| | | MJB4 mask aligner, mixed area photolithography mask | None | After which, samples were exposed to UV light for 49 seconds through the Si$_3$N$_4$ mask |
|---|---|---|---|---|
| | | Wet bench | AZ-400K developer and DIW | AZ-400K developer and DIW were prepared at a ratio of (1 ml: 40 ml). Samples were immersed in the developer for 2 minutes, then rinsed quickly in DIW for 1 second and DIW for 40 seconds. Blow drying was then performed using a nitrogen gun. These steps were performed to remove the damaged photoresist |
| 6 | First RIE process | RIE | SF$_6$ and N$_2$ | RIE was performed on the samples to etch the Si$_3$N$_4$ layer. RIE etching was performed with a power of around 50 W for about 28 minutes and at room temperature. RIE etched to approximately 200 nm of the mask |
| 7 | Photoresist lift-off | Wet bench area | Acetone, NPM1165 remover, IPA, and DIW | Photoresists were lifted off in Acetone for 10 minutes. They were then immersed in an NPM 1165 remover for 10 minutes, then dipped in IPA and DIW for 5 minutes each to clean the surface |

| 8 | ICP process | ICP | BCl$_3$ and Ar | After removing the photoresist, the T2SL was etched using chemicals of BCl$_3$ and Ar through an ICP etch tool. The etch depth was about 1.4 µm |
|---|---|---|---|---|
| 9 | Second RIE process | RIE and DEKTAK system | SF$_6$ and N$_2$ | RIE was again performed on the samples to etch the Si$_3$N$_4$. RIE etching was performed with a power of around 50 W for approximately 28 minutes and at room temperature |
| 10 | Top-contact definition: second photolithography | Nano booth: spin coater and hot plate | PMGISF11 and S1813SP15 positive photoresists | Bilayer photoresists were spun-coated on the surface of the samples. Firstly, the SF11 photoresist was applied to the surface of the samples by a spin coater (spinning parameters: 5000 rpm/20 seconds), followed by baking on a hot plate for 10 minutes at 97 °C. Secondly, the S1813 photoresist was then applied on the surface by a spin coater (spinning parameters: 6000 rpm/45 seconds), followed by baking on a hot plate for 5 minutes at a temperature of 80 °C |
| | | MJB4 mask aligner, mixed area photolithography mask | None | Samples were then exposed to UV light for 8 seconds through the top contact design of the photolithography mask |

| | | Wet bench | MF319 developer and DIW | MF319 developer and DIW were prepared. Samples were immersed in the developer for 15 seconds, then rinsed quickly in DIW for 1 second and DIW for 40 seconds. Blow drying was then performed using a nitrogen gun. These steps were performed to remove the damaged photoresist |
|---|---|---|---|---|
| 11 | Metal top-contact formation | PVD | Au and Cr | 20-nm and 300-nm thick layers of Cr and Au, respectively, were deposited on the surface of the samples using a thermal evaporator |
| 12 | Metals lift-off | Wet bench area | Acetone, NPM1165 remover, IPA, and DIW | Samples deposited were immersed in Acetone for 10 minutes, followed by them being immersed in an NPM 1165 remover for also 10 minutes to remove the SF11 photoresist, then they were dipped in IPA, and DIW for 5 minutes each to clean the surface |
| 13 | Metal bottom-contact formation | PVD | Au and Cr | 20-nm and 300-nm thick layers of Cr and Au, respectively, were deposited on the backside of the samples using the thermal evaporator |
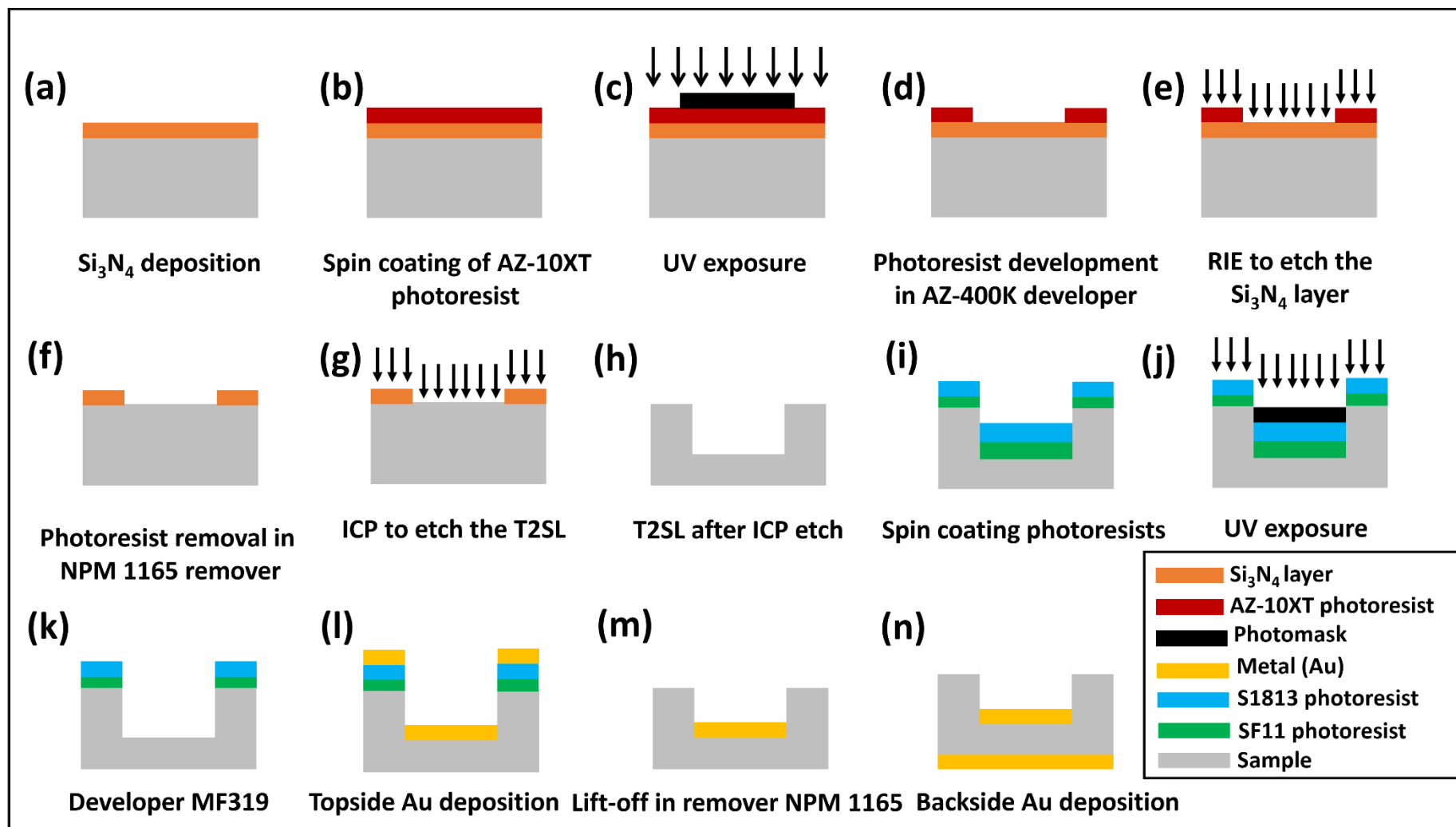
Figure 6.15: Process flow of the InAs/GaSb T2SL sample fabrication using a dry etching method.

Figure 6.16(a) shows the optical images of the Si$_3$N$_4$ etch mask deposited on the InAs/GaSb T2SL sample prior to the ICP etching of the SL. Figure 6.16(b) presents the SEM micrograph of the mesa sidewall and profile of the T2SL sample after ICP etching. It is verified that a good verticality of the etching has been maintained compared to the wet etching approach. However, there are fewer striations on the mesa sidewalls, which could be attributed to the damage caused by the etch of the Si$_3$N$_4$ layer. Optimisation of the chemistry allows for further enhancement of the etching recipe. Particularly, increasing the temperature to approximately 200°C would promote the desorption of InCl$_x$ etch by-products and is a prospective method for enhancing the sidewall morphology. Following the dry etch, a wet etch is a common method for eradicating sidewall damage. Figure 6.17 presents the optical micrograph of the finished dry + wet etched device (Sample C3), protected with a PR, with different mesa diameters varying between 440 and 90 µm.
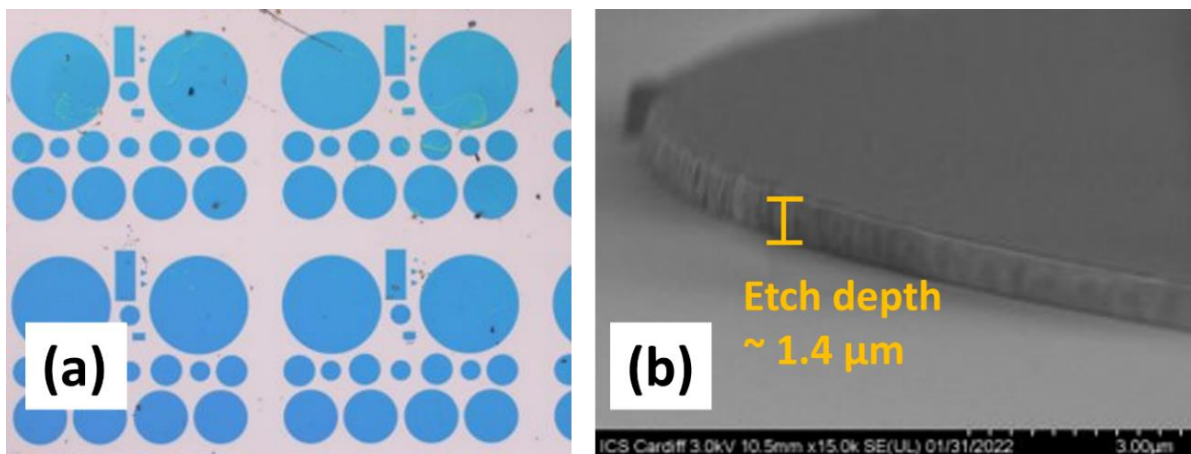


Figure 6.16: (a) Optical micrograph shows the Si$_3$N$_4$ etch mask/layer deposited on the T2SL sample, and (b) representative SEM image shows sidewalls and profiles of a T2SL sample processed employing a dry etching approach.

Figure 6.17: Optical micrograph of a MWIR InAs/GaSb T2SL fabricated device with different mesa diameters ranging from 440 to 90 μm utilising the dry + wet etch technique and surface protection with the photoresist (Sample C3).

## 6.6 Device electrical performance

A cryogenic probe station system was employed to compare the I-V characteristics of the dry-etched device (Sample C2) with those of the wet etch (Sample C1), as previously described in Section 6.3.1. The dry-etched device was also measured prior to cleaning and photoresist protection to determine the efficacy of these measures.

Figure 6.18 displays the current density versus voltage characteristics of the dry (Sample C2) and the combined dry and wet etched device (Sample C3) at different temperatures. The measured current density versus applied voltage of a 240 μm dry etched device at temperatures from 77 to 292 K is shown in Figure 6.18(a). As can be observed, the current density is 0.054 A/cm$^2$ at 77 K, and it increases to 2.837 A/cm$^2$ at 292 K at an applied voltage of -100 mV. It is worth mentioning that the dry-etched device was not passivated or protected with a photoresist, which could be the reason for this device's high dark current density. Figure 6.18(b) also shows the current density of the combined dry and wet-etched device with a mesa diameter of 440 μm. Although the mesa sidewalls of this device were protected immediately after the dry and wet etch process, an increase in the current density can still be

observed. At 120 K, the dark current density is 0.185 A/cm$^2$, and it rises to 4.523 A/cm$^2$ at 292 K at an applied voltage of -100 mV. It is believed that the increase in current density is because of wet etch, as it could add more chemical residuals into the surface sidewalls instead of cleaning them. Although the dry + wet etched samples were passivated/protected with a photoresist, the current density is believed to be increased because the recipe used was not optimum. The samples were exposed to air for a long time to measure after they were dry-etched. Some oxidations on the surface of the samples may increase the current. It is hoped that after the recipe optimisation process, the current performance should be improved as the literature shows enhanced device performance for the combined dry and wet etched devices with surface passivation [345], [346].
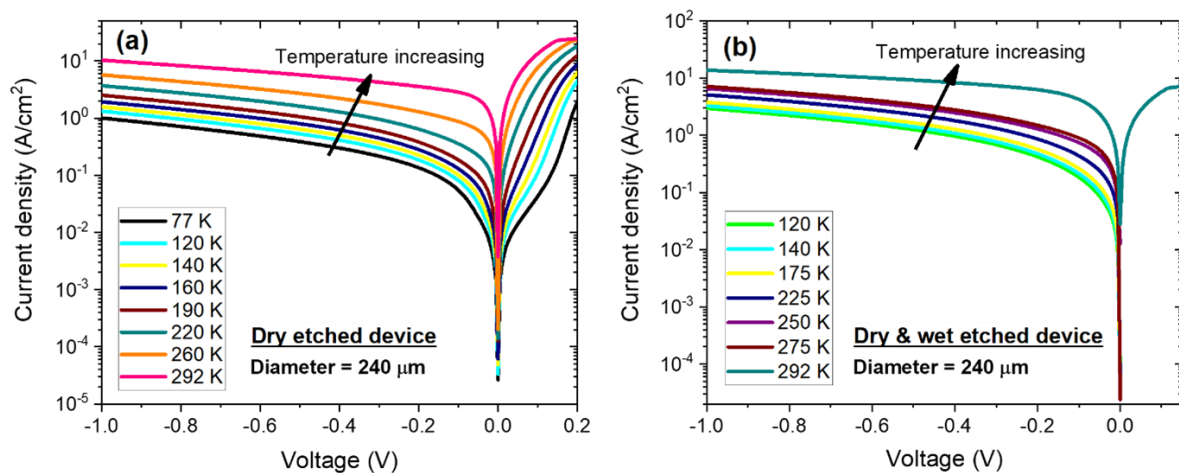


Figure 6.18: Current density-voltage characteristics for the devices with mesa diameters of 240 μm (a) the dry etched device without PR protection (Sample C2) and (b) the combined dry and wet etched device with PR protection (Sample C3).

Figure 6.19 compares the current density performance of the three devices with a diameter of 240 μm at a temperature of 90 K with different etching procedures, including wet etched (reference device using HF-based solution, Sample C1), dry etched device (Sample C2), and a combination of the dry and wet etched device (Sample C3). As can be seen, the current density of the dry-etched device did not improve after the wet etching treatment and surface protection. Comparing these results with the reference wet etched device, the current density is by far the lowest, which is almost four orders of magnitude lower than the others.
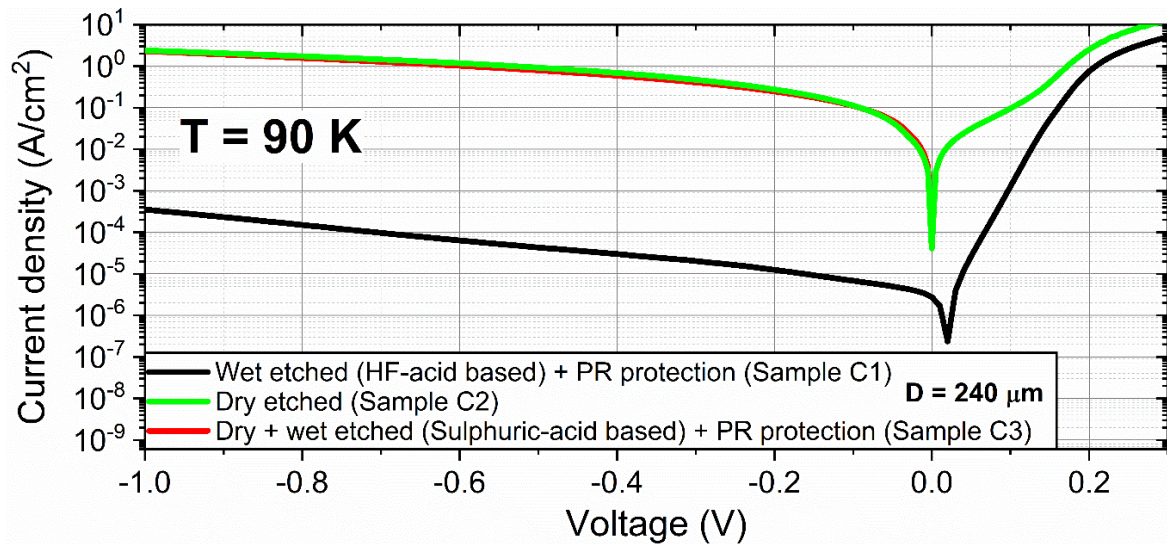
Figure 6.19: A comparative figure shows the 90 K current density of the wet etched device using HF-based solution (reference device, Sample C1), the dry etched device (Sample C2), and the dry followed by the wet etched device using the sulphuric acid-based etchant (Sample C3).

The Arrhenius plot in Figure 6.20 reveals the dark current limiting mechanisms of the devices. The current density is plotted against the inverse temperature of the etched devices with a diameter of 240 μm at an applied voltage of -100 mV. As presented previously, it appears that the current density of the reference wet etched device is limited to diffusion current at higher temperatures above 136 K and G-R current at lower temperatures below 136 K. However, it seems that the diffusion current of the newly fabricated devices of the dry and combined dry and etched devices begins at a much higher operating temperature above 170 K and G-R current at the temperature range between 77 and 170 K. Though the current density of the wet etched device (Sample C1) is four orders of magnitude lower compared to the dry etched (Sample C2) and dry + wet etched (Sample C3) devices at low temperature (77 – 150 K), the current density is reasonably comparable at higher temperatures indicating the suitability of using these devices for HOT applications.
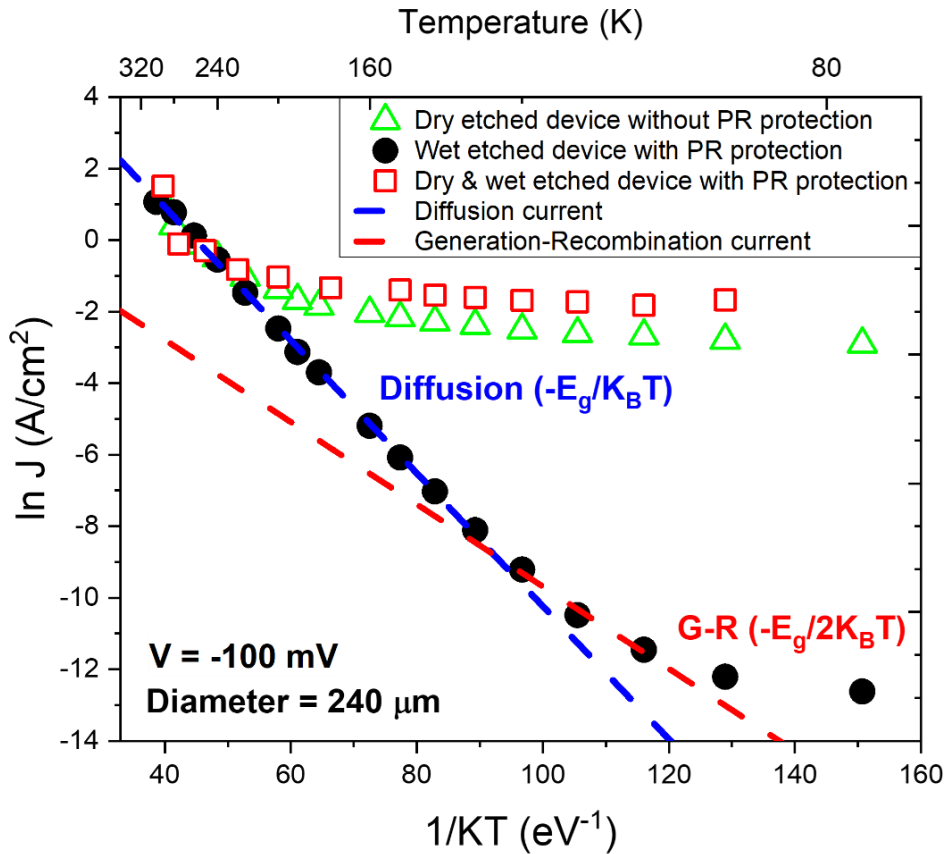
Figure 6.20: Arrhenius plot shows the current density as a function of inverse temperature for the three etched devices with a mesa diameter of 240 μm using HF-based wet etch (reference device, Sample C1), dry etch (Sample C2) and a combination of dry and wet etch (Sample C3).

Although the current density of the dry and wet etched device with surface protection is higher than the other dry etched device with no surface protection, it can be seen from the P/A ratio analysis that the dark current has only a slight variation with the P/A ratio for the protected device with a PR (Figure 6.21). This means that surface protection/passivation seems to be more effective in minimising the variations in current density since the samples were coated with a photoresist compared to the un-passivated sample.
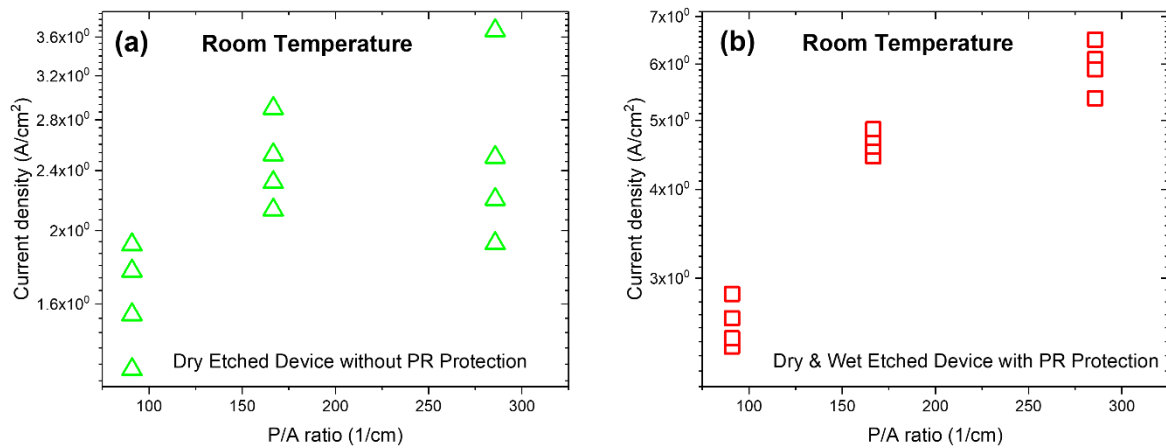
Figure 6.21: Current density versus P/A ratio analysis at room temperature and -50 mV for (a) the dry etched device without PR protection (Sample C2) and (b) the dry etched device followed by wet etching with PR protection (Sample C3).

## 6.7 Device modelling

The J-V modelling was also performed on the dry etched device (Sample C2) and the combined dry and wet etched device (Sample C3) to verify the I-V experimental results. The results are discussed in the following sections.

### 6.7.1 Modelling of the dry-etched device

To further examine the device performance, modelling of the dry etched device (Sample C2) was also performed at low, intermediate, and high temperatures of 110 K, 200 K, and 300 K, respectively. Figure 6.22 shows the measured J-V characteristics at those temperatures, and the dashed lines highlight the dark current density at an applied bias of -100 mV. As can be seen, the G-R process dominates the dark current at temperatures of 110 and 200 K at the whole applied bias from zero to -1 V. However, the diffusion current dominates at room temperature, specifically below an applied bias of -400 mV. TAT current is also predominant at high applied voltage at those modelled temperatures. These results are also consistent with the Arrhenius plot shown previously in Figure 6.20.
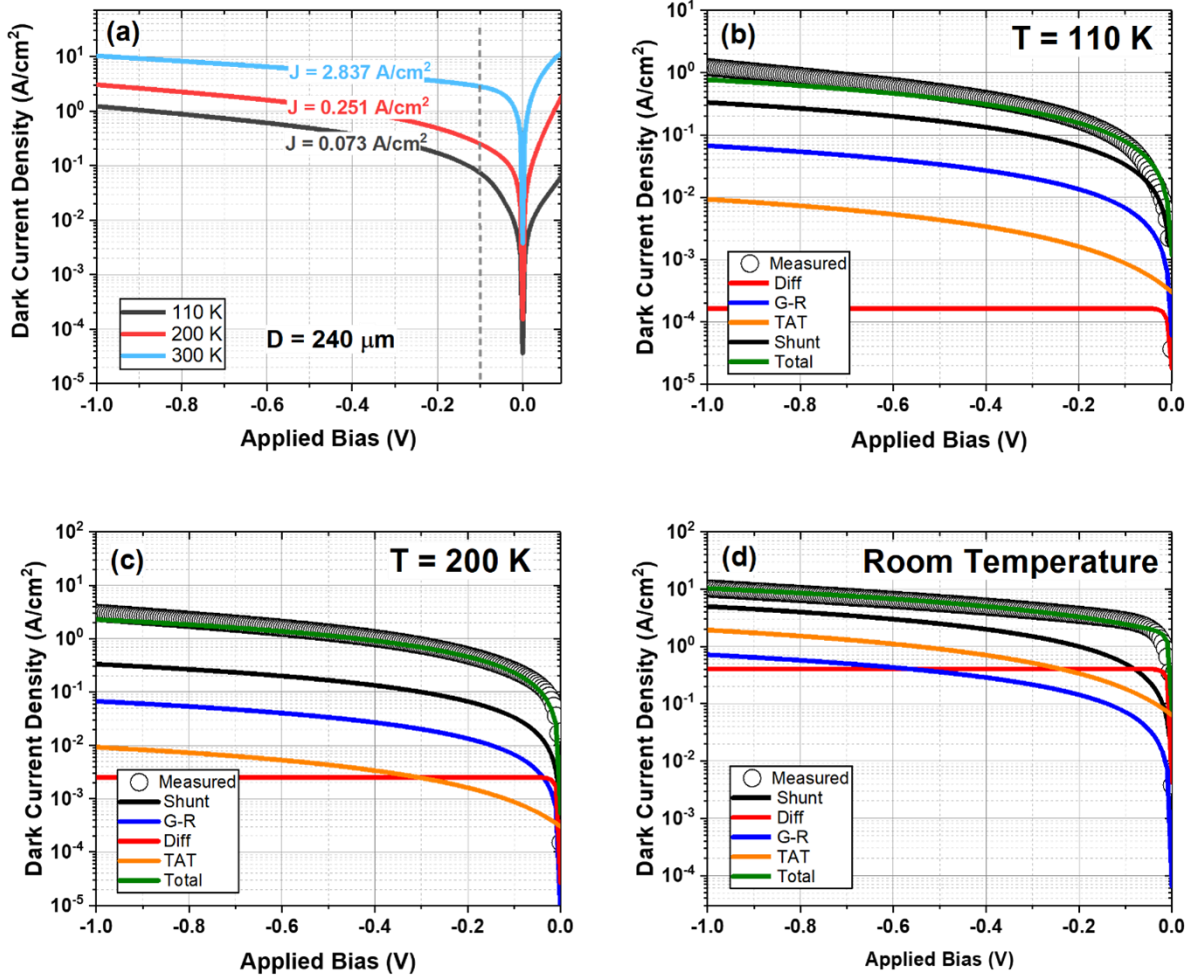
Figure 6.22: (a) Measured dark current density versus applied bias characteristics of the ICP-RIE dry etched devices with a mesa diameter of 240 μm (Sample C2) at temperatures of 110 K, 200 K, and 300 K. Modelled dark current density under applied bias at temperatures of (b) 110 K, (c) 200 K, and (d) 300 K.

### 6.7.2  Modelling of the combined dry and wet etched device

Similarly, the dry + wet etched device (Sample C3) was modelled at the same range of temperatures as shown in Figure 6.23. The J-V characteristics are herein similar to the dry etched device. As observed, the G-R process dominates the dark current at temperatures of 110 and 200 K at the whole applied bias from zero to -1 V. However, the diffusion current dominates at room temperature, specifically below an applied bias of -400 mV. TAT current is also predominant at high applied voltage at those modelled temperatures. These results are also consistent with the Arrhenius plot shown previously in Figure 6.20.
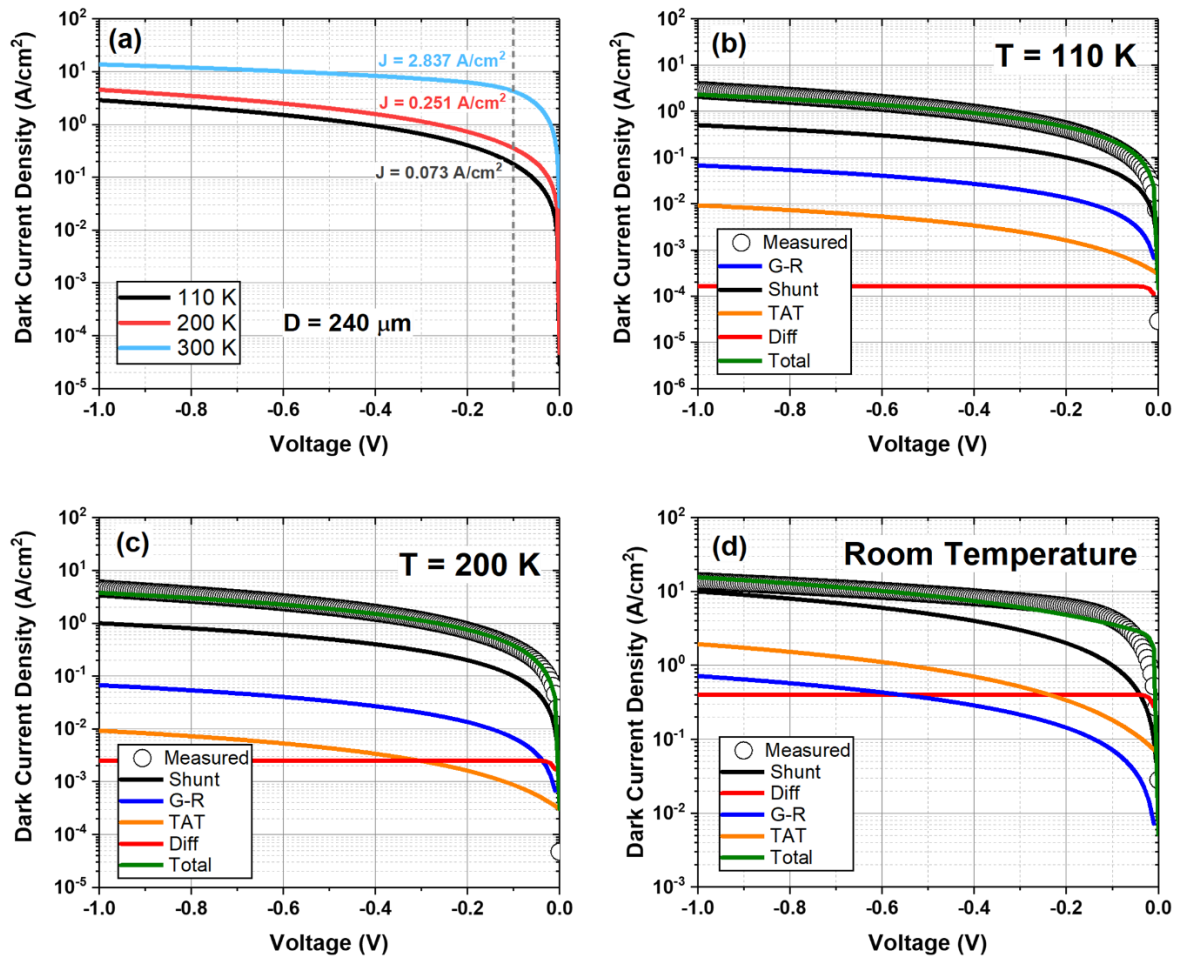
Figure 6.23: (a) Measured dark current density versus applied bias characteristics of the combined dry and wet etched devices with a mesa diameter of 240 μm (Sample C3) at temperatures of 110 K, 200 K, and 300 K. Modelled dark current density under applied bias at temperatures of (b) 110 K, (c) 200 K, and (d) 300 K.

## 6.8    Discussion/comparison of device performance

To compare the electrical performance of the fabricated devices with the current-state-of-art devices reported in the literature, the dark current density was plotted as a function of the temperature for the devices at a HOT between 120 and 250 K and an applied bias in the range between 50 and 450 mV. Herein, Figure 6.24 depicts the dark current density performance of the devices at the whole temperature range compared to the MCT's ''Rule 07''. The dark current density is compared with other photodiodes and detectors based on III-V InSb [95], InAsSb [347], InAs/GaSb T2SL [149], [246], InAs/InAsSb T2SL [175], [348], and II-VI HgCdTe (MCT) [349] barrier and non-barrier structures having cut-off wavelengths in the range between 4 and 6 μm and at an applied bias between 50 and 450 mV.

Generally, it can be observed that the current density of our devices is almost one to four orders of magnitude higher compared to the MCT's "Rule 07", but it also depends on the operating temperature and cut-off wavelength of the device. The dark current density of our wet etched device (Sample C1) is noticeably improved as the current density is almost an order of magnitude lower than the other etched devices using different methods, especially at lower operating temperatures. As can also be seen, our T2SL fabricated devices have ultimately shown a better dark current density performance compared to non-barrier photodiodes based on bulk InSb [95] and InAsSb [347]. In comparison with other T2SLs based on ''Ga-containing'' InAs/GaSb *nBn* (barriers) [246] and ''Ga-free'' InAs/InAsSb *pin* (non-barriers) [175], our device has demonstrated a somewhat increased dark current density at the temperature range of 120 to 150 K. However, the dark current density is almost comparable at a higher temperature above 160 K. As discussed earlier, the barrier designs are advantageous as they mitigate or even suppress the G-R current, which is dominant in non-barrier-based detectors. The barrier detectors have several structures, which can be *nBn* (top and bottom layers have the same doping type), *pBn* (top and bottom layers do not have the same doping type), M-structure (it has an AlSb barrier layer between the InAs and GaSb SL layers forming an electron barrier for InAs and a double QW for holes in GaSb layer). Our recent review paper contains other novel structures [350]. In the case of barrier detectors, it is observed that the current density is almost close to Rule 07 with two orders of magnitude to a few times higher than ''Rule 07'', which is due to the incorporation of the barrier layer into the structure.

Compared to the HgCdTe/MCT *nBn* [349] and InAs/GaSb T2SL *PNn* [149], ''Al-free'' barrier structures, the dark current density of our device is about one order of magnitude higher at the whole temperature range. This is due to the use of a novel barrier structure such as *PNn* and because of the longest minority carrier lifetime for the MCT [124], [125]. Lastly, as can be seen, the lowest dark current density is achieved using a Ga-free T2SL *nBn* barrier structure where the dark current density is by far almost two to three orders of magnitude lower compared to our device performance which is owing to the much longer MC lifetime [81], [82] and better defects tolerance [88] for the Ga-free material system.

These findings suggest that our devices have the potential to operate at higher temperatures; however, further improvement in dark current performance could be achieved by minimising

or even eradicating the contribution of G-R SRH current via incorporating a barrier layer above the absorption region [142], [161], [351], [352], [353] so that the recombination processes can occur within the barrier layer and not in the T2SL absorption region. In addition to that, the surface leakage current can be possibly mitigated through the use of some passivation methods by applying proper chemical materials, such as sulphide (S), ammonium sulphide $(NH_4)_2S$, or fluoride-based treatments and physical materials, including $SiO_2$, $Si_3N_4$, or $Al_2O_3$ over the mesa sidewall of the surface where this has shown a reduction in the overall dark current density of the devices by about two to three orders of magnitude compared to non-passivated devices [169], [204], [207], [256], [260], [268], [269], [354], [355], [356].
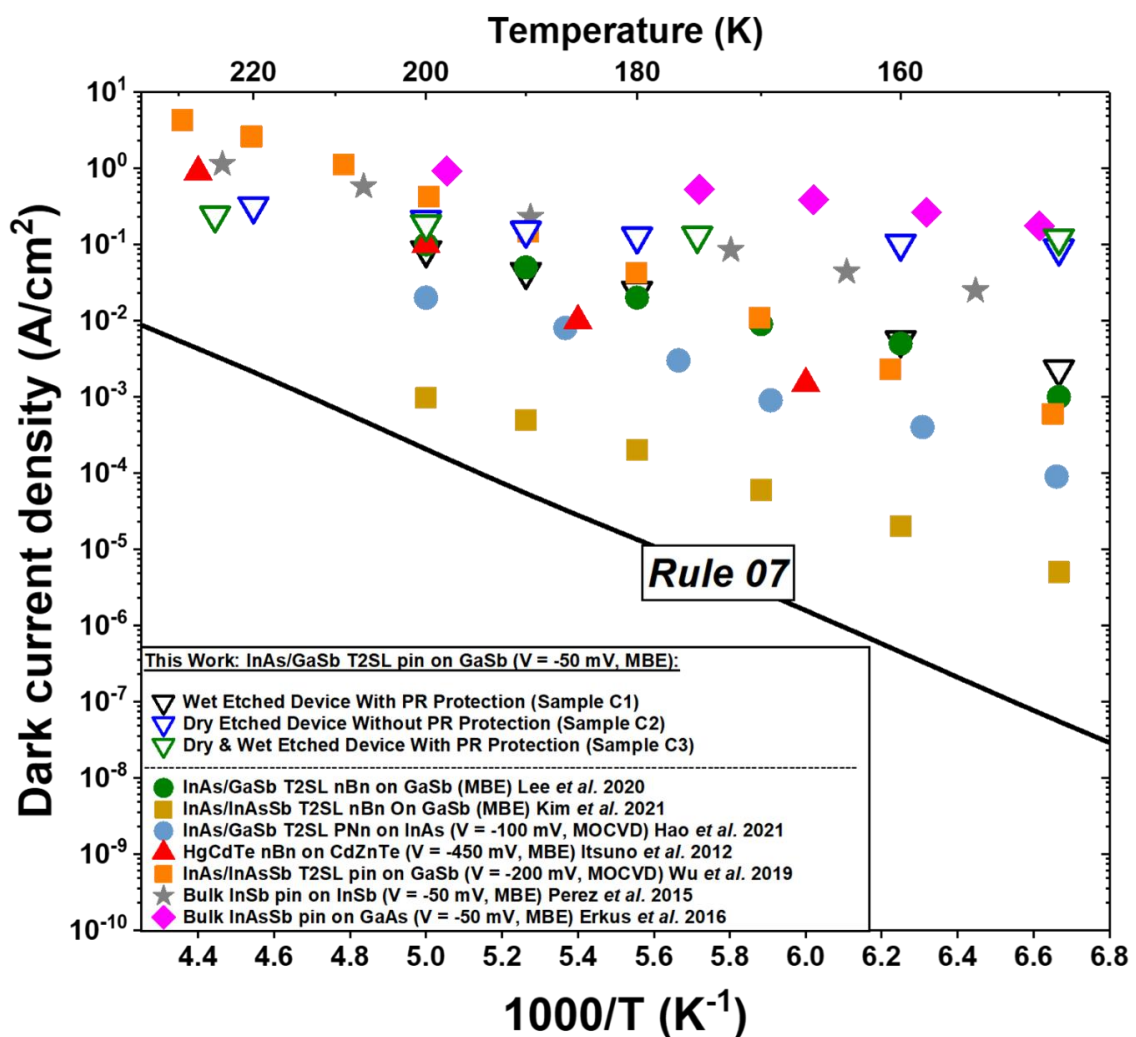


Figure 6.24: A comparative ''Rule 07'' plot of dark current density versus temperature of our T2SL devices with II-VI MCT detectors and III-V MWIR-based barriers/non-barriers, including III-V bulk InSb, InAsSb, InAs/InAsSb and InAs/GaSb T2SLs. Our work at Cardiff is included for reference.

Figure 6.25 depicts the dark current density as a function of cut-off wavelength for InAs/GaSb and InAs/InAsSb T2SL devices reported in the literature compared with MCT's ''Rule 07'' at low and HOT. The data in the figure was collected from the literature, as already presented in Table 3.2. The fabricated samples at Cardiff (C1, C2, and C3) using different etching schemes are included for reference. As can be observed, the dark current density of our fabricated samples is generally ten to seven orders of magnitude higher than the MCT's ''Rule 07'' at 77 K. However, the dark current density of our fabricated samples is almost five to four orders of magnitude comparable to the MCT's ''Rule 07'' at 150 K. It is evident that the dark current density of the wet etched sample (Sample C1) is improved by almost four orders of magnitude at low temperature and one order of magnitude at HOT compared to the other dry and combined etched samples (C2 and C3).
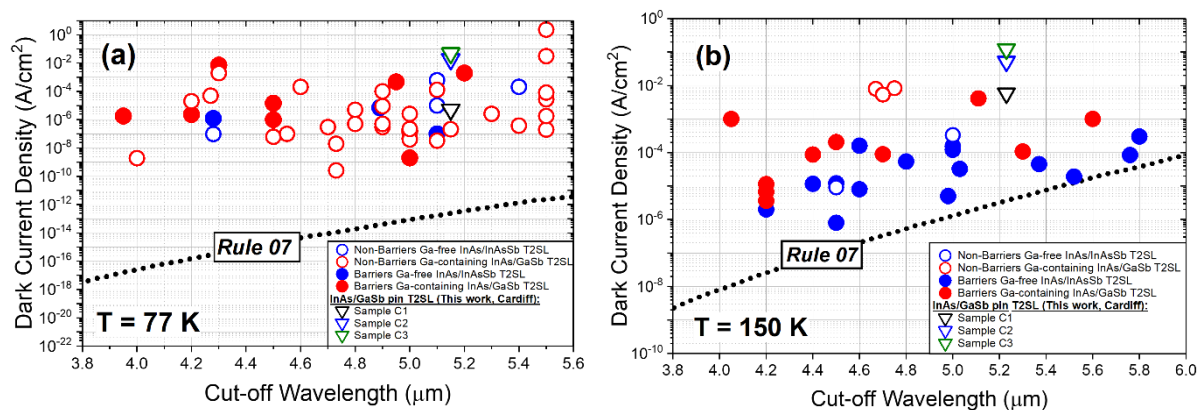


Figure 6.25: Accumulated values of dark current density versus cut-off wavelength for Ga-containing and Ga-free T2SL detectors in comparison with MCT's ''Rule 07'' at (a) low temperature of 77 K and (b) HOT of 150 K. Our work at Cardiff is included in the figure for reference.

Lastly, Figure 6.26 depicts the $R_dA$ product versus the cut-off wavelength for Ga-based and Ga-free T2SLs compared to the MCT's ''Rule 07'' at room temperature operation. Data in the plot were accumulated from different research groups, including MCT [200], Ga-free T2SL [208], [209], [210], [211], and Ga-based T2SL [96], [197], [200], [212] detectors. The $R_dA$ products of our fabricated T2SL samples (C1, C2, and C3) are also included for reference. As can be seen, the RdA products are comparable with the current state-of-the-art T2SL detectors and approach the MCTS's ''Rule 07'' at room temperature operation.
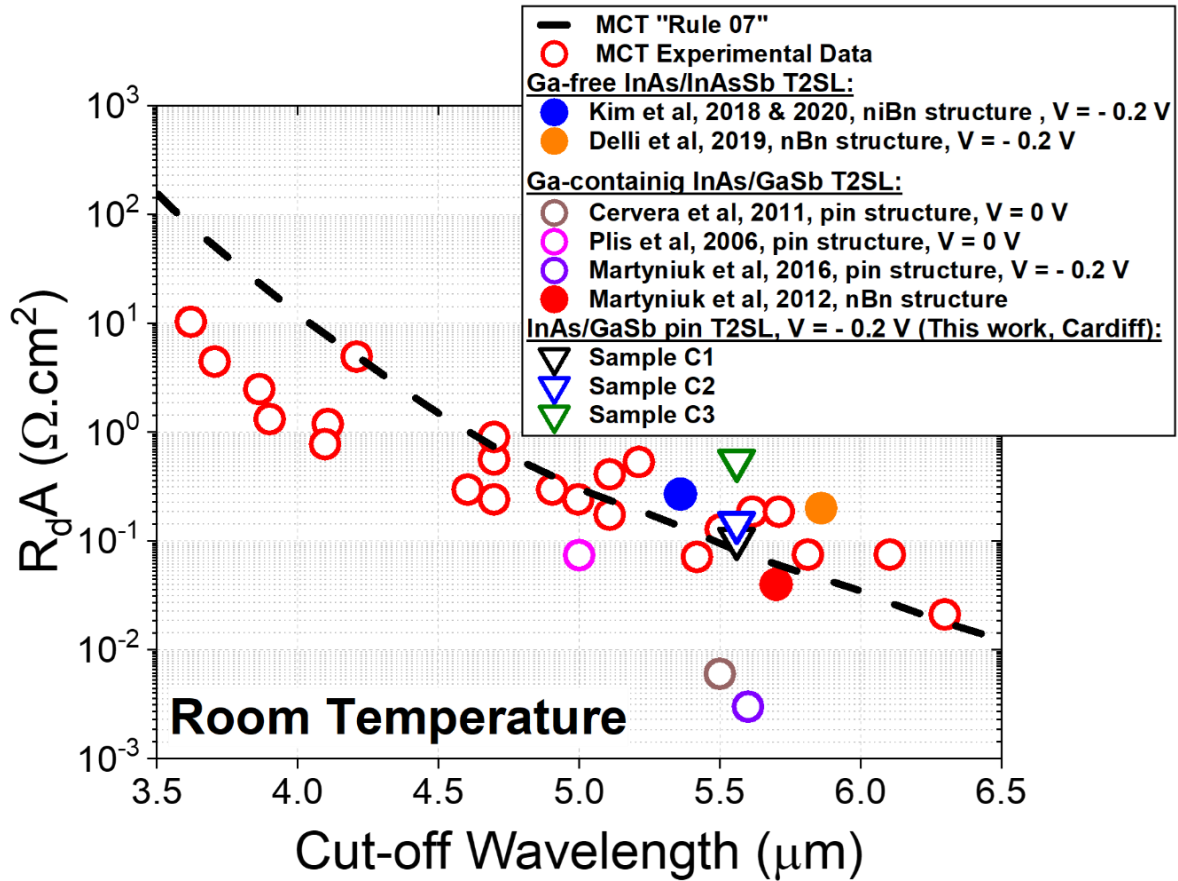
Figure 6.26: Collected values of $R_dA$ products versus cut-off wavelength of T2SL and MCT detectors at room temperature operation. Our work at Cardiff is included in the figure for reference.

## 6.9 Summary

This chapter has detailed the fabrication of MWIR Ga-containing InAs/GaSb T2SL devices using different etching techniques, including wet etch, dry etch, a combination of dry and wet etch, and surface passivation. It has been demonstrated that the etching methods play an essential role in optimising the performance of the devices. This report showed that the best-performing device is realised by the wet etch process using HF-based solution. The performance of the devices in this work was compared to that of the current state-of-art devices and the well-known MCT's Rule 07 reported in the literature. It is demonstrated that the current density of our fabricated devices is almost one to four orders of magnitude higher compared to the MCT's ''Rule 07'', but it also depends on the device's operating temperature and cut-off wavelength. It is also found that the dark current density of our HF-based wet etched device is significantly improved as the current density is almost four orders of

magnitude lower than the other etched devices using different techniques, particularly at lower operating temperatures. It is hoped that with further improvement in the device design, such as incorporating a barrier layer above the absorbing region and/or applying an effective surface passivation material, the performance of these devices could be significantly enhanced.

# Chapter 7: Wet Etching Process Developments of Antimonide-Based Structures

## 7.1    Introduction

The dry etching process has several advantages, including an anisotropic etching profile, sharp etch edges and less surface oxidation of the Al-containing material. However, the crystallographic damage to the surface caused by the ion bombardment is the main limitation of this method. An alternative approach is the wet-chemical etching mechanism, which is preferred for some applications, especially if thin films must be removed without crystallographic damage to the surface. It has been reported that InAs-based structures can be etched selectively against GaSb using a highly selective citric acid solution [248] with a maximum selectivity of about 127:1. Recently, an etchant based on hydrochloric (HCl) acid was reported with good selectivity between the InAs and GaSb materials [249]. However, a selective etchant is required for GaSb-based materials in order to selectively etch GaSb while retaining the thin layers of the other material.

Antimonide-based materials exhibit unusual etching behaviours, such as undesired weak etching and a very fast oxidation rate with atmospheric oxygen, which differs from other III-V materials, such as phosphide and arsenide [357]. It is also pointed out that HF etches plasma-exposed antimonides, unlike other III-Vs [357]. Moreover, GaSb and its alloys show poor selectivity in commonly used wet and dry etchants typical in other III-V device processing. This chapter, therefore, provides preliminary results of the wet etching process and electrical characterisation of T2SL and other III-V materials, including GaSb substrate (Sample D), InAs thin films (Samples E and F), InAs/GaSb T2SL (Sample G), InGaAs (Sample H), AlGaAsSb (Sample I), and InAs/AlSb T2SL (Sample J). Various etchants are used and investigated as an alternative to HF-based etching, including phosphoric, sulphuric, citric, and hydrochloric acids. Table 7.1 summarises the wet etch optimisation processes, recipes, and outcomes.

Table 7.1: A summary of wet etching optimisation processes, recipes, and outcomes.

| Step | Material | Type of Structure | Chemicals Used | Etch Rate (nm/min) | Outcomes | | Electrical Performance Current-Voltage (I-V) |
|------|----------|-------------------|----------------|--------------------|----------|---|----------------------------------------------|
| | | | | | Successes | Shortcomings | |
| 1 | GaSb substrate (Sample D) | Non-device | H₃PO₄ and H₂SO₄ | N/A | N/A | Rough surface and damage caused by chemical reactions | N/A |
| 2 | InAs thin film on GaAs substrate (Sample E) | Non-device | H₃PO₄ and H₂SO₄ | 1100 and 500 | Much smoother surface and smother sidewalls were observed by Dektak and the optical microscope | Mesa undercut is present, especially with longer etch time/deeper etch | Performed at room temperature, and expected I-V result was achieved |
| | InAs thin film on InAs substrate (Sample F) | *pin* device | | | | | |
| 3 | InAs/GaSb T2SL on GaAs substrate (Sample G) | | H₃PO₄ and H₂SO₄ | N/A | N/A | Rough surface and damage caused by chemical reactions. A | N/A |

Table 7.1: A summary of wet etching optimisation processes, recipes, and outcomes.

| Step | Material | Type of Structure | Chemicals Used | Etch Rate (nm/min) | Outcomes | | Electrical Performance Current-Voltage (I-V) |
|------|----------|-------------------|----------------|--------------------|----------|---|----------------------------------------------|
| | | | | | Successes | Shortcomings | |
| 1 | GaSb substrate (Sample D) | Non-device | $H_3PO_4$ and $H_2SO_4$ | N/A | N/A | Rough surface and damage caused by chemical reactions | N/A |
| 2 | InAs thin film on GaAs substrate (Sample E) | Non-device | $H_3PO_4$ and $H_2SO_4$ | 1100 and 500 | Much smoother surface and smother sidewalls were observed by Dektak and the optical microscope | Mesa undercut is present, especially with longer etch time/deeper etch | Performed at room temperature, and expected I-V result was achieved |
| | InAs thin film on InAs substrate (Sample F) | *pin* device | | | | | |
| 3 | InAs/GaSb T2SL on GaAs substrate (Sample G) | | $H_3PO_4$ and $H_2SO_4$ | N/A | N/A | Rough surface and damage caused by chemical reactions. A | N/A |

| | | | | | | possible reason is the GaSb top layer | |
|---|---|---|---|---|---|---|---|
| | | Non-devices | $C_6H_8O_7$-based etchant | N/A | N/A | A very rough surface and no etch were observed. This could also be due to the top GaSb cap layer | N/A |
| 4 | InGaAs on InP substrate (Sample H) | *pin* devices | $H_2SO_4$ | 400 | Very smooth surface and accurate etch profile | Less etch rate compared to the InAs material. This could be due to incorporating multiple thin layers of different materials within the structure. Also, a slight mesa undercut is observed by SEM images | I-V obtained |
| 5 | AlGaAsSb thin film on InP substrate | *pin* devices | HCl-based etchants | 285 | | Less smooth surface and non- | I-V obtained |

| | | | | | | | |
|---|---|---|---|---|---|---|---|
| | (Sample I) | | | | | uniform etch profile observed by Dekatk | |
| 6 | InAs/AlSb T2SL on GaSb substrate (Sample J) | Device | HCl-based etchant (Test Etch) | Determined previously | Etch observed 5.8 μm by Dektak Profiler | Very rougher surface caused by chemical reactions – over etched structure and non-uniform etch profile | I-V obtained |
| | | | HCl-and-H$_2$SO$_4$ etchants (Real Etch) | | Etch observed 1.8 μm by Dektak Profiler | Lesser rough surface caused by chemical reactions and non-uniform etch profile | I-V obtained and characteristics improved |

204

## 7.2    Preparation of etching solutions

The etchants used in the etching developments/tests for this research project are provided in Table 7.2. The phosphoric acid-based solution was prepared in the following sequences. 1 ml of deionised water (DIW) was added first, 1 ml of hydrogen peroxide ($H_2O_2$) was followed, and 1 ml of phosphoric acid ($H_3PO_4$) was added at the end. Similarly, but with a different ratio, 80 ml DIW was added first for the sulphuric acid-based etchant ($H_2SO_4$), followed by adding 8 ml of $H_2O_2$. Later, $H_2SO_4$ was added. In the case of a hydrochloric acid-based solution (HCl), 10 ml of DIW was added first, followed by 2 ml of $H_2O_2$, and lastly, I ml of HCl was added. For the citric acid-based etching, preparation was performed from anhydrous citric acid crystals, which were dissolved in DWI at a ratio of 1 g:1 ml. To mix the citric acid-based solution, 100 ml of DIW was first added, 20 ml of $H_2O_2$ was followed, and 10 ml of $C_6H_8O_7$ was added. Note that solutions in each case are left for around 10 minutes to settle down before the etching is performed.

Table 7.2: A variety of etchants used in this research project.

| Solution | Symbol | Recipe | Ratio (ml) |
|---|---|---|---|
| Phosphoric acid based | SA | $H_3PO_4$:$H_2O_2$:$H_2O$ | 1:1:1 |
| Sulphuric acid based | SB | $H_2SO_4$:$H_2O_2$:$H_2O$ | 1:8:80 |
| Citric acid based | SC1 | $C_6H_8O_7$:$H_3PO_4$:$H_2O_2$:$H_2O$ | 15:20:12:40 |
| | SC2 | | 0.54:2:1.2:40 |
| Hydrochloric acid based | SD1 | HCl:$H_2O_2$:$H_2O$ | 100:1:100 |
| | SD2 | | 1:2:10 |

## 7.3    Etching

To achieve a good and reasonable result, the author repeatedly and systematically performed experiments with different interval etching times for each material experiment. Etching was performed for 1 min, 2 min, 3 min, 4 min, and 5 min to calculate the etching rate and a

standard deviation. After etching, the photoresist was removed utilising acetone and IPA to clean the surface. A Dektak profiler was used to determine the etching depth of each material.

## 7.4 Developments of the wet etching process

Sample details and structures used to optimise recipes are depicted in Figure 7.1. It is worth remarking that some of these processes are performed as recipe development, meaning that only materials are used as a test. Herein, standard photolithography and metal deposition steps were performed to fabricate devices. Only the mesa photolithography step was carried out for non-devices to perform the initial wet etching process.
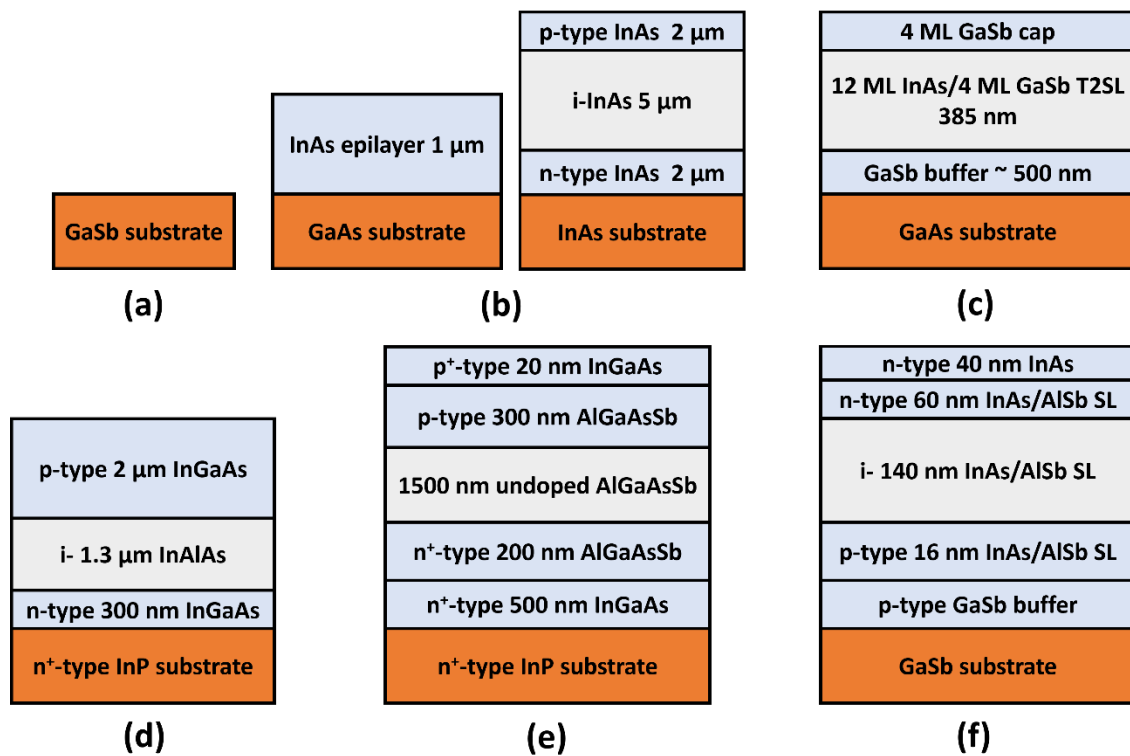


Figure 7.1: Structure of samples used to optimise the wet etch recipes in this research project. (a) GaSb substrate (Sample D), (b) InAs thin film on GaAs (Sample E) and InAs pin photodiode on InAs substrates (Sample F), (c) InAs/GaSb T2SL on GaAs substrate (Sample G), (d) InGaAs pin on InP substrate (Sample H), (e) AlGaAsSb pin on InP substrate (Sample I), and (f) InAs/AlSb T2SL on GaSb substrate (Sample J).

### 7.4.1  Phosphoric-and-sulphuric acid-based solutions

Phosphoric acid and sulphuric acid solutions were attempted for etching GaSb (Sample D), InAs (Samples E and F), and InAs/GaSb T2SL (Sample G). First, for the GaSb material, both

solutions were prepared as described earlier. The sample was dipped in the solutions several times to observe the etch rate. Figure 7.2 shows the optical micrographs of the GaSb material after etching for 1 min and 5 min. Herein, we found no etch was seen, and the chemical reactions damaged the surface.
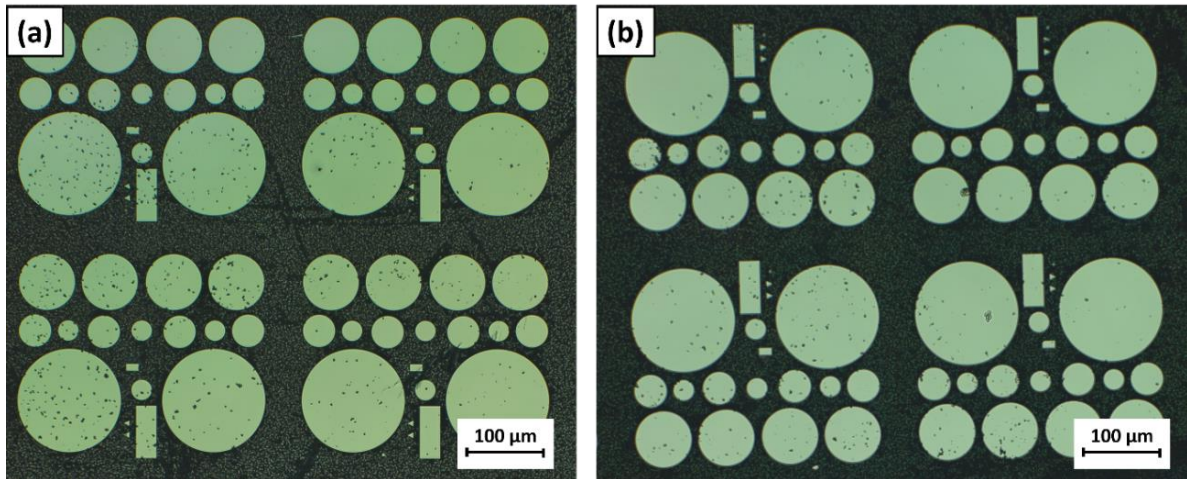


Figure 7.2: Optical micrograph shows the GaSb material (Sample D) after (a) 1 min and (b) 5 min of etching using phosphoric and sulphuric acid-based solutions.

The same solutions were used to etch the InAs *pin* photodiode structure (Sample F). Before this, trial InAs thin films on GaAs substrate samples (Sample E) were used to optimise the recipes. For the recipe calibration, interval etching times were first performed to obtain an accurate etch rate for both solutions. The sample was etched from 1 to 8 min to attain the etch rate. Figure 7.3 depicts the etch rate for solutions A and B (abbreviated as SA and SB). The etch rate for SA is 1 µm/min, much faster than that for SB (0.41 µm/min). Furthermore, the etchants appear more suitable for etching InAs against GaSb material. Figure 7.4 shows the optical micrographs of the etched InAs samples.
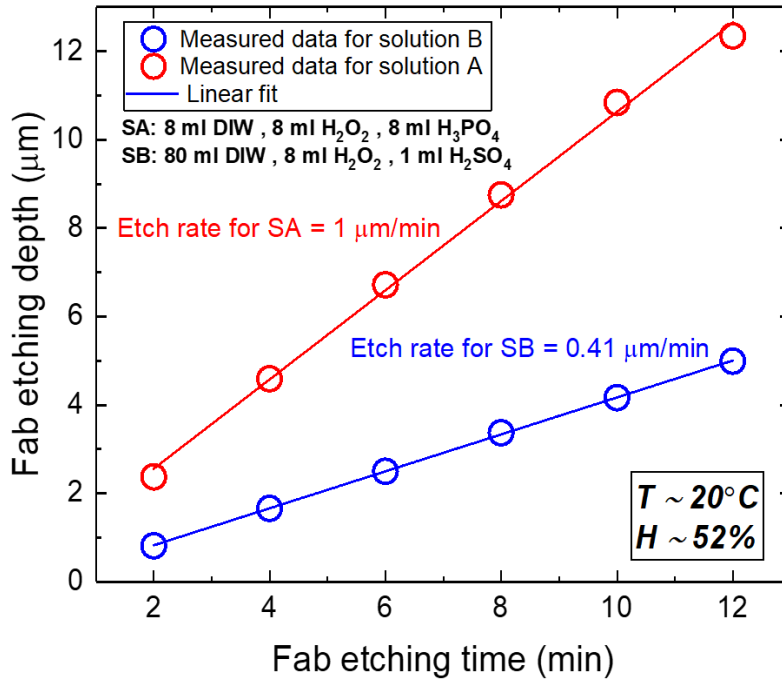
Figure 7.3: Calibration of etch rate for SA and SB using InAs thin film samples.
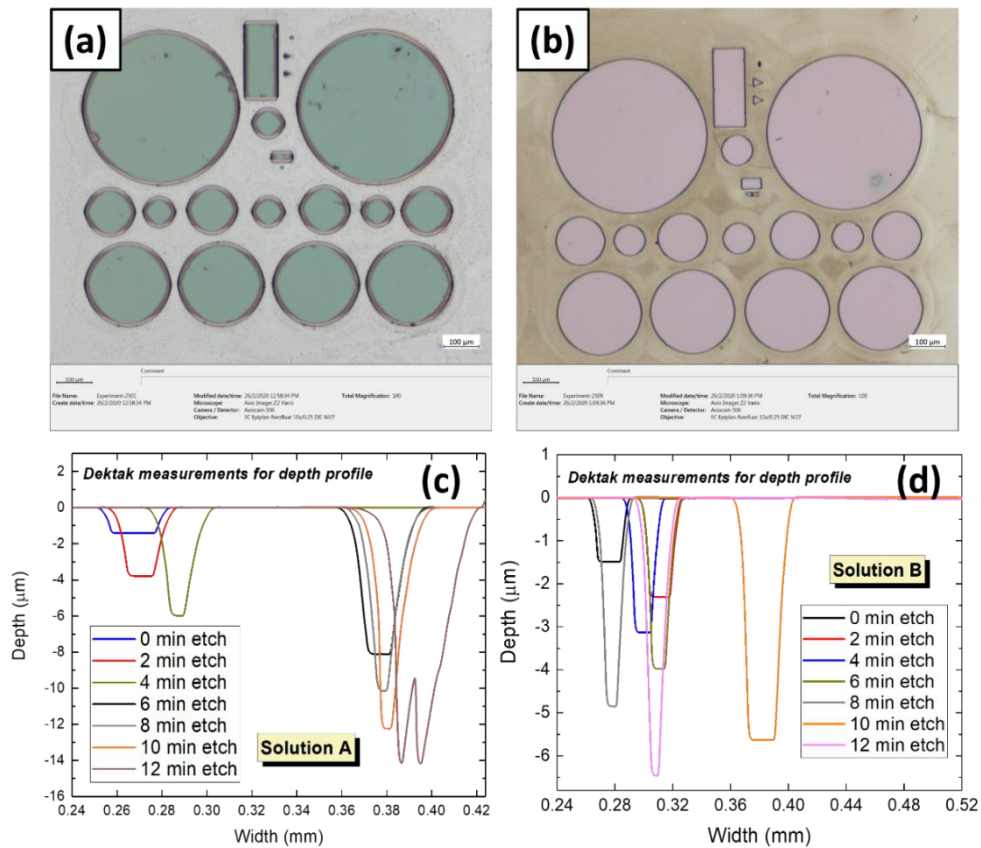


Figure 7.4: Optical micrographs of the InAs etched samples in (a) SA and (b) SB for 12 min each. Dektak profiles of the samples after etching several times to determine the etch depth in (c) SA and (d) SB.

Based on the recipe optimisation and etch rate calibration, the InAs *pin* photodiode (Sample F) was fabricated and etched in SA for 7 min and in SB for 30 seconds to get an etch depth of around 5.09 μm and smoother semiconductor surface as shown in Figure 7.5(a). Figure 7.5(b) shows the current density (J-V) characteristics of the fabricated device at room temperature. It is found that a dark current density of around 7.5 A/cm$^2$ is achieved at an applied voltage of -100 mV, which is comparable to other InAs *pin* devices reported in the literature [311].
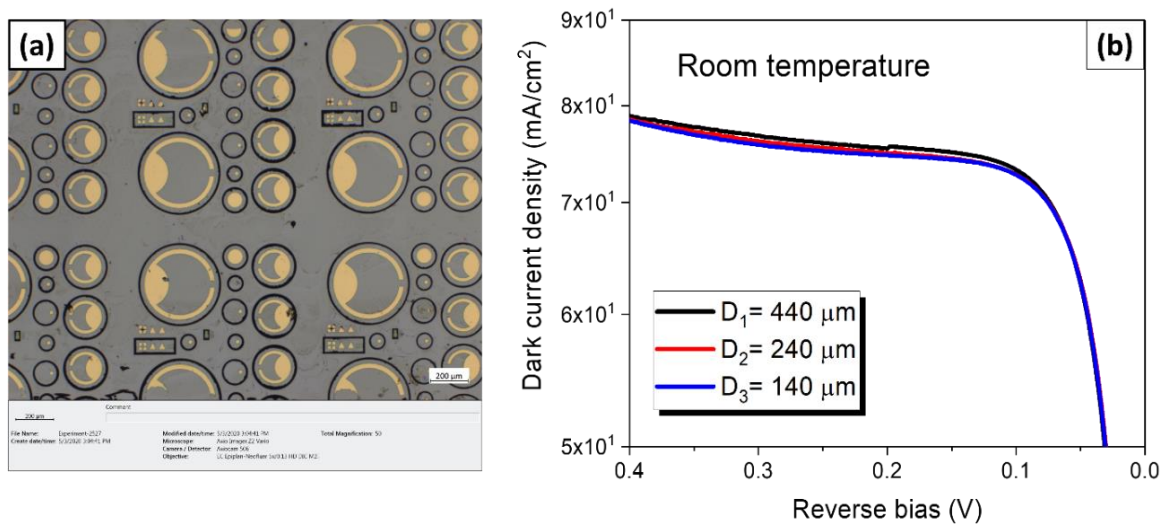


Figure 7.5: (a) Optical image of the InAs *pin* samples etched for 7 min and 30 sec in SA and SB, respectively and (b) the dark current density of the fabricated device at room temperature.

Once the InAs *pin* devices were fabricated and ensured that the recipe worked well, the InGaAs *pin* structure (Sample H) was fabricated as shown schematically in Figure 7.1(d). This structure contains layers of InGaAs and InAlAs. The optimised recipe SB was used to fabricate several devices for this structure. We carried out a standard photolithography process and metallisation. Two samples were etched; the first one was etched in SB for 7 min to achieve the desired etch depth of around 3.8 μm. Another sample was etched in the same solution for 7 min and 10 sec to get an etch depth of approximately 3.6 μm. The longer etch time should result in a deeper etch; however, since the solution was left over for more than half an hour, the etch rate became slow, resulting in a lesser etch depth. Figure 7.6 shows the optical images of the fabricated InGaAs *pin* devices. As can be seen, a clean semiconductor surface is obtained. However, the mesa sidewalls are not vertical (isotropic profile) because of the etch rate caused by the chemical etchants and reactions, as seen from the SEM images in Figure 7.7.
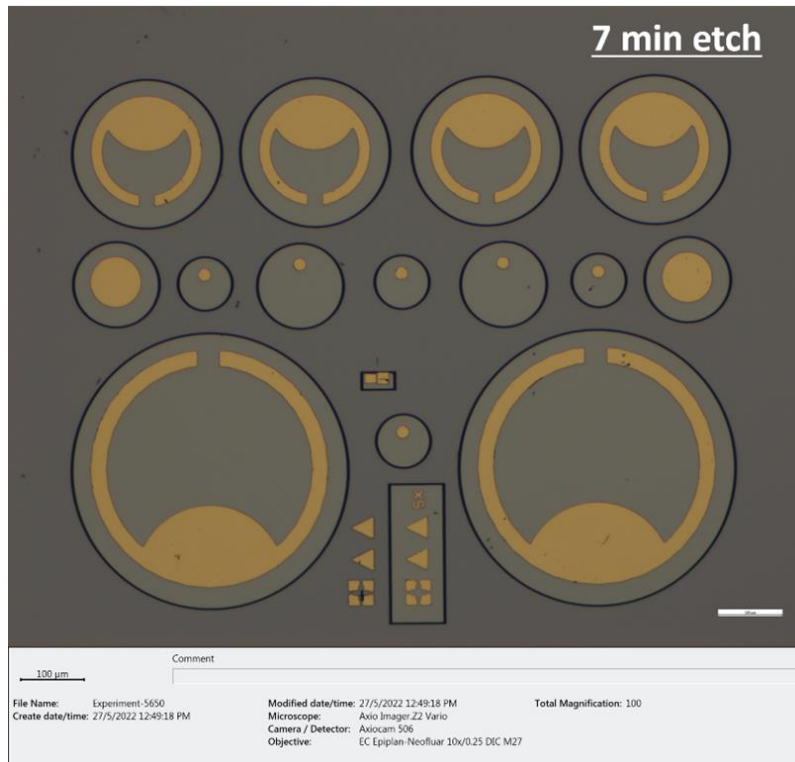
Figure 7.6: Optical micrographs of the fabricated devices of Sample H after 7 min etch using recipe SB.
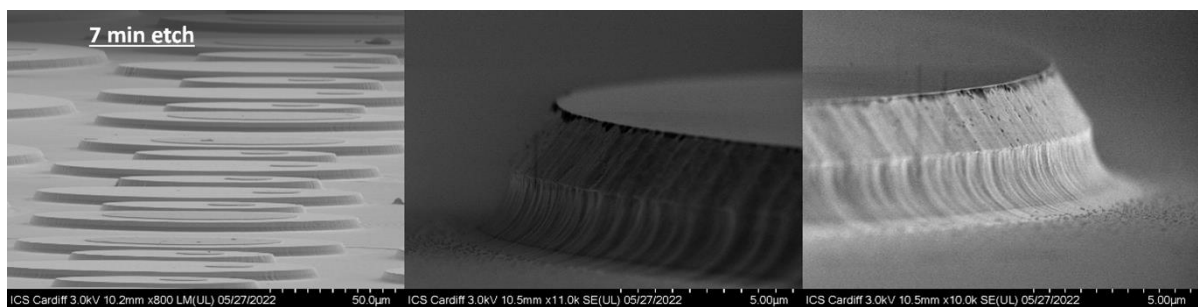


Figure 7.7: SEM micrographs of the fabricated devices from Sample H after etching time of 7 min. It is observed that the surface of the semiconductor is clean after etching, and the mesa sidewalls are not vertical (isotropic profile).

After device fabrication, the J-V characteristics were determined using the Lakeshore probe station system. Figure 7.8(a) shows the current density of the devices at room temperature. It was found that the dark current density of the devices is nearly close to $10^{-6}$ A/cm$^2$, which is very close to the reported values with a similar structure in the literature [358], [359], [360]. Figure 7.8(b) depicts the variations of current density versus P/A ratio of the fabricated devices.
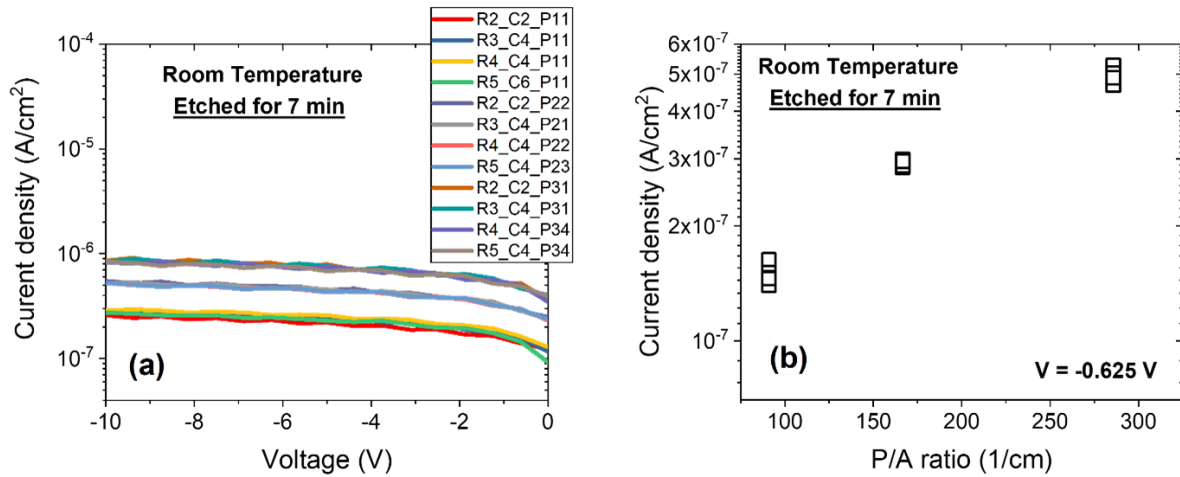
Figure 7.8: (a) Room temperature current density characteristics of the etched devices of Sample H with different mesa diameters. (b) Current density versus perimeter-to-area (P/A) ratio at an applied voltage of -0.625 V. The sample was etched for 7 min.

### 7.4.2 Citric acid-based solution

The citric acid-based solution is another alternative etchant to the HF-based solution. It is well known that GaSb material cannot be etched using citric acid on its own. For this reason, it was suggested that adding phosphoric acid to the mixture could help. Therefore, the author has looked into the literature to find recipes that can work for etching InAs/GaSb T2SL structure (c), as shown in Figure 7.1. Table 7.3 shows alternative etch recipes to HF-based solutions. Different citric acid recipes reported in the literature were attempted, but none worked. First, we tried using the recipe SC1 ($C_6H_8O_7$:$H_3PO_4$:$H_2O_2$:$H_2O$) with a ratio of 15:20:12:40, as reported by Lee et al. [246]. It was reported that the etch rate should be around 400 nm/25 sec. The T2SL samples (Sample G) were etched for an interval of 5s up to 25s, but no etch depth has been observed; instead, damage caused by the chemical reaction and a black surface is noticed, as shown in Figure 7.9. The black marks on the surface can be due to the following. (i) Before etching, some residual photoresists may have prevented etchants from reacting with the semiconductor. (ii) The residue can be due to improper exposure and development. The recipe was not optimised, similar to that reported in the paper [246], which may be why the reaction rate is prolonged.

Figure 7.9: Citric acid-based recipe SC1 used for etching the InAs/GaSb T2SL samples (Sample G). Etching times from 5s to 25s. As seen, surface damage is caused by chemical reactions.

Again, another recipe was used but with a different ratio (0.54:2:1.2:40), recipe SC2, as reported by Xu et al. [361]. This time the mixture ratio is less concentrated, so the etch rate is supposed to be lower. We tried etching multiple times to get an accurate etch rate for this solution. Herein, the T2SL samples were etched from 30 to 150 sec intervals of 30 sec each. Unfortunately, this recipe did not work for our structure. Figure 7.10 shows no etch depth was observed using the Dektak profiler and a rough black surface brought by the etchants. The GaSb top/cap layer in the T2SL structure may prevent etching using a citric acid-based recipe. This allowed investigation of other recipes which can be used to remove the first top layer of the T2SL samples (see Section 7.4.3) or use other structures which do not have a GaSb cap layer, for example, an InAs cap layer.

Figure 7.10: Optical images of the citric acid-based recipe SC2 used for etching the InAs/GaSb T2SL samples. Etching times from 30s to 150s.

Table 7.3: Wet etch recipes reported in the literature for etching Sb-based T2SL structures.

| Research Group | Year | Detector Type | Etch Recipe | Applied voltage (mV) | Current Density (A/cm$^2$) at 77 K | Reference |
|---|---|---|---|---|---|---|
| Optoelectronic Device Laboratory, Shanghai Tech University | 2019 | pin on Si | $C_6H_8O_7$:$H_3PO_4$:$H_2O_2$:$H_2O$ (1:1:4:16) and sidewalls were passivated by SU-8 | -100 | 2.3 | [245] |
| Air Force Research Laboratory, Space Vehicles Directorate, USA | 2014 | pBiBn | $BCl_3$ – ICP dry etch, passivated with SU-8 2002 PR after a short dip in a phosphoric | -100 | 1x10$^{-6}$ | [362] |

| | | | | | | |
|---|---|---|---|---|---|---|
| | | | acid-based solution $H_3PO_4:H_2O_2:H_2O = (1:2:20)$ | | | |
| Key Laboratory of Infrared Imaging Materials and Detectors, Shanghai Institute of Technical Physics, China | 2013 | *pin* (10/10 ML) | $C_6H_8O_7:H_3PO_4:H_2O_2 = (10:1:1)$ The sidewall of the mesa was protected by 300 nm thick $SiO_2$ deposited with (ICP-CVD) | -20 | $3.8 \times 10^{-7}$ | [203] |
| Department of Electrical Engineering, Chungnam National University, Daejeon, Korea | 2020 | *nBn* (10/10 ML) | $C_6H_8O_7: H_3PO_4:H_2O_2:H_2O$ (15:20:12:40) solution for 25 s, followed by immersing in $HCl:H_2O$ (1:10) solution for 60 s to remove native oxide at the surface. They were passivated with 300 nm thick $SiO_2$ using a PECVD at 250°C for 45 second | -100 | $2 \times 10^{-8}$ | [246] |
| Centre for High Technology Materials, University of | 2008 | *nBn* (8/8 ML) | $H_3PO_4:H_2O_2:H_2O = (1:2:20)$ to the middle of the barrier layer (etch | -100 | $2.3 \times 10^{-6}$ | [146] |

| | | | | | | |
|---|---|---|---|---|---|---|
| New Mexico, Albuquerque, New Mexico | | | depth ~0.15 nm) | | | |
| School of Information Science and Technology, Shanghai Tech University, Shanghai, China | 2020 | Dual-band *nBipBp* | $C_6H_8O_7$:$H_3PO_4$: $H_2O_2$:$H_2O$ = (1:1:4:16) Passivated with SU-8 PR | -500 | $1.44 \times 10^{-5}$ | [201] |
| Montpellier, France | 2009 2010 2012 | pin | $H_3PO_4$/$H_2O_2$/$H_2O$/$C_6H_8O_7$ (85%, 30%, 15% of NaClO, 100%). DIW is used in all solutions | -50 | $6.2 \times 10^{-8}$ | [96], [193], [194] |
| Siec Badawcza Łukasiewicz - Instytut Technologii Elektronowej, Al. Lotnikow, Poland | 2020 | *pin* MWIR (10/10 ML) – *pin* (14/7 ML) – LWIR | Wet etch: $H_3PO_4$:$C_4H_6O_6$: $H_2O$:$H_2O_2$ (1:1:3:1) Dry etch: $BCl_3$:Ar plasma (pr 4 mTorr, flow rate of 1 sccm for $BCl_3$ and 4 sccm for Ar) | -50 -50 | 30 (225 K) 2.8 (225 K) | [31] |

### 7.4.3 Hydrochloric acid-based solution

Two etch steps were used to remove the top GaSb layer and then to etch the InAs/GaSb T2SL structure (Sample G) using a combination of two recipes. First, the hydrochloric acid-based recipe was used for etching the first top layer of the T2SL structure. It was reported that hydrochloric acid-based etchant could etch InAs/GaSb T2SL with no selectivity. Hence, recipe SD1 ($HCl$:$H_2O_2$:$H_2O$) was used with a ratio of 100:1:100. The etch rate of this recipe should be

around 4.2 nm/sec. To calibrate the etch rate, the T2SL samples were immersed in the solution for 1 min, 6 min, and 11 min. It is seen that this recipe can etch the GaSb material, but we were not able to determine the exact etch rate. The estimated etch rate is in the range of 72-113 nm/min. Figure 7.11 shows the etched GaSb top layer of the T2SL structure using recipe SD1. After the top layer was etched, we tried to etch the T2SL structure using the SA recipe. Etching times were 1- and 2-min. Figure 7.12 depicts the optical images of the etched T2SL using recipe SA. Although we could measure an etch depth of around 1.1 µm/min, the expected etch rate as previously calibrated, the semiconductor surface becomes rough due to the damage caused by the chemical reactions. We tried ashing the samples with an $O_2$ plasma ash system, but this did not help to completely remove the contamination/residuals of the photoresist.
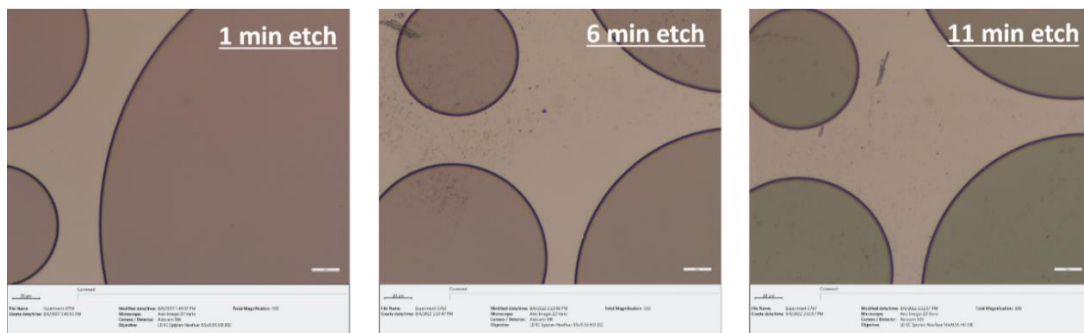


Figure 7.11: Optical micrographs of HCl acid-based recipe SD1 used for etching the top GaSb cap layer of the InAs/GaSb T2SL samples. Etching times from 1 min to 11 min.



Figure 7.12: Optical micrographs of the etched InAs/GaSb T2SL samples using a combination of recipes SD1 and SA.

The same solution was used but with a different ratio, as in Table 7.2. We herein used recipe SD2 to calibrate etch rate in order to etch the AlGaAsSb *pin*-based structure (Sample I). For the recipe optimisation, we have etched the samples several times from 1 min to 12 min to get an exact etch rate. Figure 7.13 shows the etch rate of recipe SD2. As we can see, the etch rate is around 258 nm/min, which is very close to the etch rate value reported elsewhere [247]. Our etch rate is slightly lower than the other reported value, but this is due to the difference in the ratio of the solution mixture.
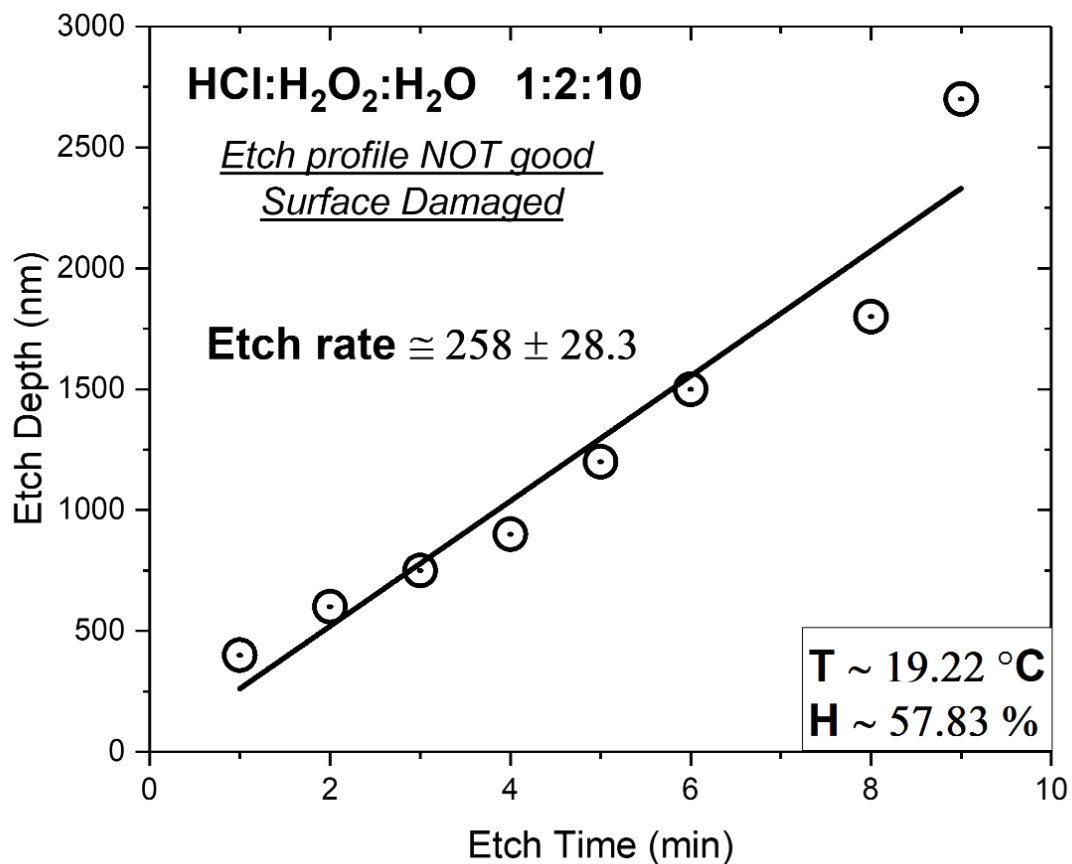


Figure 7.13: Etch rate calibration for recipe SD2 used to etch the AlGaAsSb pin-based structure (Sample I).

After recipe optimisation, real devices were fabricated. Two samples were fabricated to have different etch depths. The first one was etched for 7 minutes, and the second sample was etched for 9 minutes to get an etch depth of around 2 μm and 2.8 μm, respectively. Figure 7.14(a-b) shows the optical images and J-V characteristics at room temperature for the etched devices. As can be seen, the surface of the devices after etching is not clean, and there are

vertical and horizontal lines on the semiconductor surface and mesas, but these originated from the growth itself.
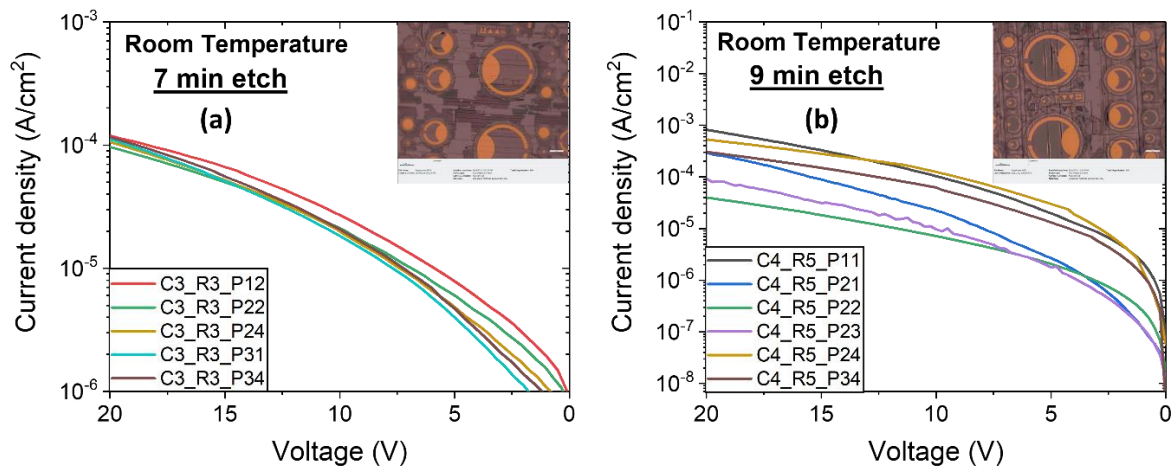


Figure 7.14: Optical images (inset) and room temperature J-V characteristics of the fabricated devices (Sample I) with (a) 7 min etch and (b) 9 min etch.

Lastly, recipe SD2 was used for etching the InAs/AlSb T2SL pin structure (Sample J), as shown schematically in Figure 7.1(f). Two samples were fabricated; the first one was etched in SD2 twice (1 min and 11 min), and the estimated etch depth was around 5.8 µm. This sample seems over-etched, meaning that the etch reached the GaSb substrate. The semiconductor surface was too rough and not clean due to the residuals caused by chemical reactions. Also, the etch profile was not uniform, as observed by the Dektak profiler. The other samples were used for etching of about 1.9 µm in 3 min in recipe SD1 and 30 sec in recipe SB as a trial to clean the surface after etching. However, this has not been sufficient to treat the issue of surface roughness. Figure 7.15(a-b) displays the optical images of the fabricated and etched samples.
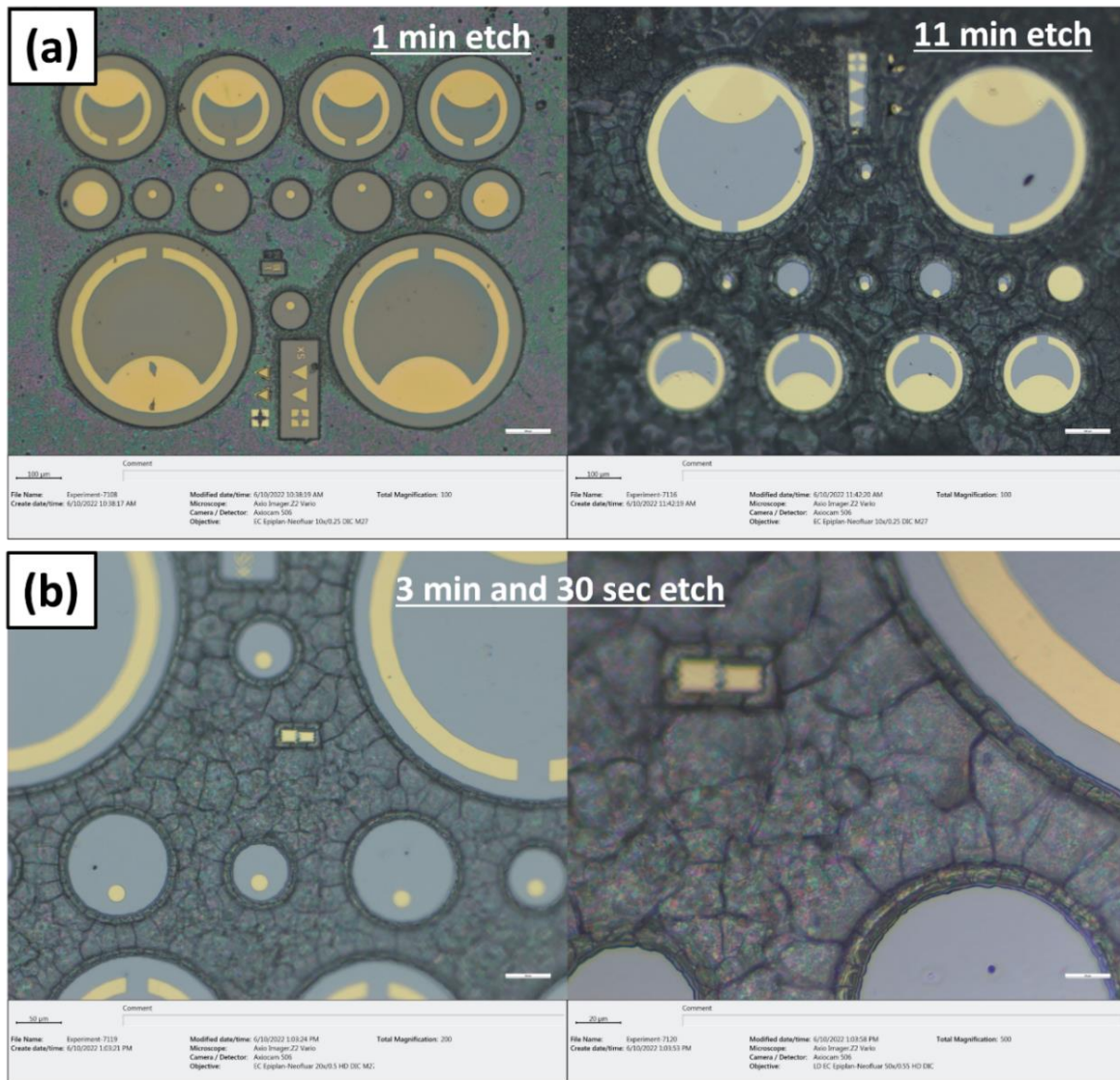
Figure 7.15: Optical micrographs of etched samples (Sample J) in recipe SD2 for (a) 1 min and 11 min and in recipe SD2 and SB for (b) 3 min and 30 sec.

In addition, the fabricated samples (Sample J) were tested using J-V characterisations to assess their electrical performance at room temperature. As seen in Figures 7.16 and 7.17, the etched sample for 11 min behaves not as good as the etched for 3 min and 30 sec. The current density characteristics seem much better, and surface leakage is much less. This is because the first sample was etched several times, which is more prone to surface oxidisation during etching and measurement under the Dektak system to measure the etch depth. In general, the dark current density is found to be around 10 A/cm$^2$ at an applied bias of -500 mV at room temperature, which is almost one to three orders of magnitudes higher compared to other reported results with similar structures [201], [363].
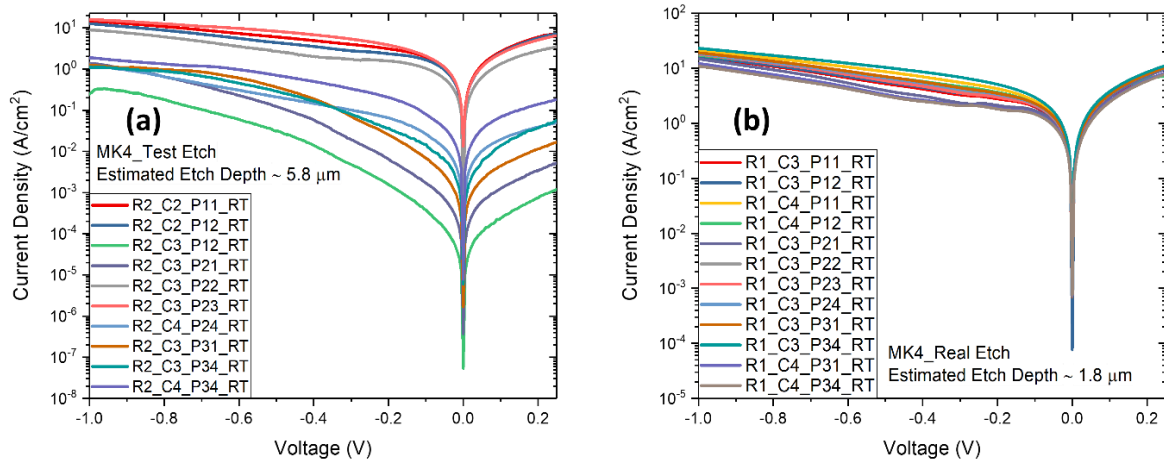
Figure 7.16: Room temperature current density characteristics of the etched samples (Sample J) with etch depth of (a) 5.8 μm and (b) 1.8 μm.
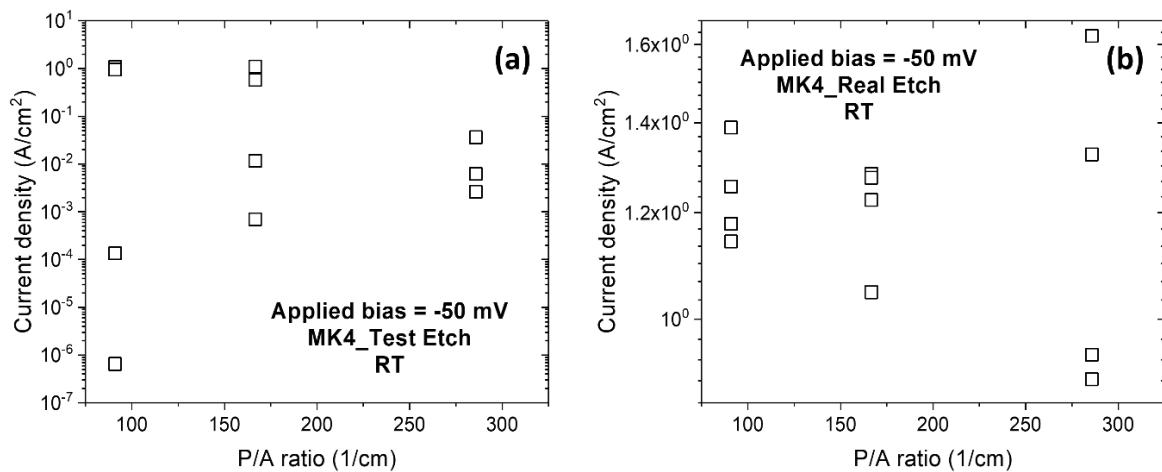


Figure 7.17: Current density versus the perimeter-to-area ratio of the etched samples (Sample J) for (a) 5.8 μm and (b) 1.8 μm depth at room temperature operation.

## 7.5 Summary

This chapter has outlined alternative etchants to HF-based solutions to etch Sb-based materials, including phosphoric, sulphuric, citric, and hydrochloric acidic solutions. A variety of III-V semiconductor materials such as InAs, GaSb, InAs/GaSb T2SL, InGaAs, AlGaAsSb, and InAs/AlSb T2SL were etched for purposes of optimisations of recipes. It is demonstrated that etchants such as phosphoric and sulphuric acids can selectively etch InAs and not GaSb with

clean semiconductor surfaces. It is also found that GaSb cannot be etched using citric acid. HCl-based etchants are found to etch InAs and GaSb with good selectivity; however, etch profile and surface are not very clean. These preliminary outcomes open a new route for optimising alternative etchants and developing Sb-based materials that can be used to etch SL structures.

# Chapter 8: Conclusion and Future Work

Progressively, the InAs/GaSb T2SL has been recognised as a prospective alternative to the current state-of-the-art MCT for MWIR detection on account of its predicted higher theoretical performance limits, improved uniformity, simplicity of fabrication, and less limiting regulations. However, MCT continues to surpass T2SLs, especially in the critical areas of dark current density and quantum efficiency performances. The aim of the current research work is, thus, to develop various techniques to enhance the T2SL material and device performance in order to attain their theoretically projected levels. In Chapter 3 and under Section 3.7, three objectives were established to accomplish this aim:

- Determining the effect of T2SL IF growth schemes on the structural and optical quality of the samples (refer to Section 3.7.1).

- Optimising the T2SLs fabrication process through wet and dry etching, a combination of both dry and wet etching, and surface protection techniques (refer to Section 3.7.2).

- Optimising the wet etching process and developments of Sb-based materials (refer to Section 3.7.3).

In this research work, we grew two samples one with an InSb IF layer and the other without. Although the intentional InSb IF layer exhibited increased compressive stain, surface roughness, and rough interfaces observed by XRD, AFM, and TEM measurements, respectively, it revealed increased PL optical response. The electrical examination of devices fabricated using different etching approaches showed that the wet etched devices passivated with a photoresist exhibited enhanced current density performance by almost four orders of magnitude lower compared to the dry etched and dry + wet etched devices. The following sections give a detailed summary of the present research aim and objectives achievements.

## 8.1    Effect of T2SL IF growth schemes on the structural and optical properties

One of the main difficulties in enhancing the performance level of InAs/GaSb T2SLs is the -0.6% lattice mismatch between InAs and GaSb, which leads to an internal interfacial strain

that restricts material quality and device thickness. As a result, the nature and sharpness of interfacial components have become major study topics. The InAs/GaSb heterostructure lacks any shared cations or anions, which results in the potential formation of various interfacial components, such as InSb-like, GaAs-like, or a combination of InAs and GaSb, resulting in ternary or quaternary interfacial intermixing [78], [219], issues like In and Sb segregation [79], [220], or IF-diffusion of atoms [221]. There are many reports on GaAs-like [222], [223], [224], [225], InSb-like [226], [227], [228], [229], [230], [231], [364], and ternary/quaternary [231], [232] IFs, which have demonstrated promising results for enhanced device performance.

Because of the strain compensation it can offer, the InSb IF is the most often used scheme, as indicated by considerable improvements in device performance [233]. This arises from the +6.3% lattice mismatch between InSb and GaSb, which acts against the -0.6% lattice mismatch between InAs and GaSb. Hence, in theory, strain compensation can be obtained by selecting a total InSb IF thickness of roughly 10% of the total InAs thickness. Furthermore, the InSb IF preserves the type-II band alignment of the T2SL and is therefore advantageous for both structural and optical quality. It is also relatively easy to realise through MEE or conventional MBE growth methods. However, multiple studies on T2SLs with InSb IFs have shown superior optical quality despite the overall inferior structural quality compared to T2SLs with other IF schemes [234], [235]. To explain why this is the case, a structural and optical comparison of InAs/GaSb T2SLs with and without InSb IFs is required. The incorporation of an intentional strain compensating InSb IF layer is found to enhance the performance of T2SL detectors [233]. Unfortunately, there is a scarcity of comprehensive characterisation studies that correlate the quality of this technique. Therefore, the processes by which this enhancement is obtained remain unknown. Thus, in light of achieving the above objective, this research aims to conduct a detailed characterisation investigation to determine the effect of interfacial schemes on the structural and optical properties of T2SLs.

For this objective, two InAs/GaSb T2SL samples were grown. The first sample, Sample A, was grown with intentional InSb IF layers on the InAs-on-GaSb and GaSb-on-InAs IFs using an MEE method. The other sample, Sample B, was grown without an intentional InSb IF layer, but an Sb-for-As growth method was utilised to potentially promote an InSb layer at the InAs-on-GaSb IF. After growth, materials were characterised using various tools, including HR-XRD, AFM, TEM, and PL. Those tools were utilised to study the structural and optical properties of

the samples. The PL measurements indicate that Sample A, with intentional InSb IFs, has stronger PL intensity and longer wavelength than Sample B. This observation was also supported by the band heterostructure simulation using Nextnano software via modelling various IF schemes, which reveals that the higher PL intensity and longer wavelength could be attributed to the higher wavefunction overlap and reduced bandgap energy, respectively. However, as observed by XRD, AFM, and TEM, Sample A has slightly lower structural quality compared to Sample B, including larger lattice mismatch, higher surface roughness, and rougher SL IFs, respectively. This could be due to the thick InSb IF layer at the SL IFs for Sample A, which has provided additional internal strain energy in the structure. This conclusion is supported by structural and optical characterisation results, which satisfy the requirements of the first objective of the current research in Section 3.7.1.

## 8.2 T2SL fabrication process optimisation via wet etch, dry etch, and surface passivation

The fabrication process and optimisation of etching methods are the second objective of this research work. For this reason, a *pin* photodiode sample was grown, characterised, and fabricated in the ICS-CR. In the case of the fabrication process, the photodiode was first fabricated using an HF and citric acid wet etch-based solution. After photodiode fabrication, I-V performance was tested using the Lakeshore cryogenic probe station system. The I-V profile implies that the photodiode is dominated by diffusion and G-R currents above and below a temperature of 136 K. The total dark current density and RA product are $5 \times 10^{-6}$ A/cm$^2$ and $6 \times 10^4$ Ω.cm$^2$ at 77 K, respectively. The I-V modelling was also carried out and is found to be consistent with the experimental findings. It is demonstrated that the G-R process limits the current at a relatively low temperature of 110 K and low applied bias. Still, even TAT dominates the current when the applied bias is increased above ~0.2 V. Nevertheless, at HOT between 200 and 300 K, the contribution of diffusion current is dominant at low applied bias ~50 mV. A significant contribution of the shunt current was also observed. This can be attributed to the lack of effective passivation since only a photoresist was applied on the mesa sidewalls as a protection layer.

For the purpose of fabrication process development, the photodiode was fabricated using alternative etching techniques. Due to the requirement for etches with a high fill factor and anisotropic profile, there has been extensive research on dry etching procedures for T2SLs [346], [365], [366], [254], [253]. Device fabrication was therefore performed using an effective dry etching process. This includes mesa realisation through dry etching, a combination of dry and wet etching methods, and mesa sidewalls protection. I-V measurements reveal that the use of this dry etching process generates dominant surface-related and G-R dark currents at temperatures below 170 K. However, no performance degradation is observed when the device is operated above this temperature, indicating that dry-etched T2SLs are suitable for the HOT required by modern military and space applications. The current density of the dry etched device is found to be 0.054 A/cm$^2$ at 77 K and 0.185 A/cm$^2$ at 120 K for the dry + wet etched device. Although the mesa sidewalls of this device were protected immediately after the dry and wet etch process, an increase in the current density can still be observed. It is believed that the increase in current density is because of wet etch, as it could add more chemical residuals into the surface sidewalls instead of cleaning them. The I-V modelling for the dry etched and dry + wet etched devices indicate that the G-R process dominates the dark current at temperatures of 110 and 200 K at the whole applied bias from zero to -1 V. However, the diffusion mechanism contributes to the current at room temperature, specifically below an applied bias of -400 mV. TAT current also appears predominant at high applied voltage at the whole temperature range.

It is concluded that the etching techniques play a significant role in optimising the device's performance. It is found that the dark current density of the HF-based wet etched device is significantly improved as the current density is almost four orders of magnitude lower than the other etched devices using different techniques, particularly at lower operating temperatures.  It has been demonstrated that the current density of the fabricated devices is nearly one to four orders of magnitude higher than the MCT's ''Rule 07''. It is hoped that with further improvement in the device design, such as incorporating a barrier layer above the absorbing region and/or applying an effective surface passivation material, the performance of these devices could be significantly enhanced. The dry etching and surface protection processes fulfil the second objective of the current research work in Section 3.7.2 by improving etch profiles and achieving comparable HOT dark current.

## 8.3    Wet etching process developments of Sb-based structures

The third objective of this research is to search for alternative etchants to HF-based solutions to etch Sb-based materials. These etchants comprise phosphoric, sulphuric, citric, and hydrochloric acidic solutions. For the purpose of optimisation processes, various III-V semiconductor materials, including InAs, GaSb, InAs/GaSb T2SL, InGaAs, AlGaAsSb, and InAs/AlSb T2SL, were etched. It is demonstrated that etchants such as phosphoric and sulphuric acids can selectively etch InAs against GaSb with clean semiconductor surfaces. It is also found that GaSb cannot be etched using citric acid. HCl-based etchants are also found to etch InAs and GaSb with good selectivity; however, etch profile and surface are not very clean, with high surface roughness. These preliminary outcomes open a new route for optimising alternative etchants and developing Sb-based materials that can be used to etch SL structures. To conclude, the third objective of this research work stated in Section 3.7.3 has been partially fulfilled at the current stage; however, more research and development are necessary to fabricate and optimise recipes for high-performance T2SLs.

## 8.4    Future work

The results of the present research endeavour highlight prospective future research avenues. These are summarised below.

### 8.4.1   Design and growth of T2SL structures

The simulation work/results for Ga-containing InAs/GaSb T2SL presented already in Chapter 5 (Section 5.4) represents a potential for material and device designs beyond what has been explored in this research work. The simulation work has already predicted several T2SL structures which are appropriate for use in MWIR applications that are still not verified experimentally. Therefore, an informative future research area would be experimentally growing, fabricating, and characterising these T2SL structures. In the simulation work of Ga-containing InAs/GaSb T2SL, as demonstrated in Chapter 5 (Section 5.4), various IF schemes have already been implemented to study their impacts on the structural and optical properties. Consequently, growing and characterising those structures and deeply

understanding their physics would be valuable. This might allow the projection and demonstration of T2SL structures to be even more optimal than the presented structures.

The simulation work and results shown in Appendix D demonstrate the possibility for material and device innovations that go beyond the scope of this research. The Ga-free InAs/InAsSb T2SL is an alternative material system to the Ga-containing T2SL. Given that this material system has a longer MC lifetime, the ability to tolerate defects, and less growth complexity (only As and Sb shutters are controlled), it is theorised that it will be competitive with the current state-of-the-art T2SL and MCT detectors. Considering the fundamental advantages of T2SL, Ga-free T2SL has the additional benefit of bandgap engineering by varying both the Sb composition and layer thickness to achieve the required cut-off wavelength. The simulation work presented in Appendix D involves simulating different Ga-free T2SL structures with various Sb compositions and layer thicknesses. Hence, the growth of these structures can be pursued to broadly understand how the T2SL periodic thickness and Sb composition impact the key parameters, including bandgap energy, effective mass, and wavefunction overlap.

### 8.4.2 Growth optimisation

It is evident from the findings of the research study of T2SLs using different IF schemes (Chapter 5) that further optimisation of the growth of the IF layer is essential to further improve the structural and optical properties of the T2SLs. This can be done by optimising the growth parameters, such as temperature and shutter sequence. This can take care of the incorporated InSb films grown at the SL IFs. Since the strain in the SL depends mainly on InSb thickness and growth method, the thickness of the InSb IF layer should also be considered when growing the SL structures, as increasing the thickness of InSb beyond the critical thickness may degrade the material property [195].

Moreover, the growth method plays a vital role in optimising material quality. For instance, Xu et al. [331] have recently grown InAs/GaSb T2SLs with InSb IF schemes using conventional MEE and modified migration epitaxy (MMEE) methods. In the case of the MMEE growth method, quite similar to MEE, but the introduction of growth stops and In deposition between Sb soaks after the growth of the InAs layer was performed. In the MMEE growth technique, no effect of increasing InSb thickness has been observed. However, employing the conventional MEE growth method would require thicker InSb IFs (approximately one ML) to

achieve strain compensation, whereas only about half of ML would be required using the MMEE technique. This means that the strain compensation efficacy of conventional MEE is less than that of MMEE. The lower strain compensation efficiency in the conventional MEE could be due to a higher As composition in the InSb IFs layer. In comparison with the growth using the conventional MEE method, two factors should be considered to explain the compensation efficiency utilising the MMEE method. On one hand, the incorporated growth stop after the growth of the InAs layer can help the reactor to decrease the As pressure; thereby, a few amounts of InAsSb will be formed between the InAs layer and soaked-after Sb. On the other hand, the In deposition sandwiched between Sb soaks can enhance the competitive advantage of the Sb to As. Using the characterisation methods described in Chapter 4, the efficacy of these measures can be evaluated.

### 8.4.3 Further fabrication and characterisation work

The superior optical quality of Sample A compared to Sample B (Chapter 5) requires further demonstration with the growth of a photodiode structure based on the growth condition of Sample A and warrants more sophisticated characterisation methods. Particularly, the enhanced detectivity of Sample A, as indicated by the improved PL peak intensity, should be confirmed via spectral response measurements. Implementing the 7/4 T2SL within a barrier IR detector such as the nBn would be informative as, theoretically, the G-R current should be suppressed at low temperatures. This would be helpful to verify whether the *nBn* 7/4 T2SL demonstrates an overall lower dark current density than the conventional *pin* 7/4 T2SL at all temperatures or whether other sources of dark current negate its benefits.

### 8.4.4 Etch optimisation and surface passivation

The wet and dry etch processes of T2SLs demonstrated in Chapter 6 require further optimisation to eliminate or minimise the surface leakage-related current generated by the etch. First, elevating the temperature at which the dry etch is performed to around 200 °C could aid in the desorption of the $InCl_x$ by-products, which have minimal volatility at 60 °C. Secondly, incorporating physical passivating layers on the mesa sidewalls of T2SLs, such as $SiO_2$, $Si_3N_4$, or SU-8, minimises surface leakage-related current. Thirdly, optimisation of the wet etch recipe used to remove the surface damage caused by the dry etch should be carried

out as the current recipe was not developed for cleaning purposes. Finally, upon successfully implementing these optimisation steps, the etch uniformity should be verified and utilised to fabricate T2SL-based single-pixels and FPAs.

To summarise, it is hoped that implementing the abovementioned recommendations could significantly contribute to demonstrating a high-performance MWIR T2SL with reduced dark current, improved absorption, and enhanced detectivity via an appropriate growth technique, optimised fabrication, and passivation processes. Such a device would be a favourable alternative to current state-of-the-art MCT in specific applications with the potential to surpass the current performance of MCT. It is lastly argued that the stated objectives of discovering novel methods for enhancing the performance levels of T2SLs have been attained via the objectives enumerated in Sections 3.7.1, 3.7.2, and 3.7.3. To achieve the first objective outlined in Section 3.7.1, two MWIR reference samples (Samples A and B) were grown using different IF schemes with and without InSb IF layers and characterised using various techniques. Although the sample with intentional InSb IF layers has revealed rough IFs and compressive strain, it has shown a superior optical property with increased wavelength. To achieve the second objective outlined in Section 3.7.2, a *pin* InAs/GaSb T2SL photodiode has been grown, fabricated, and characterised. The effect of the etching approach and surface protection on device performance has been studied, and the electrical performance of the fabricated devices has been evaluated. Thirdly, alternative wet etching recipes have been investigated to fulfil the third objective stated in Section 3.7.3, and their suitability for fabricating high-performance T2SL devices was demonstrated. Therefore, it is hoped that the overall aims and objectives of the present research project, outlined above, have been achieved.

# Appendices

## A. Derivation of Bragg's law

When the incident angle is identical to the reflecting angle, the phases of the beams in the figure below align. The incident beams maintain parallel alignment until they reach point Z. Upon reaching point Z, they impact the surface and travel upward. At point B, the second beam undergoes scattering. AB + BC is the distance travelled by the second beam. The additional distance is referred to as the integral multiple of the wavelength. Figure A.1 shows the derivation of Bragg's law from incident and reflected beams.



Figure A.1: shows the dereivation of Bragg's law from the incident and reflected beams.

$$n\lambda = AB + BC$$

We also know that AB = BC,

$$n\lambda = 2AB \qquad \text{(A.1)}$$

is the hypotenuse of the right triangle ABZ. AB is the opposite of the angle Ѳ.

$$AB = d \sin(\theta) \qquad \text{(A.2)}$$

By substituting Equation (A.2) in Equation (A.1) this will give the following equation:

$$n\lambda = 2d \sin(\Theta) \tag{A.3}$$

The Equation (A.3) above is the derived expression of Bragg's law.

Each XRD spectrum of superlattice exhibits a peak corresponding to the substrate, specifically GaSb in this case, and a primary or zeroth order peak representing a superlattice or alloy material. The disparity in peak positions indicates the degree of lattice mismatch and, consequently, the strain present in the structure. The primary peak's width indicates the roughness of the interfaces between each SL layer. Therefore, the FWHM is frequently mentioned when characterising the quality of the crystalline material. The superlattice XRD patterns typically exhibit several satellite peaks, which arise from numerous repeating layers in the superlattice structure. The inter-peak spacing provides information about the period of the various layers, which is utilised to verify growth conditions and layer thicknesses.

Single crystal HR-XRD is the main technique used to assess the quality of a formed crystal structure. This method uses the periodicity present in the single crystal to analyse the crystalline structure of the device. Here, the crystal is illuminated by X-rays, which then diffract off the atoms present in the material. The regular arrangement of atoms leads to a predictable pattern of constructive and destructive interference, determined by the angle at which the incident waves interact. In single crystal XRD, an Ω-2Θ scan is employed. This generates a scan that can be employed to ascertain the characteristics of a crystalline structure. A literature example of such a scan is depicted in Figure A.2 [367]. The phenomenon of constructive interference in an XRD scan is precisely described by Bragg's law, which can be stated as follows:

$$d = \frac{n\lambda}{2 \sin(\Theta)} \tag{A.4}$$

The distance between the primary epitaxial peak and the substrate peak indicates the extent of mismatch between the epitaxial and substrate crystal lattice constants. For it to be classified as lattice-matched, the gap between angular peaks must be typically below 100 arcseconds. The angular peak separation can be translated directly into a percentage lattice mismatch,

expressed as Δa/a, by calculating each lattice constant using the measured XRD peaks and Bragg's law. The relevant equation used for this calculation is:

$$\frac{\Delta a}{a} = \frac{d_{0th} - d_{substrate}}{d_{substrate}} \tag{A.5}$$

Which can be simplified through some algebra to the following equation [368]:

$$\frac{\Delta a}{a} = \frac{\sin(\theta_{substrate})}{\sin(\theta_{substrate} + \Delta\theta)} - 1 \tag{A.6}$$

It should be noted that this process does not calculate the strain in the system, only the degree of lattice mismatch as measured by XRD. The SL period can be determined using a similar process in the case of SL materials. In this case, the 1st order peaks on either side of the main peak are used. The relevant equation in this case can be simplified to:

$$P_{SL} = \frac{\lambda}{\sin(\theta_{R1}) - \sin(\theta_{L1})} \tag{A.7}$$

where $P_{SL}$ is the period of the superlattice, λ is the wavelength of the XRD source (1.54056 μm for the $Cu - K\alpha$ line commonly used in single crystal XRD), and the two angles are for the right and left side of the 1st-order diffraction peaks.

The performance of III-V and II-VI semiconductors is significantly influenced by factors such as the composition of ternaries, mismatch of quaternaries, mis-orientation, layer thickness, tilt, relaxation, signs of strain, curvature, stress, and area homogeneity. XRD allows for the analysis of these properties in an affordable, rapid, and non-destructive manner. Among these characteristics, mismatch holds the utmost significance since it provides insights not only into the strain, but also into the lattice constant and composition, which are closely associated with the bandgap energy. Similarly, the thickness of the layer is crucial because of the quantum size effect. In the context of a Rocking curve, it is common to observe many peaks, typically two or more, which arise due to the tilt or mismatch between the substrate and the epitaxial layers of the superlattice. Diffraction can also take place at many interfaces, resulting

in the observation of multiple small peaks. These peaks provide valuable information regarding the thickness of distinct layers. According to Bragg's law (Equation A.3), constructive diffraction occurs when the values of Θ and d meet specific conditions. Here, d represents the distance between the crystal planes, while Θ represents the Bragg angle. In crystallography, the fundamental unit responsible for diffraction is known as the unit cell. In the case of a III-V semiconductor crystal with a cubic crystal structure, we additionally possess:

$$\frac{1}{d_{hkl}^2} = \frac{h^2 + k^2 + l^2}{a^2} \tag{A.8}$$

For (004) plane used in the characterisation, we have:

$$d_{004} = \frac{a}{4} \tag{A.9}$$

where a is the lattice constant. By combining these equations, we can derive the relationship between the wavelength of X-ray and the lattice constant as follows:

$$\lambda = \frac{a}{2}\sin(\theta) \tag{A.10}$$

By utilising this equation, one can get the lattice constant, which provides valuable insights about the degree of mismatch. The main objective is to extract the thickness of each layer in the SL structure. According to Equation (A.3), we get the expressions for two neighbouring Bragg peaks,

$$N\lambda = 2\Lambda \sin(\theta_n) \tag{A.11}$$

$$(N-1)\lambda = 2\Lambda \sin(\theta_{n-1}) \tag{A.12}$$

By combining Equations (A.11) and (A.12), we may get the equation for calculating thickness as follows:

$$\lambda = 2\Lambda \left( \sin\left(\theta_n\right) - \sin\left(\theta_{n-1}\right) \right) \qquad\qquad \text{(A.13)}$$

$$\frac{2\sin\left(\theta_n\right) - 2\sin(\theta_{n-1})}{\lambda} = \frac{1}{\Lambda} \qquad\qquad \text{(A.14)}$$

The last and crucial equation is obtained by calculating the average over the positions of satellite peaks of order n in order to eliminate errors:

$$\frac{2\sin\left(\theta_n\right) - 2\sin(\theta_{SL})}{\lambda} = \pm\frac{n}{\Lambda} \qquad\qquad \text{(A.15)}$$

where $\Lambda$ is the thickness of SL period, $\lambda_{CuK\alpha} = 0.15405nm$ is the wavelength of incident X-ray, $\theta_n$ is the $n$ th-order peak in rocking curve, $\theta_{SL}$ is the zero-order peak.
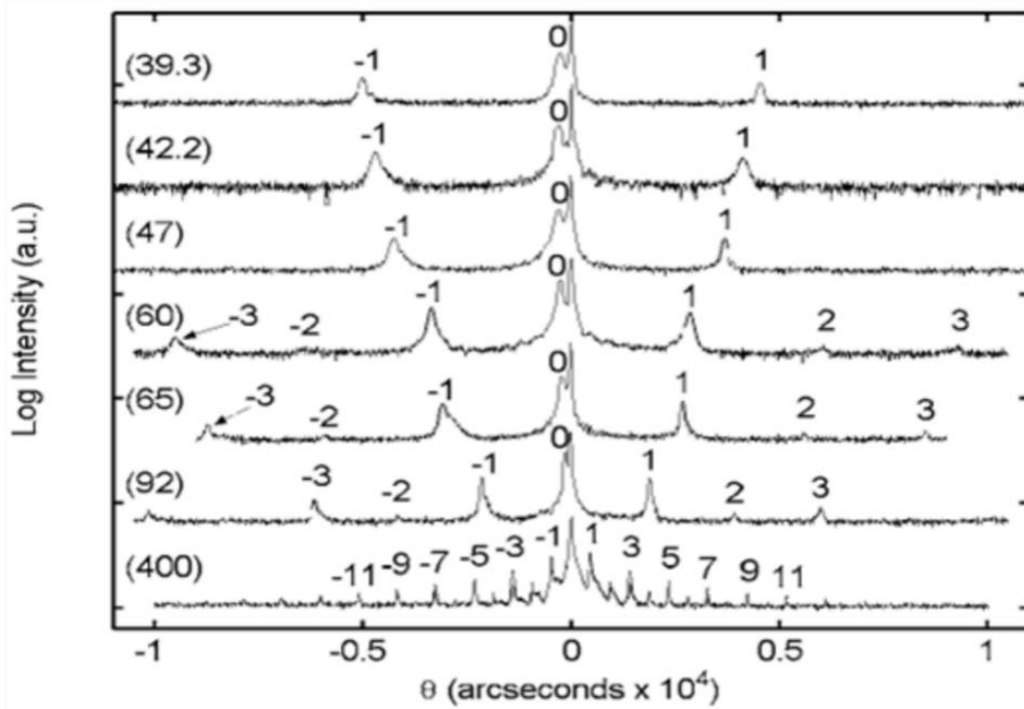


Figure A.2: Example of SL XRD rocking curves. This figure is adapted from reference [367].

234

## B. Literature examples of photoluminescence spectra

Examples of PL measurements reported in the literature are shown below. Figure (B.1a) shows the temperature-dependent PL measurements performed on a GaSb substrate. The $CO_2$ absorption line at 4.2 μm is observed in the measurement [369]. Figure (B.1b) shows the temperature-dependent PL spectra from InAs/InAsSb QWs sample, which shows the PL transition from the first electron miniband to the first heavy hole miniband and the first electron miniband to the second heavy hole miniband [370].
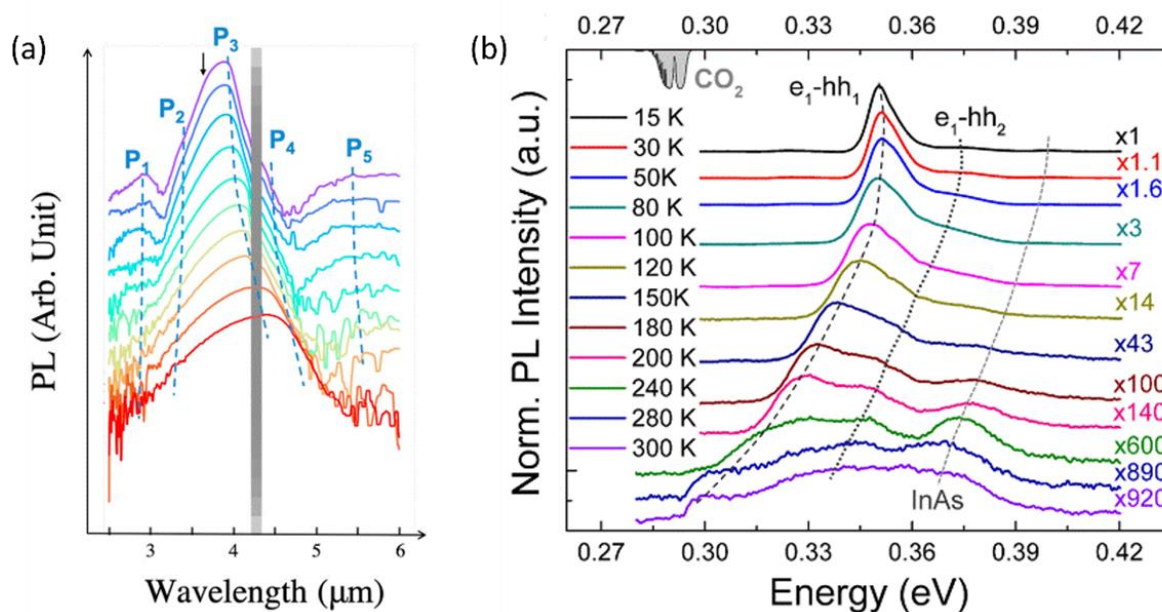


Figure B.1: Literature examples of PL measurements performed on two different structures (a) InAsSb on GaSb substrate [369] and (b) InAs/InAsSb QWs sample [370].

Figure B.2 below shows the PL intensity for three samples (A, B, and C) of InAs/InAsSb T2SLs with different Sb compositions (0.15, 0.22, and 0.23%). (a) normalized PL intensity and (b) temperature-dependent PL spectra [371].
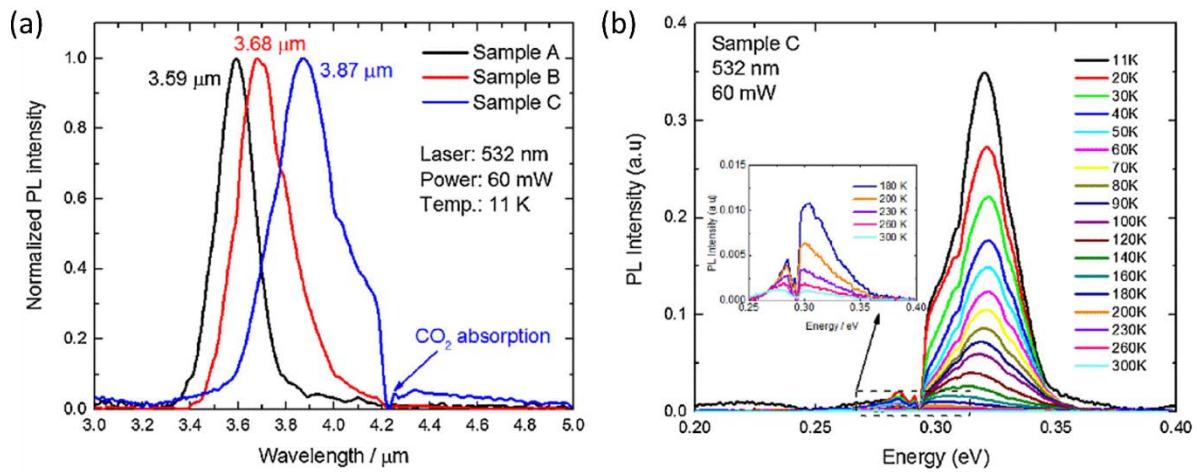
Figure B.2: Literature examples shows the PL intensity for three samples (A, B, and C) of InAs/InAsSb T2SLs with different Sb compositions (0.15, 0.22, and 0.23%). (a) normalised PL intensity and (b) temperature-dependent PL spectra. The figure is reproduced from reference [371].

The inset of Figure B.3 shows a literature example of PL Gaussian fitting for three peaks of InAs/GaSb T2SLs to determine their origins [372].
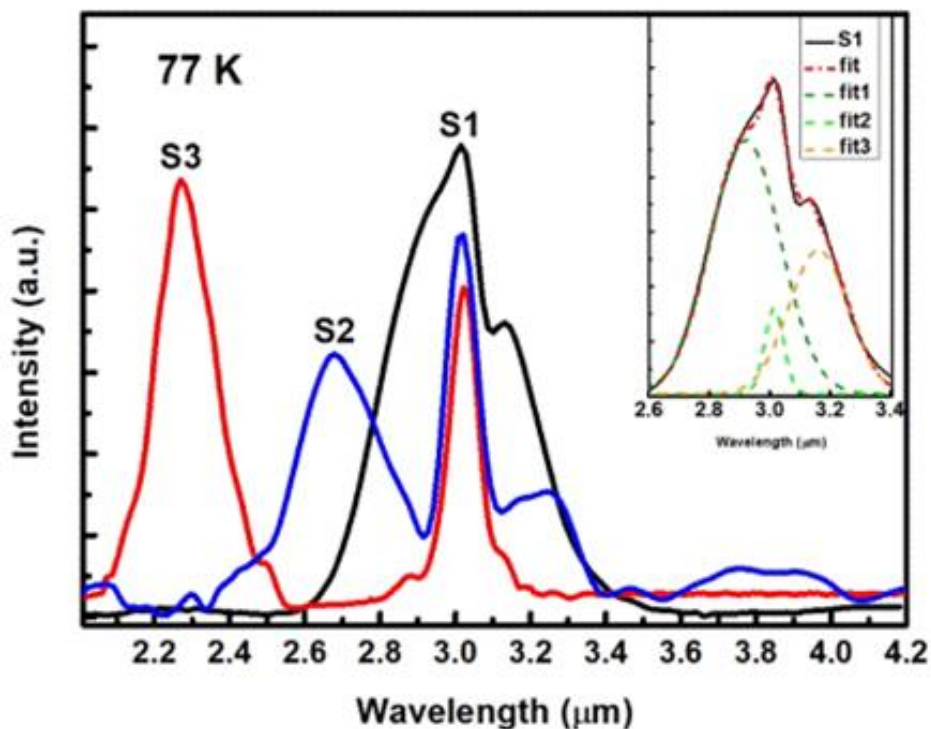


Figure B.3: A literature example of PL spectra from three different structures of InAs/GaSb T2SL samples. The inset figure shows the Gaussian fitting for three different peaks to understand their origins. The figure is adapted from reference [372].

## C. Derivation of Bloch's theorem

Below, a limited demonstration of a Bloch's theorem is presented, which is only valid when $\psi$(x) is non-degenerate. In other words, this occurs when there is no other wavefunction that possesses both the same energy and wavenumber as $\psi$(x).

We make the assumption that a periodic boundary condition is met,

$$\psi(x + N_a) = \psi(x)$$

The potential energy exhibits periodicity within a certain period (a),

$$V(x + a) = V(x)$$

Let us now examine the wave function $\psi$(x+a). To simplify the expression, we rewrite it as:

$$\psi(x + a) = T(a)\psi(x)$$

We then have the following,

$$T(a)H(x,p)\psi(x) = H(x + a,p)\psi(x + a)$$

$$= H(x,p)\psi(x + a)$$

$$= H(x,p)T(a)\psi(x)$$

In the given context, the Hamiltonian remains invariant when translated by (a),

$$H(x + a,p) = H(x,p)$$

This means that,

$$T(a)H(x,p) = H(x,p)T(a)$$

Consider that $\psi(x)$ is the eigenfunction of H(= H(x, p)) with the energy E,

$$H\psi(x) = E\psi(x)$$

We then have the following,

$$T(a)H\psi(x) = HT(a)\psi(x)$$

Or

$$H[T(a)\psi(x)] = T(a)H\psi(x) = E[T(a)\psi(x)]$$

This means that T(a)$\psi$(x) is the eigenfunction of H with the energy E. Provided that $\psi$(x) is non-degenerate, $\psi$(x+a) = T(a)$\psi$(x) is described by

$$\psi(x + a) = C\psi(x)$$

Where C is a constant. Similarly, we have

$$\psi(x + 2a) = C\psi(x + a) = C^2\psi(x)$$

$$\psi(x + 3a) = C\psi(x + 2a) = CC^2\psi(x) = C^3\psi(x)$$

From the periodic condition,

$$\psi(x + Na) = C^N\psi(x) = \psi(x)$$

We then have the following,

$$C^N = 1$$

Note that C is a complex number. $|C|^N = 1$ or $|C| = 1$.

$$C = e^{i\theta}, \qquad C^N = e^{iN\theta} = 1$$

Then, the following is obtained,

$$N\theta = 2\pi s$$

Where *s* is an integer. Or

$$\theta = \frac{2\pi s}{N} = \frac{2\pi s}{Na} a = \frac{2\pi}{L} sa = ka$$

Where

$$k = \frac{2\pi}{L} s \qquad and \qquad C = e^{ika}$$

Finally, the Bloch theorem is obtained,

$$\psi_k(x + a) = e^{ika}\psi_k(x)$$

Or

$$\psi_k(x + la) = e^{ikla}\psi_k(x)$$

Where l is an integer.

## D. Band heterostructure simulation using Nextnano software

The Nextnano simulation code used to simulate InAs/InAsSb T2SL structures is attached.

```
--------------------------------------------------------------------------
# Simulation of MWIR InAs/InAsSb T2SLs
# Created by Dhafer Alshahrani 18/09/2019
--------------------------------------------------------------------------
$QW_WID = 5                          # Width of QW (unit: nm)
$QW_SEP = 5                          # Seperation of QW-barrier (unit: nm)
$PER_WID = $QW_WID + $QW_SEP         # Widht of 1 period (layer 1 + layer 2)
$NUM_LAY = 20                        # Number of period-Number of layers
$SUP_WID = $PER_WID * $NUM_LAY       # Total widht of the active region
$SBX = 0.03                          # Antimony content of InAsSb layers
$xalloy = 1-$SBX                     # Material is InAs(x)sb(1-x)
                                     # If Sbx = 0.10 then xalloy = 1 - 0.10 = 0.90 so QW is sb = 10%
$GRID = 0.01                         # Grid resolution
--------------------------------------------------------------------------
global{
  simulate1D{}
  crystal_zb{
    x_hkl = [1,0,0]
    y_hkl = [0,1,0]
  }
  substrate{
    name = "GaSb"                    # Set the substrate material
  }
  temperature = 77                   # Set temperature in Kelvin

  periodic{x=yes}
}
--------------------------------------------------------------------------
database{
  ternary_zb{
    name = "InAs(x)Sb(1-x)"
    valence = III_V
    conduction_bands{
    Gamma{bandgap = 0.60}            # Set the conduction band value
    }
    valence_bands{
    bandoffset = -0.90               # Set the valence band value
```

Page (1)

```
    delta_SO = 0                     # Set detal split orbit value
    }
  }
  binary_zb{
    name = "InSb"
    valence = III_V
    valence_bands{
      bandoffset = 1.84
    }
  }
}
--------------------------------------------------------------------------
grid{
  xgrid{
    line{ pos = 0 spacing = $GRID}
    line{ pos = $SUP_WID spacing = $GRID}
  }
}
--------------------------------------------------------------------------
structure{
  output_region_index{boxes = no}
  output_material_index{ boxes = no}
  output_alloy_composition{ boxes = yes}

  region{
    everywhere{                      # Default region
    }
    contact {name = dummy}
    binary{
      name = "InAs"
    }
  }

  region{                            # Set paprmaeters for the first layer
    repeat_x{
      shift = $PER_WID
```

Page (2)

240

```
            num = $NUM_LAY
        }

        line{
            x = [0, $QW_SEP]
        }
        binary{
            name = "InAs"
        }
    }

    region{                           # Set parameters for the second layer
        repeat_x{
            shift          = $PER_WID
            num            = $NUM_LAY
        }
        line{
            x = [$QW_SEP, $PER_WID]
        }
        ternary_constant{
        name = "InAs(x)Sb(1-x)"
        alloy_x = $xalloy
        }
    }
}
--------------------------------------------------------------------------
impurities{}

contacts{
    fermi {name = "dummy" bias = 0}
}
classical{
    Gamma{
        output_bandedge{ averaged = no}
    }
    HH{}
    LH{}
```

Page (3)

```
        SO{}

    output_bandedges{ averaged = no}
}

poisson{}

currents{
        recombination_model{
        SRH          = no

        Auger        = no

        radiative    = no
    }
}
--------------------------------------------------------------------------
quantum{

    region{
        name = "quantum_region"
        x = [$QW_SEP/2, 1*$PER_WID + $QW_SEP/2]

        output_wavefunctions{
            max_num = 10
            amplitudes = yes
            probabilities = yes
        }

        Gamma{
            num_ev = 100
            accuracy = 1e-7
            iterations = 1000
        }
        HH{
            num_ev = 100
            accuracy = 1e-7
```

Page (4)

```
            iterations = 1000
        }
        LH{
            num_ev = 100
            accuracy = 1e-7
            iterations = 1000
        }
        SO{
            num_ev = 100
            accuracy = 1e-7
            iterations = 1000
        }
    }
}
------------------------------------------------------------------
strain{
    pseudomorphic_strain{}
}


run{
    solve_strain{}
    solve_poisson{}
    solve_quantum{}                                    Page (5)
}
```

The figure below shows the simulation result of the 77 K bandgap energy and corresponding wavelength engineering versus the Sb composition and layer thickness variations in InAs/InAsSb T2SL. Numerous simulations were performed with varying SL periods and Sb compositions to

determine the cut-off wavelength for the MWIR range (3-6 μm). The simulated periods (P) are 28, 20, 14, 10, and 6 nm, and the composition of Sb in the InAsSb QWs ranges from 0.03% to 0.14 %.
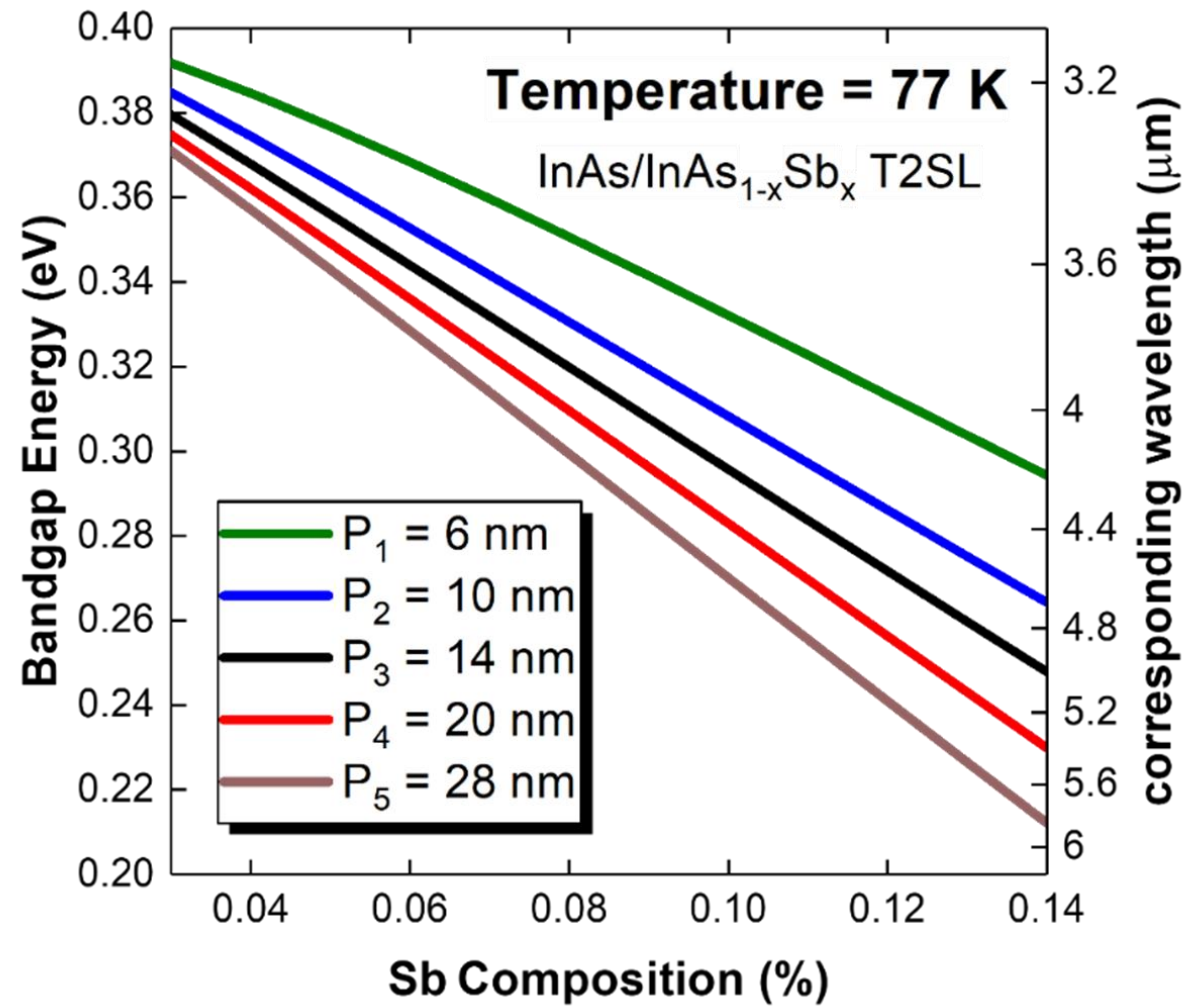
### E. Device modelling of InAs/GaSb T2SL using Silvaco software

An example of the simulation file of the T2SL 7/4 ML *pin* photodiode (Sample C) performed by Silvaco ATLAS software at room temperature.

Another simulation was performed using similar steps, but the parameters were changed depending on the temperature.

```
go atlas

set name="homojunction_MWIR_T2SL_nip"

set Pdop=1e18
set Idop=9.7e14
set Ndop=1e18


#MESH#

mesh width=1e8

x.mesh loc=0.0 spac=2.5
x.mesh loc=1.0 spac=2.5

y.mesh loc=0.0 spac=0.1
y.mesh loc=0.050 spac=0.005
y.mesh loc=0.055 spac=0.001
y.mesh loc=0.065 spac=0.001
y.mesh loc=0.070 spac=0.005
y.mesh loc=1.050 spac=0.005
y.mesh loc=1.055 spac=0.001
y.mesh loc=1.065 spac=0.001
y.mesh loc=1.070 spac=0.005
y.mesh loc=1.120 spac=0.05

qtx.mesh loc=0.0 spac=2.5
qtx.mesh loc=1.0 spac=2.5

qty.mesh loc=0.0 spac=0.1
qty.mesh loc=0.050 spac=0.005
qty.mesh loc=0.055 spac=0.001
qty.mesh loc=0.065 spac=0.001
qty.mesh loc=0.070 spac=0.005
qty.mesh loc=1.050 spac=0.005
qty.mesh loc=1.055 spac=0.001
qty.mesh loc=1.065 spac=0.001
qty.mesh loc=1.070 spac=0.005
qty.mesh loc=1.120 spac=0.05

#REGIONS AND CONTACTS#

region num=1 x.min=0 x.max=1.0 y.min=0.000 y.max=0.060 user.material=pregion
region num=2 x.min=0 x.max=1.0 y.min=0.060 y.max=1.060 user.material=SL
region num=3 x.min=0 x.max=1.0 y.min=1.060 y.max=1.120 user.material=nregion

electrode name=anode top
electrode name=cathode bottom

#DOPING#

doping unif p.type conc=$Pdop y.min=0.000 y.max=0.060
doping unif n.type conc=$Idop y.min=0.060 y.max=1.060
doping unif n.type conc=$Ndop y.min=1.060 y.max=1.120

#MATERIAL PARAMETERS#

material mat=nregion user.group=semiconductor user.default=InAs


#7/4 SL

material mat=SL user.group=semiconductor user.default=GaSb taun0=4.4e-6 taup0=4.4e-
#Nc, Nv needs to be defined for ni calculation otherwise Silvaco takes InAs bulk v
```

```
#MODELS#

#7-4 SL

mobility material=SL mun=2.6e4 mup=6.8e2 tmun=1.5 tmup=1.5

models temperature=150 ni.fermi fermi print
models analytic
models srh
models mass.tunnel=0.023 trap.tunnel
models bbt.nonlocal

#models analytic

#models arora

#models conmob

#models fldmob

#OUTPUT#

output band.temp band.param e.mob h.mob u.auger u.srh u.trap u.bbt recomb permittivity

solve init
save outf=structure_$'name'_0V.str
tonyplot structure_$'name'_0V.str

#DARK-CURRENT SIMULATION#

log outf=current_$'name'.log
solve name=anode vanode=0.2 vstep=-0.005 vfinal=0.0
solve name=anode vanode=0.0 vstep=-0.01 vfinal=-0.1
solve name=anode vanode=-0.05 vstep=-0.01 vfinal=-0.25
solve name=anode vanode=-0.25 vstep=-0.01 vfinal=-0.8

#solve name=anode vanode=-1 vstep=-0.005 vfinal=-3

tonyplot current_$'name'.log
log off

quit
```

Page (1)

## F. Mathematica script

The Mathematica script is used to solve current equations at a temperature of 110 K.

**BandGap Energy and Area of Diodes**

```
In[651]:= Eg110 = 0.238 * 1.6*^-19; (*Bandgap energy @110K, Determined by PL*)
P2 = 4.523893421*^-8; (*Area of P2 in m^2*)
P3 = 1.5393804*^-8; (*Area of P3 in m^2*)
```

**Effective DOS and ICC**

```
In[654]:= k = 1.38*^-23; (*Boltzmann constant, unit: m^2 kg s^-2 K^-1*)
h = 6.63*^-34; (*Planck's constant, unit: m^2 kg s^-1*)
m0 = 9.11*^-31; (*Free electron rest mass, unit: kg*)
me = 0.078 * m0; (**Electron effective mass in InAs layer,
unit: kg, taken from Martyniuk 2012*)
mh = 0.4 * m0; (*Hole effective mass in GaSb layer,
unit: kg, taken from Martyniuk 2012*)
Temp = 110; (*Temperature, unit: K*)
```

```
In[660]:= T = 110;
```

```
In[661]:= Nc = 2 * (((2 * Pi * me * k * T) / h^2)^1.5); (*DOS of electrons in the CB*)
Nv = 2 * (((2 * Pi * mh * k * T) / h^2)^1.5); (*DOS of holes in the VB*)
```

```
In[663]:= nicc = Sqrt[Nv * Nc] * Exp[- (Eg110 / (2 * k * T))]; (*Intrinsic carrier concentration*)
```

**Diffusion Current**

```
In[664]:= q = 1.60*^-19; (*Electron chrage, unit: Coloumb*)
A = 1.5393804*^-8; (*Area of P3 in m^2*)
Na = 1*^24; (*Acceptor concentration on the p-side regio, unit: m^-3*)
Nd = 1*^24; (*Donor concentration on the n-side region, unit: m^-3*)
mun = 0.11;
(*Minority electron mobility, unit: m^2 V s^-1,
taken from Gopal'paper 2008/Martyniuk 2012*)
mup = 0.065;
(*Minority Hole mobility, unit: m^2 V s^-1, taken from Martyniuk 2012*)
taun = 1*^-7; (*Electron lifetime, unit: s, rough estimation*)
taup = 3*^-7; (*Hole lifetime, unit:s, rough estimation*)
dp = 5*^-6; (*Hole diffusion length, unit: m, rough estimation*)
dn = 6*^-5; (*Electron diffusion length, unit: m, rough estimation*)
Ndop = 1*^9; (*doping concentration on the active region, unit: m^-3*)
```

```
In[687]:= Idiff[V_] = (((q * A * nicc^2) / Nd) * (Sqrt[((k * T * mun) / (q * taun))]) *
Tanh[Exp[(q * V) / (k * T)] - 1] (*Diffusion dark current expression*)
Out[687]= -5.4614 × 10^-13 Tanh[1 - e^{105.402 V}]
```

```
In[688]:= Abs[Idiff[V]]
Out[688]= 5.4614 × 10^-13 Abs[Tanh[1 - e^{105.402 V}]]
```

```
In[669]:= Plot[Abs[Idiff[V]], {V, -1, 1}, PlotRange → All]
```

Out[669]=
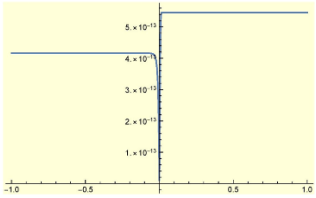


```
In[670]:= Jdiff[V_] = (((q * A * nicc^2) / Nd) * (Sqrt[((k * T * mun) / (q * taun))]) *
(Abs[Tanh[((1*^-6) / dp) * ((Exp[105.402 * V]) - 1)]])) /
P3 (*Diffusion dark current density expression*)
Out[670]= 0.0000354779 Abs[Tanh[1/5 (-1 + e^{105.402 V})]]
```

```
In[671]:= Plot[Jdiff[V], {V, -1, 1}, PlotRange → All]
```

Out[671]=
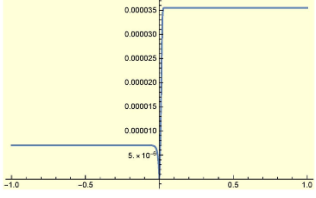


**Generation Recombination: Built-in junction voltage**

```
In[672]:= Vd = ((k * T) / q) * Log[(Nd * Na) / (nicc^2)]
Out[672]= 0.254797
```

**Depletion Region Width**

```
In[673]:= ep0 = 8.854*^-12; (*Free space permittivity, unit: F m^-1*)
eps = 15.42; (*Static dielectric constant, no unit, taken from Martyniuk 2012*)
```

```
In[675]:= Wdep = 4*^-10;
(*Depletion region width, unit: m,
calcualted using expression in Gopal's paper 2008*)
```

**Generation Recombination Current**

```
In[676]:= taugr = 6.4*^-7;
(*G-R lifetime, unit: s, taken from Martyniuk'paper
2012 and in Rogaliski's review paper 2019 is around 1x10^-6*)
```

In[677]:= Igr[V_] = If[V ≥ 0,
  Abs[((2 * A * nicc * Wdep * k * T) / (Abs[Vd - V] * taugr)) * Sinh[((q * V) / (2 * k * T))]],
  Abs[(q * A * Wdep * nicc * V) / ((Vd - V) * taugr)]];
(*G-R dark current relationship in both cases: FW bias and Rev bias*)

In[678]:= Plot[Igr[V], {V, -1, 0}, PlotRange → All]

Out[678]=
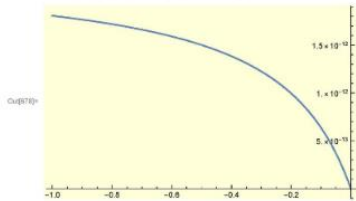

In[679]:= Jgr[V_] =
  Abs[(q * A * Wdep * nicc * V) / ((Vd - V) * taugr)] / P3 (*G-R dark current density*)

Out[679]= 0.000147327 Abs[$\frac{V}{0.254797 - V}$]

In[680]:= Plot[Jgr[V], {V, -1, 0}, PlotRange → All]

Out[680]=
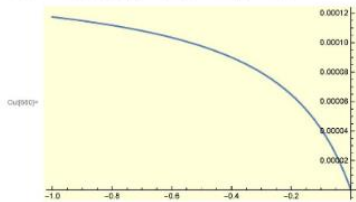

### *Trap Assisted Tunneling: Electric Field Strength (Emax)*

In[681]:= Emax[V_] = Sqrt[((2 * q * Nd * (Abs[Vd - V])) / (ep0 * eps)] (*Electric field maxima*)

Out[681]= 4.84131 × 10^7 $\sqrt{\text{Abs}[0.254797 - V]}$

In[682]:= Plot[Emax[V], {V, -1, 0}, PlotRange → All]

Out[682]=
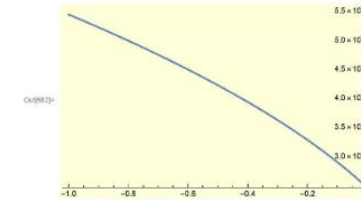

### *Electrons' Tunneling Rate*

In[683]:= M = 5.4*^-37;
(*The matrix element associated with the trap potential,
unit: V m^3, an estimated value/Fitting parameter*)

In[684]:= Et110 = Eg110 / 2 (*The position of trap levels in the bandgap*)

Out[684]= 1.904 × 10^{-20}

In[685]:= WcNc[V_] = ((Pi^2 * q * me * Emax[V] * M^2) / (h^3 * (Eg110 - Et110))) *
  Exp[-((((8 * Pi * (Sqrt[2 * me]) * ((Eg110 - Et110)^(3/2)))) / (3 * q * h * Emax[V])))]
(*Tunnelling rate of electrons, expression is found in Gopal's paper 2003*)

Out[685]= 285480. e^{-$\frac{1.43144}{\sqrt{\text{Abs}[0.254797 - V]}}$} $\sqrt{\text{Abs}[0.254797 - V]}$

In[686]:= Plot[WcNc[V], {V, -1, 0}, PlotRange → All]

Out[686]=


In[687]:= LogPlot[WcNc[V], {V, -1, 0}, PlotRange → All]

Out[687]=
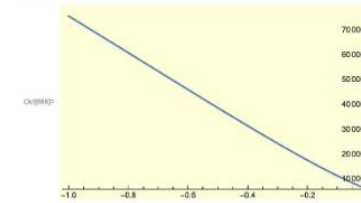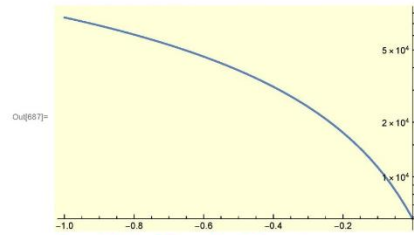


### Trap Assisted Tunneling Current

In[688]:= `Nt = 1*^17; (*Trap density, unit: m^-3, taken from Martyniuk'paper 2012*)`

In[689]:= `Itat[V_] = q * A * Nt * Wdep * WcNc[V] (*TAT dark current expression*)`

Out[689]= $2.81256 \times 10^{-14} \, e^{-\frac{1.61564}{\sqrt{\text{Abs}[0.254797-V]}}} \sqrt{\text{Abs}[0.254797-V]}$

In[690]:= `Plot[Itat[V], {V, -1, 0}, PlotRange → All]`

Out[690]=
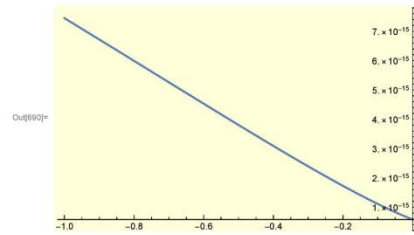


In[691]:= `LogPlot[Itat[V], {V, -1, 0}, PlotRange → All]`

Out[691]=



247
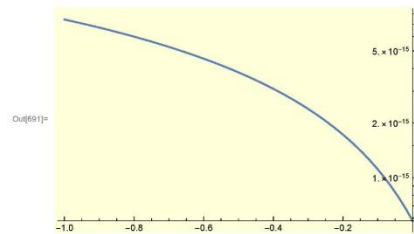
## G. Single temperature-dependent photoluminescence fittings of Samples A and B

The single temerpature-dependt PL fittings of Samples A and B are shown in the figures underneath.

## Sample A (temperature-dependent PL fittings)
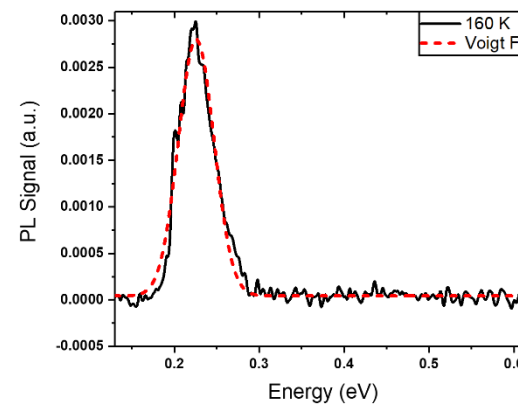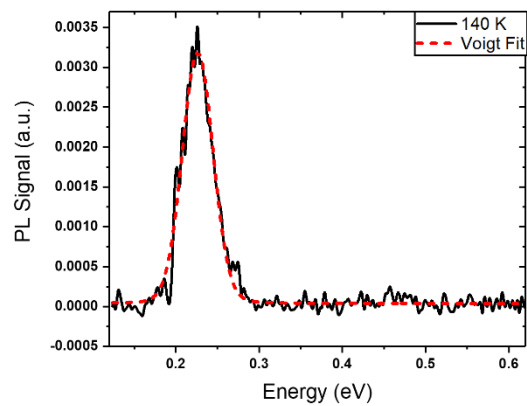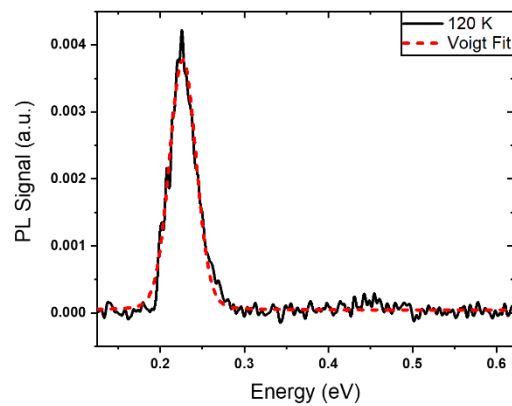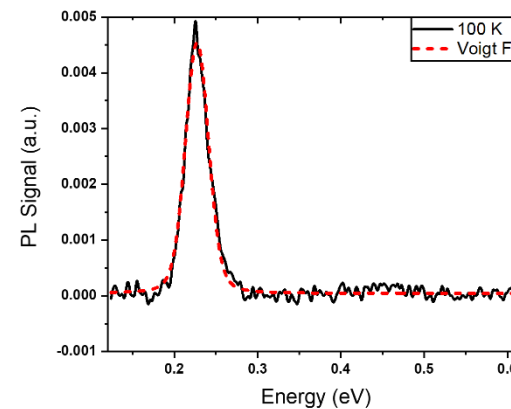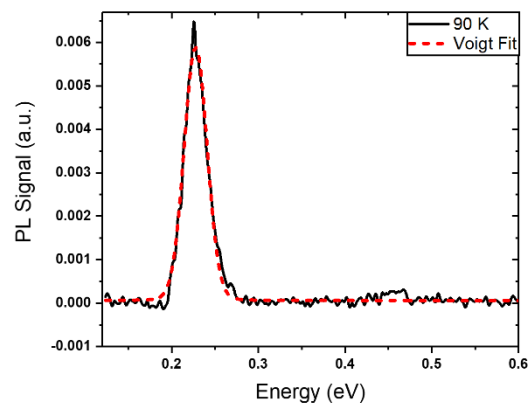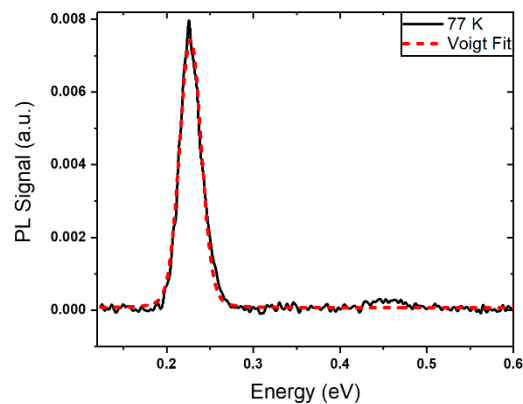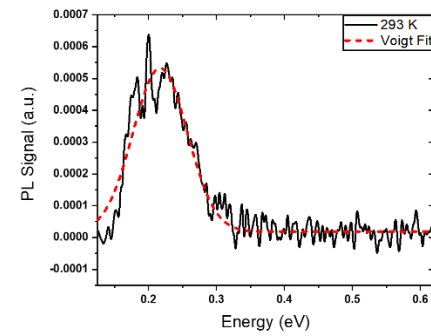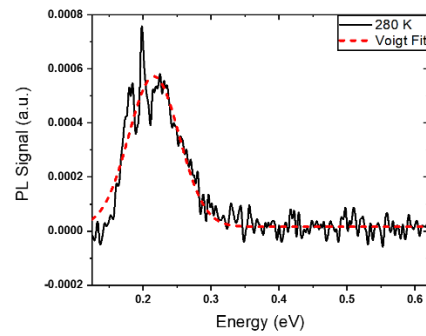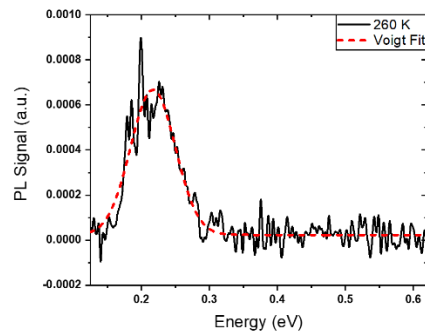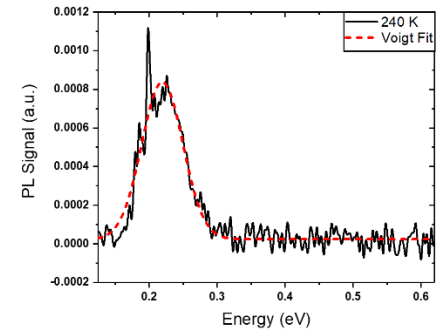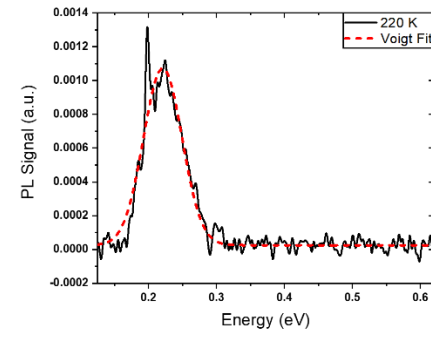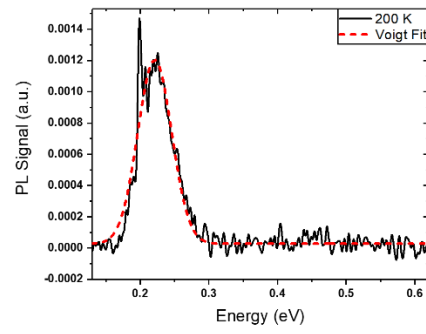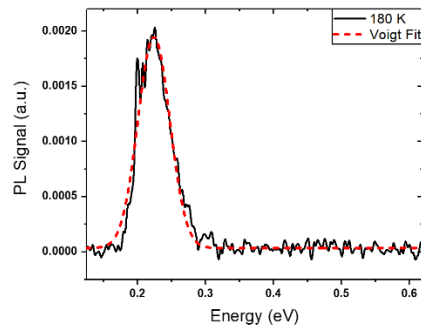
## Sample B (temperature-dependent PL fittings)
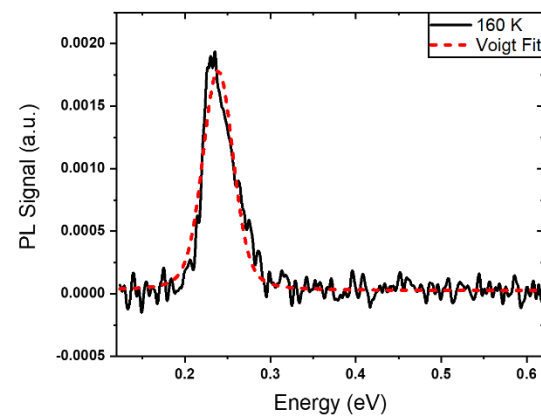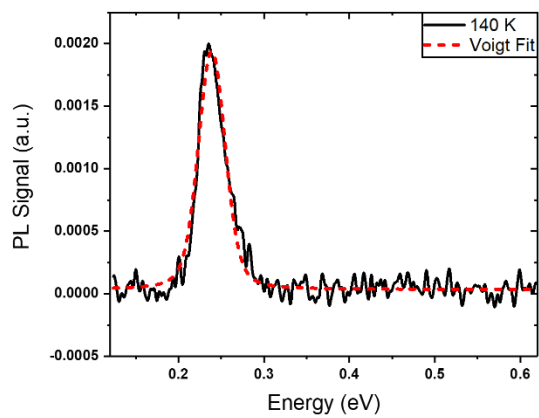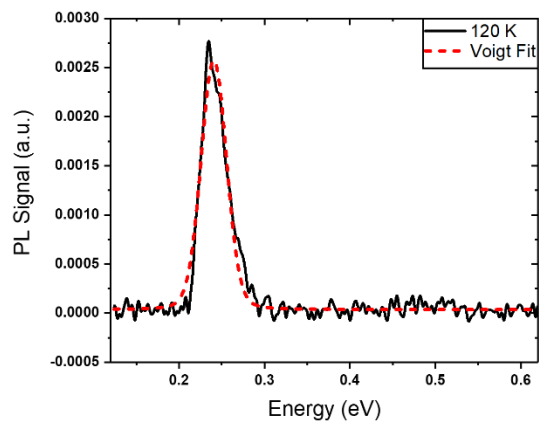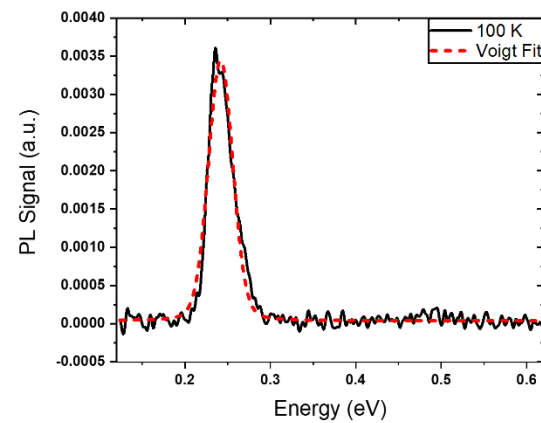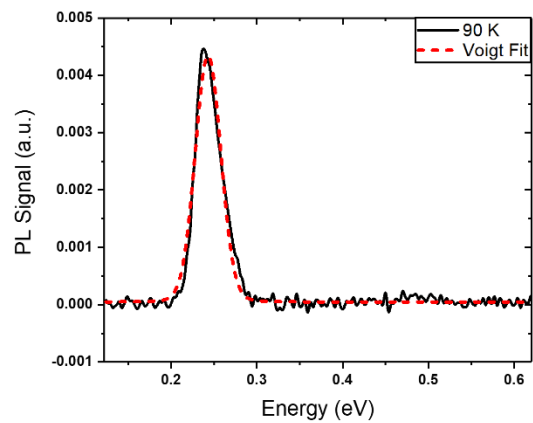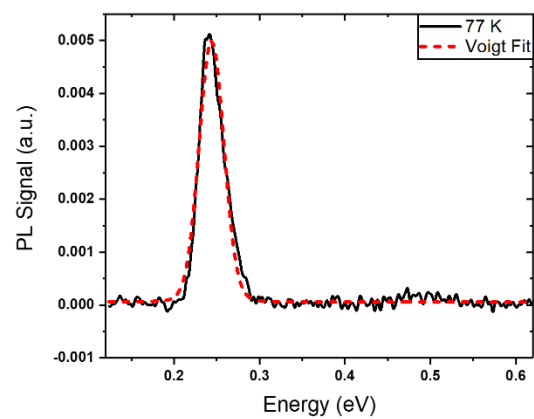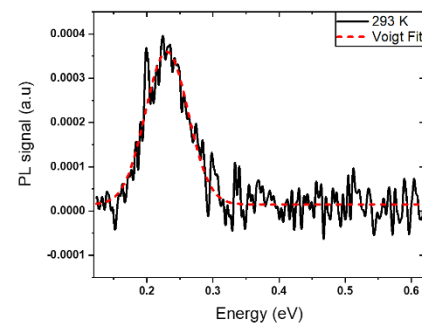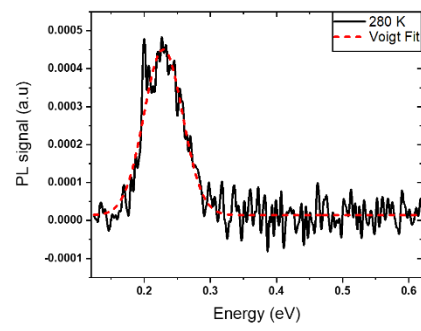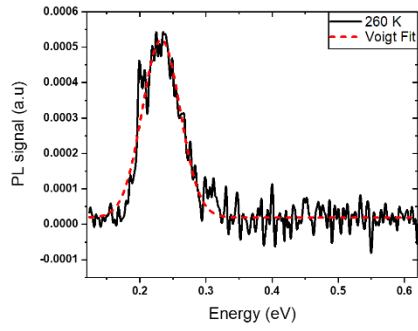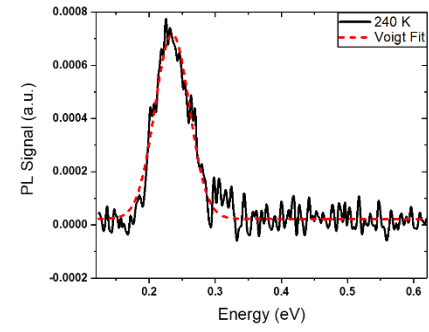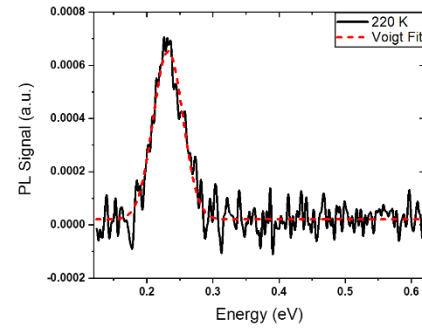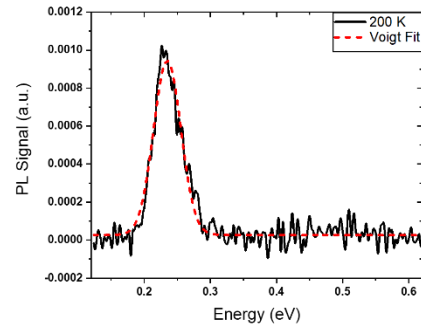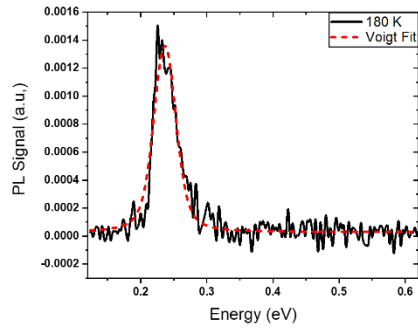
# References

[1]     M. K. Parry and A. Krier, 'Room-temperature Cd-diffused InAsSbP diodes for methane gas detection', *Semicond. Sci. Technol.*, vol. 8, no. 9, pp. 1764–1769, Sep. 1993, doi: 10.1088/0268-1242/8/9/017.

[2]     L. Fleming, D. Gibson, S. Song, C. Li, and S. Reid, 'Reducing N2O induced cross-talk in a NDIR CO2 gas sensor for breath analysis using multilayer thin film optical interference coatings', *Surf. Coat. Technol.*, vol. 336, pp. 9–16, Feb. 2018, doi: 10.1016/j.surfcoat.2017.09.033.

[3]     M. Villar, 'Mid-Infrared Absorption Spectrometer for Multi-Species Detection Using LEDs for Space Applications: Development and Flight Testing', MSc Thesis, University of Central Florida, Orlando, Florida, 2017.

[4]     D. Jung, S. Bank, M. L. Lee, and D. Wasserman, 'Next-generation mid-infrared sources', *J. Opt.*, vol. 19, no. 12, p. 123001, Dec. 2017, doi: 10.1088/2040-8986/aa939b.

[5]     A. Krier, M. Stone, Q. D. Zhuang, P.-W. Liu, G. Tsai, and H. H. Lin, 'Mid-infrared electroluminescence at room temperature from InAsSb multi-quantum-well light-emitting diodes', *Appl. Phys. Lett.*, vol. 89, no. 9, p. 091110, Aug. 2006, doi: 10.1063/1.2339036.

[6]     'European Photonics Industry Consortium'. Accessed: Mar. 20, 2021. [Online]. Available: https://www.photonics.com/Articles/Pilot_Line_Underscores_Untapped_Potential_of /a61245

[7]     J. A. Logan, 'Nitrogen oxides in the troposphere: Global and regional budgets', *J. Geophys. Res. Oceans*, vol. 88, no. C15, pp. 10785–10807, 1983, doi: https://doi.org/10.1029/JC088iC15p10785.

[8]     X. Chao, J. B. Jeffries, and R. K. Hanson, 'In situ absorption sensor for NO in combustion gases with a 5.2μm quantum-cascade laser', *Proc. Combust. Inst.*, vol. 33, no. 1, pp. 725–733, Jan. 2011, doi: 10.1016/j.proci.2010.05.014.

[9]     B. G. Miller, *Coal Energy Systems*. Elsevier Academic Press, San Diego, California, 2005.

[10]    C. Price, J. Penner, and M. Prather, 'NOx from lightning: 1. Global distribution based on lightning physics', *J. Geophys. Res. Atmospheres*, vol. 102, no. D5, pp. 5929–5941, 1997, doi: https://doi.org/10.1029/96JD03504.

[11]    J. Wojtas, A. Gluszek, A. Hudzikowski, and F. K. Tittel, 'Mid-Infrared Trace Gas Sensor Technology Based on Intracavity Quartz-Enhanced Photoacoustic Spectroscopy', *Sensors*, vol. 17, no. 3, Art. no. 3, Mar. 2017, doi: 10.3390/s17030513.

[12]    M. A. Kinch, *Fundamentals of Infrared Detector Materials*. Bellingham, Washington, USA: SPIE Press, 2007.

[13] *Directive 2011/65/EU of the European Parliament and of the Council of 8 June 2011 on the restriction of the use of certain hazardous substances in electrical and electronic equipment Text with EEA relevance*, vol. OJ L. 2011. Accessed: Mar. 26, 2021. [Online]. Available: http://data.europa.eu/eli/dir/2011/65/oj/eng

[14] A. Rogalski, P. Martyniuk, and M. Kopytko, 'Type-II superlattice photodetectors versus HgCdTe photodiodes', *Prog. Quantum Electron.*, vol. 68, p. 100228, Aug. 2019, doi: 10.1016/j.pquantelec.2019.100228.

[15] A. Rogalski, 'HgCdTe infrared detector material: history, status and outlook', *Rep. Prog. Phys.*, vol. 68, no. 10, pp. 2267–2336, Aug. 2005, doi: 10.1088/0034-4885/68/10/R01.

[16] P. Klipstein *et al.*, 'Recent progress in InSb based quantum detectors in Israel', *Infrared Phys. Technol.*, vol. 59, pp. 172–181, Jul. 2013, doi: 10.1016/j.infrared.2012.12.035.

[17] T. L. Haran, J. C. James, S. E. Lane, and T. E. Cincotta, 'Quantum efficiency and spatial noise tradeoffs for III–V focal plane arrays', *Infrared Phys. Technol.*, vol. 97, pp. 309–318, Mar. 2019, doi: 10.1016/j.infrared.2019.01.001.

[18] P. C. Klipstein *et al.*, 'Low SWaP MWIR detector based on XBn focal plane array', in *Infrared Technology and Applications XXXIX*, International Society for Optics and Photonics, Jun. 2013, p. 87041S. doi: 10.1117/12.2015747.

[19] G. A. Sai-Halasz, R. Tsu, and L. Esaki, 'A new semiconductor superlattice', *Appl. Phys. Lett.*, vol. 30, no. 12, pp. 651–653, Jun. 1977, doi: 10.1063/1.89273.

[20] D. L. Smith and C. Mailhiot, 'Proposal for strained type II superlattice infrared detectors', *J. Appl. Phys.*, vol. 62, no. 6, pp. 2545–2548, Sep. 1987, doi: 10.1063/1.339468.

[21] J. L. Johnson *et al.*, 'Electrical and optical properties of infrared photodiodes using the InAs/Ga1–xInxSb superlattice in heterojunctions with GaSb', *J. Appl. Phys.*, vol. 80, no. 2, pp. 1116–1127, Jul. 1996, doi: 10.1063/1.362849.

[22] A. Rogalski, 'Recent progress in infrared detector technologies', *Infrared Phys. Technol.*, vol. 54, no. 3, pp. 136–154, May 2011, doi: 10.1016/j.infrared.2010.12.003.

[23] S. R. Kurtz, R. M. Biefeld, and A. J. Howard, 'Magneto-optical determination of light-heavy hole splittings in As-rich, InAsSb alloys and superlattices', *Appl. Phys. Lett.*, vol. 67, no. 22, pp. 3331–3333, Nov. 1995, doi: 10.1063/1.115237.

[24] C. M. Ciesla *et al.*, 'Suppression of Auger recombination in arsenic-rich InAs1–xSbx strained layer superlattices', *J. Appl. Phys.*, vol. 80, no. 5, pp. 2994–2997, Sep. 1996, doi: 10.1063/1.363157.

[25] H. Wen and E. Bellotti, 'Optical absorption and intrinsic recombination in relaxed and strained InAsSb alloys for mid-wavelength infrared application', *Appl. Phys. Lett.*, vol. 107, no. 22, p. 222103, Nov. 2015, doi: 10.1063/1.4936862.

[26] G. C. Osbourn, L. R. Dawson, R. M. Biefeld, T. E. Zipperian, I. J. Fritz, and B. L. Doyle, 'III–V strained layer supperlattices for long-wavelength detector applications: Recent progress', *J. Vac. Sci. Technol. A*, vol. 5, no. 5, pp. 3150–3152, Sep. 1987, doi: 10.1116/1.574857.

[27] A. Rogalski, M. Kopytko, and P. Martyniuk, 'InAs/GaSb type-II superlattice infrared detectors: three decades of development', in *Infrared Technology and Applications XLIII*, International Society for Optics and Photonics, May 2017, p. 1017715. doi: 10.1117/12.2272817.

[28] J. Bajaj, G. Sullivan, D. Lee, E. Aifer, and M. Razeghi, 'Comparison of type-II superlattice and HgCdTe infrared detector technologies', in *Infrared Technology and Applications XXXIII*, International Society for Optics and Photonics, Jun. 2007, p. 65420B. doi: 10.1117/12.723849.

[29] R. Müller *et al.*, 'Advances in type-II superlattice research at Fraunhofer IAF', *Opto-Electron. Rev.*, vol. Vol. 31, Special Issue, 2023, doi: 10.24425/opelre.2023.144553.

[30] Y. Ma *et al.*, 'Impact of etching on the surface leakage generation in mesa-type InGaAs/InAlAs avalanche photodetectors', *Opt. Express*, vol. 24, no. 7, pp. 7823–7834, Apr. 2016, doi: 10.1364/OE.24.007823.

[31] D. Smoczyński *et al.*, 'The impact of mesa etching method on IR photodetector current-voltage characteristics', *Mater. Sci. Semicond. Process.*, vol. 118, p. 105219, Nov. 2020, doi: 10.1016/j.mssp.2020.105219.

[32] J. Guo, R. T. Hao, Q. R. Zhao, and S. Q. Man, 'Study of Mesa Etching for Infrared Detector Based on InAs/GaSb Superlattice', *Adv. Mater. Res.*, vol. 760–762, pp. 137–140, 2013, doi: 10.4028/www.scientific.net/AMR.760-762.137.

[33] E. Plis, 'Mid-IR type-II InAs/GaSb nanoscale superlattice sensors', PhD Thesis, The University of New Mexico, 2007. [Online]. Available: https://digitalrepository.unm.edu/ece_etds/207

[34] V. Sapritsky and A. Prokhorov, *Blackbody Radiometry: Volume 1: Fundamentals*. Springer Nature, 2020.

[35] S. H. Simon, *The Oxford Solid State Basics*. OUP Oxford, 2013.

[36] S. M. Girvin and K. Yang, *Modern Condensed Matter Physics*. Cambridge University Press, 2019.

[37] C. Kittel, *Introduction to solid state physics. (8th ed.)*. Wiley, 2005. Accessed: Feb. 22, 2024. [Online]. Available: http://repository.vnu.edu.vn/handle/VNU_123/91323

[38] M. Dresselhaus, G. Dresselhaus, S. B. Cronin, and A. Gomes Souza Filho, 'Examples of Energy Bands in Solids', in *Solid State Properties: From Bulk to Nano*, M. Dresselhaus, G. Dresselhaus, S. Cronin, and A. Gomes Souza Filho, Eds., in Graduate Texts in Physics. , Berlin, Heidelberg: Springer, 2018, pp. 55–87. doi: 10.1007/978-3-662-55922-2_4.

[39] S. M. Sze and K. K. Ng, *Physics of Semiconductor Devices: 9780470068304*. Wiley-Interscience, 2006. [Online]. Available: https://www.dawsonera.com:443/abstract/9780470068304

[40] F. C. Frank and J. H. Van der Merwe, 'One-dimensional dislocations. II. Misfitting monolayers and oriented overgrowth', *Proc. R. Soc. Lond. Ser. Math. Phys. Sci.*, vol. 198, no. 1053, pp. 216–225, 1949.

[41] J. W. Matthews and A. E. Blakeslee, 'Defects in epitaxial multilayers: I. Misfit dislocations', *J. Cryst. Growth*, vol. 27, pp. 118–125, Dec. 1974, doi: 10.1016/S0022-0248(74)80055-2.

[42] R. People and J. C. Bean, 'Calculation of critical layer thickness versus lattice mismatch for GexSi1–x/Si strained-layer heterostructures', *Appl. Phys. Lett.*, vol. APLCLASS2019, no. 1, pp. 322–324, Jun. 1998, doi: 10.1063/1.96206@apl.2019.APLCLASS2019.issue-1.

[43] C. W. Passchier and R. A. J. Trouw, *Microtectonics*. Springer Science & Business Media, 2005.

[44] E. P. O'Reilly, 'Valence band engineering in strained-layer structures', *Semicond. Sci. Technol.*, vol. 4, no. 3, pp. 121–137, Mar. 1989, doi: 10.1088/0268-1242/4/3/001.

[45] A. Rogalski, *Infrared Detectors*. CRC Press, 2010.

[46] P. Martyniuk, J. Antoszewski, M. Martyniuk, L. Faraone, and A. Rogalski, 'New concepts in infrared photodetector designs', *Appl. Phys. Rev.*, vol. 1, no. 4, p. 041102, Nov. 2014, doi: 10.1063/1.4896193.

[47] A. Rogalski, 'Progress in focal plane array technologies', *Prog. Quantum Electron.*, vol. 36, no. 2, pp. 342–473, Mar. 2012, doi: 10.1016/j.pquantelec.2012.07.001.

[48] J. Caniou, *Passive Infrared Detection: Theory and Applications*. Springer Science & Business Media, 2013.

[49] O. Temel, 'Molecular beam epitaxy growth of inp/ingaas structures for short wavelength infrared photodetectors', Master Thesis, Middle East Technical University, 2014. Accessed: May 11, 2023. [Online]. Available: https://open.metu.edu.tr/handle/11511/23449

[50] G. S. Lee, Y. Lo, Y. F. Lin, S. M. Bedair, and W. D. Laidig, 'Growth of InAsSb (0<x<1) and InSb-InAsSb superlattices by molecular beam epitaxy', *Appl. Phys. Lett.*, vol. 47, no. 11, pp. 1219–1221, Dec. 1985, doi: 10.1063/1.96334.

[51] L. R. Dawson, 'Summary Abstract: Molecular beam epitaxial growth of InAsSb alloys and superlattices', *J. Vac. Sci. Technol. B Microelectron. Process. Phenom.*, vol. 4, no. 2, pp. 598–599, Mar. 1986, doi: 10.1116/1.583384.

[52] C. H. Grein, P. M. Young, and H. Ehrenreich, 'Minority carrier lifetimes in ideal InGaSb/InAs superlattices', *Appl. Phys. Lett.*, vol. 61, no. 24, pp. 2905–2907, Dec. 1992, doi: 10.1063/1.108480.

[53] E. R. Youngdale *et al.*, 'Auger lifetime enhancement in InAs–Ga1−xInxSb superlattices', *Appl. Phys. Lett.*, vol. 64, no. 23, pp. 3160–3162, Jun. 1994, doi: 10.1063/1.111325.

[54] M. Kopytko *et al.*, 'Numerical Analysis of Dark Currents in T2SL nBn Detector Grown by MBE on GaAs Substrate', *Adv. Infrared Technol. Appl.*, vol. 27, no. 1, p. 37, 2019, doi: 10.3390/proceedings2019027037.

[55] E. A. Plis, 'InAs/GaSb Type-II Superlattice Detectors', Advances in Electronics. Accessed: Nov. 26, 2019. [Online]. Available: https://www.hindawi.com/journals/aelc/2014/246769/abs/

[56] A. W. Rogalski, M. E. Kopytko, and P. M. Martyniuk, *Antimonide-based Infrared Detectors: A New Perspective*. SPIE - The International Society for Optics and Photonics, 2018. doi: 10.1117/3.2278814.

[57] V. Gopal, E. Plis, J.-B. Rodriguez, C. E. Jones, L. Faraone, and S. Krishna, 'Modeling of electrical characteristics of midwave type II InAs/GaSb strain layer superlattice diodes', *J. Appl. Phys.*, vol. 104, no. 12, p. 124506, Dec. 2008, doi: 10.1063/1.3042232.

[58] H. Mohseni, J. S. Wojkowski, A. Tahraoui, M. Razeghi, G. J. Brown, and W. C. Mitchel, 'Growth and characterization of type-II nonequilibrium photovoltaic detectors for long-wavelength infrared range', in *Photodetectors: Materials and Devices V*, International Society for Optics and Photonics, Apr. 2000, pp. 153–160. doi: 10.1117/12.382114.

[59] P. Chakrabarti, A. Gawarikar, V. Mehta, and D. Garg, 'Effect of Trap-assisted Tunneling (TAT) on the Performance of Homojunction Mid-Infrared Photodetectors based on InAsSb', *J. Microw. Optoelectron. Electromagn. Appl. JMOe*, vol. 5, no. 1, Art. no. 1, 2006.

[60] R. C. Jones, 'A Method of Describing the Detectivity of Photoconductive Cells', *Rev. Sci. Instrum.*, vol. 24, no. 11, pp. 1035–1040, Nov. 1953, doi: 10.1063/1.1770585.

[61] A. Rogalski, 'New material systems for third generation infrared photodetectors', *Opto-Electron. Rev.*, vol. 16, no. 4, p. 458, Sep. 2008, doi: 10.2478/s11772-008-0047-7.

[62] A. Rogalski, J. Antoszewski, and L. Faraone, 'Third-generation infrared photodetector arrays', *J. Appl. Phys.*, vol. 105, no. 9, p. 091101, May 2009, doi: 10.1063/1.3099572.

[63] A. Rogalski and J. Piotrowski, 'Intrinsic infrared detectors', *Prog. Quantum Electron.*, vol. 12, no. 2, pp. 87–289, Jan. 1988, doi: 10.1016/0079-6727(88)90001-8.

[64] E. S. Barr, 'The infrared pioneers—III. Samuel Pierpont Langley', *Infrared Phys.*, vol. 3, no. 4, pp. 195–206, Dec. 1963, doi: 10.1016/0020-0891(63)90024-1.

[65] T. W. Case, 'Notes on the Change of Resistance of Certain Substances in Light', *Phys. Rev.*, vol. 9, no. 4, pp. 305–310, Apr. 1917, doi: 10.1103/PhysRev.9.305.

[66] L. Esaki and R. Tsu, 'Superlattice and Negative Differential Conductivity in Semiconductors', *IBM J. Res. Dev.*, vol. 14, no. 1, pp. 61–65, Jan. 1970, doi: 10.1147/rd.141.0061.

[67] H. Sakaki, L. L. Chang, G. A. Sai-Halasz, C. A. Chang, and L. Esaki, 'Two-dimensional electronic structure in InAs-GaSb superlattices', *Solid State Commun.*, vol. 26, no. 9, pp. 589–592, Jun. 1978, doi: 10.1016/0038-1098(78)90770-6.

[68] R. M. Biefeld, K. C. Baucom, and S. R. Kurtz, 'The growth of InAsSb/InAs strained-layer superlattices by metalorganic chemical vapor deposition', *J. Cryst. Growth*, vol. 137, no. 1, pp. 231–234, Mar. 1994, doi: 10.1016/0022-0248(94)91276-9.

[69] M. J. Pullin, P. J. P. Tang, S. J. Chung, C. C. Phillips, and R. A. Stradling, '300K light emitting devices for the 3-10um band from arsenic rich InAs/InAs., Sb, strained layer superlattices', in *Narrow Gap Semiconductors 1995: Proceedings of the Seventh International Conference on Narrow Gap Semiconductors, Santa Fe, New Mexico, 8-12 January 1995*, CRC Press, 1995, p. 8.

[70] Y. Zhang, 'Continuous wave operation of InAs/InAsxSb1−x midinfrared lasers', *Appl. Phys. Lett.*, vol. 66, no. 2, pp. 118–120, Jan. 1995, doi: 10.1063/1.113535.

[71] Y. Livneh *et al.*, 'k·p model for the energy dispersions and absorption spectra of InAs/GaSb type-II superlattices', *Phys. Rev. B*, vol. 86, no. 23, p. 235311, Dec. 2012, doi: 10.1103/PhysRevB.86.235311.

[72] P. C. Klipstein *et al.*, 'Modeling InAs/GaSb and InAs/InAsSb Superlattice Infrared Detectors', *J. Electron. Mater.*, vol. 43, no. 8, pp. 2984–2990, Aug. 2014, doi: 10.1007/s11664-014-3169-3.

[73] D. Donetsky, S. P. Svensson, L. E. Vorobjev, and G. Belenky, 'Carrier lifetime measurements in short-period InAs/GaSb strained-layer superlattice structures', *Appl. Phys. Lett.*, vol. 95, no. 21, p. 212104, Nov. 2009, doi: 10.1063/1.3267103.

[74] B. C. Connelly, G. D. Metcalfe, H. Shen, and M. Wraback, 'Time-resolved photoluminescence study of carrier recombination and transport in type-II superlattice infrared detector materials', in *Infrared Technology and Applications XXXIX*, International Society for Optics and Photonics, Jun. 2013, p. 87040V. doi: 10.1117/12.2016202.

[75] R. Kaspi, J. Steinshnider, M. Weimer, C. Moeller, and A. Ongstad, 'As-soak control of the InAs-on-GaSb interface', *J. Cryst. Growth*, vol. 225, no. 2, pp. 544–549, May 2001, doi: 10.1016/S0022-0248(01)00950-2.

[76] D. Z. Ting *et al.*, 'InAs/InAsSb Type-II Superlattice Mid-Wavelength Infrared Focal Plane Array With Significantly Higher Operating Temperature Than InSb', *IEEE Photonics J.*, vol. 10, no. 6, pp. 1–6, Dec. 2018, doi: 10.1109/JPHOT.2018.2877632.

[77] J. Steinshnider, J. Harper, M. Weimer, C.-H. Lin, S. S. Pei, and D. H. Chow, 'Origin of Antimony Segregation in GaInSb/InAs Strained-Layer Superlattices', *Phys. Rev. Lett.*, vol. 85, no. 21, pp. 4562–4565, Nov. 2000, doi: 10.1103/PhysRevLett.85.4562.

[78] Y. Ashuach, Y. Kauffmann, D. Isheim, Y. Amouyal, D. N. Seidman, and E. Zolotoyabko, 'Atomic intermixing in short-period InAs/GaSb superlattices', *Appl. Phys. Lett.*, vol. 100, no. 24, p. 241604, Jun. 2012, doi: 10.1063/1.4729058.

[79] X. Li, Y. Zhang, D. Jiang, F. Guo, D. Wang, and L. Zhao, 'Atomic intermixing and segregation at the interface of InAs/GaSb type II superlattices', *Superlattices Microstruct.*, vol. 104, pp. 390–396, Apr. 2017, doi: 10.1016/j.spmi.2017.02.052.

[80] S. P. Svensson, D. Donetsky, D. Wang, H. Hier, F. J. Crowne, and G. Belenky, 'Growth of type II strained layer superlattice, bulk InAs and GaSb materials for minority lifetime characterization', *J. Cryst. Growth*, vol. 334, no. 1, pp. 103–107, Nov. 2011, doi: 10.1016/j.jcrysgro.2011.08.030.

[81] B. V. Olson *et al.*, 'Time-resolved optical measurements of minority carrier recombination in a mid-wave infrared InAsSb alloy and InAs/InAsSb superlattice', *Appl. Phys. Lett.*, vol. 101, no. 9, p. 092109, Aug. 2012, doi: 10.1063/1.4749842.

[82] L. Höglund *et al.*, 'Influence of radiative and non-radiative recombination on the minority carrier lifetime in midwave infrared InAs/InAsSb superlattices', *Appl. Phys. Lett.*, vol. 103, no. 22, p. 221908, Nov. 2013, doi: 10.1063/1.4835055.

[83] I. Vurgaftman *et al.*, 'Interband absorption strength in long-wave infrared type-II superlattices with small and large superlattice periods compared to bulk materials', *Appl. Phys. Lett.*, vol. 108, no. 22, p. 222101, May 2016, doi: 10.1063/1.4953035.

[84] D. Z. Ting, A. Khoshakhlagh, A. Soibel, and S. D. Gunapala, 'Long Wavelength InAs/InAsSb Infrared Superlattice Challenges: A Theoretical Investigation', *J. Electron. Mater.*, vol. 49, pp. 6936–6945, Aug. 2020, doi: 10.1007/s11664-020-08349-7.

[85] D. Z. Ting *et al.*, 'Barrier infrared detector research at the Jet Propulsion Laboratory', in *Infrared Remote Sensing and Instrumentation XX*, SPIE, Oct. 2012, pp. 29–39. doi: 10.1117/12.929810.

[86] D. Z. Ting, A. Soibel, and S. D. Gunapala, 'Hole effective masses and subband splitting in type-II superlattice infrared detectors', *Appl. Phys. Lett.*, vol. 108, no. 18, p. 183504, May 2016, doi: 10.1063/1.4948387.

[87] D. Z. Ting, A. Soibel, and S. D. Gunapala, 'Type-II superlattice hole effective masses', *Infrared Phys. Technol.*, vol. 84, pp. 102–106, Aug. 2017, doi: 10.1016/j.infrared.2016.10.014.

[88] A. D. Prins, M. K. Lewis, Z. L. Bushell, S. J. Sweeney, S. Liu, and Y.-H. Zhang, 'Evidence for a defect level above the conduction band edge of InAs/InAsSb type-II superlattices for applications in efficient infrared photodetectors', *Appl. Phys. Lett.*, vol. 106, no. 17, p. 171111, Apr. 2015, doi: 10.1063/1.4919549.

[89] P. C. Klipstein *et al.*, 'InAs/GaSb Type II superlattice barrier devices with a low dark current and a high-quantum efficiency', in *Infrared Technology and Applications XL*, International Society for Optics and Photonics, Jun. 2014, p. 90700U. doi: 10.1117/12.2049825.

[90] H. J. Haugan, K. Mahalingam, F. Szmulowicz, and G. J. Brown, 'Quantitative study of the effect of deposition temperature on antimony incorporation in InAs/InAsSb superlattices', *J. Cryst. Growth*, vol. 436, pp. 134–137, Feb. 2016, doi: 10.1016/j.jcrysgro.2015.10.018.

[91] J. Lu, E. Luna, T. Aoki, E. H. Steenbergen, Y.-H. Zhang, and D. J. Smith, 'Evaluation of antimony segregation in InAs/InAs1–xSbx type-II superlattices grown by molecular beam epitaxy', *J. Appl. Phys.*, vol. 119, no. 9, p. 095702, Mar. 2016, doi: 10.1063/1.4942844.

[92] N. A. Kotulak *et al.*, 'Three-dimensional visualization of Sb segregation in InAs/InAsSb superlattices using atom probe tomography', *J. Appl. Phys.*, vol. 128, no. 1, p. 015302, Jul. 2020, doi: 10.1063/1.5143446.

[93] A. Evirgen *et al.*, 'InSb photodetectors with PIN and nBn designs', in *Quantum Sensing and Nanophotonic Devices XI*, International Society for Optics and Photonics, Jan. 2014, p. 899313. doi: 10.1117/12.2039156.

[94] A. Evirgen, J. Abautret, J. P. Perez, A. Cordat, A. Nedelcu, and P. Christol, 'Midwave infrared InSb nBn photodetector', *Electron. Lett.*, vol. 50, no. 20, pp. 1472–1473, Sep. 2014, doi: 10.1049/el.2014.2799.

[95] J.-P. Perez, A. Evirgen, J. Abautret, P. Christol, A. Cordat, and A. Nedelcu, 'MWIR InSb detector with nBn architecture for high operating temperature', in *Quantum Sensing and Nanophotonic Devices XII*, International Society for Optics and Photonics, Feb. 2015, p. 93700N. doi: 10.1117/12.2076141.

[96] C. Cervera *et al.*, 'Temperature dependence performances of InAs/GaSb superlattice photodiode', *Infrared Phys. Technol.*, vol. 54, no. 3, pp. 258–262, May 2011, doi: 10.1016/j.infrared.2010.12.025.

[97] Y. Aytac *et al.*, 'Bandgap and temperature dependence of Auger recombination in InAs/InAsSb type-II superlattices', *J. Appl. Phys.*, vol. 119, no. 21, p. 215705, Jun. 2016, doi: 10.1063/1.4953386.

[98] Z.-Y. Lin, S. Liu, E. H. Steenbergen, and Y.-H. Zhang, 'Influence of carrier localization on minority carrier lifetime in InAs/InAsSb type-II superlattices', *Appl. Phys. Lett.*, vol. 107, no. 20, p. 201107, Nov. 2015, doi: 10.1063/1.4936109.

[99] E. H. Steenbergen, J. A. Massengale, G. Ariyawansa, and Y.-H. Zhang, 'Evidence of carrier localization in photoluminescence spectroscopy studies of mid-wavelength infrared InAs/InAsSb type-II superlattices', *J. Lumin.*, vol. 178, pp. 451–456, Oct. 2016, doi: 10.1016/j.jlumin.2016.06.020.

[100] E. H. Steenbergen *et al.*, 'A recent review of mid-wavelength infrared type-II superlattices: carrier localization, device performance, and radiation tolerance', in *Quantum Sensing and Nano Electronics and Photonics XIV*, International Society for Optics and Photonics, Jan. 2017, p. 1011104. doi: 10.1117/12.2266040.

[101] B. Klein *et al.*, 'Carrier lifetime studies in midwave infrared type-II InAs/GaSb strained layer superlattice', *J. Vac. Sci. Technol. B*, vol. 32, no. 2, p. 02C101, Jan. 2014, doi: 10.1116/1.4862085.

[102] Y. Aytac *et al.*, 'Effects of layer thickness and alloy composition on carrier lifetimes in mid-wave infrared InAs/InAsSb superlattices', *Appl. Phys. Lett.*, vol. 105, no. 2, p. 022107, Jul. 2014, doi: 10.1063/1.4890578.

[103] Y. Aytac *et al.*, 'Temperature dependent carrier lifetime measurements of InAs/InAsSb T2SLs', presented at the SPIE 2015 - Quantum Sensing and Nanophotonic Devices XII, M. Razeghi, E. Tournié, and G. J. Brown, Eds., San Francisco, California, United States, Feb. 2015, p. 93700J. doi: 10.1117/12.2077753.

[104] G. Jenkins, 'Carrier Lifetime vs. Proton Radiation in Prototype III-V and II-VI Space-based Infrared Detectors', PhD Thesis, The University of New Mexico, Albuquerque, New Mexico, 2018. [Online]. Available: https://digitalrepository.unm.edu/ece_etds/441

[105] C. N. Kadlec *et al.*, 'In-situ Annealing Studies of Radiation Induced Defects in InAs/InAsSb Type-II Superlattices under Ion Irradiation', Sandia National Lab. (SNL-NM), Albuquerque, NM (United States), SAND2018-3886C, Apr. 2018. Accessed: Jul. 16, 2020. [Online]. Available: https://www.osti.gov/biblio/1575172

[106] Z. Lin, 'Study of Minority Carrier Lifetime and Transport in InAs/InAsSb Type-II Superlattices Using a Real-time Baseline Correction Method', PhD Thesis, Arizona State University, ARIZONA STATE UNIVERSITY, 2016.

[107] C. N. Kadlec *et al.*, 'Effects of 4.5 MeV and 63 MeV Proton Irradiation on Carrier Lifetime of InAs/InAsSb Type-II Superlattices', Sandia National Lab. (SNL-NM), Albuquerque, NM (United States), SAND2017-8341C, Aug. 2017. doi: 10.1117/12.2274377.

[108] L. Höglund *et al.*, 'Minority carrier lifetime in mid-wavelength infrared InAs/InAsSb superlattices: Photon recycling and the role of radiative and Shockley-Read-Hall

recombination mechanisms', *Appl. Phys. Lett.*, vol. 105, no. 19, p. 193510, Nov. 2014, doi: 10.1063/1.4902022.

[109] Z.-Y. Lin, J. Fan, S. Liu, and Y.-H. Zhang, 'Photoluminescence study of carrier recombination processes in InAs/InAsSb type-II superlattices', in *Infrared Technology and Applications XLI*, International Society for Optics and Photonics, Jun. 2015, p. 94510Q. doi: 10.1117/12.2177526.

[110] U. Zavala-Moran *et al.*, 'Structural, Optical and Electrical Characterizations of Midwave Infrared Ga-Free Type-II InAs/InAsSb Superlattice Barrier Photodetector', *Photonics*, vol. 7, no. 3, Art. no. 3, Sep. 2020, doi: 10.3390/photonics7030076.

[111] A. Soibel *et al.*, 'Mid-wavelength infrared InAsSb/InAs nBn detectors and FPAs with very low dark current density', *Appl. Phys. Lett.*, vol. 114, no. 16, p. 161103, Apr. 2019, doi: 10.1063/1.5092342.

[112] S. P. Svensson, D. Donetsky, D. Wang, P. Maloney, and G. Belenky, 'Carrier lifetime measurements in InAs/GaSb strained layer superlattice structures', in *Infrared Technology and Applications XXXVI*, International Society for Optics and Photonics, May 2010, p. 76601V. doi: 10.1117/12.849514.

[113] B. C. Connelly, G. D. Metcalfe, H. Shen, and M. Wraback, 'Study of recombination mechanisms limiting the performance of Sb-based III-V type II superlattices for infrared detectors', in *Infrared Sensors, Devices, and Applications; and Single Photon Imaging II*, International Society for Optics and Photonics, Sep. 2011, p. 81550L. doi: 10.1117/12.893964.

[114] Z. Taghipour *et al.*, 'Extraction of minority carrier diffusion length of MWIR Type-II superlattice nBp detector', in *Infrared Sensors, Devices, and Applications VII*, International Society for Optics and Photonics, Aug. 2017, p. 1040406. doi: 10.1117/12.2274591.

[115] Z. Taghipour *et al.*, 'Vertical transport study of InAs/GaSb type-II superlattice nBp MWIR detectors using electron beam-induced current measurement', in *Infrared Technology and Applications XLIV*, International Society for Optics and Photonics, May 2018, p. 106240N. doi: 10.1117/12.2309658.

[116] Z. Taghipour *et al.*, 'Temperature-Dependent Minority-Carrier Mobility in p-Type InAs/GaSb Type-II-Superlattice Photodetectors', *Phys. Rev. Appl.*, vol. 11, no. 2, p. 024047, Feb. 2019, doi: 10.1103/PhysRevApplied.11.024047.

[117] G. Belenky *et al.*, 'Properties of unrelaxed InAsSb alloys grown on compositionally graded buffers', *Appl. Phys. Lett.*, vol. 99, no. 14, p. 141116, Oct. 2011, doi: 10.1063/1.3650473.

[118] Z. Taghipour *et al.*, 'Temperature-dependent minority carrier lifetime in InAsSb nBn detectors on alternative substrates', in *Infrared Sensors, Devices, and Applications IX*,

International Society for Optics and Photonics, Sep. 2019, p. 1112905. doi: 10.1117/12.2529497.

[119] N. Baril *et al.*, 'MWIR barrier infrared detectors with greater than 5μm cutoff using bulk InAsSb grown on GaSb substrates', in *Infrared Technology and Applications XLIII*, International Society for Optics and Photonics, May 2017, p. 101771L. doi: 10.1117/12.2262503.

[120] Y. Lin, 'Optoelectronics materials and heterostructures based on metamorphic grown InAsSb', PhD Thesis, Stony Brook University, 2016. Accessed: Jul. 18, 2020. [Online]. Available: https://ir.stonybrook.edu/xmlui/handle/11401/77453

[121] D. Wang *et al.*, 'Unrelaxed bulk InAsSb with novel absorption, carrier transport, and recombination properties for MWIR and LWIR photodetectors', in *Infrared Technology and Applications XXXVIII*, International Society for Optics and Photonics, May 2012, p. 835312. doi: 10.1117/12.919451.

[122] Y. Dong, 'Auger Suppression in MWIR InSb Photodiode for Ambient Temperature Operation', MSc Thesis, George Mason University, Fairfax, VA, 2017. doi: 10.13021/G87096.

[123] Y. Chang *et al.*, 'Performance and reproducibility enhancement of HgCdTe molecular beam epitaxy growth on CdZnTe substrates using interfacial HgTe/CdTe superlattice layers', *Appl. Phys. Lett.*, vol. 86, no. 13, p. 131924, Mar. 2005, doi: 10.1063/1.1890471.

[124] M. A. Kinch, F. Aqariden, D. Chandra, P.-K. Liao, H. F. Schaake, and H. D. Shih, 'Minority carrier lifetime in p-HgCdTe', *J. Electron. Mater.*, vol. 34, no. 6, pp. 880–884, Jun. 2005, doi: 10.1007/s11664-005-0036-2.

[125] S. Krishnamurthy, M. A. Berding, and Z. G. Yu, 'Minority carrier lifetimes in HgCdTe alloys', *J. Electron. Mater.*, vol. 35, no. 6, pp. 1369–1378, Jun. 2006, doi: 10.1007/s11664-006-0270-2.

[126] I. Madni, G. A. Umana-Membreno, W. Lei, R. Gu, J. Antoszewski, and L. Faraone, 'Minority carrier lifetime in iodine-doped molecular beam epitaxy-grown HgCdTe', *Appl. Phys. Lett.*, vol. 107, no. 18, p. 182107, Nov. 2015, doi: 10.1063/1.4935154.

[127] H. Katayama, T. Takekawa, M. Kimata, H. Inada, and Y. Iguchi, 'Measurement of absorption and external quantum efficiency of an InAs/GaSb Type II superlattice', *Infrared Phys. Technol.*, vol. 70, pp. 53–57, May 2015, doi: 10.1016/j.infrared.2014.10.014.

[128] V. Letka, J. Keen, A. Craig, and A. R. J. Marshall, 'Modelling and measurement of bandgap behaviour in MWIR InAs/InAs(0.815)Sb(0.185) strained-layer superlattices', in *Electro-Optical and Infrared Systems: Technology and Applications XIV*, International Society for Optics and Photonics, Oct. 2017, p. 1043319. doi: 10.1117/12.2278733.

[129] M. E. Flatté and C. H. Grein, 'Ideal performance of and defect-assisted carrier recombination in MWIR and LWIR InAs/InAsSb superlattice detectors', in *Quantum Sensing and Nanophotonic Devices XII*, International Society for Optics and Photonics, Feb. 2015, p. 93700K. doi: 10.1117/12.2080580.

[130] T. Schuler-Sandy *et al.*, 'Gallium free type II InAs/InAsSb superlattice photodetectors', *Appl. Phys. Lett.*, vol. 101, no. 7, p. 071111, Aug. 2012, doi: 10.1063/1.4745926.

[131] A. Haddadi, R. Chevallier, G. Chen, A. M. Hoang, and M. Razeghi, 'Bias-selectable dual-band mid-/long-wavelength infrared photodetectors based on InAs/InAsSb type-II superlattices', *Appl. Phys. Lett.*, vol. 106, no. 1, p. 011104, Jan. 2015, doi: 10.1063/1.4905565.

[132] D. Wu, A. Dehzangi, J. Li, and M. Razeghi, 'High performance Zn-diffused planar mid-wavelength infrared type-II InAs/InAsSb superlattice photodetector by MOCVD', *Appl. Phys. Lett.*, vol. 116, no. 16, p. 161108, Apr. 2020, doi: 10.1063/5.0005326.

[133] R. Hao *et al.*, 'Fabrication and characterization of high lattice matched InAs/InAsSb superlattice infrared photodetector', *J. Cryst. Growth*, vol. 470, pp. 33–36, Jul. 2017, doi: 10.1016/j.jcrysgro.2017.03.052.

[134] R.-T. H. Yang Ren *et al.*, 'High Lattice Match Growth of InAsSb Based Materials by Molecular Beam Epitaxy', *Chin. Phys. Lett.*, vol. 33, no. 12, pp. 128101–128101, Dec. 2016, doi: 10.1088/0256-307X/33/12/128101.

[135] A. Dehzangi, D. Wu, R. McClintock, J. Li, and M. Razeghi, 'Planar nBn type-II superlattice mid-wavelength infrared photodetectors using zinc ion-implantation', *Appl. Phys. Lett.*, vol. 116, no. 22, p. 221103, Jun. 2020, doi: 10.1063/5.0010273.

[136] A. Dehzangi, 'Planar strained layer superlattice infrared photodetector using ion implantation', in *Image Sensing Technologies: Materials, Devices, Systems, and Applications IX*, SPIE, May 2022, pp. 9–15. doi: 10.1117/12.2623811.

[137] G. Ariyawansa, J. Duran, C. Reyner, and J. Scheihing, 'InAs/InAsSb Strained-Layer Superlattice Mid-Wavelength Infrared Detector for High-Temperature Operation', *Micromachines*, vol. 10, no. 12, Art. no. 12, Dec. 2019, doi: 10.3390/mi10120806.

[138] A. Kazemi *et al.*, 'Mid-wavelength infrared unipolar nBp superlattice photodetector', *Infrared Phys. Technol.*, vol. 88, pp. 114–118, Jan. 2018, doi: 10.1016/j.infrared.2017.11.008.

[139] J. B. Rodriguez *et al.*, 'nBn structure based on InAs/GaSb type-II strained layer superlattices', *Appl. Phys. Lett.*, vol. 91, no. 4, p. 043514, Jul. 2007, doi: 10.1063/1.2760153.

[140] E. Plis *et al.*, 'Type II InAs/GaSb strain layer superlattice detectors with p-on-n polarity', *Appl. Phys. Lett.*, vol. 91, no. 13, p. 133512, Sep. 2007, doi: 10.1063/1.2790078.

[141] C. Cervera, J. B. Rodriguez, R. Chaghi, H. Aït-Kaci, and P. Christol, 'Characterization of midwave infrared InAs/GaSb superlattice photodiode', *J. Appl. Phys.*, vol. 106, no. 2, p. 024501, Jul. 2009, doi: 10.1063/1.3174439.

[142] N. Gautam *et al.*, 'Barrier Engineered Infrared Photodetectors Based on Type-II InAs/GaSb Strained Layer Superlattices', *IEEE J. Quantum Electron.*, vol. 49, no. 2, pp. 211–217, Feb. 2013, doi: 10.1109/JQE.2012.2236643.

[143] R. Taalat, J.-B. Rodriguez, M. Delmas, and P. Christol, 'Influence of the period thickness and composition on the electro-optical properties of type-II InAs/GaSb midwave infrared superlattice photodetectors', *J. Phys. Appl. Phys.*, vol. 47, no. 1, p. 015101, Dec. 2013, doi: 10.1088/0022-3727/47/1/015101.

[144] E. Giard *et al.*, 'Quantum efficiency investigations of type-II InAs/GaSb midwave infrared superlattice photodetectors', *J. Appl. Phys.*, vol. 116, no. 4, p. 043101, Jul. 2014, doi: 10.1063/1.4890309.

[145] J. Nghiem *et al.*, 'Radiometric characterization of type-II InAs/GaSb superlattice (t2sl) midwave infrared photodetectors and focal plane arrays', in *International Conference on Space Optics — ICSO 2016*, International Society for Optics and Photonics, Sep. 2017, p. 105623Y. doi: 10.1117/12.2296053.

[146] G. Bishop *et al.*, 'nBn detectors based on InAs/GaSb type-II strain layer superlattice', *J. Vac. Sci. Technol. B Microelectron. Nanometer Struct. Process. Meas. Phenom.*, vol. 26, no. 3, pp. 1145–1148, May 2008, doi: 10.1116/1.2830627.

[147] M. Walther *et al.*, 'Growth of InAs/GaSb short-period superlattices for high-resolution mid-wavelength infrared focal plane array detectors', *J. Cryst. Growth*, vol. 278, no. 1, pp. 156–161, May 2005, doi: 10.1016/j.jcrysgro.2004.12.044.

[148] A. M. Hoang, A. Dehzangi, S. Adhikary, and M. Razeghi, 'High performance bias-selectable three-color Short-wave/Mid-wave/Long-wave Infrared Photodetectors based on Type-II InAs/GaSb/AlSb superlattices', *Sci. Rep.*, vol. 6, no. 1, Art. no. 1, Apr. 2016, doi: 10.1038/srep24144.

[149] X. Hao *et al.*, 'High-operating-temperature MWIR photodetector based on a InAs/GaSb superlattice grown by MOCVD', *J. Semicond.*, vol. 43, no. 1, p. 012303, Jan. 2022, doi: 10.1088/1674-4926/43/1/012303.

[150] K.-H. Chen, Z.-C. Xu, Z.-M. Liang, Y.-H. Zhu, J.-X. Chen, and L. He, 'Molecular beam epitaxy growth and characteristics of the high quantum efficiency InAs/GaSb type-II superlattices MWIR detector', *J. Infrared Millim. Waves*, vol. 40, no. 3, 2021, doi: 10. 11972/j. issn. 1001-9014. 2021. 03. 001.

[151] D. Lubyshev *et al.*, 'Effect of substrate orientation on Sb-based MWIR photodetector characteristics', *Infrared Phys. Technol.*, vol. 95, pp. 27–32, Dec. 2018, doi: 10.1016/j.infrared.2018.09.031.

[152] G. Deng *et al.*, 'Upside-down InAs/InAsSb type-II superlattice-based nBn mid-infrared photodetectors with an AlGaAsSb quaternary alloy barrier', *Opt. Express*, vol. 28, no. 9, pp. 13616–13624, Apr. 2020, doi: 10.1364/OE.387297.

[153] D. Wu, J. Li, A. Dehzangi, and M. Razeghi, 'High performance InAs/InAsSb Type-II superlattice mid-wavelength infrared photodetectors with double barrier', *Infrared Phys. Technol.*, vol. 109, p. 103439, Sep. 2020, doi: 10.1016/j.infrared.2020.103439.

[154] G. Deng *et al.*, 'High operating temperature pBn barrier mid-wavelength infrared photodetectors and focal plane array based on InAs/InAsSb strained layer superlattices', *Opt. Express*, vol. 28, no. 12, pp. 17611–17619, Jun. 2020, doi: 10.1364/OE.395770.

[155] M. Bouschet *et al.*, 'Influence of Pixel Etching on Electrical and Electro-Optical Performances of a Ga-Free InAs/InAsSb T2SL Barrier Photodetector for Mid-Wave Infrared Imaging', *Photonics*, vol. 8, no. 6, Art. no. 6, Jun. 2021, doi: 10.3390/photonics8060194.

[156] L. She *et al.*, 'Mid-wave infrared p+-B-n InAs/InAsSb type-II superlattice photodetector with an AlAsSb/InAsSb superlattice barrier', *Infrared Phys. Technol.*, p. 104015, Jan. 2022, doi: 10.1016/j.infrared.2021.104015.

[157] G. Chen, B.-M. Nguyen, A. M. Hoang, E. K. Huang, S. R. Darvish, and M. Razeghi, 'Suppression of surface leakage in gate controlled type-II InAs/GaSb mid-infrared photodetectors', in *Quantum Sensing and Nanophotonic Devices IX*, International Society for Optics and Photonics, Jan. 2012, p. 826811. doi: 10.1117/12.913741.

[158] C. Asplund *et al.*, 'Performance of mid-wave T2SL detectors with heterojunction barriers', *Infrared Phys. Technol.*, vol. 59, pp. 22–27, Jul. 2013, doi: 10.1016/j.infrared.2012.12.004.

[159] A. Haddadi and M. Razeghi, 'Bias-selectable three-color short-, extended-short-, and mid-wavelength infrared photodetectors based on type-II InAs/GaSb/AlSb superlattices', *Opt. Lett.*, vol. 42, no. 21, pp. 4275–4278, Nov. 2017, doi: 10.1364/OL.42.004275.

[160] S. Arikata *et al.*, 'Structural and electrical properties of InAs/GaSb superlattices grown by metalorganic vapor phase epitaxy for midwavelength infrared detectors', *Phys. Status Solidi A*, vol. 214, no. 3, p. 1600582, 2017, doi: https://doi.org/10.1002/pssa.201600582.

[161] H. Zhu *et al.*, 'High Operating Temperature InAs/GaSb Superlattice Based Mid Wavelength Infrared Photodetectors Grown by MOCVD', *Photonics*, vol. 8, no. 12, Art. no. 12, Dec. 2021, doi: 10.3390/photonics8120564.

[162] A. Rogalski, P. Martyniuk, and M. Kopytko, 'InAs/GaSb type-II superlattice infrared detectors: Future prospect', *Appl. Phys. Rev.*, vol. 4, no. 3, p. 031304, Aug. 2017, doi: 10.1063/1.4999077.

[163] P. C. Klipstein *et al.*, 'Minority carrier lifetime and diffusion length in type II superlattice barrier devices', *Infrared Phys. Technol.*, vol. 96, pp. 155–162, Jan. 2019, doi: 10.1016/j.infrared.2018.11.022.

[164] M. A. Kinch, *State-of-the-Art Infrared Detector Technology*. SPIE, 2014. doi: 10.1117/3.1002766.

[165] B. C. Connelly, G. D. Metcalfe, H. Shen, and M. Wraback, 'Direct minority carrier lifetime measurements and recombination mechanisms in long-wave infrared type II superlattices using time-resolved photoluminescence', *Appl. Phys. Lett.*, vol. 97, no. 25, p. 251117, Dec. 2010, doi: 10.1063/1.3529458.

[166] S. Bandara, P. G. Maloney, N. Baril, J. G. Pellegrino, and M. Z. Tidrow, 'Doping dependence of minority carrier lifetime in long-wave Sb-based type II superlattice infrared detector materials', *Opt. Eng.*, vol. 50, no. 6, p. 061015, Jun. 2011, doi: 10.1117/1.3590720.

[167] E. A. Kadlec *et al.*, 'Effects of electron doping level on minority carrier lifetimes in n-type mid-wave infrared InAs/InAs1−xSbx type-II superlattices', *Appl. Phys. Lett.*, vol. 109, no. 26, p. 261105, Dec. 2016, doi: 10.1063/1.4973352.

[168] K. Czuba, I. Sankowska, J. Jureńczyk, A. Jasik, E. Papis-Polakowska, and J. Kaniewski, 'Influence of Be doping placement in InAs/GaSb superlattice-based absorber on the performance of MWIR photodiodes', *Semicond. Sci. Technol.*, vol. 32, no. 5, p. 055010, Apr. 2017, doi: 10.1088/1361-6641/aa62c0.

[169] A. Gin *et al.*, 'Ammonium sulfide passivation of Type-II InAs/GaSb superlattice photodiodes', *Appl. Phys. Lett.*, vol. 84, no. 12, pp. 2037–2039, Mar. 2004, doi: 10.1063/1.1686894.

[170] W. E. Tennant, 'Rule 07 Revisited: Still a Good Heuristic Predictor of p/n HgCdTe Photodiode Performance?', *J. Electron. Mater.*, vol. 39, no. 7, pp. 1030–1035, Jul. 2010, doi: 10.1007/s11664-010-1084-9.

[171] J. Schmidt, F. Rutz, A. Wörl, V. Daumer, and R. Rehm, 'Low dark current in mid-infrared type-II superlattice heterojunction photodiodes', *Infrared Phys. Technol.*, vol. 85, pp. 378–381, Sep. 2017, doi: 10.1016/j.infrared.2017.08.001.

[172] A. Dehzangi, 'Ion-Implantation as Pixel Isolation for Fabrication of Planar Strain-Balanced Antimony-based Superlattice Infrared Photodetectors'. arXiv, May 23, 2022. doi: 10.48550/arXiv.2205.11745.

[173] D. Wu, J. Li, A. Dehzangi, and M. Razeghi, 'Mid-wavelength infrared high operating temperature pBn photodetectors based on type-II InAs/InAsSb superlattice', *AIP Adv.*, vol. 10, no. 2, p. 025018, Feb. 2020, doi: 10.1063/1.5136501.

[174] D. Wu, A. Dehzangi, and M. Razeghi, 'Demonstration of mid-wavelength infrared nBn photodetectors based on type-II InAs/InAsSb superlattice grown by metal-organic

chemical vapor deposition', *Appl. Phys. Lett.*, vol. 115, no. 6, p. 061102, Aug. 2019, doi: 10.1063/1.5100617.

[175] D. Wu, Q. Durlin, A. Dehzangi, Y. Zhang, and M. Razeghi, 'High quantum efficiency mid-wavelength infrared type-II InAs/InAsSb superlattice photodiodes grown by metal-organic chemical vapor deposition', *Appl. Phys. Lett.*, vol. 114, no. 1, p. 011104, Jan. 2019, doi: 10.1063/1.5058714.

[176] M. Razeghi *et al.*, 'Antimonite-based gap-engineered type-II superlattice materials grown by MBE and MOCVD for the third generation of infrared imagers', in *Infrared Technology and Applications XLV*, International Society for Optics and Photonics, May 2019, p. 110020G. doi: 10.1117/12.2521173.

[177] A. Haddadi, A. Dehzangi, R. Chevallier, T. Yang, and M. Razeghi, 'Type-II InAs/GaSb/AlSb superlattice-based heterojunction phototransistors: back to the future', in *Quantum Sensing and Nano Electronics and Photonics XV*, International Society for Optics and Photonics, Jan. 2018, p. 1054004. doi: 10.1117/12.2297475.

[178] Y. Wei *et al.*, 'Uncooled operation of type-II InAs⁄GaSb superlattice photodiodes in the midwavelength infrared range', *Appl. Phys. Lett.*, vol. 86, no. 23, p. 233106, Jun. 2005, doi: 10.1063/1.1947908.

[179] S. A. Pour, E. K. Huang, G. Chen, A. Haddadi, B.-M. Nguyen, and M. Razeghi, 'High operating temperature midwave infrared photodiodes and focal plane arrays based on type-II InAs/GaSb superlattices', *Appl. Phys. Lett.*, vol. 98, no. 14, p. 143501, Apr. 2011, doi: 10.1063/1.3573867.

[180] M. Razeghi, S. A. Pour, E. Huang, G. Chen, A. Haddadi, and B.-M. Nguyen, 'High-operating temperature MWIR photon detectors based on Type II InAs/GaSb superlattice', in *Infrared Technology and Applications XXXVII*, International Society for Optics and Photonics, May 2011, p. 80122Q. doi: 10.1117/12.888060.

[181] A. M. Hoang, G. Chen, A. Haddadi, and M. Razeghi, 'Demonstration of high performance bias-selectable dual-band short-/mid-wavelength infrared photodetectors based on type-II InAs/GaSb/AlSb superlattices', *Appl. Phys. Lett.*, vol. 102, no. 1, p. 011108, Jan. 2013, doi: 10.1063/1.4773593.

[182] L. Zhang, W. Sun, Y. Xu, L. Zhang, L. Zhang, and J. Si, 'Growth and electrical characterization of type II InAs/GaSb superlattices for midwave infrared detection', *Infrared Phys. Technol.*, vol. 65, pp. 129–133, Jul. 2014, doi: 10.1016/j.infrared.2014.03.012.

[183] G. Wang *et al.*, 'Growth and fabrication of a mid-wavelength infrared focal plane array based on type-II InAs/GaSb superlattices', *J. Semicond.*, vol. 34, no. 11, p. 114012, Nov. 2013, doi: 10.1088/1674-4926/34/11/114012.

[184] Y. Huang *et al.*, 'High-Performance Mid-Wavelength InAs/GaSb Superlattice Infrared Detectors Grown by Production-Scale Metalorganic Chemical Vapor Deposition', *IEEE J. Quantum Electron.*, vol. 53, no. 5, pp. 1–5, Oct. 2017, doi: 10.1109/JQE.2017.2740121.

[185] Q. Li *et al.*, 'Dark current mechanism of unpassivated mid wavelength type II InAs/GaSb superlattice infrared photodetector', *Chin. Sci. Bull.*, vol. 59, no. 28, pp. 3696–3700, Oct. 2014, doi: 10.1007/s11434-014-0511-3.

[186] Y. Shi *et al.*, 'InAs/Ga(In)Sb type-II superlattices short/middle dual color infrared detectors', in *Infrared Technology and Applications XLI*, International Society for Optics and Photonics, Jun. 2015, p. 94510L. doi: 10.1117/12.2176196.

[187] A. Jang *et al.*, 'Electrical Characteristics of a Ga-free T2SL Mid-wave Infrared nBn Detector Based on an InAs/AlAsSb/InAsSb Barrier', *J. Electron. Mater.*, May 2022, doi: 10.1007/s11664-022-09664-x.

[188] D. Z. Ting *et al.*, 'Mid-wavelength high operating temperature barrier infrared detector and focal plane array', *Appl. Phys. Lett.*, vol. 113, no. 2, p. 021101, Jul. 2018, doi: 10.1063/1.5033338.

[189] D. Z. Ting *et al.*, 'Type-II Superlattice Mid-Wavelength Infrared Focal Plane Arrays for CubeSat Hyperspectral Imaging', *IEEE Photonics Technol. Lett.*, pp. 1–1, 2022, doi: 10.1109/LPT.2022.3156048.

[190] U. Zavala-Moran *et al.*, 'Antimonide-based Superlattice Infrared Barrier Photodetectors', in *8th International Conference on Photonics, Optics and Laser Technology*, Valletta, Malta: SCITEPRESS - Science and Technology Publications, Feb. 2020, pp. 45–51. doi: 10.5220/0009004900450051.

[191] P. Christol and J.-B. Rodriguez, 'Progress on type-II InAs/GaSb superlattice (T2SL) infrared photodetector: from MWIR to VLWIR spectral domains', in *International Conference on Space Optics — ICSO 2014*, International Society for Optics and Photonics, Nov. 2017, p. 105632C. doi: 10.1117/12.2304264.

[192] R. Taalat, J. B. Rodriguez, C. Cervera, I. Ribet-Mohamed, and P. Christol, 'Electrical characterizations of asymmetric InAs/GaSb superlattice MWIR photodiodes', *Infrared Phys. Technol.*, vol. 59, pp. 32–35, Jul. 2013, doi: 10.1016/j.infrared.2012.12.006.

[193] I. Ribet-Mohamed, M. Tauvy, R. Taalat, C. Cervera, J.-B. Rodriguez, and P. Christol, 'Comparison of the electro-optical performances of symmetrical and asymmetrical MWIR InAs/GaSb superlattice pin photodiodes', in *Quantum Sensing and Nanophotonic Devices IX*, International Society for Optics and Photonics, Jan. 2012, p. 826833. doi: 10.1117/12.914455.

[194] R. Chaghi, C. Cervera, H. Aït-Kaci, P. Grech, J. B. Rodriguez, and P. Christol, 'Wet etching and chemical polishing of InAs/GaSb superlattice photodiodes', *Semicond. Sci. Technol.*, vol. 24, no. 6, p. 065010, May 2009, doi: 10.1088/0268-1242/24/6/065010.

[195] J. B. Rodriguez, P. Christol, L. Cerutti, F. Chevrier, and A. Joullié, 'MBE growth and characterization of type-II InAs/GaSb superlattices for mid-infrared detection', *J. Cryst. Growth*, vol. 274, no. 1, pp. 6–13, Jan. 2005, doi: 10.1016/j.jcrysgro.2004.09.088.

[196] A. Kazemi *et al.*, 'High quantum efficiency mid-wavelength infrared superlattice photodetector', in *Infrared Technology and Applications XLIII*, International Society for Optics and Photonics, May 2017, p. 101771M. doi: 10.1117/12.2263879.

[197] E. Plis, S. Annamalai, K. T. Posani, S. J. Lee, and S. Krishna, 'Room temperature operation of InAs/GaSb SLS infrared photovoltaic detectors with cut-off wavelength ~5 μm', in *Infrared Technology and Applications XXXII*, International Society for Optics and Photonics, May 2006, p. 62060O. doi: 10.1117/12.669172.

[198] V. Daumer *et al.*, 'Photodetector development at Fraunhofer IAF: From LWIR to SWIR operating from cryogenic close to room temperature', in *Infrared Technology and Applications XLIII*, International Society for Optics and Photonics, May 2017, p. 1017711. doi: 10.1117/12.2262509.

[199] R. Rehm *et al.*, 'Bispectral thermal imaging with quantum-well infrared photodetectors and InAs/GaSb type-II superlattices', in *Infrared Technology and Applications XXXII*, International Society for Optics and Photonics, May 2006, p. 62060Y. doi: 10.1117/12.667627.

[200] P. Martyniuk *et al.*, 'Performance modeling of MWIR InAs/GaSb/B–Al0.2Ga0.8Sb type-II superlattice nBn detector', *Semicond. Sci. Technol.*, vol. 27, no. 5, p. 055002, Mar. 2012, doi: 10.1088/0268-1242/27/5/055002.

[201] J. Huang, Z. Xie, Y. Chen, J. E. Bowers, and B. Chen, 'High Speed Mid-Wave Infrared Uni-Traveling Carrier Photodetector', *IEEE J. Quantum Electron.*, vol. 56, no. 4, pp. 1–7, Aug. 2020, doi: 10.1109/JQE.2020.3003038.

[202] J. Huang *et al.*, 'High-speed Mid-wave Infrared Uni-traveling Carrier Photodetector Based on InAs/InAsSb Type-II Superlattice', *IEEE Electron Device Lett.*, pp. 1–1, 2022, doi: 10.1109/LED.2022.3163660.

[203] J. Chen *et al.*, 'InAs/GaSb type-II superlattice mid-wavelength infrared focal plane array detectors grown by molecular beam epitaxy', *J. Cryst. Growth*, vol. 378, pp. 596–599, Sep. 2013, doi: 10.1016/j.jcrysgro.2012.12.113.

[204] H. S. Kim, 'Passivation Study of InAs/GaSb Type-II Strained Layer Superlattice in Mid-wave Infrared Photodetector', *J. Korean Phys. Soc.*, vol. 77, no. 9, pp. 714–718, Nov. 2020, doi: 10.3938/jkps.77.714.

[205] H. S. Kim, 'Performance of an InAs/GaSb Type-II Superlattice Photodiode with Si3N4 Surface Passivation', *Curr. Opt. Photonics*, vol. 5, no. 2, pp. 129–133, Apr. 2021.

[206] O. Salihoglu *et al.*, 'Passivation of type II InAs/GaSb superlattice photodetectors with atomic layer deposited Al2O3', in *Infrared Technology and Applications XXXVIII*,

International Society for Optics and Photonics, May 2012, p. 83530Z. doi: 10.1117/12.920406.

[207] O. Salihoglu, A. Muti, and A. Aydinli, 'A Comparative Passivation Study for InAs/GaSb Pin Superlattice Photodetectors', *IEEE J. Quantum Electron.*, vol. 49, no. 8, pp. 661–666, Aug. 2013, doi: 10.1109/JQE.2013.2267553.

[208] J. Kim *et al.*, 'HOT MWIR InAs/InAsSb T2SL discrete photodetector development', in *Infrared Technology and Applications XLIV*, International Society for Optics and Photonics, May 2018, p. 1062412. doi: 10.1117/12.2303973.

[209] J. Kim *et al.*, 'Characterization of HOT MWIR InAs/InAsSb T2SL discrete photodetectors', in *Optical Components and Materials XVII*, International Society for Optics and Photonics, Mar. 2020, p. 112760J. doi: 10.1117/12.2553686.

[210] E. Delli *et al.*, 'Mid-Infrared InAs/InAsSb Superlattice nBn Photodetector Monolithically Integrated onto Silicon', *ACS Photonics*, vol. 6, no. 2, pp. 538–544, Feb. 2019, doi: 10.1021/acsphotonics.8b01550.

[211] P. J. Carrington *et al.*, 'Heteroepitaxial integration of InAs/InAsSb type-II superlattice barrier photodetectors onto silicon', in *Infrared Sensors, Devices, and Applications X*, International Society for Optics and Photonics, Aug. 2020, p. 115030G. doi: 10.1117/12.2568741.

[212] P. Martyniuk *et al.*, 'Mid-wave T2SLs InAs/GaSb single pixel PIN detector with GaAs immersion lens for HOT condition', *Solid-State Electron.*, vol. 119, pp. 1–4, May 2016, doi: 10.1016/j.sse.2016.01.012.

[213] S. Maimon and G. W. Wicks, 'nBn detector, an infrared detector with reduced dark current and higher operating temperature', *Appl. Phys. Lett.*, vol. 89, no. 15, p. 151109, Oct. 2006, doi: 10.1063/1.2360235.

[214] E. Plis *et al.*, 'Mid-infrared InAs/GaSb strained layer superlattice detectors with nBn design grown on a GaAs substrate', *Semicond. Sci. Technol.*, vol. 25, no. 8, p. 085010, Jul. 2010, doi: 10.1088/0268-1242/25/8/085010.

[215] D. Zuo *et al.*, 'Direct minority carrier transport characterization of InAs/InAsSb superlattice nBn photodetectors', *Appl. Phys. Lett.*, vol. 106, no. 7, p. 071107, Feb. 2015, doi: 10.1063/1.4913312.

[216] Z. Deng, D. Guo, J. Huang, H. Liu, J. Wu, and B. Chen, 'Mid-Wave Infrared InAs/GaSb Type-II Superlattice Photodetector With n-B-p Design Grown on GaAs Substrate', *IEEE J. Quantum Electron.*, vol. 55, no. 4, pp. 1–5, Aug. 2019, doi: 10.1109/JQE.2019.2917946.

[217] B.-M. Nguyen, M. Razeghi, V. Nathan, and G. J. Brown, 'Type-II M structure photodiodes: an alternative material design for mid-wave to long wavelength infrared regimes', in *Quantum Sensing and Nanophotonic Devices IV*, International Society for Optics and Photonics, Feb. 2007, p. 64790S. doi: 10.1117/12.711588.

[218] R. Q. Yang, Z. Tian, Z. Cai, J. F. Klem, M. B. Johnson, and H. C. Liu, 'Interband-cascade infrared photodetectors with superlattice absorbers', *J. Appl. Phys.*, vol. 107, no. 5, p. 054514, Mar. 2010, doi: 10.1063/1.3327415.

[219] E. Luna, B. Satpati, J. B. Rodriguez, A. N. Baranov, E. Tournié, and A. Trampert, 'Interfacial intermixing in InAs/GaSb short-period-superlattices grown by molecular beam epitaxy', *Appl. Phys. Lett.*, vol. 96, no. 2, p. 021904, Jan. 2010, doi: 10.1063/1.3291666.

[220] H. Kim, Y. Meng, J.-L. Rouviére, D. Isheim, D. N. Seidman, and J.-M. Zuo, 'Atomic resolution mapping of interfacial intermixing and segregation in InAs/GaSb superlattices: A correlative study', *J. Appl. Phys.*, vol. 113, no. 10, p. 103511, Mar. 2013, doi: 10.1063/1.4794193.

[221] J. Cui *et al.*, 'Atomic resolution of interface diffusing in short-period InAs/GaSb superlattice', *J. Appl. Phys.*, vol. 124, no. 24, p. 245301, Dec. 2018, doi: 10.1063/1.5059350.

[222] N. Herres *et al.*, 'Effect of interfacial bonding on the structural and vibrational properties of InAs/GaSb superlattices', *Phys. Rev. B*, vol. 53, no. 23, p. 15688, Jun. 1996, doi: 10.1103/PhysRevB.53.15688.

[223] D. H. Tomich, W. C. Mitchel, P. Chow, and C. W. Tu, 'Study of interfaces in GaInSb/InAs quantum wells by high-resolution X-ray diffraction and reciprocal space mapping', *J. Cryst. Growth*, vol. 201–202, pp. 868–871, May 1999, doi: 10.1016/S0022-0248(98)01477-8.

[224] E. Plis, S. Annamalai, K. T. Posani, S. J. Lee, and S. Krishna, 'Room temperature operation of InAs/GaSb SLS infrared photovoltaic detectors with cut-off wavelength ~5 µm', *https://doi.org/10.1117/12.669172*, vol. 6206, pp. 225–233, May 2006, doi: 10.1117/12.669172.

[225] A. Jasik, I. Sankowska, D. Pierciska, K. Regiski, K. Pierciski, and J. Kubacka-Traczyk, 'Blueshift of bandgap energy and reduction of non-radiative defect density due to precise control of InAs-on-GaSb interface in type-II InAs/GaSb superlattice', *J. Appl. Phys.*, vol. 110, no. 12, p. 123103, Dec. 2011, doi: 10.1063/1.3671024.

[226] B. Arikan, G. Korkmaz, Y. E. Suyolcu, B. Aslan, and U. Serincan, 'On the structural characterization of InAs/GaSb type-II superlattices: The effect of interfaces for fixed layer thicknesses', *Thin Solid Films*, vol. 548, pp. 288–291, Dec. 2013, doi: 10.1016/J.TSF.2013.08.089.

[227] Y. Ashuach *et al.*, 'Quantification of atomic intermixing in short-period InAs/GaSb superlattices for infrared photodetectors', *J. Appl. Phys.*, vol. 113, no. 18, p. 184305, May 2013, doi: 10.1063/1.4804252.

[228] Y. Liu, C. Zhang, X. Wang, J. Wu, and L. Huang, 'Interface investigation of InAs/GaSb type II superlattice for long wavelength infrared photodetectors', *Infrared Phys. Technol.*, vol. 113, p. 103573, Mar. 2021, doi: 10.1016/J.INFRARED.2020.103573.

[229] P. Mishra *et al.*, 'Interface engineered MBE grown InAs/GaSb based type-II superlattice heterostructures', *J. Alloys Compd.*, vol. 889, p. 161692, Jan. 2022, doi: 10.1016/j.jallcom.2021.161692.

[230] B. Satpati, J. B. Rodriguez, A. Trampert, E. Tournié, A. Joullié, and P. Christol, 'Interface analysis of InAs/GaSb superlattice grown by MBE', *J. Cryst. Growth*, vol. 301–302, no. SPEC. ISS., pp. 889–892, Apr. 2007, doi: 10.1016/J.JCRYSGRO.2006.11.284.

[231] G. Jie *et al.*, 'Interfaces in InAs/GaSb Superlattices Grown by Molecular Beam Epitaxy', *Chin. Phys. Lett.*, vol. 26, no. 4, pp. 47802–047802, Mar. 2009, doi: 10.1088/0256-307X/26/4/047802.

[232] E. Plis, S. Annamalai, K. T. Posani, S. Krishna, R. A. Rupani, and S. Ghosh, 'Midwave infrared type-II InAs∕GaSb superlattice detectors with mixed interfaces', *J. Appl. Phys.*, vol. 100, no. 1, p. 014510, Jul. 2006, doi: 10.1063/1.2214222.

[233] H. J. Haugan, G. J. Brown, L. Grazulis, K. Mahalingam, and D. H. Tomich, 'Optimization of InAs/GaSb type-II superlattices for high performance of photodetectors', *Phys. E Low-Dimens. Syst. Nanostructures*, vol. 20, no. 3, pp. 527–530, Jan. 2004, doi: 10.1016/j.physe.2003.09.003.

[234] Y. Zhang *et al.*, 'Long wavelength infrared InAs/GaSb superlattice photodetectors with InSb-like and mixed interfaces', *IEEE J. Quantum Electron.*, vol. 47, no. 12, pp. 1475–1479, 2011, doi: 10.1109/JQE.2011.2168947.

[235] M. Delmas, M. C. Debnath, B. L. Liang, and D. L. Huffaker, 'Material and device characterization of Type-II InAs/GaSb superlattice infrared detectors', *Infrared Phys. Technol.*, vol. 94, pp. 286–290, Nov. 2018, doi: 10.1016/j.infrared.2018.09.012.

[236] A. Dehzangi, D. Wu, R. McClintock, J. Li, A. Jaud, and M. Razeghi, 'Demonstration of Planar Type-II Superlattice-Based Photodetectors Using Silicon Ion-Implantation', *Photonics*, vol. 7, no. 3, Art. no. 3, Sep. 2020, doi: 10.3390/photonics7030068.

[237] J. Li, R. K. Saroj, S. Slivken, V. H. Nguyen, G. Brown, and M. Razeghi, 'High Performance Planar Antimony-Based Superlattice Photodetectors Using Zinc Diffusion Grown by MBE', *Photonics*, vol. 9, no. 9, Art. no. 9, Sep. 2022, doi: 10.3390/photonics9090664.

[238] R. K. Saroj, V. H. Nguyen, S. Slivken, G. J. Brown, and M. Razeghi, 'Demonstration of Zn-diffused planar long-wavelength infrared photodetector based on type-II superlattice grown by MBE', *IEEE J. Quantum Electron.*, pp. 1–1, 2022, doi: 10.1109/JQE.2022.3172772.

[239] Y. Zhao *et al.*, 'Mid-Infrared InAs/GaSb Superlattice Planar Photodiodes Fabricated by Metal–Organic Chemical Vapor Deposition', *Chin. Phys. Lett.*, vol. 37, no. 6, p. 068501, Jun. 2020, doi: 10.1088/0256-307X/37/6/068501.

[240] P.-Y. Delaunay, A. Hood, B. M. Nguyen, D. Hoffman, Y. Wei, and M. Razeghi, 'Passivation of type-II InAs∕GaSb double heterostructure', *Appl. Phys. Lett.*, vol. 91, no. 9, p. 091112, Aug. 2007, doi: 10.1063/1.2776353.

[241] K. Swaminathan, P. E. Janardhanan, and O. V. Sulima, 'Inductively coupled plasma etching of III–V antimonides in BCl3/SiCl4 etch chemistry', *Thin Solid Films*, vol. 516, no. 23, pp. 8712–8716, Oct. 2008, doi: 10.1016/j.tsf.2008.05.029.

[242] M. Huang, J. Chen, J. Xu, F. Wang, Z. Xu, and L. He, 'ICP etching for InAs-based InAs/GaAsSb superlattice long wavelength infrared detectors', *Infrared Phys. Technol.*, vol. 90, pp. 110–114, May 2018, doi: 10.1016/j.infrared.2018.03.003.

[243] E. K. Huang, B.-M. Nguyen, D. Hoffman, P.-Y. Delaunay, and M. Razeghi, 'Inductively coupled plasma etching and processing techniques for type-II InAs/GaSb superlattices infrared detectors toward high fill factor focal plane arrays', in *Quantum Sensing and Nanophotonic Devices VI*, SPIE, Jan. 2009, pp. 309–316. doi: 10.1117/12.810030.

[244] H.-Y. Hao *et al.*, 'Wet Chemical Etching of Antimonide-Based Infrared Materials', *Chin. Phys. Lett.*, vol. 32, no. 10, p. 107302, Oct. 2015, doi: 10.1088/0256-307X/32/10/107302.

[245] Z. Deng *et al.*, 'Demonstration of Si based InAs/GaSb type-II superlattice p-i-n photodetector', *Infrared Phys. Technol.*, vol. 101, pp. 133–137, Sep. 2019, doi: 10.1016/j.infrared.2019.06.011.

[246] H. J. Lee, S. Y. Ko, Y. H. Kim, and J. Nah, 'Strain-induced the dark current characteristics in InAs/GaSb type-II superlattice for mid-wave detector', *J. Semicond.*, vol. 41, no. 6, p. 062302, Jun. 2020, doi: 10.1088/1674-4926/41/6/062302.

[247] O. Dier, C. Lin, M. Grau, and M.-C. Amann, 'Selective and non-selective wet-chemical etchants for GaSb-based materials', *Semicond. Sci. Technol.*, vol. 19, no. 11, pp. 1250–1253, Sep. 2004, doi: 10.1088/0268-1242/19/11/006.

[248] G. C. DeSalvo, R. Kaspi, and C. A. Bozada, 'Citric Acid Etching of GaAs1 − x Sb x , Al0.5Ga0.5Sb , and InAs for Heterostructure Device Fabrication', *J. Electrochem. Soc.*, vol. 141, no. 12, p. 3526, Dec. 1994, doi: 10.1149/1.2059365.

[249] L. Song, S. Degroote, K.-H. Choi, G. Borghs, and P. Heremans, 'Release of Epitaxial Layers Grown on InAs Substrates', *Electrochem. Solid-State Lett.*, vol. 6, no. 2, p. G25, Dec. 2002, doi: 10.1149/1.1536543.

[250] A. Hood *et al.*, 'Near bulk-limited R0A of long-wavelength infrared type-II InAs∕GaSb superlattice photodiodes with polyimide surface passivation', *Appl. Phys. Lett.*, vol. 90, no. 23, p. 233513, Jun. 2007, doi: 10.1063/1.2747172.

[251] R. Rehm, M. Walther, F. Fuchs, J. Schmitz, and J. Fleissner, 'Passivation of InAs∕(GaIn)Sb short-period superlattice photodiodes with 10μm cutoff wavelength by epitaxial overgrowth with AlxGa1−xAsySb1−y', *Appl. Phys. Lett.*, vol. 86, no. 17, p. 173501, Apr. 2005, doi: 10.1063/1.1906326.

[252] E. Plis, J.-B. Rodriguez, S. J. Lee, and S. Krishna, 'Electrochemical sulphur passivation of InAs/GaSb strain layer superlattice detectors', *Electron. Lett.*, vol. 42, p. 1248, Jan. 2006, doi: 10.1049/el:20062495.

[253] H. C. Jung *et al.*, 'Investigation of ICP dry etching of InAs/GaSb type-II superlattice LWIR photodetector', in *Infrared Technology and Applications XLVII*, International Society for Optics and Photonics, Apr. 2021, p. 117411V. doi: 10.1117/12.2588043.

[254] F. Tao *et al.*, 'Inductively coupled plasma (ICP) dry etching of type II InAs/GaSb superlattice for focal plane arrays', in *AOPC 2020: Display Technology; Photonic MEMS, THz MEMS, and Metamaterials; and AI in Optics and Photonics*, International Society for Optics and Photonics, Nov. 2020, p. 115650I. doi: 10.1117/12.2575638.

[255] X. Zhou *et al.*, 'Mid-wavelength type II InAs/GaSb superlattice infrared focal plane arrays', *Infrared Phys. Technol.*, vol. 78, pp. 263–267, Sep. 2016, doi: 10.1016/j.infrared.2016.08.014.

[256] M. Herrera *et al.*, 'Atomic scale analysis of the effect of the SiO2 passivation treatment on InAs/GaSb superlattice mesa sidewall', *Appl. Phys. Lett.*, vol. 93, no. 9, p. 093106, Sep. 2008, doi: 10.1063/1.2977589.

[257] H. S. Kim, 'Dark current analysis of an InAs/GaSb type II superlattice infrared photodiode with SiO2 passivation', *J. Korean Phys. Soc.*, vol. 78, no. 11, pp. 1141–1146, Jun. 2021, doi: 10.1007/s40042-021-00137-8.

[258] T. Tansel *et al.*, 'Effect of the Passivation Layer on the Noise Characteristics of Mid-Wave-Infrared InAs/GaSb Superlattice Photodiodes', *IEEE Photonics Technol. Lett.*, vol. 24, no. 9, pp. 790–792, May 2012, doi: 10.1109/LPT.2012.2188504.

[259] R. Peng, S. Jiao, D. Jiang, H. Li, and L. Zhao, 'Dark current mechanisms and spectral response of SiO2-passivated photodiodes based on InAs/GaSb superlattice', *Thin Solid Films*, vol. 629, pp. 55–59, May 2017, doi: 10.1016/j.tsf.2017.03.045.

[260] Y. Cui, J. Chen, Z. Xu, J. Xu, Y. Zhou, and L. He, 'Studies on different passivation on InAs/GaSb type-II superlattice photodetectors', in *Infrared Technology and Applications, and Robot Sensing and Advanced Control*, SPIE, Nov. 2016, pp. 878–882. doi: 10.1117/12.2247485.

[261] R. Suzuki, K. Ozaki, K. Tsunoda, and H. Nishino, 'ALD-Al2O3 passivation effects on surface characteristics of InAs/GaSb type-II superlattice infrared photodetectors', in *Infrared Technology and Applications XLV*, SPIE, May 2019, pp. 73–78. doi: 10.1117/12.2518574.

[262] T. Specht *et al.*, 'Side Wall Passivation of LWIR P-type Superlattice Detectors using Atomic Layer Deposition', in *2018 IEEE Research and Applications of Photonics In Defense Conference (RAPID)*, Aug. 2018, pp. 1–4. doi: 10.1109/RAPID.2018.8508916.

[263] O. Salihoglu *et al.*, 'Atomic layer deposited Al2O3 passivation of type II InAs/GaSb superlattice photodetectors', *J. Appl. Phys.*, vol. 111, no. 7, p. 074509, Apr. 2012, doi: 10.1063/1.3702567.

[264] G. Chen, B.-M. Nguyen, A. M. Hoang, E. K. Huang, S. R. Darvish, and M. Razeghi, 'Elimination of surface leakage in gate controlled type-II InAs/GaSb mid-infrared photodetectors', *Appl. Phys. Lett.*, vol. 99, no. 18, p. 183503, Oct. 2011, doi: 10.1063/1.3658627.

[265] H. S. Kim *et al.*, 'Performance improvement of InAs/GaSb strained layer superlattice detectors by reducing surface leakage currents with SU-8 passivation', *Appl. Phys. Lett.*, vol. 96, no. 3, p. 033502, Jan. 2010, doi: 10.1063/1.3275711.

[266] H. S. Kim *et al.*, 'Reduction of surface leakage current in InAs/GaSb strained layer long wavelength superlattice detectors using SU-8 passivation', *Appl. Phys. Lett.*, vol. 97, no. 14, p. 143512, Oct. 2010, doi: 10.1063/1.3499290.

[267] K. Jaworowicz, I. Ribet-Mohamed, C. Cervera, J. B. Rodriguez, and P. Christol, 'Noise Characterization of Midwave Infrared InAs/GaSb Superlattice pin Photodiode', *IEEE Photonics Technol. Lett.*, vol. 23, no. 4, pp. 242–244, Feb. 2011, doi: 10.1109/LPT.2010.2093877.

[268] H. Hao *et al.*, 'Sulfurizing method for passivation used in InAs/GaSb type-II superlattice photodetectors', in *International Symposium on Optoelectronic Technology and Application 2014: Infrared Technology and Applications*, International Society for Optics and Photonics, Nov. 2014, p. 93001K. doi: 10.1117/12.2072179.

[269] C. Guo *et al.*, 'Sulfide treatment passivation of mid-/long-wave dual-color infrared detectors based on type-II InAs/GaSb superlattices', *Opt. Quantum Electron.*, vol. 51, no. 3, p. 73, Feb. 2019, doi: 10.1007/s11082-019-1779-y.

[270] K. Banerjee, S. Ghosh, E. Plis, and S. Krishna, 'Study of Short- and Long-Term Effectiveness of Ammonium Sulfide as Surface Passivation for InAs/GaSb Superlattices Using X-Ray Photoelectron Spectroscopy', *J. Electron. Mater.*, vol. 39, no. 10, pp. 2210–2214, Oct. 2010, doi: 10.1007/s11664-010-1298-x.

[271] K. Banerjee *et al.*, 'Surface study of thioacetamide and zinc sulfide passivated long wavelength infrared type-II strained layer superlattice', in *Infrared Technology and Applications XXXVII*, SPIE, Jun. 2011, pp. 1323–1330. doi: 10.1117/12.900198.

[272] O. Salihoglu, A. Muti, and A. Aydinli, 'Thiol passivation of MWIR type II superlattice photodetectors', in *Infrared Technology and Applications XXXIX*, SPIE, Jun. 2013, pp. 251–256. doi: 10.1117/12.2015521.

[273] E. A. D. Jr, J. W. Little, and N. Baril, 'Addressing surface leakage in type-II InAs/GaSb superlattice materials using novel approaches to surface passivation', in *Infrared Sensors, Devices, and Applications; and Single Photon Imaging II*, International Society for Optics and Photonics, Sep. 2011, p. 815508. doi: 10.1117/12.895448.

[274] E. Plis, M. N. Kutty, S. Myers, S. Krishna, C. Chen, and J. D. Phillips, 'Passivation of long-wave infrared InAs/GaSb superlattice detectors with epitaxially grown ZnTe', in *Infrared Technology and Applications XL*, SPIE, Jun. 2014, pp. 289–296. doi: 10.1117/12.2050490.

[275] J. A. Nolde *et al.*, 'Reticulated shallow etch mesa isolation for controlling surface leakage in GaSb-based infrared detectors', *Appl. Phys. Lett.*, vol. 111, no. 5, p. 051102, Jul. 2017, doi: 10.1063/1.4997172.

[276] L. Höglund *et al.*, 'Influence of shallow versus deep etching on dark current and quantum efficiency in InAs/GaSb superlattice photodetectors and focal plane arrays for long wavelength infrared detection', *Infrared Phys. Technol.*, vol. 95, pp. 158–163, Dec. 2018, doi: 10.1016/j.infrared.2018.10.036.

[277] E. H. Steenbergen *et al.*, 'Structural and optical characterization of type-II InAs/InAs1−xSbx superlattices grown by metalorganic chemical vapor deposition', *Appl. Phys. Lett.*, vol. 99, no. 7, p. 071111, Aug. 2011, doi: 10.1063/1.3625429.

[278] Y. Huang *et al.*, 'Strain-balanced InAs/GaSb type-II superlattice structures and photodiodes grown on InAs substrates by metalorganic chemical vapor deposition', *Appl. Phys. Lett.*, vol. 99, no. 1, p. 011109, Jul. 2011, doi: 10.1063/1.3609240.

[279] G. Binnig, H. Rohrer, Ch. Gerber, and E. Weibel, 'Surface Studies by Scanning Tunneling Microscopy', *Phys. Rev. Lett.*, vol. 49, no. 1, pp. 57–61, Jul. 1982, doi: 10.1103/PhysRevLett.49.57.

[280] B. Bhushan, *Introduction to Tribology*. John Wiley & Sons, 2013.

[281] S. V. Kalinin and A. Gruverman, *Scanning Probe Microscopy of Functional Materials: Nanoscale Imaging and Spectroscopy*. Springer Science & Business Media, 2010.

[282] T. Alford, L. C. Feldman, and J. W. Mayer, *Fundamentals of nanoscale film analysis*. Springer US, 2007. doi: 10.1007/978-0-387-29261-8.

[283] W. Zhou and Z. L. Wang, *Scanning Microscopy for Nanotechnology: Techniques and Applications*. Springer Science & Business Media, 2007.

[284] K. S. Birdi, *Scanning Probe Microscopes: Applications in Science and Technology*. Boca Raton: CRC Press, 2003. doi: 10.1201/9780203011072.

[285] A. Romano, J. Vanhellemont, H. Bender, and J. R. Morante, 'A fast preparation technique for high-quality plan view and cross-section TEM specimens of semiconducting materials', *Ultramicroscopy*, vol. 31, no. 2, pp. 183–192, Oct. 1989, doi: 10.1016/0304-3991(89)90212-X.

[286] J.-M. Masur, R. Rehm, J. Schmitz, L. Kirste, and M. Walther, 'Four-component superlattice empirical pseudopotential method for InAs/GaSb superlattices', *Infrared Phys. Technol.*, vol. 61, pp. 129–133, Nov. 2013, doi: 10.1016/j.infrared.2013.07.014.

[287] K. Akel, M. Hostut, T. Akin, and Y. Ergün, 'Interband optical absorption obtained by pseudopotential method for type-II InAs/GaSb SL photodetectors', *J. Phys. Appl. Phys.*, 2021, doi: 10.1088/1361-6463/abe3ae.

[288] Y. Wei and M. Razeghi, 'Modeling of type-II InAs/GaSb superlattices using an empirical tight-binding method and interface engineering', *Phys. Rev. B*, vol. 69, no. 8, p. 085316, Feb. 2004, doi: 10.1103/PhysRevB.69.085316.

[289] J. Zhi *et al.*, 'Research on empirical tight-binding method calculation energy band of InAs/InAsSb superlattice', in *2021 International Conference on Optical Instruments and Technology: IRMMW-THz Technologies and Applications*, SPIE, Jul. 2022, pp. 76–84. doi: 10.1117/12.2619369.

[290] M. Cardona and F. H. Pollak, 'Energy-Band Structure of Germanium and Silicon: The k.p Method', *Phys. Rev.*, vol. 142, no. 2, pp. 530–543, Feb. 1966, doi: 10.1103/PhysRev.142.530.

[291] S. Boyer-Richard *et al.*, '30-band k·p method for quantum semiconductor heterostructures', *Appl. Phys. Lett.*, vol. 98, no. 25, p. 251913, Jun. 2011, doi: 10.1063/1.3600643.

[292] C. Y.-P. Chao and S. L. Chuang, 'Spin-orbit-coupling effects on the valence-band structure of strained semiconductor quantum wells', *Phys. Rev. B*, vol. 46, no. 7, pp. 4110–4122, Aug. 1992, doi: 10.1103/PhysRevB.46.4110.

[293] T. B. Bahder, 'Eight-band k.p model of strained zinc-blende crystals', *Phys. Rev. B*, vol. 41, no. 17, pp. 11992–12001, Jun. 1990, doi: 10.1103/PhysRevB.41.11992.

[294] T. Andlauer, 'Optoelectronic and spin-related properties of semiconductor nanostructures in magnetic fields', Technische Universität München, 2009. Accessed: Nov. 01, 2023. [Online]. Available: https://mediatum.ub.tum.de/681090

[295] S. Birner, 'Modeling of semiconductor nanostructures and semiconductor-electrolyte interfaces', Nov. 2011, Accessed: Nov. 01, 2023. [Online]. Available: https://www.osti.gov/etdeweb/biblio/21538992

[296] Hestenes, M. R and Stiefel, E, *Methods of Conjugate Gradients for Solving Linear Systems*, vol. 49. , J. Res. Nat. Bur. Stand., 1952.

[297] T. F. Chan and T. Szeto, 'Composite Step Product Methods for Solving Nonsymmetric Linear Systems', *SIAM J. Sci. Comput.*, vol. 17, no. 6, pp. 1491–1508, Nov. 1996, doi: 10.1137/S1064827594269202.

[298] C. J. Lanczos, 'Solution of systems of linear equations by minimized iterations', *J Res Nat Bur Stand*, vol. 49, pp. 33–53, 1952.

[299] 'nextnano++'. Accessed: Jun. 02, 2021. [Online]. Available: https://www.nextnano.de/nextnanoplus/

[300] 'nextnano3 - next generation 3D nano device simulator'. Accessed: Aug. 18, 2021. [Online]. Available: https://www.nextnano.de/nextnano3/

[301] S. B. A *et al.*, 'Modeling of Semiconductor Nanostructures with nextnano 3', *Acta Phys. Polon.*, vol. 110, pp. 111–124, 2006.

[302] I. Vurgaftman, J. R. Meyer, and L. R. Ram-Mohan, 'Band parameters for III–V compound semiconductors and their alloys', *J. Appl. Phys.*, vol. 89, no. 11, pp. 5815–5875, Jun. 2001, doi: 10.1063/1.1368156.

[303] E. Halvorsen, Y. Galperin, and K. A. Chao, 'Optical transitions in broken gap heterostructures', *Phys. Rev. B*, vol. 61, no. 24, pp. 16743–16749, Jun. 2000, doi: 10.1103/PhysRevB.61.16743.

[304] S.-H. Wei and A. Zunger, 'Predicted band-gap pressure coefficients of all diamond and zinc-blende semiconductors: Chemical trends', *Phys. Rev. B*, vol. 60, no. 8, pp. 5404–5411, Aug. 1999, doi: 10.1103/PhysRevB.60.5404.

[305] P. C. Klipstein, 'Operator ordering and interface-band mixing in the Kane-like Hamiltonian of lattice-matched semiconductor superlattices with abrupt interfaces', *Phys. Rev. B*, vol. 81, no. 23, p. 235314, Jun. 2010, doi: 10.1103/PhysRevB.81.235314.

[306] H. J. Haugan, F. Szmulowicz, J. J. Hudgins, L. E. Cordonnier, and G. J. Brown, 'Effect of antimony segregation on the electronic properties of InAs/InAsSb superlattices', in *Infrared Sensors, Devices, and Applications VII*, International Society for Optics and Photonics, Aug. 2017, p. 104040W. doi: 10.1117/12.2271047.

[307] J. A. Keen, D. Lane, M. Kesaria, A. R. J. Marshall, and A. Krier, 'InAs/InAsSb type-II strained-layer superlattices for mid-infrared LEDs', *J. Phys. Appl. Phys.*, vol. 51, no. 7, p. 075103, Jan. 2018, doi: 10.1088/1361-6463/aaa60e.

[308] M. Delmas, D. Kwan, M. Debnath, B. Liang, and D. Huffaker, 'Flexbility of Ga-containing Type-II superlattice for long-wavelength infrared detection', *J. Phys. Appl. Phys.*, 2019, doi: 10.1088/1361-6463/ab3b6a.

[309] T. F. Refaat, M. N. Abedin, V. Bhagwat, I. B. Bhat, P. S. Dutta, and U. N. Singh, 'InGaSb photodetectors using an InGaSb substrate for 2μm applications', *Appl. Phys. Lett.*, vol. 85, no. 11, pp. 1874–1876, Sep. 2004, doi: 10.1063/1.1787893.

[310] 'SILVACO ATLAS$^{TM}$ User's Manual'. Accessed: Mar. 16, 2022. [Online]. Available: https://dynamic.silvaco.com/dynamicweb/jsp/downloads/ DownloadManualsAction.do?req=silentmanuals&nm=atlas

[311] Ray-Ming Lin *et al.*, 'Room temperature unpassivated InAs p-i-n photodetectors grown by molecular beam epitaxy', *IEEE Trans. Electron Devices*, vol. 44, no. 2, pp. 209–213, Feb. 1997, doi: 10.1109/16.557708.

[312] M. Delmas, J.-B. Rodriguez, and P. Christol, 'Electrical modeling of InAs/GaSb superlattice mid-wavelength infrared pin photodiode to analyze experimental dark current characteristics', *J. Appl. Phys.*, vol. 116, no. 11, p. 113101, Sep. 2014, doi: 10.1063/1.4895983.

[313] K. Banerjee, J. Huang, and S. Ghosh, 'Modeling and simulation of long-wave infrared InAs/GaSb strained layer superlattice photodiodes with different passivants', *Infrared Phys. Technol.*, vol. 54, no. 6, pp. 460–464, Nov. 2011, doi: 10.1016/j.infrared.2011.08.003.

[314] Wolfram Research, Inc., 'Mathematica'. Wolfram Research, Inc., Champaign, Illinois, 2021. Accessed: Apr. 19, 2022. [Online]. Available: https://www.wolfram.com/mathematica

[315] Origin (Pro), 'OriginLab: Origin and OriginPro: Data Analysis and Graphing Software'. OriginLab Corporation, Northampton, MA, USA, 2017. Accessed: Apr. 19, 2022. [Online]. Available: https://www.originlab.com/

[316] V. Gopal, S. Gupta, R. K. Bhan, R. Pal, P. K. Chaudhary, and V. Kumar, 'Modeling of dark characteristics of mercury cadmium telluride n+–p junctions', *Infrared Phys. Technol.*, vol. 44, no. 2, pp. 143–152, Apr. 2003, doi: 10.1016/S1350-4495(02)00185-8.

[317] V. Gopal, N. Gautam, E. Plis, and S. Krishna, 'Modelling of current-voltage characteristics of infrared photo-detectors based on type – II InAs/GaSb super-lattice diodes with unipolar blocking layers', *AIP Adv.*, vol. 5, no. 9, p. 097132, Sep. 2015, doi: 10.1063/1.4930978.

[318] M. Seta, H. Asahi, S. G. Kim, K. Asami, and S. Gonda, 'Gas source molecular beam epitaxy/migration enhanced epitaxy growth of InAs/AlSb superlattices', *J. Appl. Phys.*, vol. 74, no. 8, pp. 5033–5037, Oct. 1993, doi: 10.1063/1.354284.

[319] W. Pickin and J. P. R. David, 'Carrier decay in GaAs quantum wells', *Appl. Phys. Lett.*, vol. 56, no. 3, pp. 268–270, Jan. 1990, doi: 10.1063/1.102805.

[320] Z. Xu *et al.*, 'Interface design and properties in InAs/GaSb type-II superlattices grown by molecular beam epitaxy', in *International Symposium on Photoelectronic Detection and Imaging 2013: Infrared Imaging and Applications*, International Society for Optics and Photonics, Sep. 2013, p. 89073J. doi: 10.1117/12.2034009.

[321] R. L. S. Devine, 'Photoluminescence characterisation of InGaAs/GaAs quantum well structures', *Semicond. Sci. Technol.*, vol. 3, no. 12, pp. 1171–1176, Dec. 1988, doi: 10.1088/0268-1242/3/12/004.

[322] J. A. Keen, E. Repiso, Q. Lu, M. Kesaria, A. R. J. Marshall, and A. Krier, 'Electroluminescence and photoluminescence of type-II InAs/InAsSb strained-layer superlattices in the mid-infrared', *Infrared Phys. Technol.*, vol. 93, pp. 375–380, Sep. 2018, doi: 10.1016/j.infrared.2018.08.001.

[323] Y. P. Varshni, 'Temperature dependence of the energy gap in semiconductors', *Physica*, vol. 34, no. 1, pp. 149–154, Jan. 1967, doi: 10.1016/0031-8914(67)90062-6.

[324] B. Klein *et al.*, 'Varshni parameters for InAs/GaSb strained layer superlattice infrared photodetectors', *J. Phys. Appl. Phys.*, vol. 44, no. 7, p. 075102, Jan. 2011, doi: 10.1088/0022-3727/44/7/075102.

[325] P. Martyniuk *et al.*, 'Modeling of midwavelength infrared InAs/GaSb type II superlattice detectors', *Opt. Eng.*, vol. 52, no. 6, p. 061307, Jan. 2013, doi: 10.1117/1.OE.52.6.061307.

[326] D. Brunner *et al.*, 'Optical constants of epitaxial AlGaN films and their temperature dependence', *J. Appl. Phys.*, vol. 82, no. 10, pp. 5090–5096, Nov. 1997, doi: 10.1063/1.366309.

[327] A. Fasolino, E. Molinari, and J. C. Maan, 'Calculated superlattice and interface phonons of InAs/GaSb superlattices', *Phys. Rev. B*, vol. 33, no. 12, pp. 8889–8891, Jun. 1986, doi: 10.1103/PhysRevB.33.8889.

[328] J. Wu, Z. Xu, J. Chen, and L. He, 'Temperature-dependent photoluminescence of the InAs-based and GaSb-based type-II superlattices', *Infrared Phys. Technol.*, vol. 92, pp. 18–23, Aug. 2018, doi: 10.1016/j.infrared.2018.05.004.

[329] M. Wojdyr, 'Fityk: a general-purpose peak fitting program', *J. Appl. Crystallogr.*, vol. 43, no. 5, pp. 1126–1128, Oct. 2010, doi: 10.1107/S0021889810030499.

[330] J. C. Kim *et al.*, 'Controlling interfacial disorder and strain of W-structured type-II superlattices using As2 flux', *J. Cryst. Growth*, vol. 303, no. 2, pp. 515–519, May 2007, doi: 10.1016/j.jcrysgro.2007.01.016.

[331] Z. Xu, J. Chen, F. Wang, Y. Zhou, C. Jin, and L. He, 'Interface layer control and optimization of InAs/GaSb type-II superlattices grown by molecular beam epitaxy', *J. Cryst. Growth*, vol. 386, pp. 220–225, Jan. 2014, doi: 10.1016/j.jcrysgro.2013.10.024.

[332] C. Weisbuch, R. Dingle, A. C. Gossard, and W. Wiegmann, 'Optical characterization of interface disorder in GaAs-Ga1-xAlxAs multi-quantum well structures', *Solid State Commun.*, vol. 38, no. 8, pp. 709–712, May 1981, doi: 10.1016/0038-1098(81)90401-4.

[333] R. Liu *et al.*, 'Mid-infrared emission from In(Ga)Sb layers on InAs(Sb)', *Opt. Express*, vol. 22, no. 20, pp. 24466–24477, Oct. 2014, doi: 10.1364/OE.22.024466.

[334] M. Jo, M. Sato, S. Miyamura, H. Sasakura, H. Kumano, and I. Suemune, 'Origin of the blueshift of photoluminescence in a type-II heterostructure', *Nanoscale Res. Lett.*, vol. 7, no. 1, p. 654, Nov. 2012, doi: 10.1186/1556-276X-7-654.

[335] E. H. Steenbergen, J. A. Massengale, V. M. Cowan, Z. Lin, Y.-H. Zhang, and C. P. Morath, 'Proton radiation effects on the photoluminescence of infrared InAs/InAsSb superlattices', in *Nanophotonics and Macrophotonics for Space Environments VII*,

International Society for Optics and Photonics, Sep. 2013, p. 887609. doi: 10.1117/12.2026872.

[336] C. G. Burguete *et al.*, 'Direct growth of InAs/GaSb type II superlattice photodiodes on silicon substrates', *IET Optoelectron.*, vol. 12, no. 1, pp. 2–4, 2018, doi: 10.1049/iet-opt.2017.0078.

[337] J.-B. Wang, D. Ding, S. R. Johnson, S.-Q. Yu, and Y.-H. Zhang, 'Determination and improvement of spontaneous emission quantum efficiency in GaAs/AlGaAs heterostructures grown by molecular beam epitaxy', *Phys. Status Solidi B*, vol. 244, no. 8, pp. 2740–2751, 2007, doi: https://doi.org/10.1002/pssb.200675612.

[338] M. Kesaria, D. Alshahrani, D. Kwan, E. Anyebe, and V. Srivastava, 'Optical and electrical performance of 5 μm InAs/GaSb Type-II superlattice for NOx sensing application', *Mater. Res. Bull.*, p. 111424, May 2021, doi: 10.1016/j.materresbull.2021.111424.

[339] K. Mahalingam, H. J. Haugan, G. J. Brown, and A. J. Aronow, 'Strain analysis of compositionally tailored interfaces in InAs/GaSb superlattices', *Appl. Phys. Lett.*, vol. 103, no. 21, p. 211605, Nov. 2013, doi: 10.1063/1.4833536.

[340] G. J. Sullivan *et al.*, 'Molecular beam epitaxy growth of high quantum efficiency InAs/GaSb superlattice detectors', *J. Vac. Sci. Technol. B Microelectron. Nanometer Struct. Process. Meas. Phenom.*, vol. 23, no. 3, p. 1144, Jun. 2005, doi: 10.1116/1.1928238.

[341] G. Feng, J. Suda, and T. Kimoto, 'Nonradiative recombination at threading dislocations in 4H-SiC epilayers studied by micro-photoluminescence mapping', *J. Appl. Phys.*, vol. 110, no. 3, p. 033525, Aug. 2011, doi: 10.1063/1.3622336.

[342] Ł. Ciura, A. Kolek, J. Wróbel, W. Gawron, and A. Rogalski, '1/f Noise in Mid-Wavelength Infrared Detectors With InAs/GaSb Superlattice Absorber', *IEEE Trans. Electron Devices*, vol. 62, no. 6, pp. 2022–2026, Jun. 2015, doi: 10.1109/TED.2015.2423555.

[343] P. Christol, C. Cervera, J. B. Rodriguez, K. Jaworowicz, and I. Ribet-Mohamed, 'Asymmetric InAs/GaSb superlattice pin photodiode to improve temperature operation', in *Quantum Sensing and Nanophotonic Devices VIII*, SPIE, Jan. 2011, pp. 381–390. doi: 10.1117/12.869631.

[344] D. Donetsky, G. Belenky, S. Svensson, and S. Suchalkin, 'Minority carrier lifetime in type-2 InAs–GaSb strained-layer superlattices and bulk HgCdTe materials', *Appl. Phys. Lett.*, vol. 97, no. 5, p. 052108, Aug. 2010, doi: 10.1063/1.3476352.

[345] H. Inada *et al.*, 'Pretreatment for surface leakage current reduction in type-II superlattice MWIR photodetectors', in *Infrared Technology and Applications XL*, SPIE, Jun. 2014, pp. 289–294. doi: 10.1117/12.2053190.

[346] S. L. Tan *et al.*, 'Dry etching and surface passivation techniques for type-II InAs/GaSb superlattice infrared detectors', in *Optics and Photonics for Counterterrorism and Crime*

*Fighting VI and Optical Materials in Defence Systems Technology VII*, International Society for Optics and Photonics, Oct. 2010, p. 783814. doi: 10.1117/12.864787.

[347] M. Erkus, O. Senel, and U. Serincan, 'Structural, optical and electrical characterization of InAsSb p-π-n photodetector grown on GaAs substrate', *Thin Solid Films*, vol. 616, pp. 141–144, Oct. 2016, doi: 10.1016/j.tsf.2016.08.011.

[348] Y. H. Kim, H. Jung, H. J. Lee, and J. Nah, 'HOT MWIR Detector Development with InAs/InAsSb T2SL nBn Structure', in *2021 International Conference on Electronics, Information, and Communication (ICEIC)*, Jan. 2021, pp. 1–2. doi: 10.1109/ICEIC51217.2021.9369772.

[349] A. M. Itsuno, J. D. Phillips, and S. Velicu, 'Design of an Auger-Suppressed Unipolar HgCdTe NBvN Photodetector', *J. Electron. Mater.*, vol. 41, no. 10, pp. 2886–2892, Oct. 2012, doi: 10.1007/s11664-012-1992-y.

[350] D. O. Alshahrani, M. Kesaria, E. A. Anyebe, V. Srivastava, and D. L. Huffaker, 'Emerging Type-II Superlattices of InAs/InAsSb and InAs/GaSb for Mid-Wavelength Infrared Photodetectors', *Adv. Photonics Res.*, vol. 3, no. 2, p. 2100094, 2022, doi: 10.1002/adpr.202100094.

[351] Y. L. Thi, Y. Kamakura, and N. Mori, 'A comparison of mechanisms for improving dark current characteristics in barrier infrared photodetectors', *Jpn. J. Appl. Phys.*, vol. 59, no. 4, p. 044005, Apr. 2020, doi: 10.35848/1347-4065/ab7e77.

[352] X. Zhang *et al.*, 'High-performance midwavelength infrared detectors based on InAsSb nBn design', *Chin. Phys. B*, vol. 29, no. 6, p. 068501, Jun. 2020, doi: 10.1088/1674-1056/ab8377.

[353] E. Gomółka *et al.*, 'Mid-wave InAs/GaSb superlattice barrier infrared detectors with nBnN and pBnN design', *Bull. Pol. Acad. Sci. Tech. Sci.*, vol. Vol. 66, no. nr 3, 2018, doi: 10.24425/123438.

[354] Y. Ji *et al.*, 'Optimization of surface passivation for suppressing leakage current in GaSb PIN devices', *Electron. Lett.*, vol. 56, no. 25, pp. 1420–1423, 2020, doi: https://doi.org/10.1049/el.2020.2063.

[355] J. Li *et al.*, 'Investigation of anodic sulfidizaiton passivation of InAs/GaSb Type-II superlattice infrared detector', *Opt. Quantum Electron.*, vol. 53, no. 7, p. 384, Jul. 2021, doi: 10.1007/s11082-021-03037-0.

[356] L. Zhang, G. Yao, X. Zhu, X. Cao, and Y. Lv, 'Anodic fluoride passivation ofInAs/GaSb superlattice for mid-/short-wavelength dual-color infrared detector', in *Seventh Symposium on Novel Photoelectronic Detection Technology and Applications*, International Society for Optics and Photonics, Mar. 2021, p. 117639Z. doi: 10.1117/12.2588327.

[357] S. Arafin *et al.*, 'Study of wet and dry etching processes for antimonide-based photonic ICs', *Opt. Mater. Express*, vol. 9, no. 4, pp. 1786–1794, Apr. 2019, doi: 10.1364/OME.9.001786.

[358] Y.-S. Lee, Naseem, P.-L. Wu, Y.-J. Chen, and J.-W. Shi, 'Neat Temporal Performance of InGaAs/InAlAs Single Photon Avalanche Diode With Stepwise Electric Field in Multiplication Layers', *IEEE Access*, vol. 9, pp. 32979–32985, 2021, doi: 10.1109/ACCESS.2021.3060824.

[359] X. Meng *et al.*, 'InGaAs/InAlAs single photon avalanche diode for 1550 nm photons', *R. Soc. Open Sci.*, vol. 3, no. 3, p. 150584, 2016, doi: 10.1098/rsos.150584.

[360] G. Karve *et al.*, 'Geiger mode operation of an In/sub 0.53/Ga/sub 0.47/As-In/sub 0.52/Al/sub 0.48/As avalanche photodiode', *IEEE J. Quantum Electron.*, vol. 39, no. 10, pp. 1281–1286, Oct. 2003, doi: 10.1109/JQE.2003.817244.

[361] X.-Y. Xu *et al.*, 'Wet Etching and Passivation of GaSb-based Very Long Wavelength Infrared Detectors', *Chin. Phys. B*, 2022, doi: 10.1088/1674-1056/ac4cc1.

[362] D. A. Ramirez *et al.*, 'High operating temperature midwave infrared photodetectors based on InAs/GaSb type II strained layer superlattices', in *Nanophotonics and Macrophotonics for Space Environments VIII*, International Society for Optics and Photonics, Sep. 2014, p. 92260Q. doi: 10.1117/12.2064045.

[363] J. Li, A. Dehzangi, D. Wu, R. McClintock, and M. Razeghi, 'Resonant cavity enhanced heterojunction phototransistors based on type-II superlattices', *Infrared Phys. Technol.*, vol. 113, p. 103552, Mar. 2021, doi: 10.1016/j.infrared.2020.103552.

[364] J. B. Rodriguez, P. Christol, L. Cerutti, F. Chevrier, and A. Joullié, 'MBE growth and characterization of type-II InAs/GaSb superlattices for mid-infrared detection', *J. Cryst. Growth*, vol. 274, no. 1–2, pp. 6–13, Jan. 2005, doi: 10.1016/J.JCRYSGRO.2004.09.088.

[365] X. Zhang *et al.*, 'Study on ICP dry etching of GaSb and InAs/GaSb super lattices', in *6th International Symposium on Advanced Optical Manufacturing and Testing Technologies: Optoelectronic Materials and Devices for Sensing, Imaging, and Solar Energy*, SPIE, Oct. 2012, pp. 274–281. doi: 10.1117/12.978177.

[366] H. J. Lee *et al.*, 'Dark current improvement due to dry-etch process in InAs/GaSb type-II superlattice LWIR photodetector with nBn structure', *Infrared Phys. Technol.*, vol. 94, pp. 161–164, Nov. 2018, doi: 10.1016/j.infrared.2018.09.009.

[367] D. M. Cornet, R. R. LaPierre, D. Comedi, and Y. A. Pusep, 'High resolution x-ray diffraction analysis of InGaAs/InP superlattices', *J. Appl. Phys.*, vol. 100, no. 4, p. 043518, Aug. 2006, doi: 10.1063/1.2335689.

[368] T. Schuler-Sandy, 'Investigation of Infrared Detectors Based on the Gallium-free Superlattice', *Electr. Comput. Eng. ETDs*, Jun. 2016, [Online]. Available: https://digitalrepository.unm.edu/ece_etds/229

[369] Z. Taghipour *et al.*, 'Photoluminescence spectroscopy of metamorphic InAsSb on GaAs and Si', *J. Lumin.*, vol. 228, p. 117581, Dec. 2020, doi: 10.1016/j.jlumin.2020.117581.

[370] E. Delli *et al.*, 'Mid-infrared type-II InAs/InAsSb quantum wells integrated on silicon', *Appl. Phys. Lett.*, vol. 117, no. 13, p. 131103, Sep. 2020, doi: 10.1063/5.0022235.

[371] Z.-D. Ning *et al.*, 'Structural and optical properties of InAs/InAsSb superlattices grown by metal organic chemical vapor deposition for mid-wavelength infrared photodetectors', *Appl. Surf. Sci.*, vol. 368, pp. 110–113, Apr. 2016, doi: 10.1016/j.apsusc.2016.01.255.

[372] Y. Chen *et al.*, 'MOCVD growth of InAs/GaSb type-II superlattices on InAs substrates for short wavelength infrared detection', *Infrared Phys. Technol.*, vol. 105, p. 103209, Mar. 2020, doi: 10.1016/j.infrared.2020.103209.